SATF 2018

Science and Applications of Thin Films, Conference & Exhibition

Proceeding Book

September 17 to 21, 2018

Grand Ontur Hotel

Cesme, Izmir, Turkey

www.satf-conf.org

This page intentionally left blank.

Preface

On behalf of the Conference Committee, I would like to warmly thank to everyone participating to the *"Science and Applications of Thin Films, Conference & Exhibition (SATF 2018)"* was held in Grand Ontur Hotel, Cesme, Izmir, Turkey, from September 17 to 21, 2018.

The first series of the conference, SATF 2014, was held in the Altin Yunus Resort & Thermal Hotel, Cesme, Izmir, Turkey, from September 15 to 19, 2014 and the second series of the conference, SATF 2016 was held in Ilica Hotel Spa & Wellness Thermal Resort, Cesme, Izmir, Turkey, from September 19 to 23, 2016. First two conferences hosted above 700 scientists, and the proceedings were published in Vacuum, Applied Surface Science and Thin Solid Films. The main objective of the SATF conferences is to provide a valuable international platform for individuals to present their research findings, display their work in progress and discuss conceptual advances in many different branches of thin films.

SATF 2018 focused on various topics related to Thin Films and novel phenomenas in Thin Film science and applications. The conference was intended to provide an opportunity to bring prominent scientists together from various countries, with a common objective to exchange information and ideas, to promote stimulus discussions and collaborations among participants and furthermore to foster young scientists. The selected Full-Text Manuscripts of SATF 2018 had been evaluated by scientific committee and published in SATF 2018 Proceeding Book. This conference was supported by TUBİTAK 2223B program.

Additionally, Izmir hosts a large number of extremely important architectural and cultural sites. The town is nicknamed as the Pearl of the Aegean and Cesme in İzmir is surrounded by the Aegean Sea in three sides at the very western end of Urla Peninsula and is neighbor of the Sakiz (Chios) Island. My wish is that you took little extra time to enjoy the unique beauty of Cesme and its surroundings.

Finally, we want to express our special gratitude to all the participants, and we would also like to thank our colleagues in the Conference Committee, whose commitment enabled us to achieve our goal. In addition, we appreciate our sponsors for their generous support. In the spirit and tradition of Turkish hospitality, we once more thank you all to participate SATF 2018, I hope you had a nice and enjoyable stay in the Cesme, and you all returned to home feeling recharged and ready to continue the invaluable explorations.

Best regards,

Lutfi Ozyuzer
Chair

Scope of the SATF 2018 Conference & Exhibition

The SATF 2018 international conference will focus on various topics related to Thin Films and novel phenomena in Thin Film science and applications.

More specifically,

- Science of Thin Films and Quantum Effects
- Theory of Structure, Surface and Interface
- Thin Film Growth & Epitaxy
- Nanostructured Growth
- Optical, Optoelectronic and Dielectric Coatings
- Organic Thin Films
- Thin Films in Biology
- Superconducting Thin Films
- Thin Films in Photovoltaic Cells and Energy
- Metallurgical Coatings
- Applications of Electrochemical and Electroless Depositions
- Advances in Deposition Techniques
- Characterization and Instrumentation
- Large Scale Coating and Industry

International Organizing Committee

International Steering Committee

Lutfi Ozyuzer	IZTECH, TURKEY
Gulnur Aygun	IZTECH, TURKEY
Kamil Kosiel	Institute of Electron Technology, POLAND
John L. Reno	Sandia National Laboratories, USA
Mehtap Ozdemir	IZTECH, TURKEY

Local Organizing Committee

Mustafa Guden (Honorary Chair)	Rector of IZTECH, TURKEY
Lutfi Ozyuzer (Chair)	IZTECH, TURKEY
Gurcan Aral	IZTECH, TURKEY
Serkan Ates	IZTECH, TURKEY
Gulnur Aygun	IZTECH, TURKEY
Cem Celebi	IZTECH, TURKEY
Baris Cicek	IZTECH, TURKEY
Mehtap Ozdemir	IZTECH, TURKEY
Ozge Saglam	IUE, TURKEY
Koray Sevim	IZTECH, TURKEY
Enver Tarhan	IZTECH, TURKEY

Scientific Committee

Lutfi Ozyuzer (Chair)	IZTECH, TURKEY
Aysun Aksit	Dokuz Eylul University, TURKEY
Hakan Altan	Middle East Technical University, TURKEY
Serkan Ates	IZTECH, TURKEY
Gulnur Aygun	IZTECH, TURKEY
Petre Badica	National Institute of Materials Physics, ROMANIA
Deepak Kumar Basa	Utkal University, INDIA
Bahar Basım	Ozyegin University, TURKEY
Necdet Basturk	Hacettepe Univ., TURKEY
Basak Bengu	Arçelik Inc., TURKEY
Musa Mutlu Can	İstanbul University, TURKEY
Ayten Cantas	Pamukkale University, TURKEY
Cem Celebi	IZTECH, TURKEY
Kuei-Hsien Chen	National Taiwan University, TAIWAN
Li-Chyong Chen	National Taiwan University, TAIWAN

Supporting Students

Bengü Ata	IZTECH, TURKEY
Merve Ekmekçioğlu	IZTECH, TURKEY
Hasan Köseoğlu	IZTECH, TURKEY
Ece Meriç	IZTECH, TURKEY
Aileen Noori	IZTECH, TURKEY
Sina Rouhi	IZTECH, TURKEY
Uğur Mert Ulutanır	IZTECH, TURKEY
Zemzem Uyanık	IZTECH, TURKEY
Yesim Alduran	IZTECH, TURKEY
Mehmet Yakar	IZTECH, TURKEY
Jose Enrique Martinez Medina	IZTECH, TURKEY

This page intentionally left blank.

TABLE OF CONTENTS

PROCEEDING PAPERS

Friction and wear properties of Nb-V-C-N coatings on AISI 4140 steel by thermo-reactive deposition
Eray Abakay, Bülent Kılınç, Mustafa Durmaz, Şaduman Şena and Uğur Şen 1

The Effect of Deposition Parameters on The Wear and Scratch Properties of TiAlZrN Coatings
Yasar Sert, T. Kucukomeroglu, L. Kara, I. Efeoglu 13

The Surface-Plasmon - Optical Soliton Photonic Josephson Junction
Kaan Güven 23

Sol-gel processed niobium-doped titanium dioxide for transparent conductive coatings
Mirjam Skof, Adam Walker, Geraldine Durand, Nicholas Farmilo, Aseel Hassan 31

Crystal structure and surface phase composition of palladium oxides thin films for gas sensors
Alexander Samoylov, Stanislav Ryabtsev, Olga Chuvenkova, Sergey Ivkov, Mikhail Sharov, Sergey Turishchev 43

Nonlinear optical properties of hydrogenated amorphous silicon-chalcogen alloys thin films
Shawqi Al Dallal, Khalil Ebrahim Jasim, and Fryad Henari 57

The effect of Mg:ZnO films deposit on porous ceramic for the structural, morphological and photocatalytic properties
D. Bouras, A. Mecif, B. Regis, A. Harabi and M. Zaabat 67

Investigation of Bacterial Adhesion to Plasma-Modified Polypropylene Surface
Dogan Mansuroglu, Busra Aktas and Ilker U. Uzun-Kaymak 75

Plasma Characteristics Aiding the Enhancement of Surface Properties of Polyethylene
Dogan Mansuroglu, Devrim Ozdemir and Ilker U. Uzun-Kaymak 81

Co-doped ZnO Thin Film Nanocomposites as Model Nanocatalysts
Asghar Ali, James Aluha, Redhouane Henda, Nicolas Abatzoglou 87

Thin silver film synthesis on polymeric composite surfaces via electroless deposition technique
İpek Yoldaş, Berrin İkizler, Seçkin Erden 103

Investigation of mechanical and tribological properties of BCN thin films
Gökhan Gülten, İhsan Efeoglu, Yaşar Totik, Ayşenur Keles, Kıvılcım Ersoy, Göksel Durkaya 113

Superconducting Properties of Bi-2212 thin films produced by Pulsed Laser Deposition
B. Özçelik 121

Study of Thin films of Nickel Oxide (NiO) Deposited by the Spray Pyrolysis Method
Antar Bouhank, Y. Bellal, H .Serrar, A.Khiter 125

PEG40St Squeeze out from Lipid Monolayers
Sevgi Kilic and Ekrem Ozdemir 133

Optimization of zinc oxide based metal-semiconductor junction interface properties for optoelectronic device applications
Enver Tarhan and A. Halis Guzelaydin……..…139

Synthesis of MnCo2O4 nanowires on flexible carbon fiber cloth for high-performance supercapacitors
Yasar Ozkan Yesilbag, Fatma Nur Tuzluca and Mehmet Ertugrul..……..149

Efficiency Analysis of CZTS Based Solar Cells
A Cantas and G. Aygun…….157

PROCEEDING PAPERS

This page intentionally left blank.

Science and Applications of Thin Films, Conference & Exhibition (SATF 2018)
Izmir Institute of Technology, Izmir, Turkey, September 17-21, 2018

Friction and wear properties of Nb-V-C-N coatings on AISI 4140 steel by thermo-reactive deposition

Eray Abakay[a]*, Bülent Kılınç[b], Mustafa Durmaz[a], Şaduman Şena and Uğur Şen[a]

[a]*Sakarya University, Department of Metallurgical and Materials Engineering, 54187, Sakarya, Turkey*
[b] *Sakarya University, Arifiye Vocational High School, Department of Machine and Metal Technology, Sakarya, Turkey*

Abstract

Thermo-reactive deposition (TRD) technique is an effective method for obtaining hard coatings that are resistant to wear on the surface of the steel. In this study, Nb-C-N, V-C-N, and Nb-V-C-N based hard coatings were applied on AISI 4140 steel and dry friction and wear properties were investigated. Cylindrical shaped AISI 4140 steel samples were first subjected to nitriding in order to have a nitrogen-rich surface. Subsequently, the TRD coating process was carried out at 1000 ° C for 4 hours with pack cementation technique for all compositions. Ball on disc wear tests via alumina ball as a counterpart at atmospheric conditions was realized. From the test results, the friction coefficients were determined according to applied loads. The depths of the traces formed on the surface of the samples were measured by 2D profilometer and the wear rates were calculated. Wear traces were investigated using scanning electron microscopy (SEM) and energy dispersive X-ray spectroscopy (EDS).

Keywords: Wear, Thermo-Reactive Deposition, Niobium Vanadium Carbonitride Coatings.

Introduction

Although many new materials have been developed, today's steel is still widely used in manufacturing many machine parts. Wear on parts made of steel causes a considerable amount of material loss and consequently a significant cost to manufacturers. The studies to prevent the causes of wear and other materials loss have been continuing for many years. Rather than being resistant to abrasion of an entire part, it is often preferred to obtain a wear-resistant layer on the surface of the workpiece for cost reasons. Methods such as physical vapor deposition, thermal spray coatings, chemical vapor deposition, electrolytic coatings, and thermo reactive deposition are now successfully used for coating material surfaces [1]–[5]. Thermo-reactive diffusion (TRD) method is used to obtain hard coating layers which contain carbide, nitride, carbo-nitride and boride phases of reactive transition metals on the surface of steel parts. The TRD method, which has the advantages of low cost, simple equipment and the physical and mechanical properties of the coated part according to other coating methods, has been used industrially for nearly 50 years. In this method, carbon, nitrogen or boron exist in the substrate material reacts with the transition elements such as vanadium, chromium, niobium, and titanium which are consist of the coating bath. In order to form a coating layer by this method, the substrate material selected must contain enough Carbon, boron or nitrogen. If a lower carbon material is used, it is necessary to make the surfaces rich by carbon, nitrogen or boron elements by applying surface modification processes such as carburization, nitriding, boronizing. The coating process can be realized by using molten salt, fluidized bed, and pack cementation media. In the pack cementation process, the

desired piece is applied by placing in a mixture of powdered bath components in steel or graphite crucibles. In this method, coating layers having a thickness of about 25 μm can be obtained between 850°C and 1150 °C, depending on the increasing time [6]–[10].

In the past, researchers have obtained coating layers containing carbide, nitride or boride phases on steel materials by TRD method and their microstructure, wear and corrosion properties have been investigated. Among the mentioned coatings, the carbide, nitride and boride forms of niobium and vanadium have attracted attention with the high hardness, wear and corrosion resistance they provide and the most studied ones have been studied. Recently, the examination of the properties of coating layers containing carbide forms of two different transition metals subject is interesting. However, in the literature, there is no study of coatings containing nitride forms of two transition elements [10] – [12].

In this study, coating layers containing carbide and nitride phases of niobium and vanadium were obtained by TRD method on AISI 4140 steel surface. The microstructure, dry friction, and wear properties of the coatings obtained were compared with those containing Nb-C-N and V-C-N.

Experimental

AISI 4140 steel substrate material is provided in the form of a rod of 20 mm diameter. The spectral analysis of the substrate is given in Table 1. The samples were first cut to a thickness of 5 mm in height, then gradually grounded to 1200 grid emery paper and cleaned with acetone for 5 minutes. After surface preparation, the samples were nitrided to obtain a nitrogen-rich surface. The active nitration time was 6 hours.

Table 1. The chemical composition of AISI 4140 steel that used in this study.

Element	C	Si	Mn	P	S	Cr	Mo
Mass Percentage (wt. %)	0.41	0.20	0.62	0.02	0.02	0.96	0.19

Nb-C-N, V-C-N and Nb-V-C-N coating processes of the samples after the pretreatment were carried out by the pack cementation process. The coating bath used in this process consists a mixture of ferrous niobium and ferrous vanadium, alumina, ammonium chloride and naphthalene powders. Ferrous-alloys powders provide the necessary niobium and vanadium for the desired coating layer. Commercial ferrous alloys were obtained from AVEKS Company and milled to size of -45 μm by using ring mill. Other bath components; as the alumina filler, ammonium chloride activator and naphthalene were added to remove oxygen contained in the crucible. The coating was carried out at 1000 °C for 4 hours using stainless steel crucibles. Compositions of the coating bath of the produced samples are given in Table 2. The coated samples were taken from the bath after the process, and cleaned with boiling water and the hot air was dried.

Table 2. The chemical composition of coating baths that used in this study

	Ferrous Niobium (wt. %)	Ferrous Vanadium (wt. %)	Alumina (wt. %)	NH_4Cl (wt. %)	Naphthalene (wt. %)
NbCN	50	-	35	14	1
VCN	-	50	35	14	1
NbVCN	25	25	35	14	1

The microstructural examinations and chemical analyzes of the coated samples were realized using scanning electron microscope (SEM - Model JEOL JSM-6060, FEI Co., Japan) coupled with energy dispersive X-ray spectroscopy (EDS). Preparations for metallographic examination of the samples include cutting, molding, grinding, polishing and etching steps. XRD patterns of the samples in Bragg-Brentano θ-2θ geometry were realized with the help of a Rigaku diffractometer (Model D/MAX-B/2200/PC, Rigaku Co., Japan) using copper (Cu) Kα radiation, continuous scanning with a speed of 2°/min. and scanning angles ranging from 20° to 90°.

A ball-on-disc tribometer which made in accordance with ASTM G133-05 standard was used for the dry sliding wear tests. The tests were conducted at room conditions with an alumina ball in 10 mm diameter the as the counter-body. The sliding speed was selected as 0.1 m/s, 0.3 m/s and 0.5 m/s, and sliding distance was 250 m. The applied loads were, 2.5N, 5 N and 10 N. Mean Hertzian contact pressures calculated for the alumina ball under the applied loads were 389 N/mm2, 491 N/mm2, and 618 N/mm2, respectively. Friction coefficient - distance and wear rate - load graphs were plotted using the SigmaPlot 12.5 program. Wear tracks on the samples were examined using by SEM images and EDS analysis.

Results/Discussion

The cross-sectional images show the NbCN, VCN and NbVCN coated AISI 4140 steel, respectively. It is seen that the NbCN coating layer has a smoother, homogeneous and porosity free structure. For VCN and NbVCN coated samples, a transition layer is formed under the coating layer and there are some porosities in the coated layer. Porosity formation occurred in different studies of vanadium nitride coating by TRD method. Although the NbVCN coated sample includes transition layer between steel matrix and coating layer. It was not so much as the transition layer formed in the interface of the VCN-coated samples. The coating layer thickness for the NbCN coated sample is much higher than that of the VCN and NbVCN coatings.

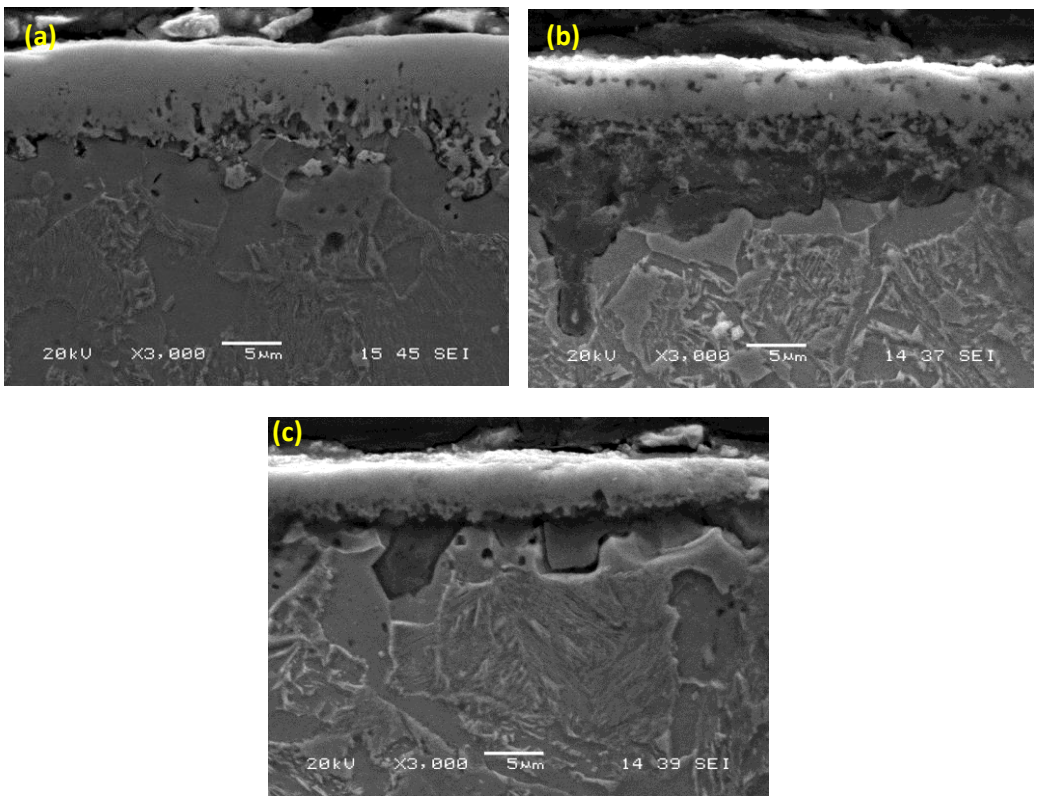

Fig. 1. SEM images of (a) Nb-C-N, (b) V-C-N, and (c) Nb-V-C-N coated samples.

EDS analyzes taken from the section for the NbVCN coated sample are given in the figure 2. The coating layer consists of niobium, and transition zone includes iron and vanadium. In the analysis 3 and 4, the chemical composition of the substrate material was found. Accordingly, for the AISI 4140 steel, a layer formation consisting of carbide, nitride and carbonitride phases formed as a result of the reaction of niobium and vanadium with carbon and nitrogen found in the substrate material. The diffusion of vanadium in the nitrogen and carbon-poor region was realized under the coating and a transition zone containing iron and vanadium phases was formed.

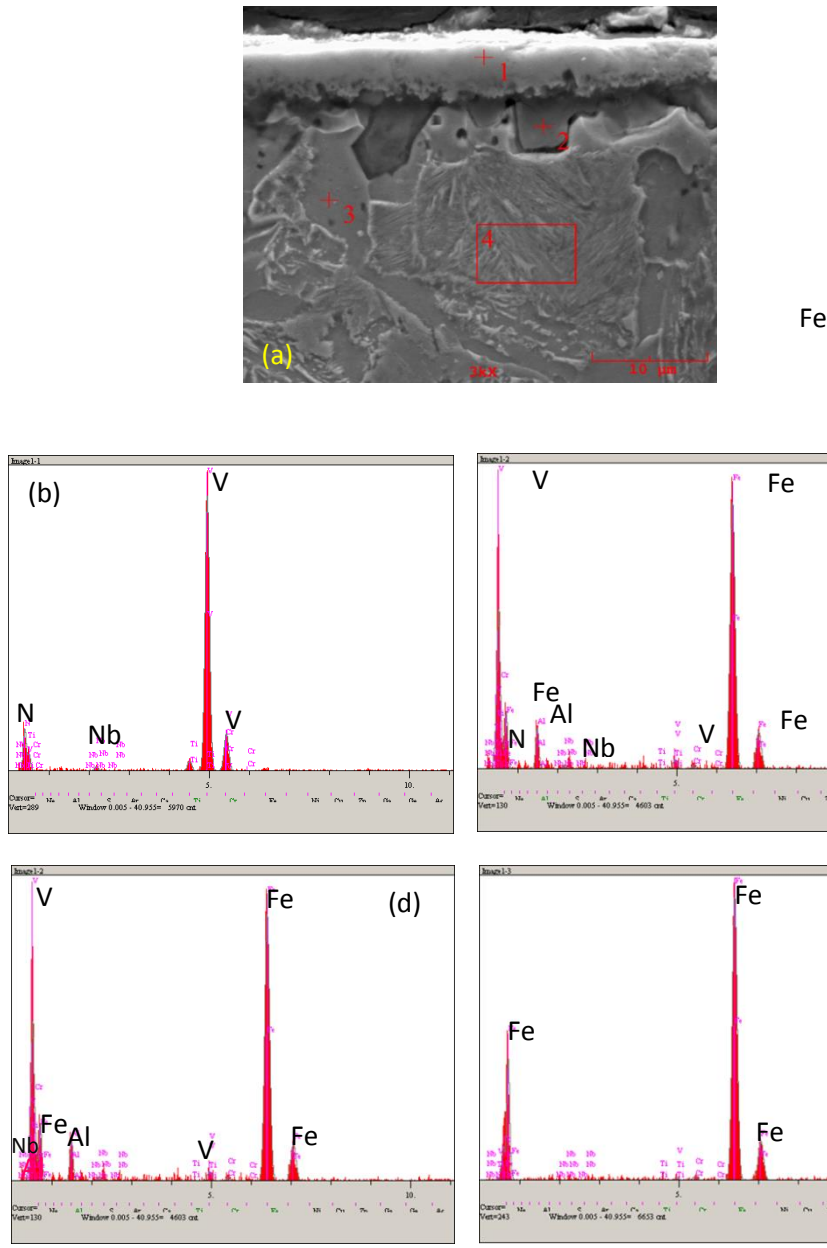

Fig. 2. (a) SEM microstructure from the section of Nb-V-C-N coated sample, (b) - (e) EDS analysis from different regions on the SEM image.

Fig. 3 shows the X-ray diffraction of the coated samples. Nb2CN, NbN and Fe-Cr phases were found for the NbCN coated sample. Similar phases were found in the structure for the previous study by Kocaman and Sen. When the Gibbs free energies are taken into consideration, it is common for said phases of the niobium

to be present in the structure [14], [15]. V6C5 and Fe phases were formed for the VCN coated sample while no nitride based phase was found. In the study conducted by Biesuz and Sglavo, no nitride phase formation was observed in the structure and the situation was thought to be related to carbon diffusion [11]. For the NbVCN coated sample it is seen that the phases in both VCN and NbCN coated samples are formed.

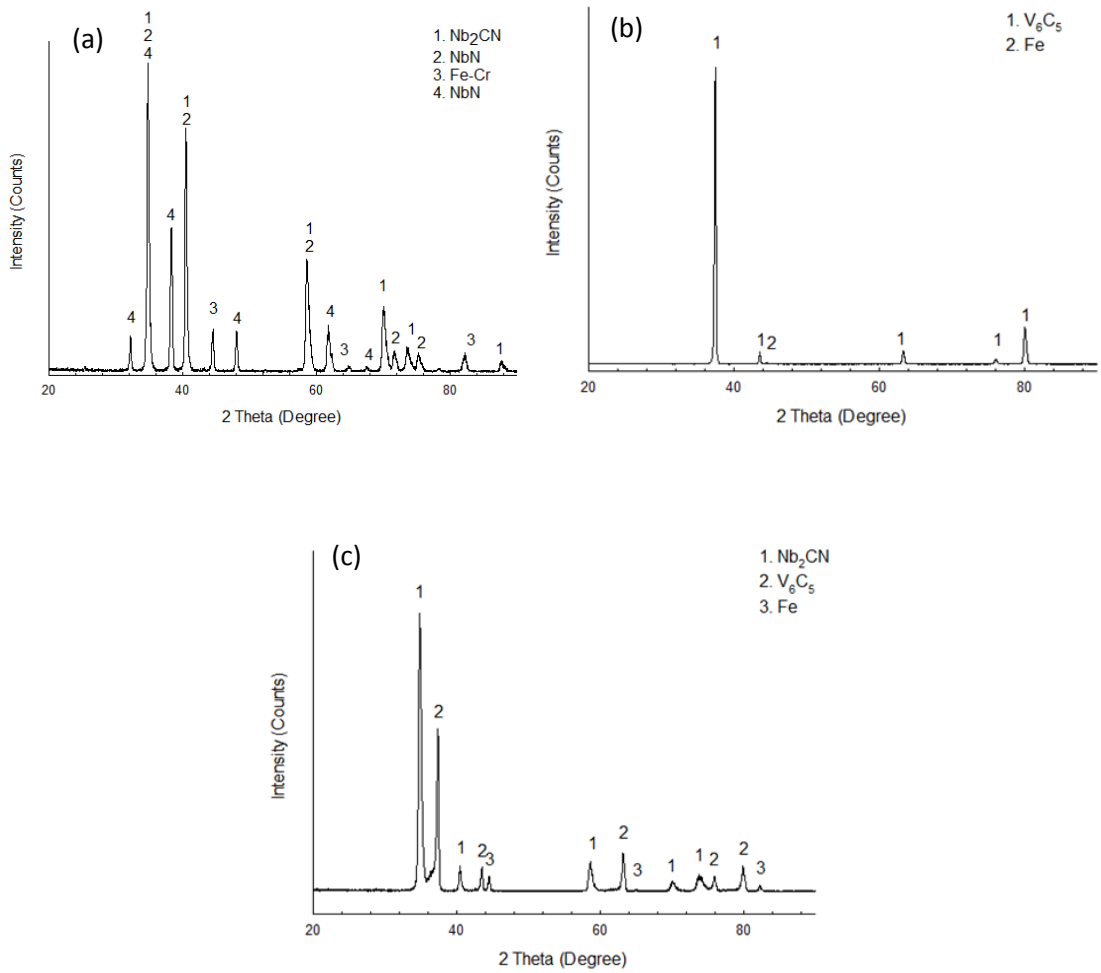

Fig. 3. XRD patterns of (a) Nb-C-N, (b) V-C-N, and (c) Nb-V-C-N coated samples

In the figures 4, friction coefficient-distance graphs are given for loads of 2.5N, 5N and 10N for the samples coated with NbCN, VCN and NbVCN, respectively. The coefficient of friction of NbCN coatings was getting increase up to 10 m and then getting steady state at the sliding conditions of 2.5 N load. The COF was about 0.25+- 0.05. When the applied load increased 5N, the COF was getting increase upto 150m sliding distance and the COF was about 0,48+-0,04. When the applied load was getting increase 10N, the COF was

getting increase up to 50 m sliding distance and then, getting to steady state. The COF value was about 0,48+-0,04. It was similar with the COF measured the loads of 5N. For the VCN coated sample, the coefficient of friction has increased linearly from 0.4 to 0.6 after the running-in distance of approximately 90 m. For the NbVCN coated sample, there was a similar behavior to the VCN-coated sample, but the coefficient of friction showed an increase from 0.2 to 0.4.

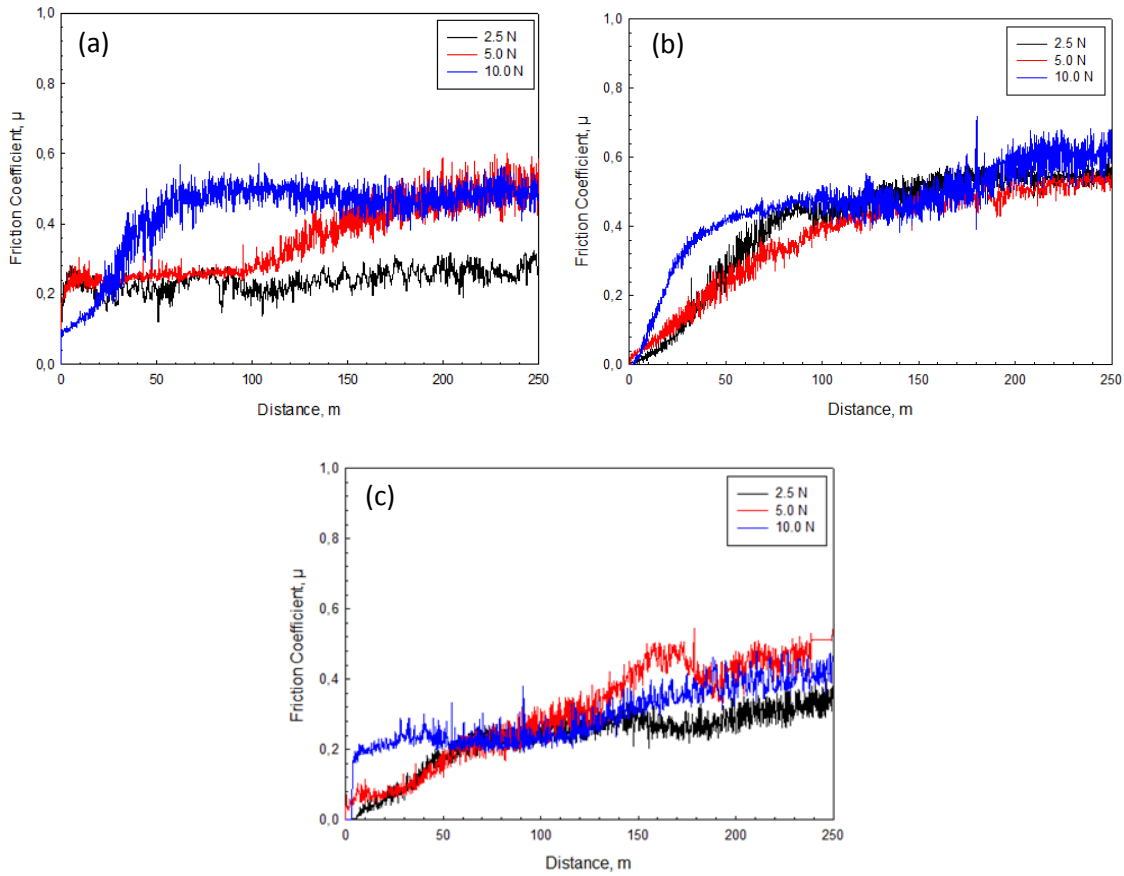

Fig. 4. Friction coefficient – distance graphs of (a) Nb-C-N, (b) V-C-N, and (c) Nb-V-C-N coated samples.

The figure 5 shows the wear rates of the coated samples samples. There was a linear wear behavior for all coatings. The wear rates of NbVCN coating were much lower than that of the VCN and NbCN coatings. The wearv rates of the NbCN, VCN and NbCN coatings were changing between $1.9e^{-4}$ - $2.56e^{-4}$ mm^3/m, $8.59e^{-6}$ - $8.55e^{-5}$ mm^3/m and $1.33e^{-5}$ - $3.57e^{-5}$ mm^3/m, respectively.

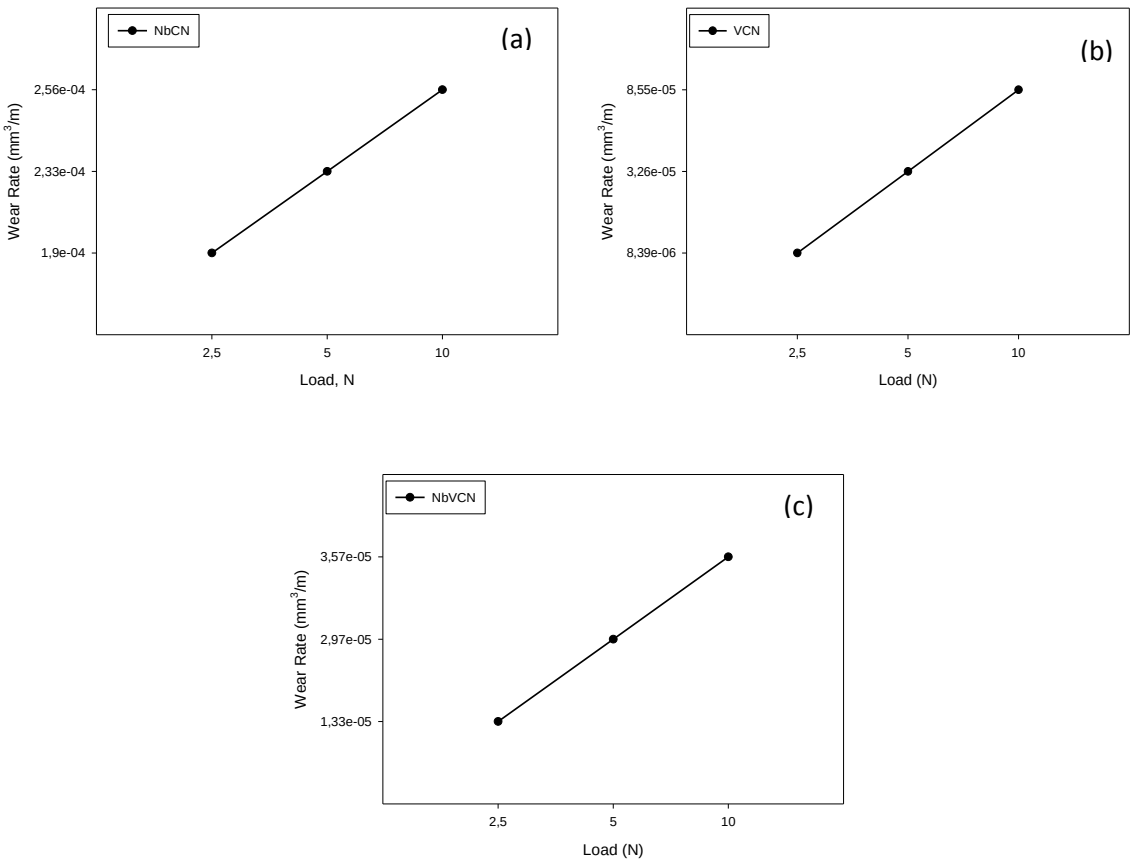

Fig. 5. Wear Rate – load graphs of (a) Nb-C-N, (b) V-C-N, and (c) Nb-V-C-N coated samples.

SEM images of wear tracks formed under 5N load for the coated samples are given in the figure 6. There is no any scratch, cracks or laminations observed on the worn surface of the coated sample with NbCN and it showed only polishing wear. For the VCN coated sample, significant fatigue crack is observed and lamination formation has occurred in some regions on the worn track. NbVCN coated sample showed that polishing wear and some fatigue cracks on the worn track.

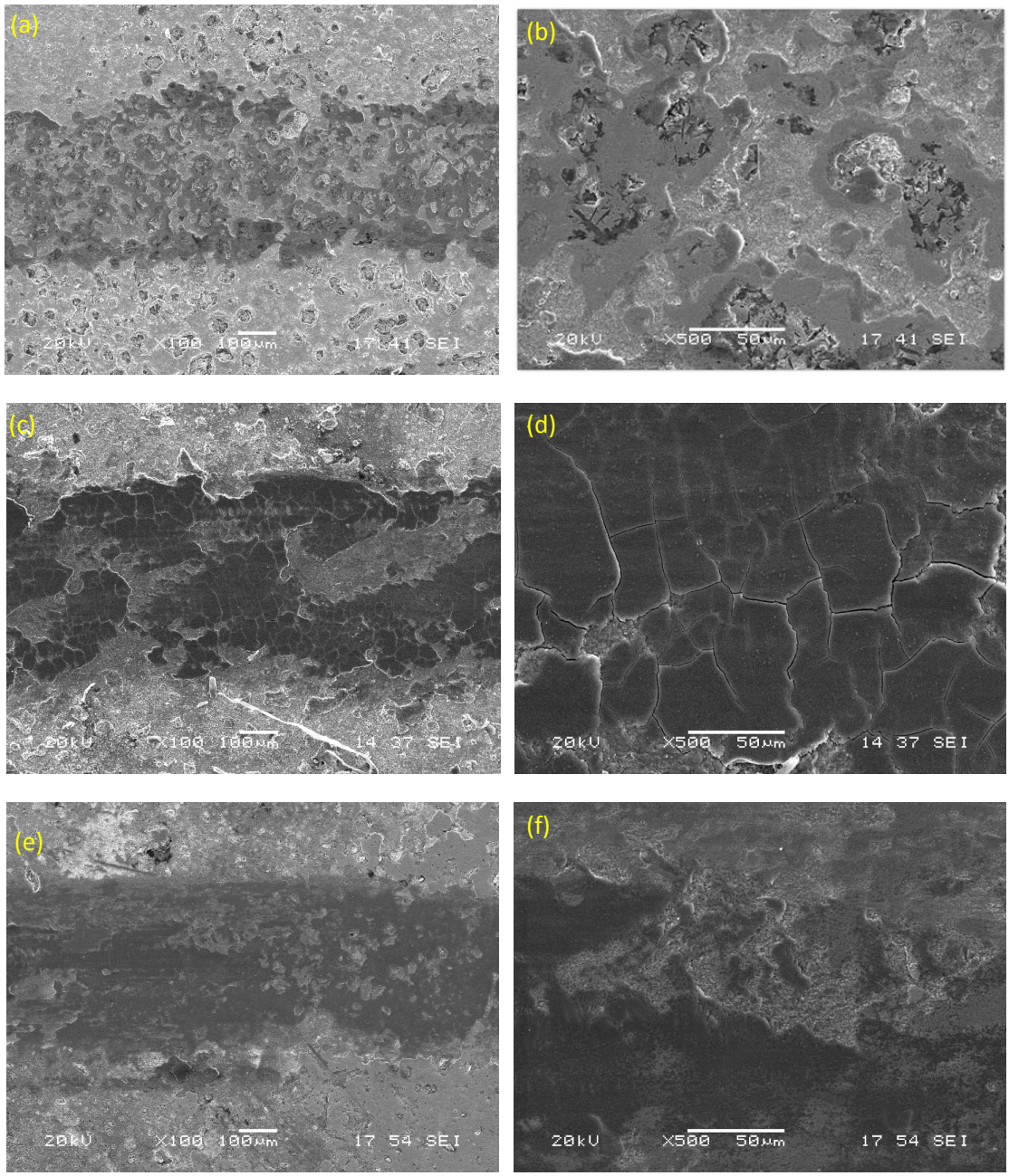

Fig. 6. SEM images of wear tracks for (a)-(b) NbCN, (c)-(d) VCN, and (e)-(f) NbVCN under 5N.

The figure shows the EDS analyzes taken from the wear track formed on the NbVCN coating (for 5N load). In addition to vanadium and niobium, aluminum is also present on the surface. In the presence of aluminum, it can be said that the adhesion of the parts that breaks off the ball during the wear test is effective.

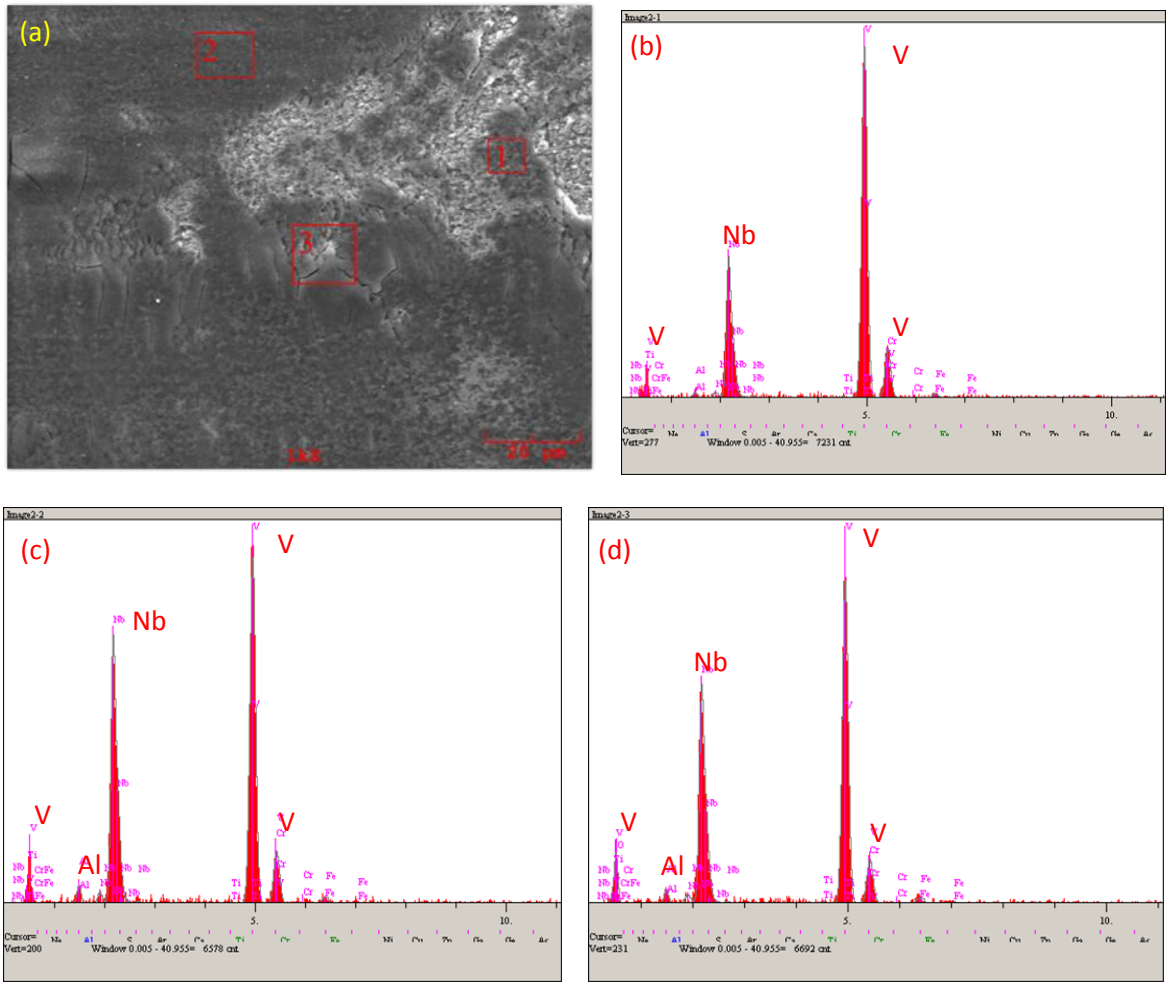

Fig. 7. (a) SEM image and (b)-(d) EDS analyzes of wear tracks for NbVCN coating under 5N.

Conclusion

In this study, NbVCN based coatings were obtained and their properties were compared with NbCN and VCN based coatings. Accordingly, the NbVCN coated sample exhibits similar properties with both NbCN and VCN coated samples. However, it is seen that NbVCN coatings have a high wear resistance compared to NbCN coatings when compared with the wear properties and there is no lamination occurring on the surface of VCN coatings. For the tests carried out under different loads, the friction coefficient was found to be lower for the 5 N and 10 N loads compared to the NbCN and VCN coatings.

References

M. Rezapoor, M. Razavi, M. Zakeri, M.R. Rahimipour, L. Nikzad, 2018. Fabrication of Functionally Graded Fe-TiC Wear Resistant Coating on CK45 Steel Substrate by Plasma Spray and Evaluation of Mechanical Properties. Ceramics International 44, p. 22378-22386.

Tran V. N., Yang S., Phung T. A., 2018. Microstructure and Properties of Cu/TiB2 Wear Resistance Composite Coating on H13 Steel Prepared by In-Situ Laser Cladding. Optics & Laser Technology 108, p. 480-486.

Hacisalihoglu I., Yildiz F., Alsaran A., 2017. Wear Performance of Different Nitride-Based Coatings on Plasma Nitrided AISI M2 Tool Steel in Dry and Lubricated Conditions. Wear 384–385, P. 159-168.

Staszuk M., Pakuła D., Chladek G., Pawlyta M., Pancielejko M., Czaja P., 2018. Investigation of the structure and properties of PVD coatings and ALD + PVD hybrid coatings deposited on sialon tool ceramics, Vacuum 154, p. 272-284.

Bonin L., Vitry V., Delaunois F., 2019. The TiN Stabilization Effect on the Microstructure, Corrosion and Wear Resistance of Electroless NiB Coatings, Surface and Coatings Technology 357, p. 353-363.

T. Arai, 2015. The thermo-reactive deposition and diffusion process for coating steels to improve wear resistance, in "*Thermochemical Surface Engineering of Steels"* E. J. Mittemeijer ve M. A. J. Somers, EditorWoodhead Publishing, Oxford, p. 703-735.

OrjuelaG. A., Rincón R., Olaya J. J., 2014. Corrosion Resistance of Niobium Carbide Coatings Produced on AISI 1045 Steel via Thermo-Reactive Diffusion Deposition", Surface and Coatings Technology 259, p. 667-675.

Oliveira C. K. N., Benassi C. L., Casteletti L. C., 2006. Evaluation of Hard Coatings Obtained on AISI D2 Steel by Thermo-Reactive Deposition Treatment, Surface and Coatings Technology 201, p. 1880-1885.

Tavakoli H., Mousavi Khoie S. M., 2010. An Electrochemical Study of the Corrosion Resistance of Boride Coating Obtained by Thermo-Reactive Diffusion, Materials Chemistry and Physics 124, p. 1134-1138.

Biesuz M., Sglavo V. M., 2016. Chromium and Vanadium Carbide and Nitride Coatings Obtained by TRD Techniques on UNI 42CrMoS4 (AISI 4140) Steel, Surface and Coatings Technology 286, p. 319-326.

Castillejo F. E., Marulanda D. M., Olaya J. J., Alfonso J. E., 2014. Wear and Corrosion Resistance of Niobium–Chromium Carbide Coatings on AISI D2 Produced Through TRD, Surface and Coatings Technology 254, p. 104-111.

Ghadi A., Soltanieh M., Saghafian H., Yang Z. G., 2016. Investigation of Chromium and Vanadium Carbide Composite Coatings on ck45 steel by Thermal Reactive Diffusion, Surface and Coatings Technology 289, p. 1-10.

Sen S., Kocaman K., 2011. Structural Properties and Kinetics of Nitro-Niobized Steels, J Mater Sci. 46, p. 7784-7792.

Kwon H., Kim J., Kim W., 2014. Stability Domains of Nb(CN) During the Carburization/Nitridation of Metallic Niobium, Ceramics International 40, p. 8911-8914.

This page intentionally left blank.

The Effect of Deposition Parameters on The Wear and Scratch Properties of TiAlZrN Coatings

Yasar Sert[a,*], T. Kucukomeroglu[a], L. Kara[b], I. Efeoglu[c]

a Department of Mechanical Engineering, Karadeniz Technical University, 61080, Trabzon, Turkey
b Department of Mechanical Engineering, Erzincan University, Erzincan, Turkey
c Department of Mechanical Engineering, Ataturk University, Erzurum, Turkey

*Corresponding author
E-mail address: ysert0015@gmail.com
Phone: +90538-706-7304

Abstract

The crucial aim of this study to elevate the scratch and wear resistance of heat treated AISI H13 (X40CrMoV5-1) hot work tool steel which is extensively used in aluminium extrusion process as a mold material. With the intention of increase scratch and wear resistance, prelusively, surface of this steel was nitreded. Thereafter, TiAlZrN coating using Pulsed DC closed field unbalanced magnetron sputtering method with different deposition parameters were coated the surface of this steel. Deposition parameters for this coating technique were designated by using Taguchi experimental design method. The coatings thickness and morphological properties of this coatings were investigated using scanning electron microscopy. The results showed that the TiAlZrN-graded composite coatings have 2-3 μm thickness and a dense and columnar structure. Wear properties were determined by a high temperature ball on disk tribotester. Thereafter, the worn surfaces of this coatings were analyzed by an optical profilometer. Wear resistance tests showed that the highest wear strength was attained at 5 A Zr target content, 90 V bias voltages and $2x10^{-3}$ Torr working pressure deposition parameters. Besides, this coating exhibited the highest scratch resistance (79N) compare the other coating samples. Hence, in light of this results, this aforementioned coating parameters were obtained optimum deposition parameters.

[keywords] AISI H13, TiAlZrN, Wear resistance

1.Introduction

Hot work tool steels have been extensively used in a wide range of applications such as an extrusion, injection and forging dies, hot working punchs, aluminum allow casting, hot cutting tools, etc [1]. The most popular amongst this steels being the AISI H13 steel owing to high toughness and ductility, resistance to softening, high level of machinability and high abrasion properties [2-4]. In recent years, due to advancing technology and manufacturing requirement, there is a need to improve mechanical and wear properties of H13 steels in order to enhance service life and production quality. For this aim, researches hard thin coating films on the steel surface have gained momentum. As a result of this researches, it has been determined that the transition metal nitride coatings are conspicuous for previously mentioned applications due to their

tribological and mechanical properties [5-7]. TiN is the first produced coating amongst the transition metal nitrides. However, their properties are not enough for applications as well [8]. Therefore, some of the transition metal elements can be added to enhance scratch and wear resistance of TiN coatings [9,10]. For example, ıt has been established that the wear properties of TiN coatings increase with the addition of the Al [11]. On the other hand, the researchers indicated that the wear properties of quaternary transition metal nitrides were more excellent as to turnary transition metal nitrides [12]. Conducted studies showed that adding Si inside the TiAlN increased the wear resistance of coating [13,14]. Other elements were also studied by the researchers. Addition of Zr into TiAlN coatings also showed remarkable oxidation, mechanical and thermal properties [15,16]. However wear properties and scratch resistance properties of TiAlZrN coating was not investigated efficiently.

As a consequence of these observations, in this study, we investigated the chemical, structural, morphological, scratch and wear resistance properties of TiAlZrN coating which was applied on nitreded AISI H13 steel substrate by pulse DC closed field unbalanced magnetron sputtering deposition. Also during this deposition process, we used some variable deposition parameters to determine the effects on the coatings.

2. Experimental Procedure

In this study, AISI H13 hot work tool steel which is commonly used as a mold material, was purchased from the market. The purchased steels were prepared in the specified dimensions (30mm x 4mm). The disk-shaped samples were heat threated in accordance with literature to prepare for the nitriding process. The nitriding process was performed at 525 ^{o}C for 8 hours. Before the deposition process, the surfaces of the nitrated samples were grounded with SiC papers with 400, 800, 1000, 1500 and 2000 grit and then polished with diamond suspension. The surface roughness value of the samples were measured as 0,05µm±0,002.

After this processes, TiAlZrN- graded composite coatings were deposited by using pulse DC closed unbalanced magnetron sputtering technigue. Pure Ti, Al, Zr elements was used as a targets, N_2 was used as a reactive gas and argon was used as a sputtering gas for deposition. Ti, Al, Zr target currents, frequency, duty time, deposition duration and Ti target current of interlayer were keep constant, bias voltage and working pressure were selected variable parameters as given in Table 1.

Table 1. Deposition Parameters

Constant Parameters	
Target Currents; Ti / Al / Zr (A)	6 / 2 /5
Interlayer Target Current Ti (A)	6
Deposition Duration (min.)	60
Duty Time (µs)	2,5
Frequency (kHz)	100

	Variable Parameters	
Sample Number	**Bias Voltage (-V)**	**Working Pressure (Torr)**
R1	50	$3x10^{-3}$
R2	75	$2,5x10^{-3}$
R3	90	$2x10^{-3}$

Before deposition, ion cleaning was carried out for 15 minutes to remove contamination on the substrate surface. For he purpose of increasing the adhesion of coatings, oxidation resistance and decreasing the residual stress between coating and substrate, the deposition started with Ti under layer for 5 minutes. After that, in order to decrease the thermal stress due to high temperature, TiN layer was coated for 15 minutes. Lastly, TiAlN/TiAlZrN for each layer was deposited for 20 minutes as shown in Figure 1. During the deposition, glass plate and silicon wafer substrates were coated at the same time for using microstructural and cross sectinal analysis.

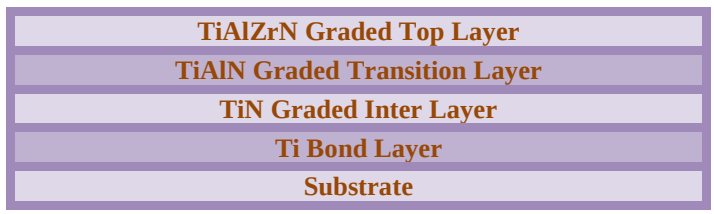

Figure 1. Design consept of the graded composite of TiAlZrN coating

The surface and cross section morphology of coatings were observed by using scanning electron microscope (SEM). Energy dispersive spectroscopy (EDS) were used for elemental analysing. Micro hardness values were measured by Struers Vickers micro hardness tester at 245,3 mN constant load. Adhesion of the TiAlZrN-graded composite films was determined by scratch tester-CSM Revester equipped with a Rockwell C diamond stylus. Worn surfaces were characterized with SEM. The wear properties of coatings were evaluated by using ball-on-disk tribometer. The wear experiment parameters are given in Table 2.

Table 2. Wear experiment parameters

Normal Load (N)	Track Diameter (mm)	Sliding Speed (mm/sn)	Cycle	Counter Body
2	10	60	1600	Al_2O_3

After the wear experiments, wear rates of coatings were measured with optical profilometer and worn surfaces were characterized with SEM.

3. Results and Discussions

3.1. Surface and Cross Section Morphology

The surface morphological SEM photos of coatings are given in Figure 2. The grain size measurements were performed for using SEM photos. The average grain size of coatings are given in Table 3.

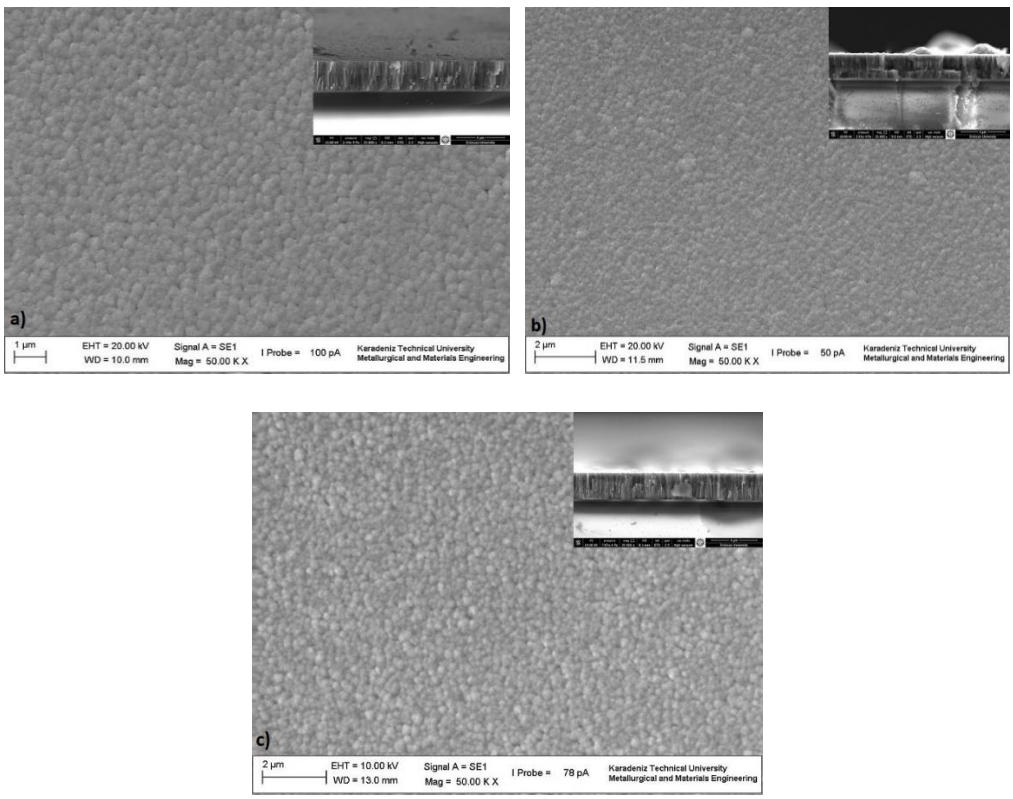

Figure 2. The surface morphology of coatings a) R1 b) R2 c) R3

Table 3. Grain size values of coatings

Sample Number	Grain Size (nm)
R1	430±50
R2	380±50
R3	280±50

All coatings showed granular structure as shown in Figure 2. As Figure 2 and result of the grain size measurements, grain size of R3 coating is relatively smaller than the others and has finer and more compact structure. This can be related with the higher mobility of the adatoms (absorptive atoms) at high bias voltage and low working pressure during deposition process. The results obtained by Yu et al confirmed our finding in this study [17]. Because, of the high bias voltage and low working pressure, the grain size of R3 is smaller than the others due to the sputtered atoms can collide the less amount of gas atoms during their movements to the substrate surface [18].

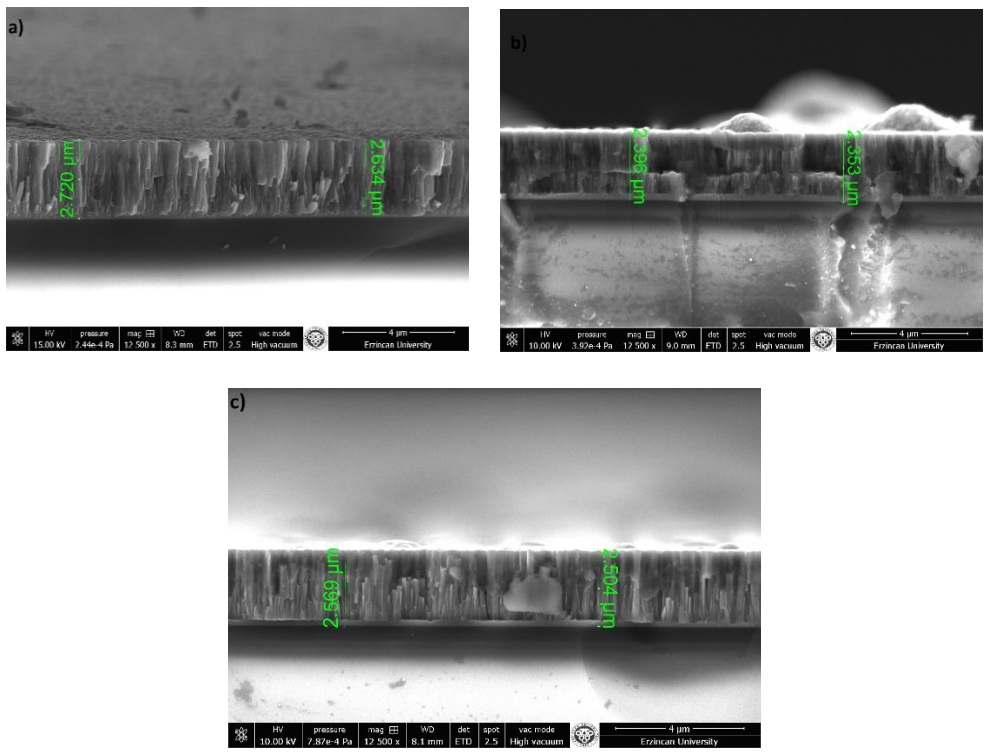

Figure 3. The cross section photos of coatings a) R1 b) R2 c) R3

Table 4. The thicknesses of coatings

Sample Number	Coating Thickness (µm)
R1	2,7
R2	2,3
R3	2,5

Thicknesses of the TiAlZrN coatings were determined using SEM photos of the cross sections obtained by brittle fracture in the radial direction of the films deposited on the glass plates. SEM images of the cross-sectional are shown in Figure 3, and coating thicknesses obtained using SEM images are given in Table 4. The highest coating thickness was measured as 2,7 µm on the R1 sample. The minimum coating thickness was measured as 2.3 µm at R2. It can be seen in Figure 3 that the coatings exhibit a dense and thin columnar structure.

3.2. Elemental Analysis

The chemical composition of coatings are given in Table 5. As seen in Table 5, increasing bias voltage increased the N amounts and decreased the Ti, Zr and Al amounts in the coatings. This may be related with the re-sputtering mechanism. High energetic particles re-sputtered Ti,Al and Zr atoms from coatings at higher bias voltage.

Table 5. Chemical composition of coatings

	Chemical composition (% Atomic)			
Sample Number	Ti	Al	Zr	N
R1	49,92	8,29	11,02	31,01
R2	46,71	8,05	7,37	37,69
R3	45,00	6,10	7,32	41,53

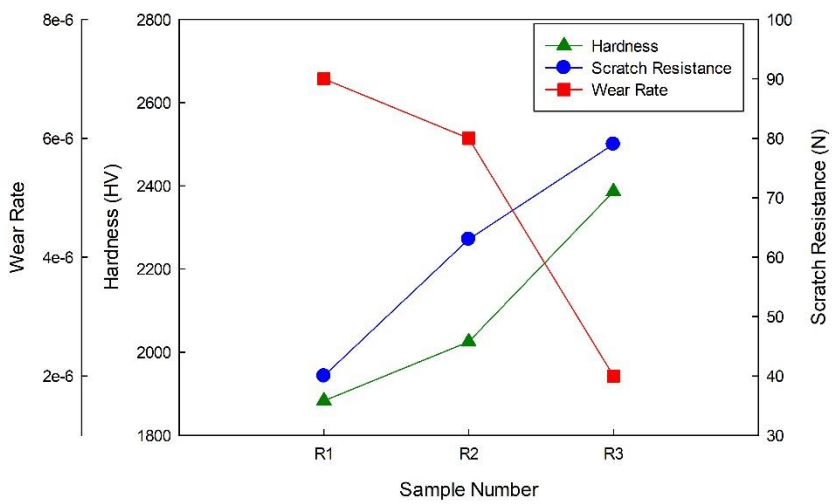

Figure 4. The changes of hardness, scratch resistance and wear rate of the coatings

Hardness Properties

The changes of hardness of coatings are given in Figure 4. As seen in Figure 4, the highest hardness was attained in R3 with highest bias voltage and lowest working pressure. The reason for this is high ion bombardment during coating process as a result of highest bias voltage and lowest working pressure. The same results and interpretations were obtained in studies conducted by some researchers [19]. In a different study on this subject, it was noted that with increasing bias voltage increases the compactness of coatings, hardness by reducing the deterioration of the lattice structure.

Scratch Properties

Residual stresses in the structures of the coatings are due to effects such as lattice parameters of the base material and coating material, thermal expansion coefficients, interatomic voids, and recrystallization. In this study, Ti was coated on the surface of the substrate in order to reduce this difference between the substrate and the coating, and then continued with the transition layer and the TiAlZrN layer was coated on the top.

Scratch resistance change of coatings are seen in Figure 4, also scratch values are seen in Table 6.

Table 6. Scratch resistance values of coatings

Sample Number	Scratch Resistance (N)
R1	40
R2	63
R3	79

The highest scratch resistance was attained from R3 sample, the lowest scratch resistance was attained from R1 sample as given Figure 4 and Table 6. With the increase of the bias voltage, the combination of high energy ions and the energy of ionized atoms enhanced the scratch resistance as a result of implantation in the substrate surface. Besides, as seen in morphological analysis, R3 (higher bias voltage and lower working pressure) has a lower grain size and higher hardness value so has a higher plastic deformation resistance. Hence, scratch resistance improved with increasing plastic deformation resistance.

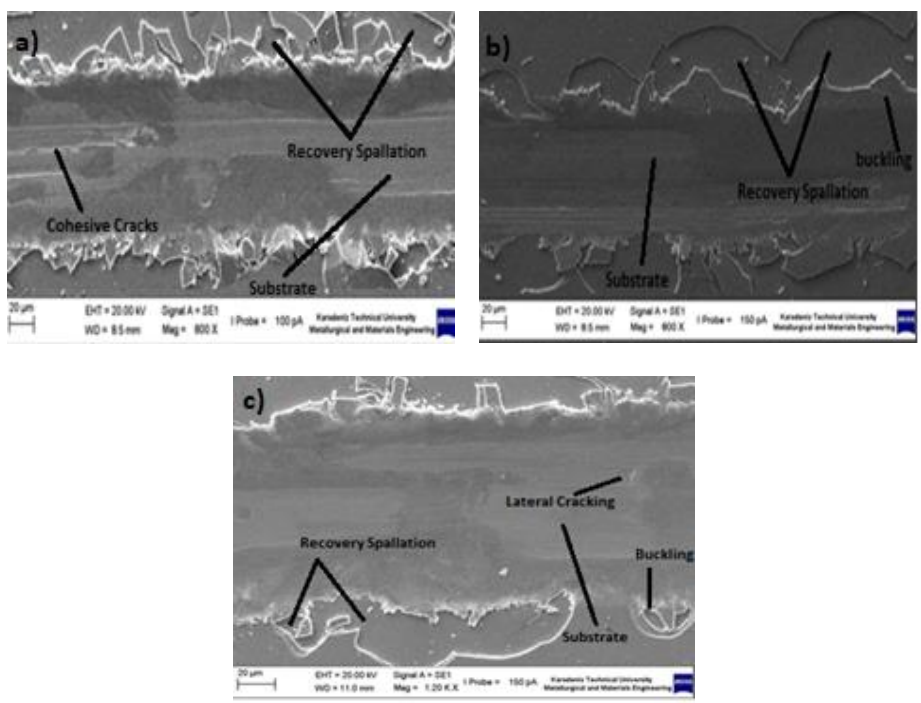

Figure 5. Scratch pattern of coatings a) R1 b) R2 c) R3

The scratch mechanism of samples were obtained by using SEM. Cohesive cracks, buckling and lateral cracking mechanisms were observed for R1, R2, R3 respectively. Additionaly, recovery spallation mechanism was observed for all coatings as shown in Figure 5.

Wear Properties

The friction coefficient of coatings are given in Figure 6. The friction coefficient curve of coatings consists of two sections. At early stage of experiments is running in stage (between zero and 500 cycles) and the rest is steady state stage. In addition to, the lowest friction coefficient was obtained from R3 sample which is produced with highest bias voltage and lowest working pressure due to high hardness and scratch resistance.

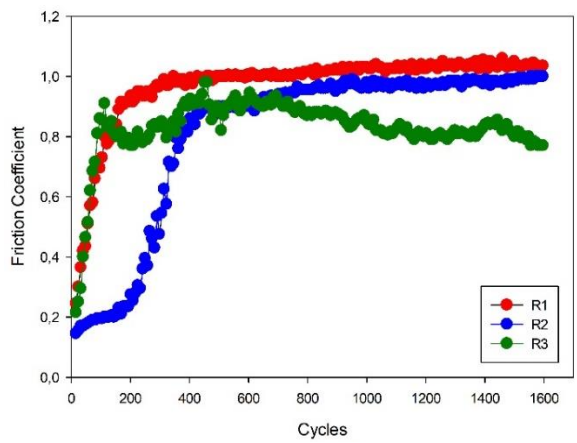

Figure 6. The friction coefficient of coatings

Table 7. The wear rate of coatings and uncoated H13 steel

Samples	Wear Rate (mm^3/Nm)
R1	$7{,}13x10^{-6}$
R2	$6{,}42x10^{-6}$
R3	$2{,}24x10^{-6}$
Uncoated (Nitreded) H13 steel	$2{,}13x10^{-4}$

The wear rates of coatings are shown in Table 7. According to Table 7, all coatings have higher wear resistance than uncoated (nitreded) H13 steel. If the coatings were compared among themselves, it can be seen that, the lowest wear rate was attained from R3 (highest bias voltage and lowest working pressure). Besides, TiAlZrN coatings especially R3 deposition condition increases the wear resistance of nitreded H13 steel approximately 100 times.

4. Conclusions

In this study, The TiAlZrN-graded coatings were successfully deposited on nitreded AISI H13 steel by pulced dc close field unbalanced magnetron sputtering system with the different deposition parametres. And the effect of bias voltage and working pressure on the surface morpholgy, scratch and wear properties of TiAlZrN coatings were investigated. Following conclusions were obtained;

- The lowest grain size was attained with -90 V bias voltage and $2x10^{-3}$ working pressure deposition parameter.
- The highest hardness was obtained with highest bias voltage and lowest working pressure
- There is a relation between hardness, scratch and wear resistance. The coating which has highest hardness also showed highest scratch and wear resistance. The coating which has lowest hardness also showed lowest scratch and wear resistance.
- TiAlZrN coatings have been succesful in enhancing the wear resistance of nitreded H13 steel. The wear resistance of this steel enhanced by 100 times owing to TiAlZrN coatings.

Acknowledgements

his research is partially supported by TUBITAK (Scientific and Technical Research Council of Turkey) project number 116M734

References

[1]. T. Björk, R. Westergard, and S. Hogmark: Wear, , vol. 249 (3–4), pp. 316–23. (2001).
[2]. G. Roberts, G. Krauss, R.Kennedy, Tool Steels, 5th ed.ASM International, 219–250 (1998).
[3]. P.L. Ge, M.D. Bao, H.J. Zhang, K. You, and X.P. Liu, Surface Coating Technolgy 146-150 (2012).
[4]. S.V. Shah and N.B. Dahotre: J. Mater. Process. Technol., vol. 124 (1–2), pp.105–12, (2002)
[5]. Y.-Y. Chang, W.-T. Chiu, J.-P. Hung, Surface Coating Technology 303 18–24 (2016).
[6]. D. Dinesh Kumar, N. Kumar, S. Kalaiselvam, S. Dash, R. Jayavel, Ceram. Int. 41 9849–9861 (2015).
[7]. C. Montero-Ocampo, E.A. Ramírez-Ceja, J.A. Hidalgo-Badillo, Ceram. Int. 41 11013–11023 (2015)
[8]. B. Deng, Y. Tao, Z. Hu, Applications of Surface Science, 284 405–411 (2013).
[9]. I. Efeoglu, A. Celik, Materials Characterization 46 311–316 (2001).
[10]. L. Kara, T. Küçükömeroğlu, Ö. Baran, İ. Efeoğlu, K. Yamamoto, Metallurgical and Materials Transactions 45 2123–2131 (2014).
[11]. A. Hörling, L. Hultman, M. Odén, J. Sjölén, L. Karlsson, Surface and Coatings Technology, 191(2), 384-392 (2005).
[12]. Q. Luo, W.M. Rainforth, L.A. Donohue, I. Wadsworth, and W.D. Mu¨ nz: Vacuum, 53 (1–2), pp. 123–26 (1999).
[13]. D. Philippon, V. Godinho, P.M. Nagy, M.P. Delplancke-Ogletree, A. Fernández, Wear, 270(7), 541-549 (2011).
[14]. S. Carvalho, N.M.G. Parreira, M.Z. Silva, A. Cavaleiro, L. Rebouta, Wear, 274, 68-74 (2012).
[15]. S.A. Glatz, R. Hollerweger, P. Polcik, R. Rachbauer, J. Paulitsch, P.H. Mayrhofer, Surface and Coatings Technology, 266, 1-9 (2015).
[16]. T.D. Nguyen, Y.J. Kim, J.G. Han, D.B. Lee, Thin Solid Films, 517(17), 5216-5218 (2009).
[17]. Dua H., Ji X., H., Z., Wuc Y., Wana W. ve Wangaa L., Applied Surface Science (2013).
[18]. Wang, X., Wang, L., S., Qi, Z., B., Yue, G., H., Chen, Y., Z., Wang, Z., C. ve Peng, D., L., Journal of Alloys and Compounds, 502,1 243-249 (2010).
[19]. Niu, E., W., Li, L., Lv, G., Chen, H., H., Li, X., Z., Yang, X., Z., ve Yang, S., Z., Applied and Surface Science, 254, 13 3909-3914 (2008).

This page intentionally left blank.

Science and Applications of Thin Films, Conference & Exhibition (SATF 2018)
Izmir Institute of Technology, Izmir, Turkey, September 17-21, 2018

The Surface-Plasmon - Optical Soliton Photonic Josephson Junction

Kaan Güven*

Physics Department, Koç University, Sarıyer, Istanbul 34450, Turkey

*Corresponding author. Tel.: +90-212-338-1697; fax: +90-212-338-1548.
E-mail address: kguven@ku.edu.tr

Abstract

An evanescently coupled, co-propagating optical soliton and a surface plasmon can exhibit bosonic Josephson junction dynamics similar to that of Bose-Einstein condensates in double-well traps. Moreover, the self-focusing of the soliton generates an inherently intensity (i.e., photon population) dependent coupling, which exhibit unique dynamical features. Here, we review the dynamical properties of this photonic Josephson junction based on a heuristic model and discuss recent extensions involving plasmon-soliton-plasmon double Josephson junctions and Rosen-Zener like transitions generated by spatially modified coupling. With the advancement of photonic materials, realization of this optical system may enable new abilities to control and utilize the propagation of light.

Keywords: Surface-plasmon – soliton; Josephson junction.

1. Introduction

The Josephson junction dynamics arises between two macroscopic quantum states under weak coupling. Originally predicted in a system of two superconductors with a dielectric spacing by Josephson 1962, and named after him, it has been demonstrated shortly after by Anderson, 1963 and kept on revealing itself in various physical systems such as Bose-Einstein condensates of atoms confined in a double-well optical trap, Javanainen 1986, and two superfluids tunneling through a nano aperture, Pereverzev, 1997.

Recently a resonant interaction between optical solitons and surface-plasmons on a planar metal surface through a dielectric spacing has been suggested by Bliokh 2009. As such, the model system has the proper ingredients to constitute a Josephson junction, Eksioglu, 2011, with the unique feature that the coupling inherently depends on the soliton amplitude. In this paper, we review the dynamical features of this Josephson junction based on the semiclassical formulation of the soliton and surface plasmon states that are weakly coupled. In particular, we consider first a dissipationless single Josephson junction consisting of a soliton and a surface-plasmon co-propagating in parallel. This is followed by incorporating several dissipation mechanisms that are adopted from Josephson junctions of Bose-Einstein condensates. A further extension is based on varying the coupling spatially along the propagation to induce Landau-Zener like transitions.

2. Model and Formulation

2.1. Dissipationless single soliton – surface-plasmon Josephson junction

We begin by a brief description of the semiclassical model of this photonic Josephson junction which is derived from the heuristic model introduced by Bliokh, 2009. The model assumes that the soliton propogates in a nonlinear dielectric channel parallel to a metal surface with a linear dielectric spacing. The evanescent lateral extend of the soliton excites and interacts with the surface plasmons on the metal surface, which are assumed to be co-propagating with the soliton. Hence the total electromagnetic field of the weakly coupled soliton – surface-plasmon system can be written by a superposition ansatz as:

$$\Psi(x,z) = c_p(z)\psi_p(x) + c_s(z)\psi_s(x,|c_s|) \tag{1}$$

Here, $c_{s,p}(z)$ denote respectively the soliton and surface plasmon longitudinal amplitudes and $\psi_s(x,|c_s|)$, $\psi_p(x)$ denote their transverse amplitudes. We note that the soliton transverse profile depends on c_s as a result of Kerr nonlinearity of the propagation medium (i.e. self-focusing effect). The system is essentially two-dimensional which is set as the $z-x$ plane in this formulation. Under steady state propagation, the longitudinal amplitudes are governed by coupled nonlinear (soliton) and linear (surface-plasmon) oscillator equations along the propagation axis (z) as follows:

$$\begin{aligned} \frac{\partial^2 c_p}{\partial z^2} + \beta_p^2 c_p &= q(|c_s|)c_s \\ \frac{\partial^2 c_s}{\partial z^2} + \beta_s^2 c_s &= q(|c_s|)c_p \end{aligned} \tag{2}$$

where $\beta_p = \frac{k_p}{k}$ and $\beta_s = \frac{k_s}{k} \cong \varepsilon_K + \frac{\gamma|c_s|^2}{4}$ are wavevector parameters of the surface-plasmon and soliton, ε_K is the linear part of the Kerr dielectric and γ is the nonlinearity parameter. $q(|c_s|)$ is the soliton amplitude dependent coupling function.. Eq(2) is linearized through substitution $c_{s,p} = C_{s,p}(z)e^{iz}$, and by employing slowly varying amplitude approximation for modulation amplitudes $C_{s,p}$(z):

$$-i\frac{\partial}{\partial z}\begin{bmatrix} C_p \\ C_s \end{bmatrix} = \begin{bmatrix} \beta_p - 1 & -q(|C_s|)/2 \\ -q(|C_s|)/2 & \beta_s - 1 \end{bmatrix}\begin{bmatrix} C_p \\ C_s \end{bmatrix} \tag{3}$$

Finally, introducing phase functions $\phi_{s,p}$ through $C_{s,p}(z) = A_{s,p}\exp\left(i\phi_{s,p}(z)\right)$, the relative phase $\phi = \phi_s - \phi_p$, and the relative population imbalance variable $Z = (|C_s|^2 - |C_p|^2)/(|C_s|^2 + |C_p|^2)$, the soliton – surface-plasmon Josephson junction (SSPJJ) equations are obtained. Here, we take the total number of photons conserved and normalized i.e.$|C_s|^2 + |C_p|^2 = 1$. Hence, $Z \in [-1,1]$. The relative phase is defined in the symmetric range $\phi \in [-\pi,\pi]$.

$$\begin{aligned} \frac{\partial Z}{\partial z} &= -q(Z)\sqrt{1-Z^2}\sin\phi \\ \frac{\partial \phi}{\partial z} &= \Delta E + \Lambda Z + q(Z)\frac{Z}{\sqrt{1-Z^2}}\cos\phi \end{aligned} \tag{4}$$

In eq. 4, we further define the parameters $\Delta E = \Lambda - (\beta_p - 1)$ and $\Lambda = \gamma/8$ for the analogy with the Josephson junction formulation of Bose-Einstein condensates in double well traps. Indeed, the dynamic equations of a bosonic Josephson junction (BJJ) in semiclassical formulation are given by Smerzi, 1997, Raghavan 1999 as:

$$\begin{aligned} \frac{\partial Z}{\partial t} &= -q\sqrt{1-Z^2}\sin\phi \\ \frac{\partial \phi}{\partial t} &= \Delta E + Z(t) + q\frac{Z}{\sqrt{1-Z^2}}\cos\phi \end{aligned} \tag{5}$$

The most striking difference is that the coupling is a constant parameter (q) in BJJ whereas it is a function of the soliton amplitude $|C_s|$ in SSPJJ, as the coupling depends on $\psi_s(x, |c_s|)$.

$$q(Z) = \left(\frac{1+Z}{2}\right) e^{-kd\sqrt{2\Lambda(1+Z)}} \tag{6}$$

Here, kd is the wavevector-scaled distance between the center of the soliton channel and the metal surface. This functional form provides the exponential decay in the strong soliton limit ($1 - Z \ll 1$) and sublinear enhancement by the soliton intensity ($|C_s|^2$) in the strong surface-plasmon limit ($1 + Z \ll 1$).

2.2. Phase space and dynamical features of the dissipationless SSPJJ

Equation set (4) describes the dynamics of the SSPJJ in the $\phi - Z$ phase space. The stationary states are given by $\{\partial_z Z = 0, \partial_z \phi = 0\}$ which occur at $\phi^* = 0, \pi$ and at values Z^* that satisfy

$$\Delta\tilde{E} + Z^* \pm \tilde{q}(Z^*)\frac{Z^*}{\sqrt{1-Z^{*2}}} = 0 \tag{7}$$

where the + (-) correspond to $\phi^* = 0, (\pi)$ respectively. $\Delta\tilde{E} = \frac{\Delta E}{\Lambda}$ and $\tilde{q}(Z) = \frac{q(Z)}{\Lambda}$ are scaled parameters. Stable stationary points provide bound orbits with nonzero average value of the population imbalance, which is known as the macroscopic self-trapping in BJJ. Here, we illustrate the phase space for two different sets of $\{\Delta\tilde{E}, kd\}$ values. In Figure 1(a) one $\phi^* = 0$ four $\phi^* = \pi$ stationary points can be observed for $\{\Delta\tilde{E} = 0, kd = 8\}$. With values $\{\Delta\tilde{E} = -0.01, kd = 13\}$, Figure 1(b) shows that $\phi^* = 0$ stationary point shifts upwards (soliton dominant) due to nonzero $\Delta\tilde{E}$. A saddle point at $\phi^* = \pi$ is visible, and there are two more stationary points close to the $Z = \pm 1$ values (not visible in the figure scale, please see Figure 2(b)). Note that the bound states around the stationary points for $\phi^* = \pi$ provide macroscopic self-trapping with soliton-dominant and surface-plasmon dominant average values respectively. The color-coded arrows indicate the gradient distribution in the phase space whose components are given by Eq.4. By increasing kd from 8 to 13 the trajectories are flattened horizontally, indicating the weakened coupling between the soliton and the surface plasmon.

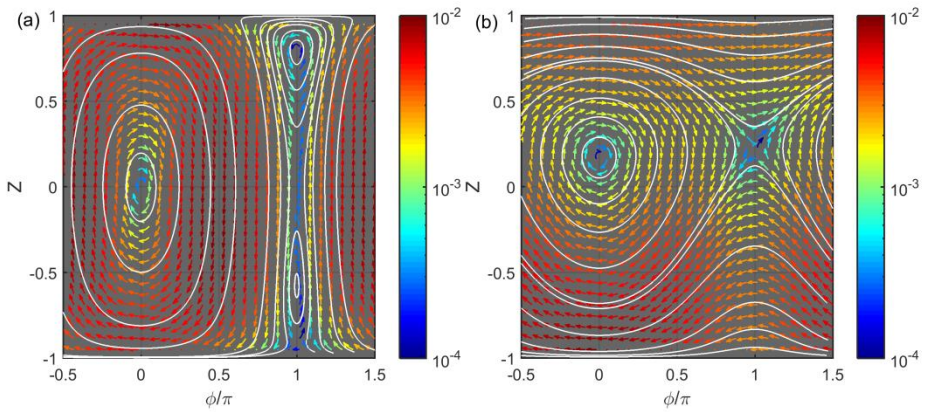

Figure 1: Phase space plot of the SSPJJ for (a) $\{\Delta\tilde{E} = 0, kd = 8\}$ and (b) $\{\Delta\tilde{E} = -0.01, kd = 13\}$. The colored arrows indicate the gradient and the white curves indicate sample trajectories.

The Z-dependence of the coupling renders the phase space asymmetric about the $Z = 0$ axis, even for $\Delta E = 0$ case. This is essentially different than the phase space of the BJJ, which would be symmetric for $\Delta E = 0$, unless the barrier separating the double well is made asymmetric, Smerzi, 1997.

Since the soliton – surface plasmon spacing parameter kd can be controlled trivially, analysing its effect on the phase space is feasible. Figure 2 shows the distribution of (a) $\phi^* = 0$ and (b) $\phi^* = \pi$ stationary points on the Z-axis as a function of $5 < kd < 15$, for $\Delta\tilde{E} = 0$ and $\Delta\tilde{E} = -0.01$, respecively. Note that for $\Delta\tilde{E} = 0$, $Z^* = 0$ is a always a critical point as can be inferred from Eq. (6). For nonzero $\Delta\tilde{E}$ values, the stationary point at $\phi^* = 0$ becomes kd dependent as shown inFigure 2. The stationary points at $\phi^* = \pi$ show a nontrivial distribution and up to 4 stationary points can be generated at certain values of $\{\Delta\tilde{E}, kd\}$. The $kd = 8$ and $kd = 13$ correspond to the values used in Figure 1. A detailed analysis of the phase space for SSPJJ system can be found in Eksioglu, 2011 and Eksioglu, 2013, albeit with a slightly different coupling function, and in the presence of dissipation. The SSPJJ model including dissipation mechanisms is discussed in section 2.4.

2.3. Dissipative model extensions of the single soliton – surface-plasmon Josephson junction

The analogy to the double-well BJJ can be extended to incorporate similar dissipation mechanisms in the SSPJJ. One dissipation mechanism present in BJJ is about the tunneling between the excited states of two Bose-Einstein condensates in the *same* trap, that populate different hyperfine levels. This generates a damping proportional to the population imbalance in its rate of change. Although an analogous mechanism in the SSPJJ is arguable, it is introduced in an ad hoc manner for comparison:

$$\begin{aligned} \frac{\partial Z}{\partial z} &= -q(Z)\sqrt{1-Z^2}\sin\phi - \zeta Z \\ \frac{\partial \phi}{\partial z} &= \Delta E + \Lambda Z + q(Z)\frac{Z}{\sqrt{1-Z^2}}\cos\phi \end{aligned} \tag{8}$$

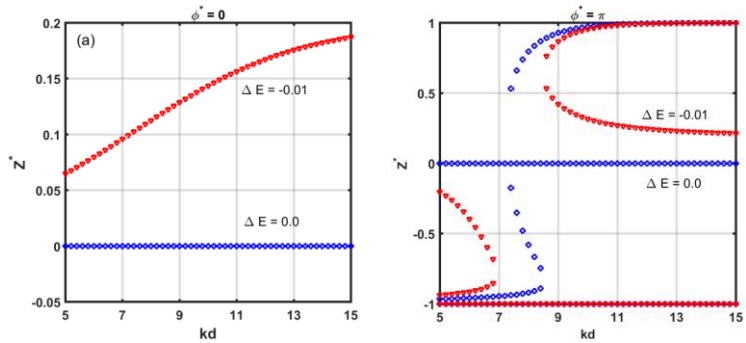

Figure 2: The stationary points as a function of soliton – surface-plasmon spacing for different values of ΔE. (a) $\phi^* = 0$, (b) $\phi^* = \pi$.

A more relevant dissipation is due to the incoherent exchange of photons between the soliton and the surface-plasmon. This is represented by a phase-velocity proportional term in the population imbalance rate, adopted from Marino, 2009:

$$\frac{\partial Z}{\partial z} = -q(Z)\sqrt{1-Z^2}\sin\phi - \eta\frac{\partial \phi}{\partial z}$$
$$\frac{\partial \phi}{\partial z} = \Delta E + \Lambda Z + q(Z)\frac{Z}{\sqrt{1-Z^2}}\cos\phi \qquad (9)$$

The first dissipation mechanism generates various bifurcations in the system depending on the model parameters as shown in Figure 3 (a). Here, the $\phi^* = 0, Z^* = 0$ critical point acts as a strong sink and one (upper) critical point near $\phi = \pi$ becomes a source, whereas another (lower) critical point near $\phi = \pi$ becomes a weak sink. For nonzero $\Delta\tilde{E}$ values, this dissipation mechanism can generate limit-cycles, thus providing unique macroscopically trapped states, Eksioglu, 2011. The second dissipation mechanism creates the so-called "phase-slip" phenomenon known in BJJ systems, in which the trajectories from $\phi = \pi$ stationary states decay into the $\phi = 0$ stationary state (Figure 3(b)).

We ought to note that the surface-plasmons are inherently dissipative and this can be taken into account by introducing imaginary parts to their propagation constants, $\beta_{s,p} \rightarrow \beta_{s,p} + i\gamma_{s,p}$, Bliokh, 2009. In this case, the total number of photons is not conserved and decays to zero. When the propagation length of surface-plasmon is sufficiently large compared to the relevant length scales in which the aforementioned dynamical features take place, this dissipation may be omitted.

2.4. Soliton – surface-plasmon Josephson junction with spatially modified coupling

Since the coupled soliton – surface-plasmon essentially forms a two-state system, it is natural to exploit some mechanisms that can generate diabatic/adiabatic transition between the two states. Bliokh et al., 2009 investigated resonant transitions induced in the presence of a small damping. In a recent study, Aydindogan, 2017 employed a varying spacing between the soliton and the surface-plasmon to modify the coupling spatially and hence induce population transitions. With a smooth variation of the spacing, the paraxial approximation is applicable and the dynamics of the SSPJJ are still given by equation 4, where the coupling now takes the form

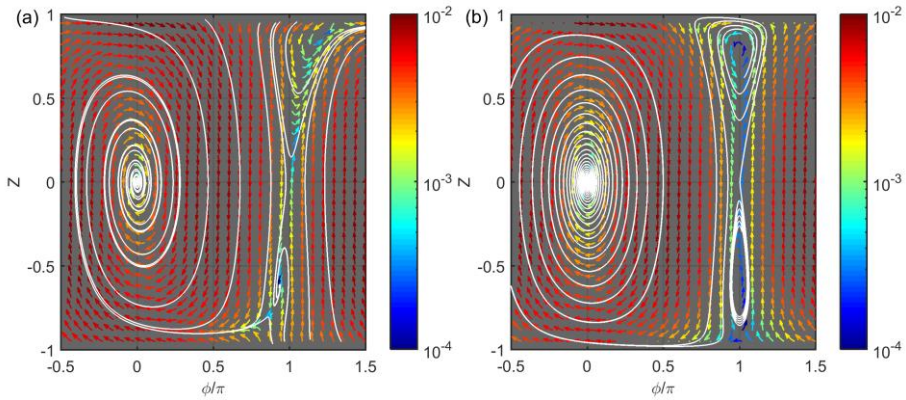

Figure 3: Phase space of the SSPJJ with (a) population imbalance and (b) phase rate dissipation mechanisms.

$$q(z,Z) = \left(\frac{1+Z}{2}\right) e^{-\sqrt{2\Lambda(1+Z)}} e^{-k\sqrt{d^2+\alpha^2 z^2}} \tag{10}$$

That is, the consant spacing, d is now replaced by the hyperbolic spacing $\sqrt{d^2+\alpha^2 z^2}$, where d is the minimum spacing, z is the propagation axis, and α is the asymptotic slope. By tuning the spatial modulation parameters d, α, full population transfer, population splitting, merging can be generated, as shown in Figure 4. The full population transfer resembles the asymmetric Rosen-Zener adiabatic transitions where the uncoupled soliton and surface-plasmon represent.

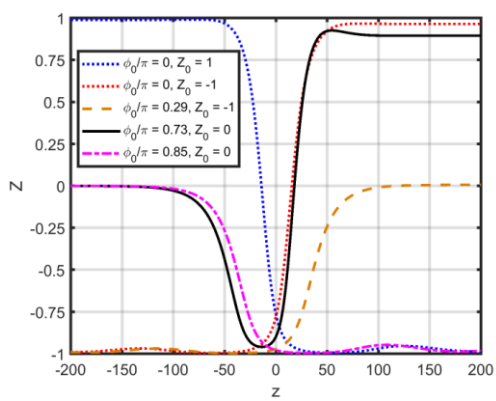

Figure 4: Population transfer between soliton ($Z = 1$), surface-plasmon ($Z = -1$), and equipopulated ($Z = 0$) states.

2.5. Soliton – surface-plasmon double Josephson junction

The soliton channel running along between two parallel metal surfaces forms a double Josephson junction. The single SSPJJ model described in section 2.1 can be extended in a straightforward manner for this case:

$$-i\frac{\partial}{\partial z}\begin{pmatrix} C_{p1} \\ C_s \\ C_{p2} \end{pmatrix} = \begin{pmatrix} \beta_{p1}-1 & -q_1/2 & 0 \\ -q_1/2 & \beta_s - 1 & -q_2/2 \\ 0 & -q_2/2 & \beta_{p2}-1 \end{pmatrix}\begin{pmatrix} C_{p1} \\ C_s \\ C_{p2} \end{pmatrix} \quad (11)$$

Here, β_i is the propagation constant for the respective soliton or surface plasmon and $q_{1,2}$ is the coupling between the soliton and the respective surface-plasmon. For a dissipationless system, the sum of intensities is normalized: $|C_s|^2 + |C_{p1}|^2 + |C_{p2}|^2 = 1$. The dynamics become substantially more complicated but also provide features unique to coupling of three states. Notably, the soliton can be in a stationary state while mediating a coupling between the two surface-plasmon states. Evidently, an analogy to that of the BJJ of Bose-Einstein condensates in triple wells, Liu, 2007, Viscondi, 2011 can be drawn here as well. Population transfer among the soliton and surface-plasmon states can be investigated by the three level Landau-Zener formulation, Carroll, 1986. Due to the article length limitations here, we refer the reader to Aydindogan, 2018 for the details of this analysis.

3. Conclusion

The coupling between an optical soliton – surface-plasmon can give rise to new hybridized propagation modes that can be utilized to control surface plasmons via solitons. Within a semiclassical formulation, the dynamics of the coupled system can be cast into that of a Josephson junction with unique features stemming from the nonlinearity of the soliton. The present paper reviewed some of these features involving the onset of macroscopic trapping, dissipation induced population trapping, and asymmetric Rosen-Zener like transitions via spatially varying coupling.

Quite recently, experimental realization of soliton – surface-plasmon coupling in planar waveguides with a geometry very similar to that discussed here has been reported, Kuriakose, 2018. This encourages to pursue the studies to utilize this system in photonic applications.

Acknowledgements

K. Güven acknowledges support of Turkish Academy of Sciences (TUBA).

References

Anderson PW., Rowell JM., 1963. Probable observation of the Josephson superconducting tunneling effect. Phys. Rev. Lett. 10, 230.

Aydindogan G, Guven K., 2017. Asymmetric Rosen-Zener – like transition through a soliton – surface-plasmon photonic Josephson junction with spatially varying coupling. Phys. Rev. A 96, 053803.

Aydindogan G., Guven K. 2018 (to be published).

Bliokh KY., Bliokh YP., Ferrando A., 2009. Resonant plasmon-soliton interaction. Phys. Rev. A 79, 041803(R).

Carrol C.E., Hioe F.T., 1986. Generalization of the Landau-Zener calculation to three levels. J. Phys. A: Math. Gen. 19, 1151.

Eksioglu Y. Mustecaplioglu OE., Guven K. 2011. Dynamical analysis of a weakly coupled nonlinear dielectric waveguide – surface plasmon model as another type of Josephson junction. Phys. Rev. A 84, 033805.

Eksioglu Y. Mustecaplioglu OE., Guven K. 2013. Dissipative Josephson junction of an optical soliton and a surface-plasmon. Phys. Rev. A 87, 023823.

Javanainen J. 1986. Oscillatory exchange of atoms between traps containing Bose condensates. Phys. Rev. Lett. 57,3164.

Josephson BD., 1962. Possible new effects in superconducting tunneling. Phys. Lett. 1, 251.

Kuriakose T., Halenkovic T, Elsawy MRM, Nemec P., Nazabal V., Renversez G., Chauvet M. 2018. "Experimental demonstration of soliton – Plasmon coupling in planar waveguides," SPIE Proc. Nonlinear Optics and Applications. Strasbourg, France, paper #10684

Liu B. Fu L-B, Yang S-P. Liu J., 2007. Josephson oscillation and transition to self-trapping for Bose-Einstein condensates in a triple-well trap. Phys. Rev. A 75, 033601.

Perverzev S., Loshak A., Backhaus S., Davis JC., Packard RE., 1997. Quantum oscillations between two weakly coupled reservoirs of superfluid ^{3}He. Nature 388, 449.

Raghavan S., Smerzi A., Fantoni S., Shenoy SR. 1999. Coherent oscillations between two weakly coupled Bose-Einstein condensates: Josephson effects, π-oscillations, and macroscopic quantum self-trapping. Phys. Rev. A 59, 620.

Smerzi A., Fantoni S., Giovanazzi S. 1997. Quantum coherent atomic tunneling between two trapped Bose-Einstein condensates. Phys. Rev. Lett. 79, 4950.

Viscondi TF., Furuya K., 2011. Dynamics of a Bose-Einstein condenstate in a symmetric triple-well trap. J. Phys. A: Math. Theor. 44, 175301.

Walasik W., Nazabal V., Chauvet M., Kartashov Y., Renversez G., 2012. Low-power plasmon-soliton in realistic nonlinear planar structures. Optics Letters 37, 168477.

Science and Applications of Thin Films, Conference & Exhibition (SATF 2018)
Izmir Institute of Technology, Izmir, Turkey, September 17-21, 2018

Sol-gel processed niobium-doped titanium dioxide for transparent conductive coatings

Mirjam Skof[a,c]*, Adam Walker[b], Geraldine Durand[b], Nicholas Farmilo[c], Aseel Hassan[c]

[a] *National Structural Integrity Research Centre (NSIRC), Granta Park, Cambridge, CB21 6AL, United Kingdom*
[b] *TWI Ltd., Granta Park, Cambridge, CB21 6AL, United Kingdom*
[c] *Sheffield Hallam University, Howard Street, Sheffield, S1 1WB, United Kingdom*

*Corresponding author. Tel.: +44-114-225 3500;
E-mail address: mirjam.skof@student.shu.ac.uk

Abstract

In the present work, the sol-gel method was utilised to fabricate titanium dioxide thin films with doping levels of 3-8% niobium, non-doped TiO_2 films were prepared as reference. The precursors, titanium ethoxide and niobium ethoxide, were dissolved in anhydrous ethanol, acetic acid was used to control reaction kinetics. The films were spun onto glass substrates and subjected to natural hydrolysis while being sintered at 550°C in air.
The prepared films had a blue hue that changed with increasing Nb doping. Electron microscopy and EDX studies showed smooth and homogeneous films with a grainy structure. Grain sizes were found to increase with increasing doping level.
All samples exhibited excellent transparency, with absorption values in the visible range of below 10%. Tauc plots gave band gap values of below 3.6 eV, conductivity was measured with films deposited on platinum interdigitated electrodes and highest for the sample with 8% Nb doping. In all coatings the desired anatase polymorph could be confirmed via XRD.

Indium free; transparent conductive coating; sol-gel; titanium dioxide; NTO

1. Introduction

High integrity transparent conductive coatings (TCCs) play an important role in a huge range of different applications, reaching from antireflective and low-emissivity coatings to using them for protection against electromagnetic interferences as well as in flat-panel screens and PV cells. (Chen, et al., 2011) In fact, the demand for TCCs in the renewable energy and electronics sectors is rapidly growing, as interests in solar cells, thin film LEDs and touch-screen displays are rising. (Sunde, et al., 2012; Stadler, 2012)

The industrial standard for transparent conducting coatings is indium tin oxide (ITO), which accounts for over 90% of the TCC market, due to its excellent electrical conductivity and high light transmission. (Song, et al., 2011; Sunde, 2013) ITO typically consists of up to 90% indium. (J. Liu, 2009; Kwak, et al., 2011) This strong focus on indium-based materials, leaves the industry facing a range of problems. Indium is scarce and found to be a critical technology material, showing a high and volatile price structure with limited export quota. (Furubayashi, et al., 2006; Jariwala, et al., 2015; South American Silver Cooperation, 2012) At the

same time, the production of TCCs is continuously rising, thus increasing the demand for indium. Finding an alternative is therefore highly desired.

In recent years, thin films based on titanium dioxide are generating significant interest, due to their band gap energy lying in the UV wavelength region and the resulting transparency for visible light. When suitably doped with a second metal, such as niobium, TiO_2 demonstrates good electrical conductivity (Bhachu, et al., 2014) and high transparency of up to 90%. Additionally, titanium dioxide is commercially viable because of its relatively low price and non-toxicity (Joshi, et al., 2013; Farooq & Kamran, 2013).

Conventionally, TCCs are deposited by sputter coating and subsequent wet chemical etching with concentrated acids, or by laser ablation. This route has significant limitations in cost and process efficiency, and typically achieves low yields of no more than 50% including recycling. It is therefore highly desirable to replace it with a more cost-effective, non-vacuum deposition process, such as the sol-gel method (Dsy & Ta, 2018; Song, et al., 2011).

The sol-gel method facilitates mixing of substances at a molecular level, with chemical reactions occurring in solution and at relatively low temperature, thus enabling the design of highly homogeneous materials with defined stoichiometry. In reality, different reaction kinetics of the precursors and phase separation during the gelation stage are two big drawbacks of solution-based routes.

Numerous studies have been conducted on titanium isopropoxide (Husain, et al., 2017; Bartic, et al., 2014; Ruiz, et al., 2004), however papers on titanium ethoxide are limited. To further the understanding of the usability of titanium ethoxide as precursors, in the scope of this work, titanium (IV) ethoxide and niobium (V) ethoxide have been studied. Anhydrous ethanol was used as solvent to precisely manage water addition and eliminating the possibility of alcoholysis reactions. Acetic acid is a common additive in titanium-based systems, especially to facilitate the hydrolysation stage of the sol-gel process, as discussed by Cimieri, et al., 2012. In this work acetic acid has been used to address the problem of inhomogeneous reaction speeds of the two precursors, titanium ethoxide and niobium ethoxide. The effect of niobium doping on optical, structural and electrical properties of the titanium dioxide matrix in sol-gel prepared films was evaluated. Spin-coated thin films were prepared to examine the influence of niobium on the anatase crystal structure and grain size.

2. Materials and Methods / Experimental / Theory Calculations

The sol-gel method was selected to prepare the liquid samples for spin coating. All solutions were prepared inside a glovebox with nitrogen atmosphere in order to precisely control the amount of water present in the samples before the coating step, which took place in ambient air. Chemicals were processed as received, with no additional purification.

To prepare the titanium containing sol, in a first step, anhydrous ethanol (Merck, ≥99.5%) was mixed with glacial acetic acid (≥99%, Merck). Then titanium ethoxide ($Ti[OCH_2CH_3]_4$) (≥99%, VERTEC ET, Alfa Aesar) was added dropwise under vigorous stirring, to form a 0.4 M solution. The molar ratio for acetic acid to titanium ethoxide was 4:1. To produce solutions with 3-8% Nb doping, the samples were stirred for 30 minutes before slowly adding niobium ethoxide ($Nb[OCH_2CH_3]_5$) (99.95%, Merck).

All samples were then aged for 24 hours in a glovebox prior to being taken out and deposited with an Ossila spin coater at 2000 rpm for 20 seconds in air to allow for natural hydrolysis of the thin films. Glass slides and platinum interdigitated electrodes on glass (DropSens) were used as substrates. To clean the substrates before spin coating, they were first rinsed with deionised water and detergent and then immersed in isopropanol and ultrasonicated for 10 minutes. After a second rinse with deionised water, the substrates were put into acetone and ultrasonicated for 10 minutes again, before being rinsed with deionised water in a last step and were finally blown dry with nitrogen gas. The interdigitated electrodes (IDEs) were taped at the end

that connects to the measurement unit during spin coating, to ensure that no film deposition would take place on this particular part of the IDEs, as illustrated in Fig. 1a. The tape was then removed before drying, which took place on a hot plate at 40°C for 30 minutes. The coated slides were then transferred to a Carbolite furnace and sintered in air as illustrated in Fig. 1b.

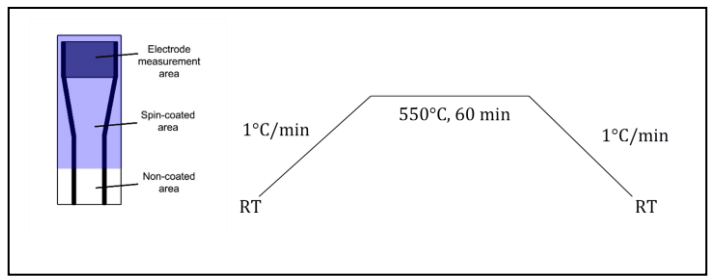

Fig. 1: (a) Illustration of IDE with coated (blue) and non-coated sections, (b) sintering program of spin-coated films

The optical assessment of the sintered films deposited on glass slides was carried out using a VARIAN Cary 50 Scan UV-visible spectrophotometer, while the VARIAN Cary WinUV software was used for data acquisition and analysis. Samples were mounted onto a sample holder and scanned over the wavelength range of 300-1000 nm. Energy bandgaps of the films were calculated using Tauc equation (Tauc, 1974):

$$(\alpha h\nu)^n = A(h\nu - E_g) \quad (1)$$

where α is the absorption coefficient, $h\nu$ is the photon energy, A is a constant and E_g is the bandgap. For semiconductors with direct allowed transition, the coefficient n takes the value ½.

A Variable Angle Spectroscopic Ellipsometry (J.A Woollam VASE) was utilised to determine the thickness as well as the extinction coefficient "k" and refractive index "n" of samples spun onto glass slides. The measurement took place over a wavelength range of 350-1700 nm with the angle of incident light set to 70°. Data analysis was undertaken with the CompleteEase 4.92 program where optical constants were calculated from the angles ψ and Δ for the wavelength of 632.8 nm.

Scanning electron microscopy (SEM) images were taken using a Quanta 3D Nano Scanning electron microscope and elemental analysis were carried out using an Oxford Instruments X-MAX EDX detector.

The formation of the desired anatase crystal structure was examined using an EMPYREAN Powder Diffractometer with a cobalt filament as X-ray source. For all measurements, the instrument was set to a voltage of 40 kV and a tube current of 40 mA. The scans were performed over the angle range of 25-70°2θ.

Current-Voltage measurements were performed on films spun onto IDEs in ambient conditions using a Keithley 4200-SCS over the measurement range of 0-2 V. The electrical conductivity, σ, was then estimated using the following equation:

$$\sigma = \frac{I}{V} \cdot \frac{L}{W \cdot t \cdot n}$$

where the term I/V represents the gradient of the ohmic part of the measured curves, L is the gap between the fingers of the interdigitated electrode (5µm), W is the overlapping length (7mm), t is the film thickness (an average of 100 nm) and n stands for the total number of electrode fingers (500).

3. Results /Discussion

3.1 Optical Properties

The visible assessment of the sintered films is demonstrated in **Error! Reference source not found.**Fig. 2. It shows a comparison of the non-doped TiO_2 (TE0NB) sample and a film with 5% Nb doping (TE5Nb). The blue hue is changing with niobium concentration, this was also found by Bhachu, et al., 2014. The films exhibit a smooth and homogeneous appearance with no visible cracks.

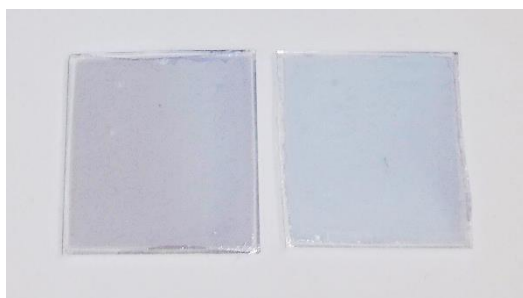

Fig. 2: Sintered films on glass, exhibiting a change in blue colour between TE0Nb (left) and TE5Nb (right)

Fig. 3 shows UV-visible spectra of pure and Nb-doped TiO_2 films. The spectra confirm the low absorption of a maximum of 10% in the visible region and a sharp increase upon reaching the UV region of the measurement range. The non-doped sample also exhibits the lowest absorption at higher wavelengths, however it shows a first absorption onset at a wavelength of around 450 nm before the typical increase in absorption for UV light. The doped films do not demonstrate this behaviour, which could be ascribed to defects in the undoped (TE0Nb) sample. Furthermore, this could be ascribed to a different electronic structure of the films and hence different excitation behaviour. This may be associated with the presence of both the brookite and the anatase phases in the produced TiO_2 as will be confirmed later in the XRD data. The onset of the absorption peak correlates with the optical band gap and thus varies with the concentration of niobium in the sample. Fig. 4 shows a comparison of average and maximum absorption values in the visible region (400-700 nm) vs. niobium doping level. The higher transparency for undoped films and the sharp increase in absorption is also discussed by Lee, et al., 2014.

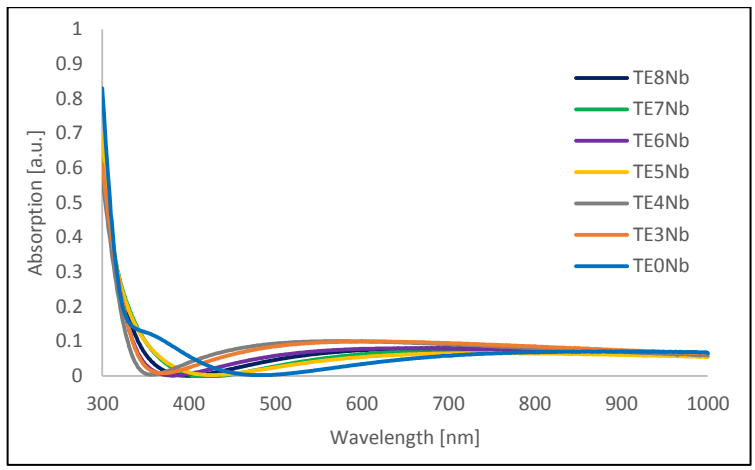

Fig. 3: Absorbance spectra of doped and undoped TiO_2:Nb films

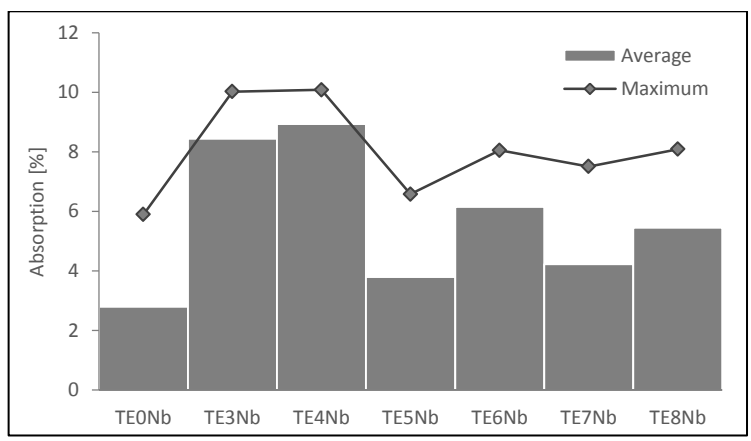

Fig. 4: Correlation of max. (line) and average absorbance (columns) from 400-700 nm with doping level

Energy band gaps of pure and Nb-doped TiO_2 films have been calculated using Tauc equation, as illustrated in Fig. 5 (analysis is shown for 7% Nb-doped TiO_2 as an example), and obtained values are summarised in Table 1. A change in band gap can arise from variations in chemical composition and probably from different grain sizes. Band gaps vary from 3.017 eV for the 5% doped sample (TE5Nb) to 3.616 eV for the undoped TiO_2 film. The values obtained in this study show the lowest band gap for the sample with 5% Nb, followed by the sample with 8% doping. This furthermore is reflected in the conductivity measurements, where those two samples exhibit the best performance. The band gap for anatase is reported to be around 3.4 eV, which is slightly lower than the bandgap obtained for the non-doped titania sample TE0Nb. One reason for this could be the occurrence of two different TiO_2 crystal structures, as can be seen in the XRD graphs. Furthermore, with samples being annealed in air, oxygen defects might play a role in raising the band gap.

Lee & Robertson, 2013 found that in case of annealing TiO_2 in an oxygen rich atmosphere, the donor effect of the dopant can be reduced, which influences the bandgap.

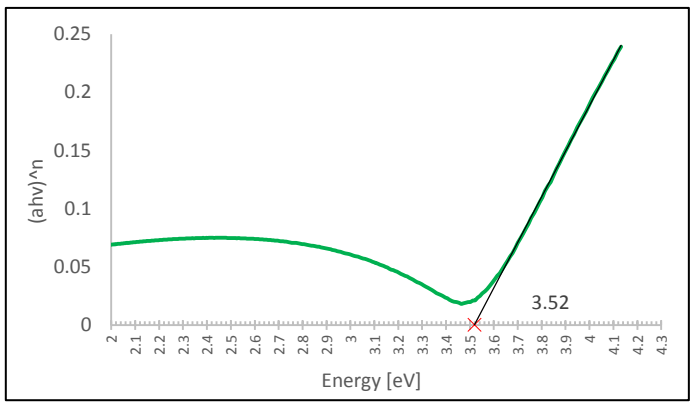

Fig. 5: Tauc plot for 7% doped TiO_2 as an example

Film thickness and optical constants were obtained using spectroscopic ellipsometry. Calculated film thicknesses range from 84.74 for the 3% doped sample to 128.32 nm for the 5% Nb doped TiO_2 film. Variations in thickness are thought to be due to changes in viscosity in the sol with Nb doping level. In Table 1 a summary of absorption values, optical constants and film thickness can be found. The lowest value for the refractive index "n" of 1.816 was found in the case of 8% Nb doped TiO_2, while the highest value of 1.871 was obtained in the sample with 3% doping. All values obtained are lower than typical n values for anatase TiO_2, which are around 2.5. These findings correlate with work undertaken by Manolea, et al., 2013. A falling trend can be observed with the extinction coefficient "k", where values range from $2.66x10^{-5}$ to $3.72x10^{-4}$, for TE4Nb and TE3Nb respectively. The obtained values for the refractive index and the extinction coefficient "k" are decreasing with increasing doping concentration, as shown in Fig. 6.

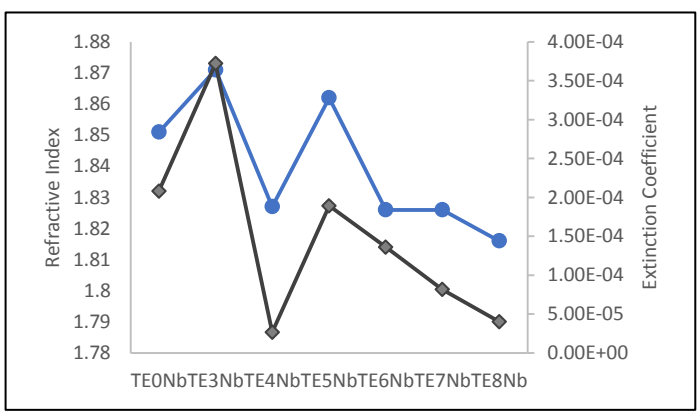

Fig. 6: Variation of refractive index (grey) and extinction coefficient (blue) with increased doping levels

Table 1: Summary of values for absorption, band gap, optical constants and film thickness

Sample	Absorption Onset (nm)	Absorption (400-700 nm) AVG (%)	Absorption (400-700 nm) MAX (%)	Band gap (eV)	n @632.8 nm	k @632.8 nm	Thickness (nm)
TE0Nb	483.977	2.798	5.897	3.616	1.851	2.08E-04	85.02
TE3Nb	368.980	8.441	10.027	3.436	1.871	3.72E-04	84.78
TE4Nb	357.946	8.935	10.089	3.519	1.827	2.66E-05	122.83
TE5Nb	431.967	3.797	6.580	3.017	1.862	1.89E-04	128.32
TE6Nb	382.012	6.151	8.054	3.416	1.826	1.36E-04	110.10
TE7Nb	420.025	4.233	7.511	3.520	1.826	8.16E-05	104.61
TE8Nb	397.029	5.459	8.091	3.285	1.816	4.02E-05	110.06

3.2 Film Formation

Fig. 7 shows a SEM micrograph of the non-doped TiO_2 sintered films as representative example. The formation of clusters, consisting of smaller grains can be seen. Furthermore, the coatings exhibit a very smooth and crack-free structure. The results indicate a change in grain structure with increased doping levels. An estimation of the grain size in TiO_2 films, both pure and Nb-doped, shows values between 30 and 50 nm, which correlates with the data obtained via XRD measurements.

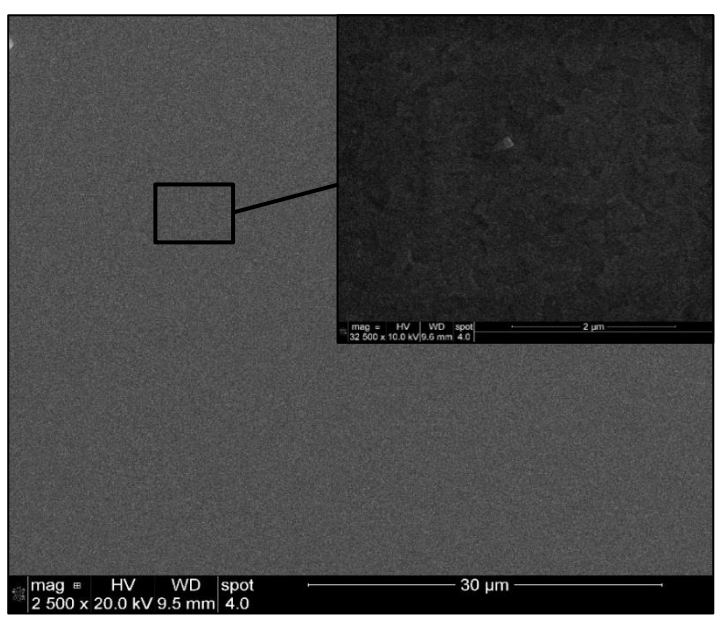

Fig. 7: SEM micrographs showing formation of clusters and grainy structure of TE0Nb coating

Furthermore, the samples were analysed via EDX to visualise the elemental distribution of titanium and niobium in TiO_2 coatings. Fig. 8 shows a TiO_2 film with 3% niobium doping as a representative result. All coatings demonstrate a homogeneous distribution of both elements.

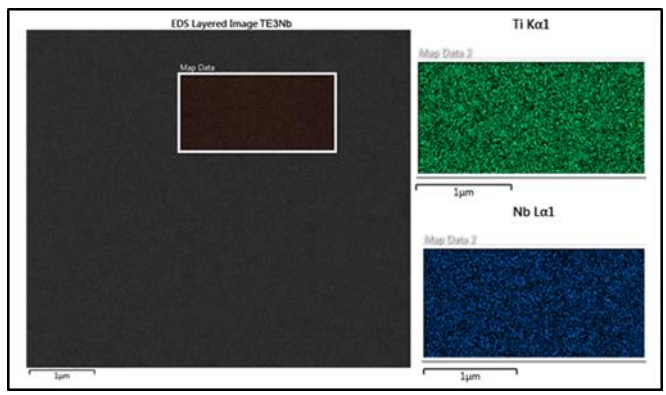

Fig. 8: EDX analysis of sample with 3% Nb concentration, showing homogeneous distribution of elements

3.3 Crystal Structure

XRD measurements were carried out in order to determine the crystalline structure of the TiO_2 films. The data confirms the formation of the desired TiO_2 anatase polymorph in all samples, as can be seen in Fig. 9. In the non-doped films, beside anatase, a second phase, namely brookite, could be detected (ICDD card number: 01-073-1764 and 04-019-9878 for anatase and brookite respectively). Gillispie, et al., 2007 have discussed the destabilisation of the anatase structure and the possible formation of the rutile phase at sintering temperatures of as low as 400°C. However, in this study, no rutile phase was present.

While there was no trend observable for other peaks, the anatase (004) peak in the thin film samples showed a gradual increase with Nb concentration. Peak shifts, as seen for the anatase (100) peak are thought to be due to stresses resulting from the incorporation the slightly larger niobium into the titanium dioxide structure.

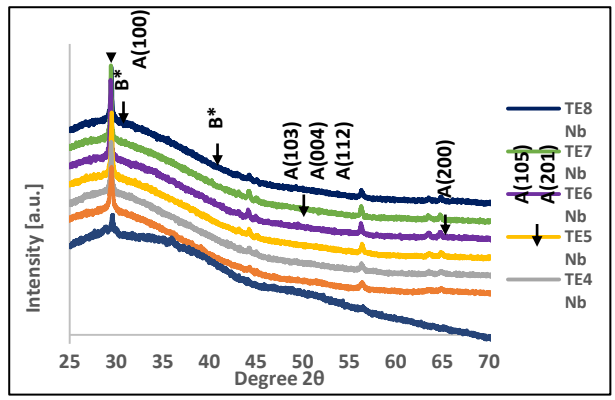

Fig. 9: XRD diffraction patterns, confirming the desired anatase crystal structure (A) and a second brookite structure (B*) occurring in TE0Nb

Hung, et al., 2011; Singh, et al., 2017 and several others have shown the incorporation of Nb into the crystal structure by substituting Ti atoms. This was confirmed by Rietveld analysis carried out in this work, as can be observed in the unit cell parameters displayed in Table 2. The ionic radii of Ti(IV) and Nb(V) are 0.0605 nm and 0.064 nm respectively (Joshi, et al., 2013), hence only a small change in the lattice parameters is seen. For all compositions, except TE7Nb, the lattice parameter a is gradually increasing however no clear trend for c can be observed.

Table 2: Summary of changes in TiO_2 lattice parameters and cell volume with increasing Nb incorporation into the anatase structure

Samples	Unit Cell (Å)		Cell Volume ($Å^3$)
	a	c	
TE0Nb	3.776(0)	9.486(0)	135.25
TE3Nb	3.790(1)	9.500(3)	136.43
TE4Nb	3.792(3)	9.514(9)	136.79
TE5Nb	3.7925(8)	9.509(3)	136.77
TE6Nb	3.793(1)	9.507(5)	136.78
TE7Nb	3.789(4)	9.501(9)	136.41
TE8Nb	3.795(1)	9.510(3)	136.95

The Debye-Scherrer formula was used to calculate grain sizes in pure and Nb doped TiO_2 films. The non-doped sample exhibits a grain size of 24.52 nm, while calculations show an increase in grain size in the 3, 4, 6 and 7% doped films with values of 31.60 nm, 48.89 nm, 52.68 nm, 54.71 nm respectively. The trend is interrupted by the 5% and 8% samples with particle sizes of 46.79 nm and 42.23 nm.

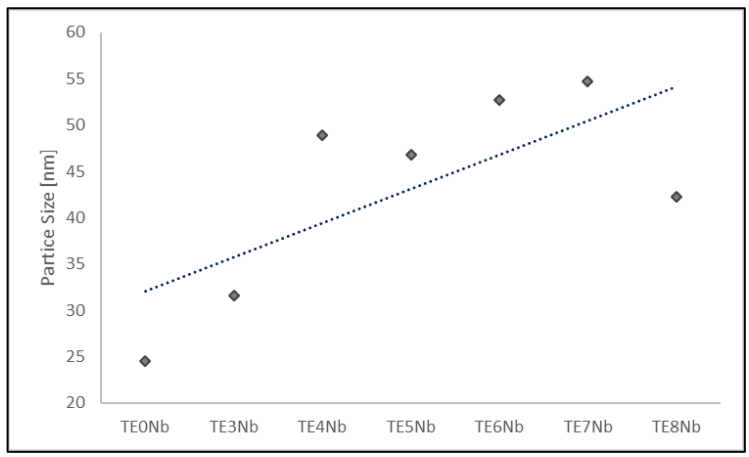

Fig. 10: Particle size distribution with changing doping level

3.4 *Conductivity*

To calculate the conductivity from I-V curves, a thickness of 100 nm for the coatings was chosen, due to average values obtained from spectroscopic ellipsometry measurements of previous samples deposited on glass slides. The highest calculated value was achieved for the sample with 8% Nb doping, followed by the 5% doped sample. The lowest conductivity was found in the sample with a concentration of 7% niobium, as can be seen in Table 3. Fig. 11 illustrates the change in conductivity with increasing doping level.

Table 3: Summary of conductivity measured for thin films on IDEs

Sample	Conductivity (S/cm)
TE0Nb	1.60×10^{-6}
TE3Nb	1.18×10^{-6}
TE4Nb	1.13×10^{-6}
TE5Nb	5.49×10^{-5}
TE6Nb	1.31×10^{-6}
TE7Nb	2.07×10^{-7}
TE8Nb	1.17×10^{-4}

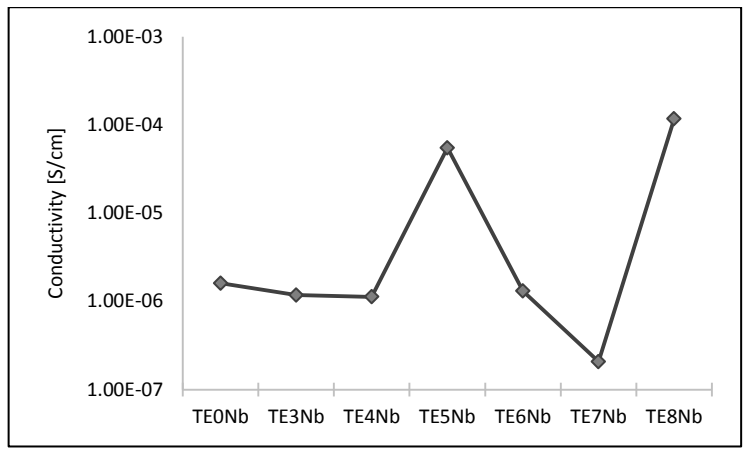

Fig. 11: Variation of conductivity of TiO_2 films with Nb doping concentration

4 Conclusion

Niobium doped titanium dioxide films were successfully prepared with the sol-gel method. All samples exhibited a blue colour that changed with increasing Nb concentration. UV-visible spectroscopy measurements showed low absorption of below 10% for the coatings over the whole measurement range. TiO_2 films exhibited the lowest energy bandgaps for samples with 5 and 8% Nb doping. Spectroscopic Ellipsometry suggests that optical constants, such as refractive index and extinction coefficient, decreased with increasing dopant level and reached a minimum for samples with 4% and 8% Nb respectively. Electron microscopy shows a smooth and crack-free coating with small grains forming clusters. EDX scans reveal a homogeneous distribution of niobium in the titanium dioxide matrix. For all samples the desired anatase crystal structure could be confirmed via XRD analysis, however the un-doped sample also contained brookite phase. The anatase (100) peak showed a slight shift to lower angles with increasing Nb concentration, which is thought to be due to stress caused by the incorporation of niobium into the lattice. Best conductivity was measured for TiO_2 films with 8% Nb doping.

Acknowledgements

This work has been carried out as part of the INFINITY project, which has received funding from the European Union's Horizon 2020 research and innovation programme under grant agreement No. 641927.

References

Bartic, M., Sacarescu, L. & Harabagiu, V., 2014. Structural , morphological and optical properties of TiO 2 films prepared using aqueous sol – gel methods. J Mater Sci: Mater Electron, Volume 25, pp. 454-460.

Bhachu, D. S. et al., 2014. Solution Processing Route to Multifunctional Titania Thin Films: Highly Conductive and Photcatalytically Active Nb:TiO2. Advanced Functional Materials, 24(32), pp. 5075-5085.

Cimieri, I. et al., 2012. Sol-gel preparation of pure and doped TiO 2 films for the photocatalytic oxidation of ethanol in air. Journal of Sol-Gel Science and Technology, Volume 63, pp. 526-536.

Dsy, J. & Ta, N. P., 2018. Overview on Transparent Conducting Oxides and State of the Art of Low-cost Doped ZnO Systems. SF Journal of Material and Chemical Engineering, 1(1), p. 1004.

Farooq, A. & Kamran, M., 2013. Effect of Sol Concentration on Structural and Optical Behavior of ZnO Thin Films Prepared by Sol-Gel Spin Coating. International Journal of Applied Physics and Mathematics, 2(6), pp. 430-432.

Furubayashi, Y. et al., 2006. Novel transparent conducting oxide: Anatase Ti1-xNbxO2. Thin Solid Films, Volume 496, p. 157 – 159.

Gillispie, M. A. et al., 2007. Sputtered Nb- and Ta-doped TiO2 transparent conducting oxide films on glass. Journal of Materials Research, 22(10), pp. 2832-2837.

Hung, K.-H.et al., 2011. Transparent conducting oxide films of heavily Nb-doped titania by reactive co-sputtering. Journal of Alloys and Compounds, 509(42), pp. 10190-10194.

Husain, S. et al., 2017. Influence of cobalt doping on the structural, optical and luminescence properties of sol-gel derived TiO2 nanoparticles. Philosophical Magazine, 97(1), pp. 17-27.

J. Liu, D. W. S. Z., 2009. Influence of temperature and layers on the characterization of ITO films. Journal of Materials Processing Technology, 209(8), pp. 3943-3948.

Jariwala, C. et al., 2015. Preparation and Characterization of Antimony Doped Tin Oxide Thin Films Synthesized by Co-Evaporation of Sn and Sb using Plasma Assisted Thermal Evaporation. Journal of Nano- and Electronic Physics, 5(2), pp. 1-5.

Joshi, B. N., Yoon, H., Hest, M. F. A. M. v. & Yoon, S. S., 2013. Niobium-doped titania photocatalyst film prepared via a nonaqueous sol-gel method. Journal of the American Ceramic Society, 96(8), pp. 2623-2627.

Joshi, B. N., Yoon, H., van Hest, M. F. A. M. & Yoon, S. S., 2013. Niobium-doped titania photocatalyst film prepared via a nonaqueous sol-gel method. Journal of the American Ceramic Society, 96(8), pp. 2623-2627.

Kwak, D.-J.et al., 2011. Comparison of transparent conductive indium tin oxide, titanium-doped indium oxide, and fluorine-doped tin oxide films for dye-sensitized solar cell application. Journal of Electrical Engineering and Technology, 6(5), pp. 684-687.

Lee, D. Y. et al., 2014. Effect of Nb doping on morphology, crystal structure, optical band gap energy of TiO2 thin films. Current Applied Physics, 14(3), pp. 421-427.

Lee, H. Y. & Robertson, J., 2013. Doping and compensation in Nb-doped anatase and rutile TiO2. Journal of Applied Physics, 113(213706).

Manolea, A. V. et al., 2013. Optical properties of Nb-doped TiO2 thin films prepared by sol-gel method. Ceramics International, Volume 39, pp. 4771-4776.

Ruiz, A. M. et al., 2004. Insights into the Structural and Chemical Modifications of Nb Additive on TiO 2 Nanoparticles. Chemistry of Materials, 16(5), pp. 862-871.

Singh, S., Sharma, V. & Sachdev, K., 2017. Investigation of effect of doping concentration in Nb-doped TiO2 thin films for TCO applications. Journal of Materials Science, 52(19), pp. 11580-11591.

Song, K. et al., 2011. Solution-processable tin-doped indium oxide with a versatile patternability for transparent oxide thin film transistors. Journal of Materials Chemistry, 21(38), pp. 4646-14654.

South American Silver Cooperation, 2012. South American Silver Cooperation. [Online] Available at: www.soamsilver.com [Accessed September 2018].

Stadler, A., 2012. Transparent Conducting Oxides—An Up-To-Date Overview. Materials, 5(4), pp. 661-683.

Sunde, T. O. L., 2013. In: Aqueous sol-gel processing of transparent conducting rare earth doped indium tin oxide. Trondheim: Thesis at NTNU-Trondheim, p. 93.

Sunde, T. O. L. et al., 2012. Transparent and conducting ITO thin films by spin coating of an aqueous precursor solution. Journal of Materials Chemistry, 22(31), pp. 15740-15749.

Tauc, J., 1974. Optical Properties of Amorphous Semiconductors. In: T. J., ed. Amorphous and Liquid Semiconductors. Boston, MA: Springer, pp. 159-214.

Science and Applications of Thin Films, Conference & Exhibition (SATF 2018)
Izmir Institute of Technology, Izmir, Turkey, September 17-21, 2018

Crystal structure and surface phase composition of palladium oxides thin films for gas sensors

Alexander Samoylov*, Stanislav Ryabtsev, Olga Chuvenkova, Sergey Ivkov, Mikhail Sharov, Sergey Turishchev

Voronezh State University, University Sq.,1, Voronezh, 394018, Russian Federation

*Corresponding author. Tel.: +7-473-259-6515; fax: +7-473-220-8735.
E-mail address:samoylov@chem.vsu.ru

Abstract

At detection of ozone and nitrogen dioxide gas sensors based on palladium (II) oxide thin and ultrathin films have shown good sensitivity, signal stability, operation speed, short recovery period, and reproducibility of the sensor response. In this work the influence of oxidation temperature on crystal structure and surface properties of palladium (II) oxide thin films prepared by oxidation at dry oxygen on SiO_2/Si (100) substrates has been studied by X-ray diffraction (XRD), electron probe microanalysis (EPMA), and X-ray photoelectron spectroscopy (XPS). By EPMA EDX it has been established that oxygen atom concentration increased in PdO/SiO_2/Si heterostuctures with the rise of oxidation temperature. At oxidation temperature interval T = 570 – 1020 K the values of lattice parameters and unit cell volume of PdO film tetragonal crystal structure increased also. Regardless of oxidation temperature by XPS measurements it has been found that palladium oxide films had three components of each Pd 3*d* 5/2 peaks which can be attributed to PdO, PdO_2, and $Pd(OH)_x$. Analysis of peak component contribution has shown that palladium (II) oxide was the dominant surface phase with relatively low value of the pronounced PdO_2 component. The obtained experimental data specify that the deviation from stoichiometry, excess oxygen concentration, and *p*-type conductivity can be caused by interstitial oxygen atoms in PdO films.

Keywords: palladium oxides; gas sensor; ozone; nitrogen dioxide; crystal structure; XPS measurements; surface state

1. Introduction

It is well known that most of the atmospheric ozone (~90%) is located in the stratosphere with a maximum concentration between 17 and 25 km above sea level [1]. However, since 1995 in industrialized countries the ecologists observe an ozone permanent accumulation at the earth's surface that can be very dangerous. World Health Organization (WHO) and United States Environmental Protection Agency (US EPA) declared that three out of six common air pollutants (also called as "criteria pollutants") are the oxidizing gases: sulfur dioxide, nitrogen oxides, and low level ozone (or tropospheric ozone) [2, 3]. The negative impact on human health of noxious oxidizing gases (nitrogen oxides, ozone, sulfur dioxide, and chlorine) formed as the by-product of many modern technologies is very serious. Breathing ozone and nitrogen oxides can trigger a variety of human health problems, particularly for children, the elderly, and people who have lung diseases [2, 3]. On toxicity ozone is comparable to the chemical weapon phosgene. Moreover, interaction of O_3 and NO_x with the volatile hydrocarbons can produce many toxic organic compounds [4].

Unlike many other toxic gases, for example, hydrogen sulphide or ammonia, ozone has no strongly pronounced characteristic smell, therefore it is very difficult to establish its presence in atmospheric air without special apparatuses [1]. The design of the portable individual devices, which are capable to define precisely the ozone and nitrogen dioxide concentration within admissible values, is extremely urgent task. For these reasons, the various types of the binary, ternary and quaternary metal-oxide semiconductors have been widely studied for oxidizing gas detection. In most cases for this purpose the *n*-type semiconductors such as SnO_2 [5–6], ZnO [7–8], WO_3 [9–10], In_2O_3 [11–12], and TiO_2 [13] are traditionally studied.

In recent years, the search for the materials, which could lower the detection limit of oxidizing gases, became more active. With the increasing attention the scientists study *p*-type semiconductors and composites on their basis [14]. For example, the sensor materials based on Cu_2O nanoflowers [15], NiO nanofibers [16], porous NiO microspheres [17], and copper (II) oxide nanostructures [18–19] have been synthesized. For the detection of oxidizing gases the nanocomposites with *p*-*n*-heterojunction have been used [20–21] as well as the composites based on graphene with *p*-*n*-heterotransitions are of great interest too [22–23].

In 2016 the experimental results on palladium (II) oxide thin and ultra thin film gas sensor properties were published for the first time [24–25]. The choice of palladium (II) oxide as the material for gas sensors was not incidental. It was done for some reasons. Firstly, a long recovery process and high stability could be referred to the main disadvantages of the SnO_2-based oxidizing gases sensors [26–28]. Secondly, late transition metals, such as Pd, Pt and Au, are widely used as additives to improve gas-sensing performance of tin dioxide, indium oxide and others *n*-type metal oxide semiconductors [29]. Thirdly, there is an opinion that for oxidizing gases detection the metal oxide semiconductors with *p*-type conductivity would be more effective than materials with *n*-type conductivity [14].

The measurement results of Seebeck coefficient and Hall effect verified the fact of *p*-type conductivity of PdO thin films [30–31], which was known from previous publications [32–33]. Palladium (II) oxide nanostructures demonstrated convincingly that they are the promising candidates for the detection of oxidizing gases in atmospheric air [4, 24–25]. At O_3 and NO_2 detection the gas sensors based on PdO nanostructures such as ultrathin and thin films have shown an excellent sensitivity, signal stability, operation speed, short recovery period, and reproducibility of the sensor response [30–31, 34].

So far there is no exact and definite answer to the question of the nature of the intrinsic point defects which are responsible for the nonstoichometry and *p*-type conductivity of palladium (II) oxide. In this work one step forward to the solution of this problem has been taken.

The main purpose of this study is to recognize the evolution of chemical composition of surface phase and crystal structure of palladium (II) oxide thin films upon the oxidation temperature in dry oxygen.

2. Experimental

2.1. X-ray diffraction study of PdO films

In detail the two-stage procedure of palladium oxide thin film synthesis was described previously [24–25, 30–31, 34]. Firstly, the initial Pd films (with thickness ~ 35 – 40 nm) were formed by thermal sublimation of palladium foil (purity 99.99 per cent) in a high vacuum chamber evacuated to 6.65×10^{-4} Pa. The condensation of Pd metal vapours was performed on Si (100) substrates with SiO_2 layer (thickness d ~ 300 nm). SiO_2/Si (100) substrates were used to prevent the possible interaction of Pd and Si at high temperature. This approach has yielded the positive results (Figure 1).

***a*)** ***b*)**

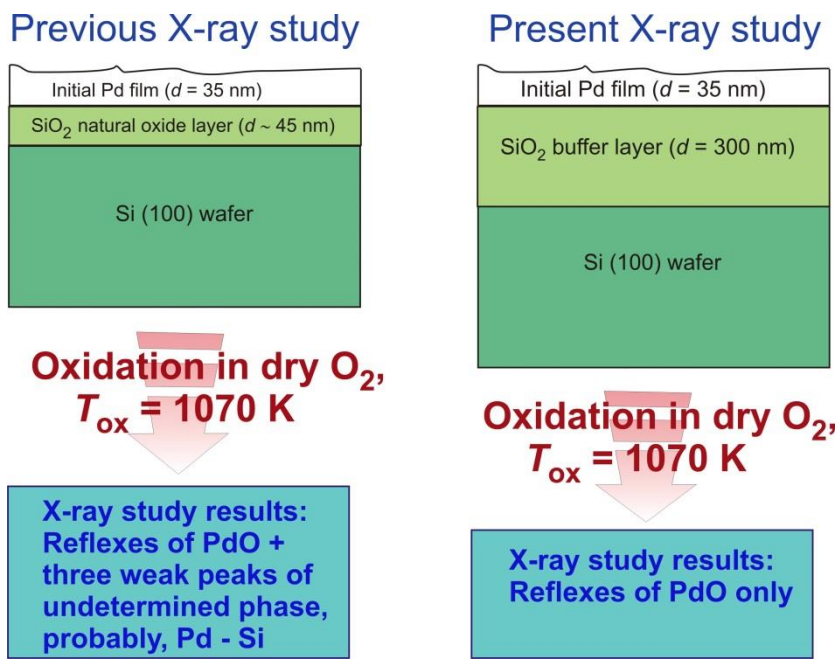

Fig. 1. Illustration of previous (*a*) and new advanced approach (*b*) for preparation and research of PdO films on Si substrates.

Initial Pd layers were annealed at dry oxygen atmosphere for 2 hours at temperatures T_{ox} = 570, 670, 770, 870, 970, and 1070 K. According to previous X - ray diffraction (XRD) results [30] the oxidation of initial Pd at temperature range T_{ox} = 770 – 870 K led to the formation of homogenous polycrystalline PdO films (space group $P4_2/mmc$). It has been determined that PdO films prepared by oxidation at T_{ox} = 1070 K showed three weak peaks of XRD patterns that could not be assigned to palladium (II) oxide [30]. The reflex number did not allow us to determine precisely what phase or phases they belong to. With equal probability and equal inaccuracy these peaks meet $Pd_{3.5}O_4$ phase or one of palladium silicides. As it can be seen in Figure 2 *c*, PdO films synthesized on Si (100) substrates with SiO_2 layer (thickness d ~ 300 nm) are homogenous also.

It should be noted that in this work the data on evolution of palladium (II) oxide film crystal structure depending upon the oxidation temperature are obtained for the first time. Therefore X - ray diffraction (XRD) experiment and quantitative calculations of PdO lattice parameters have been executed with special thoroughness. At the first stage in 2Θ region of 20 – 120 degrees XRD patterns of PdO films were obtained with filtered Cu$K\alpha$-radiation (λ = 0.15405 nm) on DRON - 4 M diffractometer with 0.02 degree step-by-step movement and sample rotation. These results (Figure 2) have shown that all PdO films prepared by oxidation in dry oxygen at T_{ox} = 670 –1070 K were homogeneous. At the second stage the profiles of PdO film XRD reflexes have been obtained on DRON - 4 M (Co$K\alpha$-radiation, λ = 0.178897 nm) and Philips PANanalytical X'Pert (Cu$K\alpha$-radiation, λ = 0.15405 nm) diffractometers with 0.01 degree step-by-step movement. The single crystal Si (100) substrates were used as internal standards to minimize the random errors. The diffraction angle values were determined as the XRD reflex centroids taking into account the peak asymmetry.

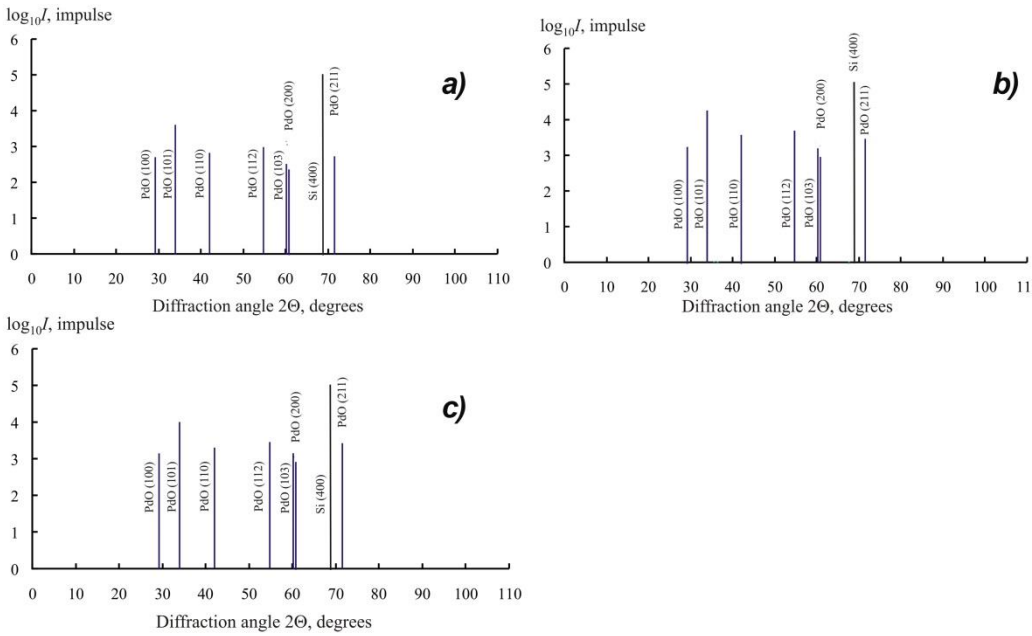

Fig. 2. XRD patterns of palladium (II) oxide films on Si (100) substrates prepared by oxidation in dry oxygen at different temperature: *a*) T_{ox} = 670 K; *b*) T_{ox} = 870 K; *c*) T_{ox} = 1070 K.

The values of lattice constant *a* and *c* of palladium (II) oxide tetragonal structure (Figure 3) have been calculated using the special software based on solution algorithm for quadric equation system with two unobvious parameters. Nelson-Riley approximation for 2Θ = 180 degrees diffraction angle has been performed for the refinement and more precise determination of *a* and *c* lattice constant values.

$$f(\theta) = 0.5 \times \left(\frac{\cos^2 \theta}{\theta} + \frac{\cos^2 \theta}{\sin \theta} \right) \quad , \tag{1}$$

where Θ is diffraction angle (radian).

The target values of *a* and *c* lattice constants, for example a_0, have been calculated by linear approximation of $a = k \times f(\Theta) + a_0$ using the least-squares method.

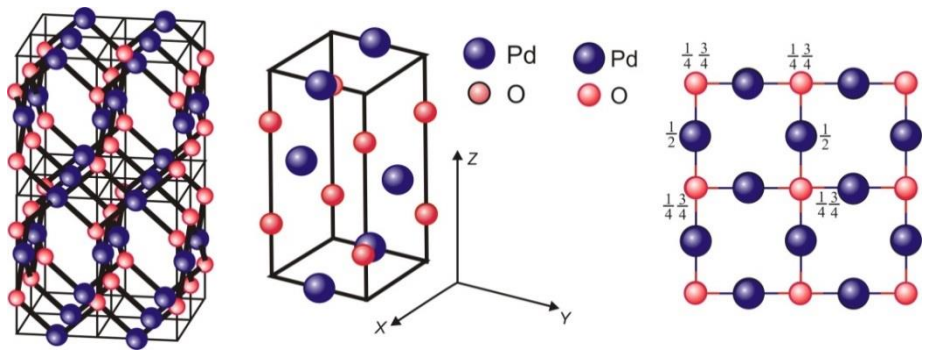

Fig. 3. Tetragonal crystal structure of palladium (II) oxide (*a*); unit cell of PdO crystal structure (*b*); projection of four PdO unit cells onto (001) plane – *XOY* plane (*c*).

2.2. Analysis of chemical composition of PdO films

The chemical composition of $PdO/SiO_2/Si$ heterostructures was studied by electron probe microanalysis (EPMA) on JEOL JSM 6380 LV equipped with Oxford Instruments INCA X-sight LN2 energy dispersion spectrometer (EDX). In a scanning mode EPMA EDX measurements were performed in five regions of each PdO sample (Figure 4). EDX measurement error was defined by statistical data manipulation and was evaluated as $\Delta x = \pm 0.15$ atomic percent.

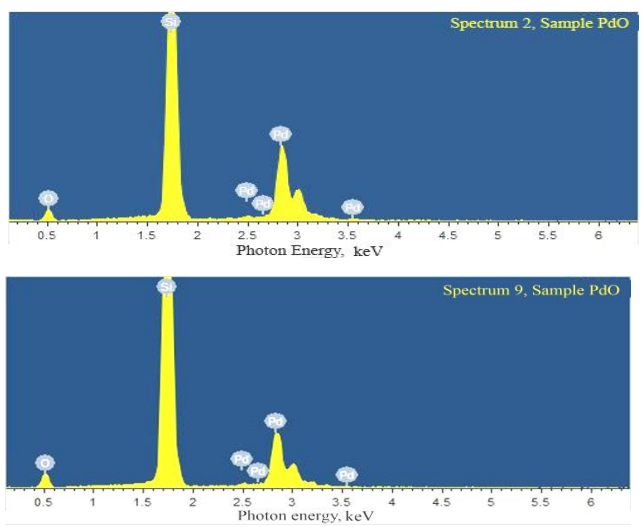

a)

b)

Fig. 4. EDX spectra of $PdO/SiO_2/Si$ heterostructures prepared by oxidation in dry oxygen at different temperature: *a*) T_{ox} = 670 K; *b*) T_{ox} = 870 K.

2.3. X-ray photoelectron spectra of PdO films

X-ray photoelectron spectra of palladium (II) oxide films were obtained with the use of highly brilliant synchrotron radiation of Helmholtz Zentrum Berlin (Berlin, Germany) BESSY II storage ring. Russian-German beamline (RGBL) was used together with multitask spectrometer equipped with SPECS PHOIBOS

150 hemispherical electron energy analyzer. Synchrotron photon energy used to excite Pd 3*d* core level was 800 eV with instrumental broadening ~ 0.1 eV, the highest photon flux of 10^{12} photons/sec, storage ring current of 250 mA in top-up operation mode. The analysis depth was found to be about 1.5 nm [35]. Ultra high vacuum conditions in analytical chamber necessary to conduct high resolution XPS experiment were maintained at 10^{-10} Torr. The calibration and the normalization of the spectra were carried out using a signal of pure gold film and the position of its core 4*f* level and the Fermi level under the recording conditions identical to those of the studied samples. During the XPS measurements, the registered core level energies were also controlled by the position of the C 1*s* level of hydrocarbon contamination residuals on the sample surfaces reduced to the known value of 285.0 eV [36–37].

3. Results and Discussion

3.1. Phase characterization of palladium (II) oxide films

XRD patterns of samples prepared by oxidation of initial Pd films in dry oxygen atmosphere at T_{ox} = 670, 770, 870, 970, and 1070 K are shown in Figure 2. It is necessary to note that owing to a small thickness of the prepared palladium (II) oxide films in Figure 2 the values of XRD reflex intensities are presented in a logarithmic scale since the intensity of Si (400) peak exceeds practically the intensity of PdO peaks by two orders of magnitude. According to XRD results (Figure 2), the oxidation of initial Pd layers on Si (100) wafers with SiO_2 layer (thickness ~ 300 nm) at temperature range T_{ox} = 570 – 1070 K led to the formation of homogenous polycrystalline PdO films. This fact contradicts the data published earlier [30] which were obtained in the study of palladium (II) oxide films on Si substrates with thinner layer of silicon dioxide. In all probability, the SiO_2 layer with 300 nm thickness prevented an interaction of palladium and silicon.

3.2. Chemical composition of PdO/SiO_2/Si heterostructures

Table 1. EDX analysis data of PdO films on SiO_2/Si (100) substrates (oxidation atmosphere - dry oxygen).

		Oxidation temperature T_{ox} = 870 K	
Element	X-ray spectrum line	Mass fraction ω%, percent	Mole fraction *x*, percent
Palladium	*L* - line	36.64	11.85
Oxygen	*K* - line	11.34	24.40
Silicon	*K* - line	52.02	63.75
Total:		100.00	100.00
Composition		***x*(Pd) : *x*(O) = 1 : 2.059 ± 0.004**	
		Oxidation temperature T_{ox} = 1070 K	
Element	X-ray spectrum line	Mass fraction ω%, percent	Mole fraction *x*, percent
Palladium	*L* - line	36.475	11.78
Oxygen	*K* - line	11.40	24.47
Silicon	*K* - line	52.125	63.75
Total:		100	100
Composition		***x*(Pd) : *x*(O) = 1 : 2.080 ± 0.004**	

The quantitative element composition of homogeneous PdO films on SiO_2/Si substrates was studied by EPMA EDX method. In Table 1 the EDX measurement data which have been obtained with the maximum possible measures directed at increasing of the accuracy and reproducibility results are presented.

Undoubtedly, EDX results of the determination of oxygen atom concentration in PdO/SiO_2/Si heterostructures are not exact and ultimate (Table 1, Figure 4). These data testify that the region of the EDX analysis was not limited by PdO film and stretched into SiO_2 layer and silicon substrate. Nevertheless, the presence of systematic procedural bias does not interfere with tracking the tendency of oxygen atom concentration change in PdO/SiO_2/Si heterostructures.

The calculation results of the ratio of oxygen mole fraction and palladium mole fraction

$$\chi = \frac{x_O}{x_{Pd}} \quad , \qquad (2)$$

where x_O – mole fraction of oxygen atoms, x_{Pd} – mole fraction of oxygen atoms in PdO/SiO_2/Si heterostructure, are shown in Figure 5.

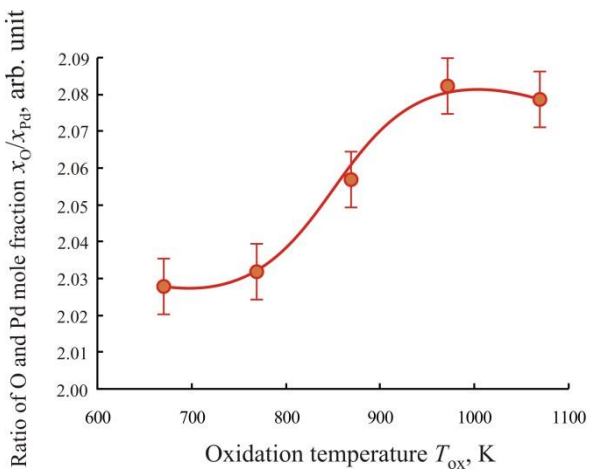

Fig. 5. Dependence of palladium and oxygen mole fraction ratio χ in PdO/SiO_2/Si heterostructures upon the oxidation temperature.

The data in Table 1 and curve $\chi = x_O/x_{Pd} = f(T_{ox})$ in Figure 5 show the increase in the oxygen atom concentration with the rise of oxidation temperature up to T_{ox} = 970 K. Valence-saturated and the most stable chemical bond between Si and O atoms causes extremely narrow homogeneity region of silicon dioxide, what it is impossible to expect for palladium (II) oxide. Evidently, the increase in oxygen atom concentration in PdO/SiO_2/Si heterostructures (Figure 5) cannot be explained by interaction of O_2 molecules with SiO_2 layer. Therefore, the increase in the oxygen atom concentration is caused by O_2 interaction with palladium atoms during oxidation process (Figure 4). The conclusion that with the rise of oxidation temperature the oxygen concentration increases due to saturation of palladium (II) oxide is quite reasonable. Some reduction of oxygen atom concentration at T_{ox} = 1070 K is explicable in view of the known facts about palladium (II) oxide thermal decomposition in the temperature range of about T = 1070 – 1120 K [38].

3.3. Evolution of crystal structure of palladium (II) oxide films

In Figure 6 the calculation results of *a* and *c* lattice constant of palladium (II) oxide film with tetragonal crystal structure (Figure 3) are shown. As it can be seen, the *a* and *c* unit cell parameter values increase

monotonously with the rise of oxidation temperature up to T_{ox} = 970 K. Incidentally, the lattice values of constant *a* are higher than ASTM etalon *a* value for oxidation temperature interval T_{ox} = 770 – 1070 K (Figure 6 *a*). The interval of oxidation temperature at which *c* values are above the ones for ASTM etalon, is essentially narrower: from T_{ox} = 870 to T_{ox} = 1070 K only (Figure 6 *b*).

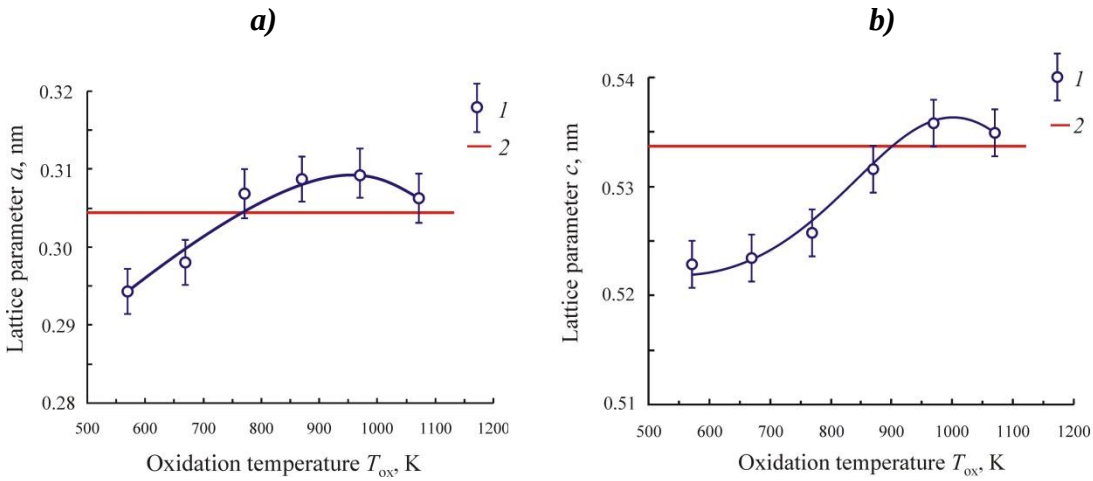

Fig. 6. Dependence of lattice constant *a* (*a*) and lattice constant *c* (*b*) of PdO film tetragonal crystal structure upon the oxidation temperature: *1* – experimental results; *2* – ASTM etalon data [39].

As it can be seen from the calculation results, the volume *V* of unit cell of palladium (II) oxide film crystal structure (Figure 7) increases monotonously at oxidation temperature rise from T_{ox} = 670 to T_{ox} = 970 K. The values of *V* for PdO film unit cell exceed the volume of ASTM etalon unit cell [39] in the temperature range *T* = 770 – 1070 K.

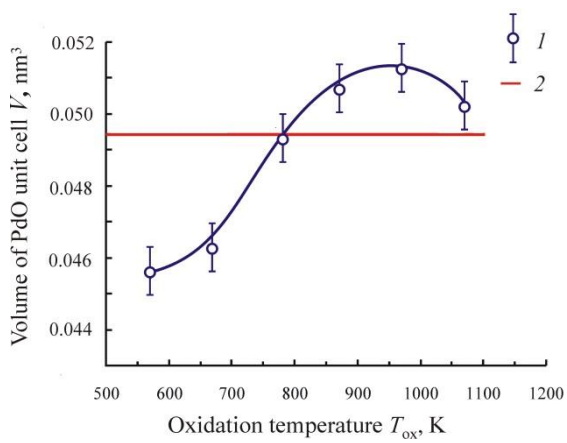

Fig. 7. Dependence of unit cell volume *V* of PdO films upon the oxidation temperature: *1* – experimental results; *2* – ASTM etalon data [39].

It is also informative to trace the evolution of unit cell parameters ratio *c*/*a* of PdO films depending upon the oxidation temperature (Figure 8). At oxidation temperature range T_{ox} = 570 – 820 K the decrease in *c*/*a* value indicates an anisotropic distortion of PdO film tetragonal crystal lattice mainly by virtue of the parameter *a* increasing. Therefore, the enlargement of PdO unit cell (Figure 7) is predominantly caused by increase in parameter *a* values. At further rise of oxidation temperature up to T_{ox} = 920 K the continued enlargement of PdO unit cell is accompanied by the decrease in the anisotropic distortion of PdO film tetragonal crystal lattice (Figure 3). At T_{ox} = 1070 K the insignificant reduction of the values of PdO film crystal structure *a* and *c* parameters (Figure 6) does not contradict the EDX data on the decrease in oxygen atom concentration at this temperature (Figure 5). Probably, the phase diagram of palladium (II) oxide is characterized by the retrograde solidus line.

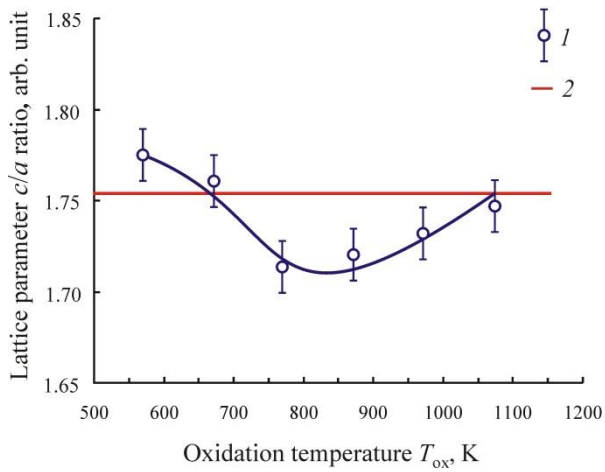

Fig. 8. Dependence of lattice constant *c* and lattice constant *a* ratio of PdO film tetragonal crystal structure upon the oxidation temperature: *1* – experimental results; *2* – ASTM etalon data [39].

3.4. XPS study of surface state of palladium (II) oxide films

Figure 9 demonstrates the comparison of XPS surveys recorded for palladium oxide films prepared at T_{ox} = 870 and 1070 K. For the comparison of XPS relative intensity distribution features these spectra have been rearranged under one intensity (spectrometer counts) ratio. Core levels peaks of palladium (3*p*, 3*d* and 4*d* states), oxygen (1*s* states) and carbon (1*s* states) can be clearly observed for both samples as well as palladium Auger MNN transition feature. Carbon states are usually observed on the surface of samples taken from the ambient and are characteristic of the surface hydrocarbon contaminants. For the sample prepared by oxidation at T_{ox} = 1070 K the low-intensity feature of silicon (2*p* states) is also detected and most likely originates from the substrate used. This observation can be explained

It should be noted that the energy position of 1*s* oxygen states are overlapped with $3p_{3/2}$ states of palladium according to the known core levels binding energy values [35, 37, 40–41]. The relative intensity ratio between O1*s* + Pd 3*p* peaks and Pd 3*d* doublet is nearly the same, which indicates the similarity of surface chemical state in both studied samples.

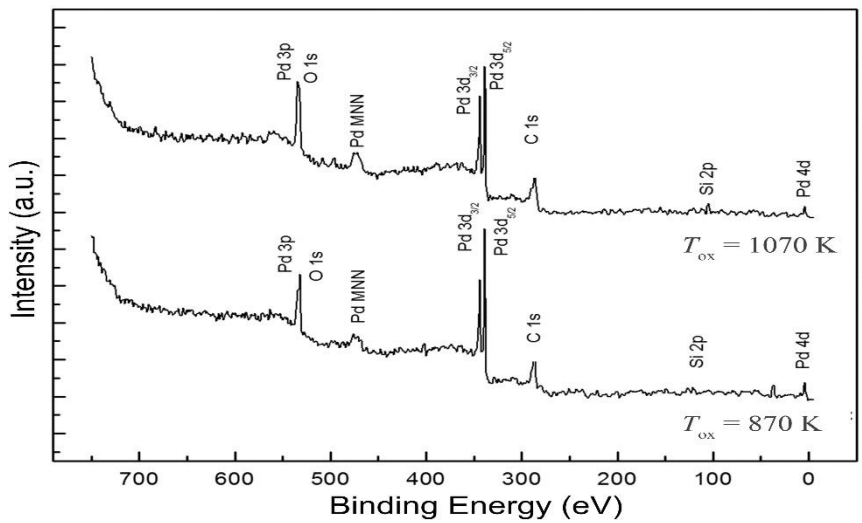

Fig. 9. XPS surveys recorded for palladium oxide films prepared by oxidation at T_{ox} = 870 K and 1070 K. Synchrotron quanta excitation energy was 800 eV.

Because of similarity between the O1*s* and Pd 3*p* binding energies values, we have decided to consider more precisely the most intensive (Figure 9) $3d_{5/2}$ core level of palladium. Figure 10 displays XPS spectra of Pd $3d_{5/2}$ core level taken from the samples oxidized at T_{ox} = 870 K and 1070 K. For the component fitting presented in Figure 10 we have used standard Shirley procedure of background removal [42].

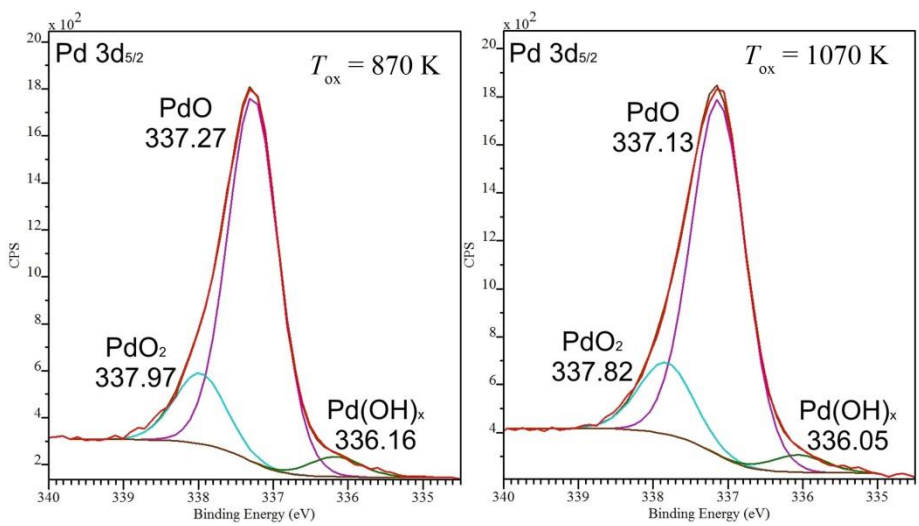

Fig. 10. High resolution XPS Pd 3*d*5/2 core level for palladium oxide films prepared by oxidation at T_{ox} = 870 K (*a*) and 1070 K (*b*).

Both recorded spectra have three distinct components that are peculiar to palladium oxide PdO [43, 44], PdO_2 [43 – 45], and $Pd(OH)_x$ [43, 44]. Very close relative intensity ratio of three components for both samples indicates the similar palladium oxidation states in the investigated surface layers. These observations of three components simultaneously are in good agreement with the known binding energy values for PdO, $Pd(OH)_x$, and PdO_2 phases discussed previously [43–44]. Thus, the oxidation of palladium films at T_{ox} = 870 and 1070 K does not cause the noticeably changes in the surface composition of palladium oxide films.

3.5. Summarizing of the experimental results

The detection of XPS signal corresponding to palladium dioxide PdO_2 deserves a special consideration (Figure 10). This fact can be interpreted as confirmation of presence on the surface of PdO films of an insignificant quantity of palladium atoms in extra (+4) oxidation state. In other words, on PdO film surface there are the excess oxygen atoms which can oxidize palladium atoms to extra (+4) oxidation state. In PdO films the presence of Pd (+4) atoms assumes the other coordination of palladium atom with oxygen ones, which should differ from Pd – O coordination in PdO crystal structure (Figure 3).

The authors of previous publications maintained that palladium (II) oxide samples were characterized by a small excess of oxygen atoms compared to stoichiometry ratio of the elements [46–47]. Besides, the hypothesis exists that *p*-type conductivity of PdO films with excess concentration of oxygen is caused by the formation of palladium vacancies V_{Pd} [47]. Within the framework of solid state chemistry and Kröger – Vink notation the *p*-type conductivity of undoped PdO can be explained by the formation of intrinsic point defects both of palladium vacancies $V_{Pd}^{\times}$ and oxygen atoms in interstitials $O_i^{\times}$ [48]:

1. The formation of palladium vacancies V_{Pd} during oxidation of initial Pd films:

$$Pd^{(S)} + O_2^{(G)} \rightarrow Pd_{Pd} + 2O_O + V_{Pd}^{'} \quad (3)$$

The neutral Pd vacancies $V_{Pd}^{\times}$ can ionize with the generation of holes:

$$V_{Pd}^{'} \leftrightarrow V_{Pd}^{\cdot} + h^{\bullet} \quad (4\ a)$$

or

$$V_{Pd}^{'} \leftrightarrow V_{Pd}^{\cdot\cdot} + 2h^{\bullet}, \quad (4\ b)$$

where $V_{Pd}^{\prime}$ is singly ionized palladium vacancy, $V_{Pd}^{\prime\prime}$ is doubly ionized palladium vacancy, $h^{\bullet}$ is hole.

2. The formation of oxygen atoms in interstitials $O_i^{\times}$ during oxidation of initial Pd films:

$$Pd^{(S)} + O_2^{(G)} \rightarrow Pd_{Pd} + O_O + O_i^{'} \quad (5)$$

The neutral oxygen atoms in interstitials $O_i^{\times}$ can ionize with the holes formation

$$O_i^{'} \leftrightarrow O_i^{\cdot} + h^{\bullet} \quad (6\ a)$$

or

$$O_i^{'} \leftrightarrow O_i^{\cdot\cdot} + 2h^{\bullet}, \quad (6\ b)$$

where $O_i^{\prime}$ is singly ionized interstitial oxygen atom, $O_i^{\prime\prime}$ – doubly ionized interstitial oxygen atom, $h^{\bullet}$ – hole.

4. Conclusion

The analysis of the experimental data obtained in this work allows us to state the oxidation temperature impact on the oxygen atom concentration and crystal structure distortion of palladium (II) oxide films. In PdO films the rise of oxidation temperature from T_{ox} = 570 to T_{ox} = 970 – 1020 K leads to the increase in oxygen atom concentration which is accompanied by anisotropic increase in crystal structure unit cell volume mainly due to the increase in *a* lattice constant value. In total with presence of palladium dioxide PdO_2 established by XPS measurements the obtained experimental data specify that the deviation from stoichiometry, excess oxygen concentration, and *p*-type conductivity can be caused by interstitial oxygen atoms O_i in the crystal structure of PdO films.

Acknowledgements

Stanislav Ryabtsev, Olga Chuvenkova, and Sergey Turishchev gratefully acknowledge the Ministry of Education and Science of Russian Federation (State Tasks for Higher Education Organizations in Science for 2017–2019, project 16.8158.2017/8.9).

References

[1] Korotcenkov, G., Brinzari, V., Cho B.K., 2016. In_2O_3- and SnO_2-Based Thin Film Ozone Sensors: Fundamentals, Journal of Sensors, Article ID 3816094, p. 1.
[2] Health Aspects of Air Pollution with Particulate Matter, Ozone and Nitrogen Dioxide. Report on a WHO Working Group. Bonn, Germany, 13–15 January 2003. © World Health Organization, 2003. 94 p.
[3] Estimating Mortality Risk Reduction and Economic Benefits from Controlling Ozone Air Pollution, 2008. Report of the US National Academies of Sciences. The National Academies Press, Washington, 286 p.
[4] Samoylov, A.M., Ryabtsev, S.V., Popov, V.N., Badica, P., 2018. Palladium (II) Oxide Nanostructures as Promising Materials for Gas Sensors. In "Novel Nanomaterials Synthesis and Applications" George Kyzas Editor. UK, London : IntechOpen Publishing House, London, p. 211.
[5] Oros, C., Horprathumb, M., Wisitsoraat, A., Srichaiyaperk, T., Samransuksamer, B., Limwichean, S., Eiamchai, P., Phokharatkul, D., Nuntawong, N., Chananonnawathorn, C., Patthanasettakul, V., Klamchuen, A., Kaewkhaoe, J., Tuantranont, A., Chindaudom P., 2016. Ultra-sensitive NO_2 sensor based on vertically aligned SnO_2 nanorods deposited by DC reactive magnetron sputtering with glancing angle deposition technique, Sensors & Actuators B 223, p. 936–945.
[6] Stanoiu, Adelina, Somacescu, Simona, Calderon-Moreno, Jose Maria, Teodorescu, Serban Valentin, Florea, Ovidiu Gabriel, Sackmann, André, Simion Cristian, Eugen, 2016. Low level NO_2 detection under humid background and associated sensing mechanism for mesoporous SnO_2, Sensors & Actuators B 231, p.166–174.
[7] Jiao, Mingzhi, Viet Chien, Nguyen, Van Duy, Nguyen, Duc Hoa, Nguyen, Van Hieu, Nguyen, Hjort, Klas, Nguyen, Hugo, 2016. On-chip hydrothermal growth of ZnO nanorods at low temperature for highly selective NO_2 gas sensor. Material Letters.169, p. 231–235.
[8] Lontio Fomekong, R., Lahem, D., Debliquy, M., Yunus, S., Lambi Ngolui, J., Delcorte, A., 2016. $Ni_{0.9}Zn_{0.1}O$/ZnO nanocomposite prepared by malonate coprecipitation route for gas sensing, Sensors & Actuators B 231, p. 520–528.
[9] Rishabh Jaina, Yu Leib, Radenka Maric, Ultra-low NO_2 detection by gamma WO_3 synthesized by Reactive Spray deposition technology, Sens. Actuators B 236 (2016) 163–172.
[10] Phung Thi Hong Van, Do Duc Dai, Nguyen Van Duy, Nguyen Duc Hoa, NguyenVan Hieu, 2016. Ultrasensitive NO_2 gas sensors using tungsten oxide nanowires with multiple junctions self-assembled on discrete catalyst islands via on-chip fabrication, Sensors & Actuators B 227, p. 198–203.
[11] Ilin, A., Martyshov, M., Forsh, E., Forsh, P., Rumyantseva, M., Abakumov, A., Gaskov, A., Kashkarov, P., 2016. UV effect on NO_2 sensing properties of nanocrystalline In_2O_3, Sensors & Actuators B 231, p. 491–496.
[12] Bingxin Xiao, Fei Wang, Chengbo Zhai, Pan Wang, Chuanhai Xiao, Mingzhe Zhang, 2016. Facile synthesis of In2O3 nanoparticles for sensing properties at lowdetection temperature, Sensors & Actuators B 235, p. 251–257.
[13] Navale, S.T., Tehare, K.K., Shaikh, S.F., Patil, V.B., Pawar, B.N., Naushad, Mu. Stadler, F.J., Mane, R.S., 2016. Hexamethylenetetramine-mediated TiO_2 films: facile chemical synthesis strategy and their use in nitrogen dioxide detection, Material

Letters 173, p. 9–12.
[14] Hyo-Joong Kim, Jong-Heun Lee, 2014. Highly sensitive and selective gas sensors using *p*-type oxide semiconductors: Overview // Sensors & Actuators B. 192, p. 607– 627.
[15] Shixiu Cao, Hui Chen, Tao Han, Cong Zhao, Lingling Peng, 2016. Rose-like Cu_2O nanoflowers via hydrothermal synthesis and their gas sensing properties. Material Letters 180, p. 135–139.
[16] Jong-Myoung Choia, Joon-Hyuk Byun, Sang Sub Kim, 2016. Influence of grain size on gas-sensing properties of chemiresistive p-type NiO nanofibers. Sensors & Actuators B 227, p. 149–156.
[17] Kuan Tian, Xiao-Xue Wang, Hua-Yao Li, Reddeppa Nadimicherla, Xin Guo, 2016. Lotus pollen derived 3-dimensional hierarchically porous NiO microspheres for NO_2 gas sensing. Sensors & Actuators B 227, p. 554–560.
[18] Kneer, J., Wöllenstein, J., Palzer, S., 2016. Manipulating the gas–surface interaction between copper (II) oxide and mono-nitrogen oxides using temperature. Sensors & Actuators B 229, p. 57–62.
[19] Jae-Hun Kim, Akash Katoch, Sun-Woo Choi, Sang Sub Kim, 2015. Growth and sensing properties of networked p-CuO nanowires. Sensors & Actuators B 212, p. 190–195.
[20] Zou, C.W., Wang, J., Xie, W., 2016. Synthesis and enhanced NO_2 gas sensing propertiesof ZnO nanorods/TiO_2 nanoparticles heterojunction composites. Journal Colloid Interface Sci. 478, p. 22–28.
[21] Wenjun Yan, Ming Hu, Jiran Liang, Dengfeng Wang, Yulong Wei, Weiyi Zhang,Yuxiang Qin, 2016. Preparation and room temperature NO_2-sensing performances of n-porous silicon/n-WO_3 nanowires heterojunction. Material Research Bulletin 83, p. 453–458.
[22] Srivastava, V., Jain, K., 2016. At room temperature graphene/SnO_2 is better than MWCNT/SnO_2 as NO_2 gas sensor. Material Letters. 169, p. 28–32.
[23] Yan Xiao, Qiuyue Yang, Zhenyu Wang, Rui Zhang, Yuan Gao, Peng Sun,Yanfeng Sun, Geyu Lu, 2016. Improvement of NO_2 gas sensing performance based on discoid tin oxide modified by reduced graphene oxide. Sensors & Actuators B 227, p. 419–426.
[24] Ryabtsev, S.V., Shaposhnik, A.V., Samoylov, A.M., Sinelnikov, A.A., Soldatenko, S.A., Kuschev, S.B., Ievlev, V.M., 2016. Thin films of palladium oxide for gas sensors. Dokl. Phys. Chem. 470, p. 158–161
[25] Ievlev, V.M., Ryabtsev, S.V., Shaposhnik, A.V., Samoylov, A.M., Kuschev, S.B., Sinelnikov, A.A., 2016. Ultrathin Films of Palladium Oxide for Oxidizing Gases Detecting, Procedia Engineering 168, p. 1106-1109.
[26] Korotcenkov, G., Cho, B.K., 2012. Ozone measuring: what can limit application of SnO_2-based conductometric gas sensors. Sensors & Actuators B 161, p. 28–44.
[27] Marikutsa, A.V., Rumyantseva, M.N., Gaskov, A.M., Samoylov, A.M., 2015. Nanocrystalline tin dioxide: basics in relation with gas sensing phenomena. Part I. Physical and chemical properties and sensor signal formation, Inorganic Materials 51, p. 1329–1347.
[28] Marikutsa, A.V., Rumyantseva, M.N., Gaskov, A.M., Samoylov, A.M., 2016. Nanocrystalline tin dioxide: basics in relation with gas sensing phenomena.Part II. Active Centers and Sensor Behavior, Inorganic Materials 52, p. 1327–1354.
[29] Ievlev, V.M., Sinel'nikov, A.A., Soldatenko, S.A., Ryabtsev, S.V., Samoilov, A.M., Kushchev, S.B., Bosykh, M.A., 2016. Structure of heterosystems formed by a SnO_2 film and island metal (Ag, Au, or Pd) condensate. Inorganic Materials. 52 (7), p. 700-707.
[30] Ryabtsev, S.V., Ievlev, V.M., Samoylov, A.M., Kuschev, S.B., Soldatenko, S.A., 2017. Microstructure and electrical properties of palladium oxide thin films for oxidizing gases detection. Thin Solid Films 636, p.751-759.
[31] Ievlev V.M., Ryabtsev S.V., Samoylov A.M., Shaposhnik A.V., Kuschev S.B., Sinelnikov A.A. Thin and Ultrathin Films of Palladium Oxide for Oxidizing Gases Detection. Sensors and Actuators B: Chemical. – 2018. – V. 255, N. 2. Pages 1335 – 1342.
[32] Nilsson, P.O., Shivaraman, M.S., 1979. Optical properties of PdO in the range of 0.5-5.4 eV. Journal of Physics. C: Solid State Physics 12, p. 1423–1427.
[33]. Rey, E., Kamal, M.R., Miles, R.B., Royce, B.S.H., 1978. The semiconductivity and stability of palladium oxide // Journal of Materials Science 13, p. 812–816.
[34] Samoylov, A.M., Ievlev, V.M., Ryabtsev, S.V., Shaposhnik, A.V., Sinelnikov, A.A., 2017. Palladium oxide thin films for oxidizing gases detection // 21st American Conference on Crystal Growth and Epitaxy (ACCGE-21) and 18th US Workshop on Organometallic Vapor Phase Epitaxy (OMVPE-18), Santa Fe, USA, July 30 - August 4, 2017. - book of abstracts. - p. 147 - 148. http://www.crystalgrowth.org/AACG_Ebook_V09.pdf.
[35] Henke, B.L., Gullikson, E.M., Davis, J.C., 1993. X-ray interactions: photoabsorption, scattering, transmission, and reflection at *E*=50-30,000 eV, Z=1-92. Atomic data and nuclear data tables 54, p. 181-342.
[36] Crist, B.V., 1999. PDF Handbooks of Monochromatic XPS Spectra. Volume 1. The Elements and Native Oxides. XPS International Published by XPS International, LLC, 754 Leona Lane, Mountain View, California 94040, USA, p. 84.
[37] www.xpsdata.com.
[38] Greenwood, N.N., Earnshaw, A., 1997. Chemistry of the Elements (2nd ed.) Oxford: Butterworth-Heinemann, 1340 p..
[39] JCPDS - International Centre for Diffraction Data. © 1987–2005. JCPDS-ICDD. Newtown Square, PA 19073. USA, card number 43-1024, Grier D., McCarthy, G., 1991. North Dakota. State University, Fargo, N. Dakota, USA, ICDD Grant-in-Aid.
[40] Militello, M., Simko, S., 1997. Elemental Palladium by XPS. Surface Science Spectra 3 (4), p. 387-394.
[41] Militello, M., Simko, S., 1997. Palladium Oxide (PdO) by XPS. Surface Science Spectra 3 (4), p. 395-401.
[42] Shirley, D.A., 1972. High-resolution X-ray photoemission spectrum of the valence bands of gold. Physical Review **B5**, p.4709.
[43] Yan Yang, Wei Wang, Yanqin Liu, Fengxia Wang, Dan Chai, Ziqiang Lei, 2015. Pd nanoparticles supported on phenanthroline modified carbon as high active electrocatalyst for ethylene glycol oxidation. Electrochimica Acta 154, p. 1–8.
[44] Lei, H., Sun, W., Sun, Zh., 2017. Amorphous Co_3O_4-Decorated Pd as an Efficient Electrocatalyst for Methanol Oxidation NANO:

Brief Reports and Reviews 12 (6), P. 1750078-1 - 1750078-8.
[45] Ivanova, A.S., Slavinskaya, E.M., Gulyaev, R.V., Zaikovskii, V.I., Stonkus, O.A., Danilova, I.G., Plyasova, L.M., Polukhina, I.A., Boronin A.I., 2010. Metal–support interactions in Pt/Al_2O_3 and Pd/Al_2O_3 catalysts for CO oxidation. Applied Catalysis B: Environmental 97., p. 57–71.
[46] Avila, J.I., Favre, M., Volkmann, U.G., Cabrera, A.L., Lederman, D., 2006. Optical spectroscopy of PdO and Pd thin films under hydrogen exposure, in: APS March Meeting, Baltimore, MD, p. 204.
[47] García-Serrano O., Andraca-Adame A., Baca-Arroyo R., Peña-Sierra R., Romero-Paredes G.R. Thermal Oxidation of Ultra Thin Palladium (Pd) Foils at Room Conditions // Proceedings of Electrical Engineering Computing Science and Automatic Control (CCE), 2011 8th International Conference on 26-28 Oct. 2011. Merida City, Mexico. – p. 456–460.
[48] Kröger, F.A., 1964. The Chemistry of Imperfect Crystals, North-Holland Publishing Company, Amsterdam, 650 p.

Science and Applications of Thin Films, Conference & Exhibition (SATF 2018)
Izmir Institute of Technology, Izmir, Turkey, September 17-21, 2018

Nonlinear optical properties of hydrogenated amorphous silicon-chalcogen alloys thin films

Shawqi Al Dallal[a*], Khalil Ebrahim Jasim[b], and Fryad Henari[c]

[a]*College of Graduate Studies and Research, Ahlia University, P. O. Box 10878, BAHRAIN*
[b]*Department of Physics, University of Bahrain, P. O. Box 32038, BAHRAIN*
[c]*Department of Basic Medical Sciences, Royal College of Surgeon in Ireland, University of Bahrain, P. O. Box 15503, BAHRAIN*

*Corresponding author Phone: +973 39664218, Fax: +973 17290083
Shawqi Al Dallal, shaldallal@gmail.com

Abstract

Hydrogenated amorphous silicon-chalcogen alloys thin films were grown by capacitively coupled radio frequency glow discharge technique. Chalcogens used in this experiment are mainly sulphur and selenium. Diluted SiH_4, and H_2S or H_2Se gas mixtures were used in the preparation process to reduce potential hazardous outcome. Infrared spectroscopy shows that the material exhibits characteristic vibrational modes of sulphur or selenium in a silicon matrix. Nonlinear properties of the silicon alloys were investigated using z-scan technique. The measurements were carried out at various excitation powers using continuous HeNe laser source at excitation wavelengths of 632.8 nm. For each excitation power, the nonlinear absorption and nonlinear refractive index coefficients were measured. It was found that these films are dominated by a reverse saturation absorption process and a positive refractive index. The origin of nonlinearities was discussed in terms of single photon absorption and reverse saturation absorption. The third order nonlinear optical susceptibility $\chi^{(3)}$ was calculated for given input power. It was shown that a-Si, S:H and a-Si, Se:H alloys exhibit significant optical limiting properties.

Keywords: Thin films; amorphous silicon- sulphur/selenium alloys; z-scan; coefficient of nonlinear absorption; reverse saturable absorption.

1. Introduction

Hydrogenated amorphous silicon-chalcogen alloys have been shown to exhibit attractive optical and electronic properties [Aljishi et. al, 1991; Al Dallal et. al., 1991, 2010; Al Dallal, 2015]. An interesting feature of this material is that has potential applications in a wide range of optical devices. The silicon-chalcogen bond is stronger than the silicon-silicon bond, and therefore, the introduction of chalcogen atoms in the silicon matrix enhances appreciably the stability of this material against aging. Optical nonlinearity is a key process in characterizing materials to probe their potential applications in optical devices. Nonlinear effects include various types of phenomenon, such as third order nonlinear susceptibility, free carrier absorption, reverse saturation absorption (optical limiting), self-focussing, and self-defocusing. The nonlinear optical properties of silicon based materials, such as amorphous silicon, silicon nanocrystal, and porous silicon, have been the subject of intense research work during the past decade [Parkash et. al., 2002; Henari and Blau, 1992; Derkowska et. al., 2004; Banfi et. al., 1994]. Nonlinearities in a-Si are manifested as an intensity dependent

absorption, giving rise to optical limiting behaviour via saturation trapping states. Since these states exhibit a slow relaxation time, it should be possible to measure the nonlinear behaviour at low power irradiation.

In this work we report measurements of the nonlinear properties of hydrogenated amorphous silicon-chalcogen alloys thin films using continuous 632.8 nm HeNe laser line. Measurements were carried out using z-scan technique for various laser light powers. Both nonlinear absorption and nonlinear refractive index were measured. However, it was found that at this excitation wavelength the nonlinear absorption was the dominant effect, whereas the nonlinear refractive index is relatively weak. For the nonlinear absorption, an estimation of the excited state cross section has been carried out. We also demonstrate how nonlinear absorption can be used to characterize the optical limiting properties of the material.

2. Experiments

Hydrogenated silicon-chalcogen alloys thin films were prepared by capacitively coupled r.f. glow discharge technique. A controlled flow of gas mixtures of (5% SiH_4 + 95%He) and (2% H_2S or H_2Se +98% He) has been used to deposit thin films of the alloys on 7059 Corning glass substrate. Helium gas was employed for safety purposes. The substrate temperature was held at 250 C^o and the process pressure was maintained at 0.4 Torr. The total plasma power was kept at 30 Watts, and the corresponding power density is 160 mW/cm^2. The total flow rate was maintained at 40 sccm. Under these conditions the growth rate was about 2Å/s for equal flow rates of silane (SiH_4) and hydrogen sulphide (H_2S) or Hydrogen selenide (H_2Se) mixtures. The deposition rate was found to be a function of the gas volume ratio R_v = [chalcogen/silane]. Linear absorbance of samples were measured using dual beam spectrophotometer.

The nonlinear properties of the samples were characterized using z-scan set up, as illustrated schematically in Fig.(1). The coefficient of refraction has been determined by placing an aperture in front of the detector and measuring the transmitted light (close aperture configuration). This approach increases the sensitivity of measurement to beam spreading or beam focusing. In this set-up the sample displaying nonlinear refraction will act as a lens that exhibits variable focal length as it transit along the z-axis. For measurements of the nonlinear absorption coefficient the aperture was removed (open aperture configuration). The transmittance versus the sample position is now symmetric around the focus, because the intensity distribution of the laser's Gaussian beam is also symmetric around the focus.

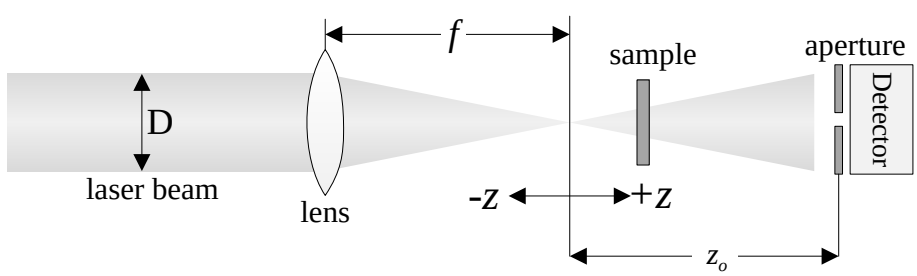

Figure (1): Closed aperture z-scan set up to measure the nonlinear refractive index coefficient.

3. Result and discussion

3.1. *Nonlinear absorbance*

Figure (2) shows the absorbance of a-Si, S:H and a-Si, Se:H alloys. The absorbance increases rapidly at wavelength below 500 nm. Figure (3) depicts the normalized transmission for z-scan open aperture configuration for typical a-Si, S:H alloy thin film at different excitation powers. Similar variation has been obtained for a-Si, Se:H alloy thin films.

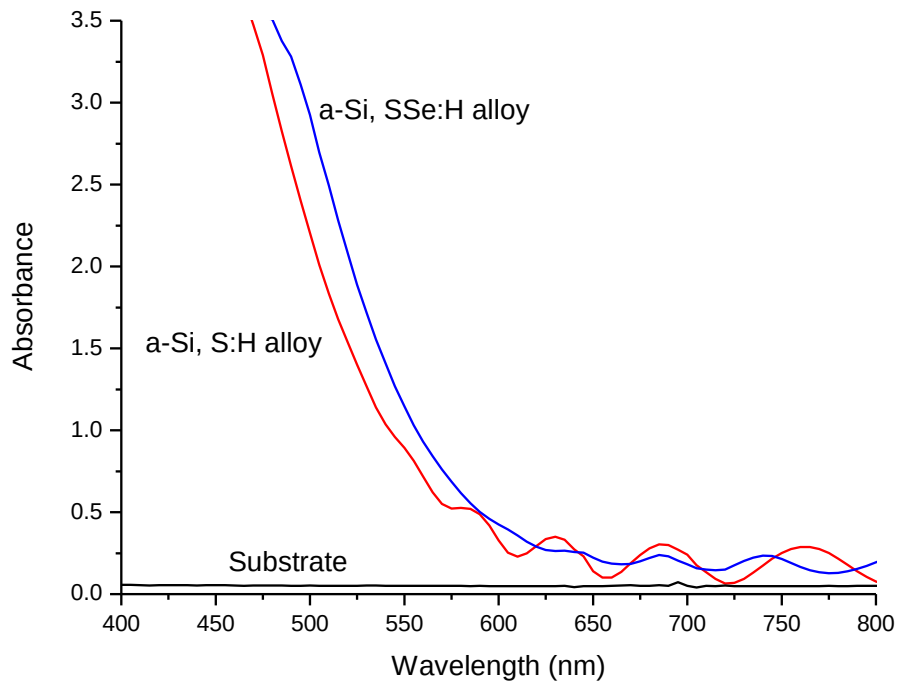

Figure (2). Linear absorbance of typical a-Si, S:H y and a-Si, Se:H alloys deposited on Corning glass substrate.

The normalized transmission for open z-scan is given by [Sheik-Bahaa et. al., 1990]:

$$\Delta T = 1 - \frac{\Delta\varphi}{\left(1 + \frac{z^2}{z_o^2}\right)} \tag{1}$$

Where $z_0 = \pi\omega_0^2/\lambda$ is the Rayleigh radius of the Gaussian beam, ω_0 is the beam waist, and $\Delta\varphi$ is the phase distortion. The nonlinear absorption coefficient is given by [Vinitha and Ramalingam, 2008]:

$$\beta = \frac{2\sqrt{2}\ \Delta\varphi}{I_o L_{eff}} \tag{2}$$

Where $I_0 = 2P_0/\pi\omega_0^2$, and $\pi\omega_0^2$ is the cross section area of the laser beam waist at the focus. In the above equation L_{eff} is the effective length of the sample, and is given by

$$L_{eff} = [1 - \exp(-\alpha l)]/\alpha \tag{3}$$

Where ℓ is the thickness of the sample α is the linear absorption coefficient.

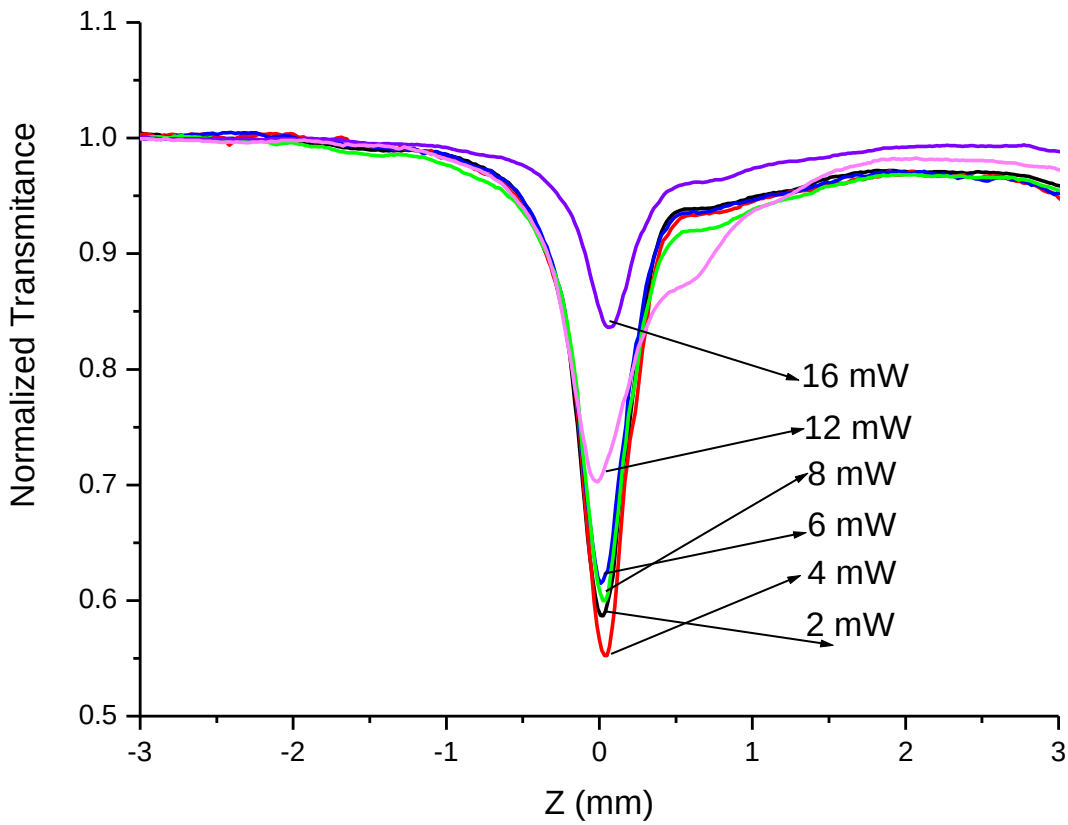

Fig.(3): Normalized transmittance for z-scan open aperture configuration for typical a-Si, S:H alloy at different excitation powers.

Taking $\Delta\varphi = P_1$ as fitting parameter, and $z_0 = \pi\omega_0^2/\lambda = P_2$ as a second fitting parameter, we get $I_0 = 2P_0(mW)/\lambda P_2$, hence:

$$\beta = \frac{\sqrt{2}\lambda P_1 P_2}{P_o(mW)L_{eff}} \tag{4}$$

From Figure (2) we obtain $\alpha \approx 7.6 \times 10^5$ m^{-1} for both types of alloys. Using $\ell = 1$ μm in Eq.(3), we obtain L_{eff}

= 0.699 μm. For λ = 632.8 nm, Eq.(4) becomes,

$$\beta = \frac{1.28 P_1 P_2}{P_o(mW)} \tag{5}$$

Figures (4) and (5) show typical open-aperture z-scan for a-Si, S:H and a-Si, Se:H alloys at 632.8 nm excitation wavelength respectively. On the same figures are shown the best fit of the data for P_0 = 8 mW using Eq.(5). The transmission is symmetric with respect to the focus (z = 0), where it reaches its minimum value. This behaviour is typical of induced absorption such as reverse saturation absorption. Figures (6) and (7) depict the variation of the nonlinear absorption coefficient with excitation power for both types of alloys considered in this work. In these figures we observe a decrease followed by saturation in nonlinear absorption as the excitation power increases.

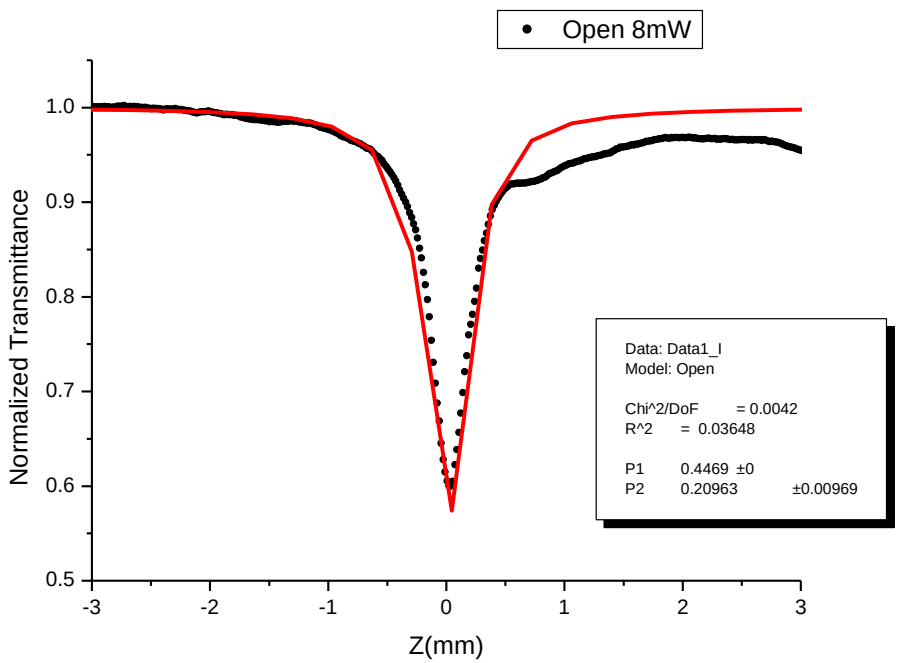

Figure (4): Open aperture z-scan response for a-Si, S:H at 8 mW excitation power. The line corresponds to the best fit of the data.

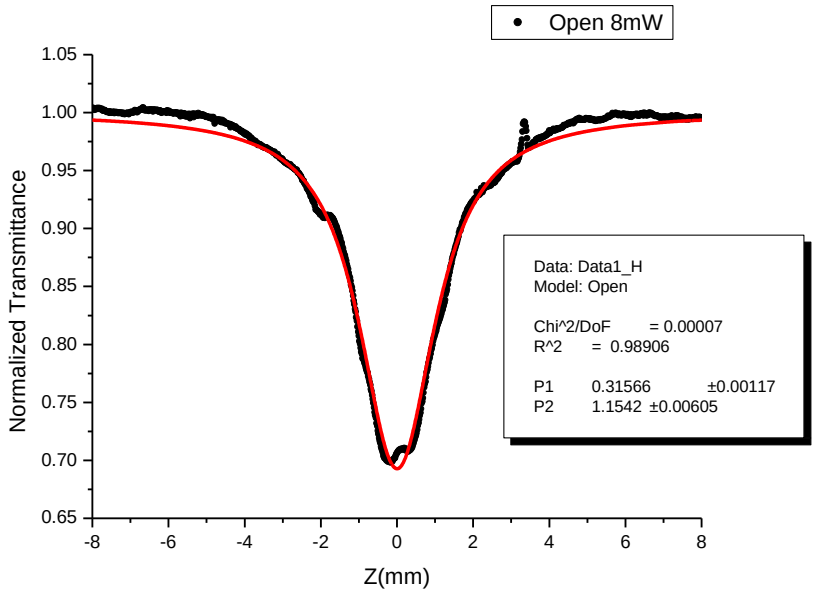

Figure (5): Open aperture z-scan response for a-Si, Se:H at 8 mW excitation power. The line corresponds to the best fit of the data.

The nonlinear absorption coefficient β can also be expressed in terms of the change in absorption cross section Δσ through the relation [Andrade et. al., 2006]:

$$\beta = \frac{\lambda N_o \Delta\sigma}{4\pi I_s} \tag{6}$$

Where $\Delta\sigma = \sigma_{exc} - \sigma_{gr}$ is the difference between the excited state and ground state absorption coefficients, N_0 is the concentration of defect states, and I_s is the saturation intensity, and is given by:

$$I_s = hc / \lambda \sigma_{gr} \tau \tag{7}$$

Here hc/λ is the photon energy, and τ is the response life time, and is taken as equal to 12 ms [Henari, 2008]. N_0 depends upon the gas volume ratio (R_v). For $R_v = 0.044$, $N_0 \approx 2\times10^{20}$ cm^{-3} for both a-Si, S:H and a-Si, Se:H alloys [Aljishi et. al, 1991]. $\sigma_{gr} = \alpha/N_0 = 1\times10^{-17}$ cm^2, hc/λ = 1.96 eV, and hence I_s = 26.17 kW/m^2. Using the above data and Eq.(6), Δσ can be calculated for both alloys. For a-Si, S:H the change in the absorption coefficient Δσ decreases from 6.81×10^{-15} to 9.39×10^{-16} cm^2 as the power increases from 2.1 mW to 16.5 mW. The corresponding σ_{exc} obtained for a-Si,S:H alloy ranges between 6.81×10^{-15} and 4.90×10^{-16} cm^2. For a-Si, Se:H Δσ decreases from 1.628×10^{-14} to 6.70×10^{-15} cm^2 for the same change in excitation power. The corresponding σ_{ex} obtained for a-Si,Se :H alloy ranges between 1.629×10^{-14} and 6.51×10^{-15} cm^2. In all cases σ_{ex} is greater than σ_{gr}, which is typical requirement for reverse saturation absorption. In this process electrons are optically generated by single photons, and are promoted to the higher states of the conduction band. Electrons are then relaxed to trapping levels (defect states). The lack of saturation of these excited states indicates that the relaxation from excited state level into trapping states is very fast, whereas the relaxation

time from these states to the ground state is slow. Excited states absorption would then occur from the trapping states to a higher excited state level within the conduction band.

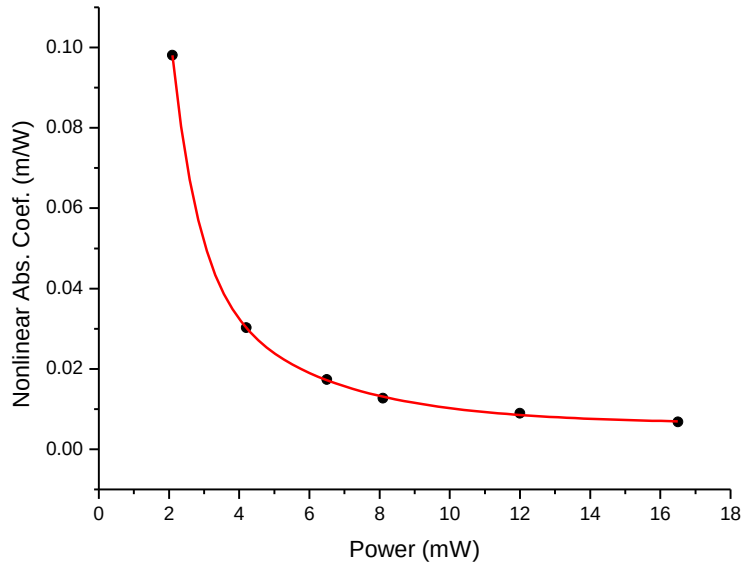

Figure (6): Nonlinear absorption coefficient for a-Si, S:H at different excitation powers.

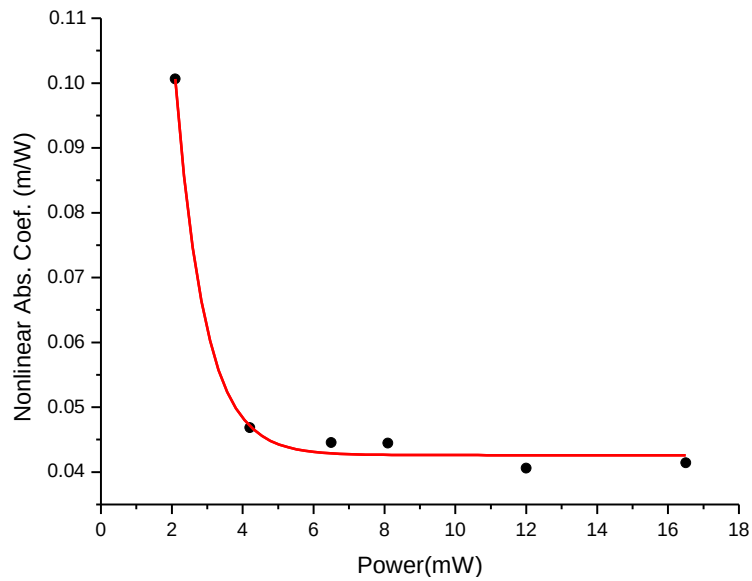

Figure (7): Nonlinear absorption coefficient for a-Si, Se:H at different excitation powers.

3.2. Nonlinear refractive index

The nonlinear refractive index has been determined from closed aperture configuration. Figure (8) shows the normalized transmission for the closed aperture configuration. The normalized transmission is given in this case by [Sheik-Bahaa et. al., 1990; Andrade et. al., 2006]:

$$\Delta T = 1 + 2\Delta\phi\left[\frac{2x}{(1+x^2)(9+x^2)}\right] - 2\Delta\varphi\left[\frac{3+x^2}{(1+x^2)(9+x^2)}\right] \tag{8}$$

Where $x = z/z_0$ and,

$$\Delta\phi = \frac{2\pi}{\lambda} I_o \gamma L_{eff} \tag{9}$$

In the above equation γ is the nonlinear refractive index. A fit of Eq.(8) to the experimental data is shown in Figure (8). As it can be seen in this figure, the sample possesses positive nonlinear index of refraction indicating self-focusing action. Substituting the fitting parameter $P_1 = \Delta\phi$ into Eq (9), the value of $\gamma = 2.97\times10^{-9}$ m^2/W was obtained.

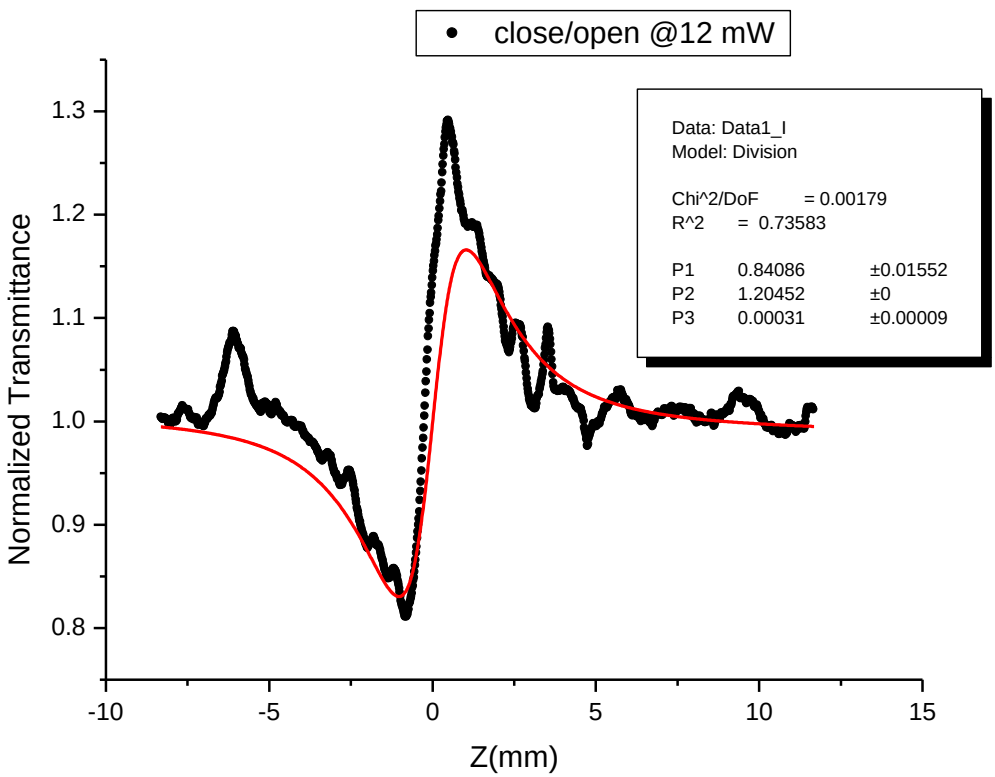

Figure (8): Close aperture z-scan response for a-Si, Se:H at 12.0 mW excitation power. The line corresponds to the best fit of the data.

3.3. Third order susceptibility

The third order nonlinear optical susceptibility $\chi^{(3)}$ can be calculated using the following relations [Rekha et. al., 2009; Sun et. al., 2006]:

$$\mathrm{Re}\,\chi^{(3)}(esu) = \left(\frac{\varepsilon_0 c^2}{10^4 \pi}\right) n_0^2\, n_2 \quad (cm^2/W) \tag{10}$$

$$\mathrm{Im}\,\chi^{(3)}(esu) = \left(\frac{\varepsilon_0 c^2}{4\times 10^2 \pi^2}\right) n_0^2\, \lambda\, \beta \quad (cm/W) \tag{11}$$

$$\left|\chi^{(3)}\right| = \sqrt{\left(\mathrm{Re}\,\chi^{(3)}\right)^2 + \left(\mathrm{Im}\,\chi^{(3)}\right)^2} \tag{12}$$

Here c is the speed of light in vacuum, and ε_0 is the permittivity of free space and $n_0 = 1.51$ is the linear index of the sample. For example at excitation power P_0 = 12 mW we have $n_2 = 2.97\times10^{-5}$ cm^2/W and β = 4.06 cm/W, thus from equations (10),(11) and (12) we have: Re $\chi^{(3)} = 1.72\times10^{-3}$ esu, Im $\chi^{(3)} = 1.18\times10^{-3}$ esu and $|\chi^{(3)}| = 2.09\times10^{-3}$ esu.

3.4. Optical limiting

Optical limiters exhibit normally low transmittance for sudden increase of light intensity, and thus they are used to protect the human eye as well as optical instruments from potential damage. Our samples are characterized by very low transmittance at short wavelengths, but they are transparent in higher wavelengths. Optical limiting was evaluated by employing fluence-dependent transmission measurements using HeNe laser at 632.8 nm. Figure (9) depicts the optical limiting behaviour of typical a-Si, S:H thin film where the fluence increases linearly and then starts to saturate at higher fluence values.

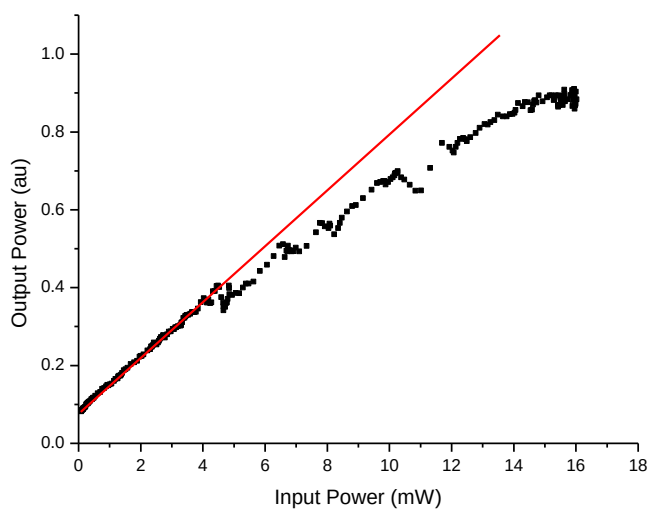

Figure (9): Optical limiting in a-Si, S:H alloy. As the input power increases the output transmitted power saturates at a fixed value.

4. Conclusion

Single beam z-scan technique has been employed to determine the nonlinear refraction index and the nonlinear absorption coefficient as a function excitation power. The measurements were carries out at various excitation powers using continuous HeNe laser source at excitation wavelengths of 632.8 nm. It was shown that the nonlinear absorption coefficient decreases and then reaches a saturation values with increasing excitation power. The nonlinear behaviour was explained in terms of single photon absorption and reverse saturation absorption. The symmetry of the normalized transmittance for z-scan open aperture configuration indicates that reverse saturation absorption is the main mechanism for the observed nonlinearity. This model was confirmed by verifying that the excitation cross section is greater than the ground state cross section. It was found that thin films of this material exhibit positive nonlinear index of refraction indicating self-focusing action. Measurements of fluence-dependent transmittance indicate that these films exhibit optical limiting behaviour.

5. References

Al Dallal, S., Hammam, M., Al-Alawi, S. M., and Aljishi, S. , 1991. Thin Solid Films, 205, p. 89
Al Dallal, S., Al Alawi, S. M., and Hammam, M., 2010. J. of Non Crystalline Solids, 356, p. 2323-2326
Al Dallal, S., 2015. *Superalloys*, Ed. M. Aliofkhazraei, p. 31-50
Aljishi, S., Al Dallal, S., Al-Alawi, S. M., Hammam. M., Al-Alawi, H. S., Stutzmann, Jin, S., Muschik, T., and Schwarz, R., 1991. *Solar Energy Materials*, 23, p. 334.
Andrade, A. A., T. Catunda, T., Lebullenger, R., Hernandes, A. C., Baesso, M. L., 2006. J. Non-Cryst. Solids 273, p. 257.
Banfi, G. P., Degiorgio, V., Ghiglizza, M., Tau, H. M., Tomaselli, A., 1994. Phys. Rev. B50, p. 5699.
Derkowska, B., Wojdyla, M., Placiennik, P., Sahraoui, B., Bala, W., 2004. Opto-Electron. Rev. 12(4), p. 405.
Henari, F., Blau, W., 1992. J. Appl. Phys. 72(5), p. 1.
Henari, F. Z., 2008. Optics Communications, 28, p. 5894-5897.
Rekham, R. K., and Ramalingam, A., 2009. Nonlinear characterization and optical limiting effect of carmine dye, Indian journal of Science and Technology, 2(8), p. 29-31.
Parkash, G. V., Gazzanelli, M., Gaburro, Z., Pavesi, L., Iacona, F., Franzo, G., Priolo, F., 2002. J. Appl. Phys. 7, p. 91.
Sheik-Bahaa, M., Said, A. A., Wei, T. H., Hagan, D. J., Van Stryland, E. W., 1990. IEEE J. Quantum Electron. 26, p. 760.
Sun, X. B., Wang, X. Q., Ren, Q., Zhang, G. H., Yang, H. L., and Feng, L., 2006. Third- order nonlinear optical properties of bis (tetrabuty-lammonium)bis (4,5-dithiolato-1, 3-dithiole-2-thion) copper, *Materials Research bulletein* 41, p. 177-182.
Vinitha, G., and Ramalingam, A., 2008. Laser Physics, 18, p. 37-42.

Science and Applications of Thin Films, Conference & Exhibition (SATF 2018)
Izmir Institute of Technology, Izmir, Turkey, September 17-21, 2018

The effect of Mg:ZnO films deposit on porous ceramic for the structural, morphological and photocatalytic properties

D. Bouras [a,*], A. Mecif [a], B. Regis[b], A. Harabi [c] and M. Zaabat[a]

[a]*Laboratory of Active Components and Materials, Larbi Ben M'hidi University, Oum El Bouaghi 04000, Algeria*
[b]*MOLTECH-Anjou, Université d'Angers/UMR CNRS 6200, 2 Bd Lavoisier, 49045 Angers, France*
[c]*Ceramics Lab, Mentouri University of Constantine, Constantine 25000, Algeria*

**Corresponding author. Tel.: +213696693770; fax: +213 32 42 20 36 .*
E-mail address: bouras.dhikra@yahoo.fr.

Abstract

In the purpose of preparation of purification elements at low cost in our daily life, thin layers of undoped and magnesium doped zinc oxide were deposited on ceramic pellets constituted of cristobalite, mullite and zircon. These substrates are made from abundant local raw materials. The thin films are prepared by dip-coating. The effects of the magnesium doping on the physical and photocatalytic properties have been studied using several techniques such as X-ray diffraction, scanning electron microscopy, energy-dispersive X-ray spectroscopy and UV-visible spectrophotometry. The photocatalytic effectiveness was tested on an aqueous solution of Orange II under UV light. The results obtained show that only porous substrate, consisting essentially of mullite and zircon, gives an important photocatalytic activity. This important effect can be related to the high rate of open porosity in these substrates (due to the consumption of the SiO_2 vitreous phase by zirconia). The presence of the open porosity, able to be filled with ZnO:Mg, makes the specific surface larger and improves the photocatalytic effect.

Keywords: Ceramic substrate; Zirconia; Dip-coating; ZnO:Mg; Degradation rate

Introduction

Membrane filtration is an essential technology for clarification, concentration, purification, salt separation and recycling in the food, pharmaceutical and surface treatment industry [1]. The use of efficient membrane techniques makes it possible to improve water treatment and the production of drinking water [2]. The membrane processes open new possibilities in the exploitation of sources of water, in particular the oceans, which were not easily usable before technical or economic reasons [3]. Moreover, the economical aspect implies the development of processes that consume little reagents and require low-cost and space-saving installations.

Due to specific properties such as refractoriness, chemical stability or mechanical resistance to compression, as well as the wide variety of microstructures, porosities and accessible geometries [4, 5], ceramics are a class of materials that cannot be ignored for many industrial processes currently or in the process of being developed, for the protection of the environment [6]. This article provides an illustration of this by discussing applications for filtration, heterogeneous catalysis, and adsorption or coupled operations, for example in membrane catalytic reactors, based on the multifunctionality of materials [7].

The study have been devoted of thin layers ZnO:Mg to give good results for purification of colorant organic [8, 9]. Many properties of ZnO can thus be modulated by doping Mg [10, 11]. The Mg doping can increase

the band gap and reject the absorption coefficient, which is essential for application in the region of invisible light [12, 13], also to enlarge band gap [14, 15]. The solubility of ZnO in MgO is 40 to 50% of atoms [16].
The objective of this study is to synthesize Mg films doped by ZnO by a dip-coating technique on porous substrates (mullite-zircon) at a deposition temperature of 500 ° C and to study the effect of the Mg content in the range on the structural and photocatalys properties of these films.

Experimental procedure

Preparation of porous substrate

Prepared pellets from clay powders DD3 with 38% zirconium oxide (DD3 + 38 wt% ZrO_2) added using a 13 mm matrix. At the end, an open porosity reaches 33% for a heat treatment at 1300ºC for 2 hours with an annealing speed of 5ºC / min [4].

Preparation of Mg-doped ZnO nanostructures

Mg doped ZnO thin layers were deposited on ceramic substrates by the sol-gel technique. Zinc acetate dehydrate (Zn $(CH_3COO)_2$ $.2H_2O$) was dissolved in absolute ethanol at 70 °C with monoethanolamine (MEA) acting as a stabilizer. Magnesium acetate tetrahydrate ($Mg(CH_3COO)_2$ $.4H_2O$) was added to the solution for Mg doping. A serie of samples were prepared by dip coating ceramic substrates, preheating at 200 °C for 3 min in oven, and by repeating the process 50 times. Finally, they were annealed at 500 °C for 2 h to produce Mg doped ZnO thin films [17, 18].

Results and Discussions

Structural analysis

The figure 1.a shows the X-ray diffraction patterns for undoped and Mg-doped ZnO thin layers deposited on a ceramic substrate consisting mainly of millite and zircon (DD3+38 wt% ZrO_2-clays). Mullite, Zircon, Zirconia and cristobalite has essential phases of ceramics. The XRD spectrum (Fig.1.b) indicates that the peak (101) obtained after the deposition of 50 layers of undoped ZnO is polycrystalline with a hexagonal wurtzite structure (JCPDS 03-0891). The insertion effect of 6% of Mg on the crystalline structure of the pellets was observed by a shift towards the highest angles, demonstrating a small crystalline size (Table.1). It is concluded that Mg atoms with a smaller ionic radius (r_{Mg}^{2+} = 0.65 Å) replace Zn (r_{Zn}^{2+} = 0.74 Å) and Zr (Zr^{4+}=0.72 Å) atoms in the lattice. The addition of Zn and Mg contributes to the lattice parameter variation which leads to a slight shift of the peaks and occupy interstitial sites. It should be noticed that the calculation of the grain particle size may be determined by the Debye-Scherrer relationship [19]:

$$D = \frac{0.9\,\lambda}{\beta\cos\theta} \qquad (1)$$

Where λ is the wavelength of the anticathode (λ_{Cu} = 1.541Å), β is FWHM (half-value width), θ is the diffraction angle and D is the diameter of particle size.

Table 1: Crystallite size of pellets

Phase	(hkl)	2θ (º)	β (º)	D (nm)
$ZrSiO_4$	(200)	27.017	0.188	43.195
$ZrSiO_4$ (6MgZO)	(200)	27.041	0.329	25.009
ZrO_2	(-111)	28.196	0.209	39.696
ZrO_2 (6MgZO)	(-111)	28.263	0.351	23.430

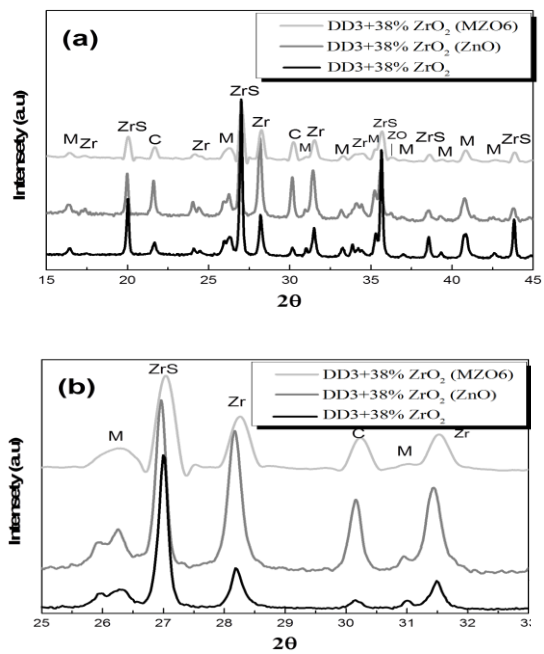

Fig. 1. XRD patterns of thin films of ZnO and Mg doped ZnO deposited on the DD3+38 wt% ZrO_2 substrates. ZrS: Zircon ($ZrSiO_4$), Zr: Zirconia (ZrO_2), C: Cristobalite (SiO_2), M: mullite ($3Al_2O_3.2SiO_2$), ZO: ZnO.

SEM images and EDX analysis

The morphologies and microstructures of DD3+38% wt ZrO_2 pellet ceramic without and with Mg-doped ZnO thin layers are shown in Fig.2.(a) and (b)) respectively. As it can be seen, the flower-like structure is retained after the doping of Mg. In order to get the chemical composition of the synthesized samples we use the energy dispersive x-ray spectroscopy (Fig.3) The chemical composition of the synthesized samples was measured by energy dispersive x-ray spectroscopy (Fig.3). The Zn, O, Mg, Al, Zr and Si elements can be clearly observed in the figure 3(b). Their corresponding atomic percents are 7.04 %, 65.31 %, 1.72 %, 7.06 %, 7.76 % and 8.11 %, respectively.

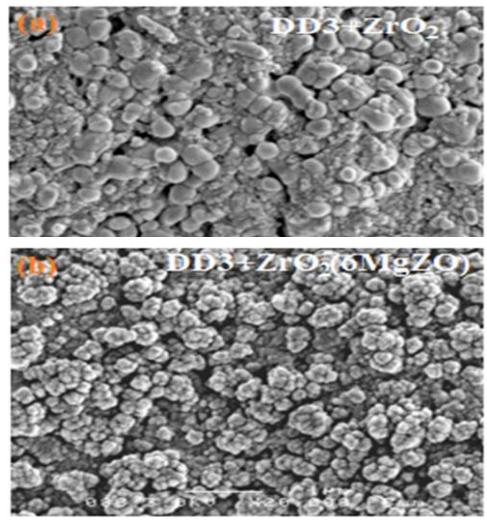

Fig. 2. SEM micrograph of the pellets: a) DD3+38 wt ZrO_2 and b) DD3+38 wt ZrO2 (6% Mg-doped ZnO).

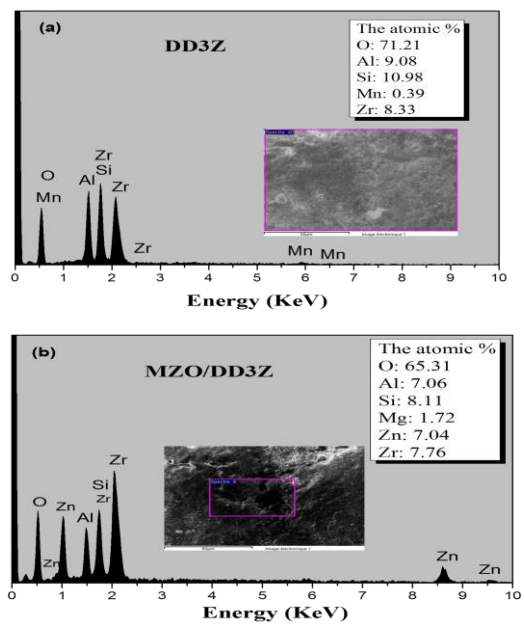

Fig. 3. EDX spectrum of the pellets: a) DD3+38 wt ZrO_2 and b) DD3+38 wt ZrO2 (6% Mg-doped ZnO).

AFM analyses

The typical cross section view of the samples (Fig. 12) reveals a porous ceramic substrate covered by the thin film and, on top of this, the active Mg: ZnO layer. The texture and morphology of this layer can be observed in Fig. 4. The layer thickness and the grain increases with the amount of deposited thin films. The granular morphology (Fig. 4b) might enhance the photocatalytic activity of the layer, since it increases the exposure area of active particles. According to the AFM results the average particle size is 0.93 µm and the layer roughness is 134 nm. These values are much smaller than the ones without active layers DD3Z (Fig. 4b), Where he was to 0.56 µm and 100 nm for the grain size and roughness (Table.I), respectively. Since the catalytic performance is similar, the actual solution is more interesting from a practical point of view, since it facilitates the surface cleaning by common means.

Table 2: Grain size and the roughness of the samples

Substrates	***DD3+38%ZrO_2-clays***	
Samples	***DD3+38%ZrO_2***	***MZO-DD3 +38%ZrO_2***
Grain size (µm)	0.56	0.93
Roughness (nm)	100	134

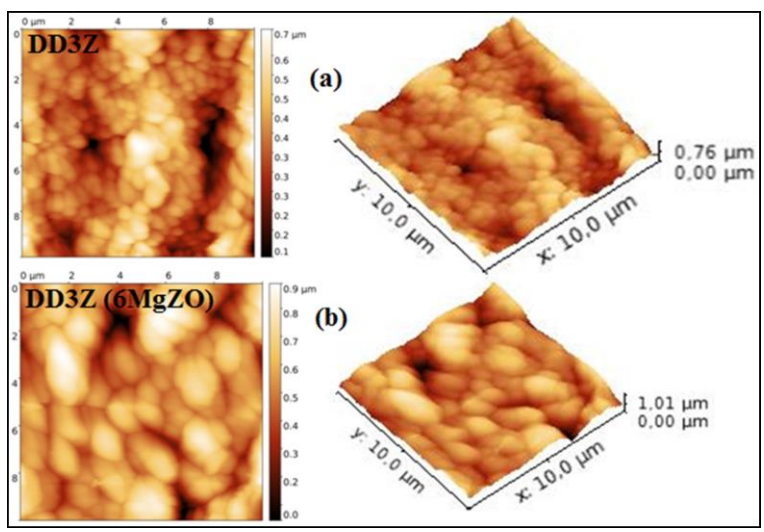

Fig. 4. AFM topography of the pellets: (a) DD3+38 wt ZrO_2 and (b) DD3+38 wt ZrO2 (6% Mg-doped ZnO).

Confocal spectrum

The confocal spectrum showed the optical properties of the samples. One emission bands could be observed. The broad emission is in the visible region [400- 800 nm]. Fig.5 show that the intensities of the

samples of the porous substrates decrease after the addition of the thin layers of ZnO and Mg: ZnO. Because of the Zn and Mg ions doping this emission band is broadened, it can be speculated that the band width of the ceramic is widened owing to the replacement by the Zn^{2+} and Mg^{2+} [20]. At the same time, it is obvious that the ratio of the intensity of the UV emission decreases to deep level, and this may be caused by the increasing amount of Mg-doping. Also it's can be returned to the degree of electron / hole recombination are clearly decreases with magnesium doping. Hence, it is believed that the prepared MZO/DD3Z thin film with high particle size, high surface area and high surface defects would allow better results on the photocatalytic activity [21]. Pellets with thin layers (MZO) increased the free-charge periphery and has a longer life. As a result, the mobility of the MZO / DD3Z sample increased, while the resistivity was reduced for the Mg-doped sample.

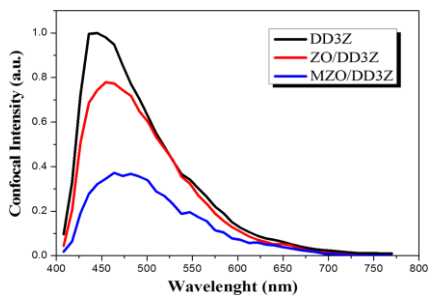

Fig. 5. Confocal spectra of the pellets.

Photocatalytic activity

The photocatalytic activity of Mg-doped ZnO thin layers was investigated by means of the degradation of orange II (OII) in aqueous solution under visible light at room temperature. Blue light lamp 4W (VL-4LC) was used as UV source. The photocatalytic degradation was determined by measuring the absorbance of OII solution every 1 hour using a UV-vis spectrophotometer (V- 630, JASCO) in the wavelength range of 250-650 nm. The degradation efficiency of OII can be calculated by the formula [22]:

$$\text{Degradation \%} = \frac{A_0 - A_t}{A_0} \times 100 \qquad (2)$$

The figure 6 shows that the effect of 6 % Mg-doped ZnO, deposition on the porous substrate, on the degradation rate of orange II varies as a function of the time exposition to UV. After 6 hours of UV exposure, 80 % of degradation of the orange II solution was obtained. This result is attributed to the increase of the effective surface leading to a deceleration of the photocatalytic process.

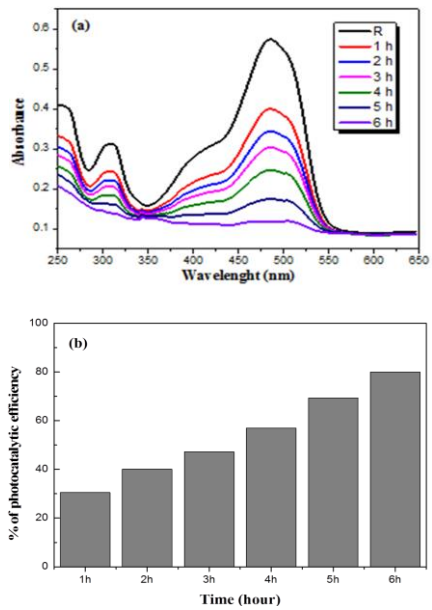

Fig. 6. Degradation rate of Orange II versus UV exposure time for a ZnO:Mg thin film deposited on a porous substrate (DD3+38 wt% ZrO_2- clay)

Conclusion

The project consists in the implementation of processes for the production of composite membranes based on local clay materials such as DD3, for use in the treatment of pollution waters. The syntheses will be carried out by sol-gel processes. All the characterizations demonstrate the properties of the membranes obtained: The substrate and the membranes prepared have been characterized by the structural, morphological, and photocatalytic activity. The X-ray diffraction results show that the samples with thin layers have shifted peaks towards larger angles. The SEM results display that the structure of Mg: ZnO is flower-like. The pores size and the porosity (33%) obtained of the ceramic substrate after deposition will be decelerated in the filtration and purification of orange II solution. A maximum degree of purification of 80% is obtained with an active layer of Mg doped ZnO for an exposure time of 6 hours. The use of this doping process and local materials in the same time lower the cost of the purification operation

Acknowledgements

This work has been supported by the Laboratory of Active Components and Materials (LACM) of Larbi Ben M'hidi University - Oum El Bouaghi, Algeria and the laboratory of Moltech-Anjou-Lunam, Angers University, France.

References

[1] Jacangelo, J.G., Ghellam, S and Bonacquisti, T. P., 2000. Treatment of surface water by double membrane systems: assessment of fouling, permeate water quality and costs, In: water Supply 18, p.438-441.

[2] Ghouil, B., Harabi, A and Bouzerara, F., 2016. Elaboration and characterization of ceramic membrane supports from raw materials used in microfiltration, Desalination and Water Treatment 57, p.5241-5245.

[3] Kouras, N., Harabi, A., Bouzerara, F., Foughali, L., Policicchio, Al., Stelitano, S., Galiano, F. and Figoli , A., 2017. Macro-porous ceramic supports for membranes prepared from quartz sand and calcite mixtures, Journal of the European Ceramic Society 37, p.3159-3165.

[4] Mecif, A., Soro, J., Harabi, A. and Bonnet, J. P., 2010. Preparation of Mullite- and Zircon-Based Ceramics Using Kaolinite and Zirconium Oxide: A Sintering Study, Journal of the American Ceramic Society 93, p.1306 –1312.

[5] Bouzerara, F., Harabi, A., Achour, S and Larbot, A., 2006. Porous ceramic supports for membranes prepared from kaolin and doloma mixtures, Journal of the European Ceramic Society 26, p.1663–1671.

[6] Khemakhem, S., Ben Amar, R., Ben Hassen, R., Larbot, A., Medhioub, M., Ben Salah, A. and Cot, L., 2004. New ceramic membranes for tangential waste-water filtration, Desalination 167, p.19-22.

[7] Bai, H.W., Liu, Z.Y., & Sun, D.D., 2012. Hierarchical nitrogen-doped flowerlike ZnO nanostructure and its multifunctional environmental applications, Asian Journal of Chemistry 7, p.1772-1780.

[8] Pearton, S.J., Norton, D.P., Ip, K., Heo, Y.W. and Steiner, T.,2005. Recent progress in processing and properties of ZnO, Progress in materials science 50, p.293-340.

[9] Saikia, L., Bhuyan, D., Saikia, M., Malakar, B., Dutta, D.K. and Sengupta, P.,2015. Photocatalytic performance of ZnO nanomaterials for self sensitized degradation of malachite green dye under solar light, Applied Catalysis A: General 490, p.42-49.

[10] Yang, J., Wang, Y., Kong, J., Yu, M. and Jin, H., 2016. Synthesis of Mg-doped hierarchical ZnO nanostructures via hydrothermal method and their optical properties, Journal of Alloys and Compounds 657, p.261-267.

[11] Wang, Y., Zhao, X., Duan L.,, Wang, F., Niu, H., Guo, W. and Ali, A., 2015. Structure, luminescence and photocatalytic activity of Mg-doped ZnO nano-particles prepared by auto combustion method, Materials Sciencein Semiconductor Processing 29, p.372–379.

[12] Das, A., Roy, P. G., Dutta, A., Sen, S., Pramanik, P., Das, D., Banerjee, A. and Bhattacharyya, A.,2016. Mg and Al co-doping of ZnO thin films: Effect on ultraviolet photoconductivity, Materials Sciencein Semiconductor Processing 54, p.36–41.

[13] Peng, S.Y., Xu, Z.N., Chen, Q.S., Wang, Z.Q., Lv, D.M., Sun, J., Chen, Y.M. and Guo, G.C.,2015. Enhanced stability of Pd/ZnO catalyst for CO oxidative coupling to dimethyl oxalate: effect of Mg^{2+} doping, ACS Catalysis 5, p.4410-4417.

[14] Wang, M., Yi, J., Yang, S., Cao, Z., Huang, X., Li, Y., Li, H. and Zhong, J., 2016. Electrodeposition of Mg doped ZnO thin film for the window layer of CIGS solar cell, Applied Surface Science 382, p.217–224.

[15] Yu, X.X., Wu, Y., Dong, B., Dong, Z.F. and Yang, X., 2015. Enhanced solar light photocatalytic properties of ZnO nanocrystals by Mg-doping via polyacrylamide polymer method, Journal of Photochemistry and Photobiology A: Chemistry 10225, p.1–8.

[16] Segnit, E.R. and Holland, A.E., 1965. The System MgO-ZnO-SiO_2, J. American Ceramic Society 48, p.409-412.

[17] Bouras, D., Mecif, A., Mahdjoub, A., Harabi, A., Zaabat, M., Benzitouni, S., Regis, B., 2017. Photocatalytic degradation of orange ii by active layers of cu-doped zno deposited on porous ceramic Substrates, Journal of Ovonic Research 13, p. 271 – 281.

[18] Bouras, D., Mecif, A., Barille, R., Harabi, A., Rasheed, M., Mahdjoub, A., Zaabat, M., 2018. Cu:ZnO deposited on porous ceramic substrates by a simple thermal method for photocatalytic application, Ceramics International.

[19] Arda, L., Ozturk, O., Asikuzun, E. and Ataoglu, S.,2013. Structural and mechanical properties of transition metals doped ZnMgO nanoparticles, Powder Technology 235, p.479–484

[20] Yousefi R., Sheini F.J., Muhamad M.R., and More M.A., 2010. Characterization and field emission properties of ZnMgO nanowires fabricated by thermal evaporation process, Solid State Sci 12, p 1088–1093.

[21] Zhan C., Chen F., Yang J., Dai D., Cao X. and Zhong M., 2014. Visible light responsive sulfated rare earth doped TiO2@fumed SiO2composites with mesoporosity: Enhanced photocatalytic activity formethyl orange degradation, Journal of Hazardous Materials 267, p.88– 97.

[22] Rego, E., Marto, J., Marcos, P. S. and Labrincha, J.A., 2009. Decolouration of Orange II solutions by TiO_2 and ZnO active layers screen-printed on ceramic tiles under sunlight irradiation, Applied Catalysis A: General 355, p.109–114.

Science and Applications of Thin Films, Conference & Exhibition (SATF 2018)
Izmir Institute of Technology, Izmir, Turkey, September 17-21, 2018

Investigation of Bacterial Adhesion to Plasma-Modified Polypropylene Surface

Dogan Mansuroglu[a,*], Busra Aktas[b] and Ilker U. Uzun-Kaymak[c]

[a]*Department of Physics, Canakkale Onsekiz Mart University, Canakkale, 17100, Turkey*
[b]*Department of Molecular Biology and Genetics, Burdur Mehmet Akif Ersoy University, Burdur, 15030, Turkey*
[c]*Department of Physics, Middle East Technical University, Ankara, 06800, Turkey*

Corresponding author. Tel.: +90-286-218-1800/1933; fax: +90-286-218-0533.
E-mail address: mansurdogan@gmail.com

Abstract

The adhesion of non-pathogenic bacteria *Enterococcus faecalis* on the polypropylene surface is investigated before and after exposure to plasma generated using a capacitively coupled 13.56 MHz radio frequency source. Different gas discharges are generated using oxygen and nitrogen gases. Various studıes show that plasma exposure effectively improves the surface properties of the polypropylene without changing its bulk properties. The chemical changes on the surfaces are characterized using a Fourier transform infrared-attenuated total reflection spectroscopy. The plasma exposure leads to form the oxygen-containing and the nitrogen-containing polar groups on the PP surfaces. Moreover, new functional groups formed on the surfaces have a high degree of crosslinking structures. The presence of the crosslinking structures importantly increases the attachment of the bacteria culture to the PP surfaces. Bacterial adhesion is analysed by measuring the cell population attached to the surface. The results showed that oxygen plasma exposure increased the bacterial adhesion to the surface relative to the nitrogen plasma exposure.

Keywords: Surface modification; bacterial adhesion; RF plasma discharge; polypropylene.

Introduction

Discharges generated using a capacitively coupled radio frequency (RF) source are highly preferred to enhance the surface properties of polymers since they do not change the polymer's bulk properties and provide good control over the gas chemistry (Liston et al., 1993, Vesel and Mozetic, 2017, Barton et al., 1999). The plasma discharge effectively improves the poor polymer surface properties by allowing the formation of additional functional groups such as the carbonyl, carboxyl, hydroxyl, and the amine to the polymer surface (Liston et al., 1993, Zille et al., 2015, Grace and Gerenser, 2003). This technique is used for various applications mostly in textile, automotive, packaging, electronic, and biological industries (Zille et al., 2015, Pankaj et al., 2014, Sanchis et al., 2018, Gomathi et al., 2008, Bhat and Upadhyay, 2002). Most importantly, crosslinking structures generated by free radicals provide excellent biocompatibility due to higher concentrations of active molecules on the polymer surface (Gomathi et al., 2008).

Our previous studies show that the RF discharge significantly improves the surface properties of the polypropylene (PP) after the plasma exposure (Mansuroglu and Uzun-Kaymak, 2018, Mansuroglu et al., 2018). PP is a promising material with excellent chemical and mechanical resistance, transparency, and low density (Morent et al., 2008, Bhat et al., 2002). These properties make it very favorable to be utilized in many

fields of the industry (Zille et al., 2015, Pankaj et al., 2014, Sanchis et al., 2018, Carrino et al., 2002). The recent studies show that the PP material can also be used in biomedical areas (Gomathi et al., 2008, Slepička et al., 2013, Bhanthumnavin et al., 2016). In this study, we are investigating bacterial adhesion of the modified PP surface. A non-pathogenic bacteria culture, *Enterococcus faecalis* ATCC29212 is used to test the adhesion properties. The plasma discharge is generated using oxygen, and nitrogen gases separately. A capacitively coupled 13.56 MHz RF source generates the gas discharge. Experiments are repeated at similar conditions while parameter scans are performed for the RF input power (50 W, 100 W, and 150 W) and for the plasma exposure time (2 min, 5 min, and 10 min). The surfaces are chemically characterized using a Fourier transform infrared-attenuated total reflection (FTIR-ATR) spectroscopy. Bacterial adhesion is analyzed by measuring the cell population attached to the modified surface.

Experimental

RF plasma system

The RF plasma system consists of two parallel aluminum electrodes. 13.56 MHz RF source is used to generate the gas discharge. The pressure of the vacuum chamber initially pumps down to a base pressure of 10^{-3} Torr, and then a gas is filled using an MKS multi-gas controller 647C. All experiments are employed at the gas pressure of 1.2 x 10^{-1} Torr. The granular PP, $(C_3H_6)_n$, melting at 160 ˚C, is purchased from PETKIM©. A hot-press machine is used to process a flat sheet of PP granules with a thickness of 0.6 mm. Then, the sheet is cut into small samples in sizes of 1x1 cm^2. All experiments are conducted at the same conditions by varying the RF input power (50 W, 100 W, and 150 W) and the exposure time (2 min, 5 min, and 10 min). O_2 or N_2 gas flow rate is kept constant at 50 sccm. The results are chemically examined using a Thermo Scientific Nicolet iS10 FTIR-ATR spectrometer.

In vitro bacterial adhesion

Non-pathogenic bacteria, *Enterococcus faecalis* ATCC29212, is used in this study. *E. faecalis* stock culture is maintained in a MRS broth, with 25 % (v/v) glycerol at -80 °C. Working culture is prepared from frozen stocks by two sequential transfers in the MRS broth. Incubation is conducted at 37 °C for 18 h. 1 cm^2 of PP polymers are sterilized in 70 % ethanol for 10 min and rinsed in 0.85% NaCl (w/v). 1 ml of bacterial culture at ~ 4x10^8 CFU/ml is added into 24-well plate, and the sterile samples exposed to O_2 or N_2 plasmas or the samples without plasma exposure are placed treated-side down, into the each well. After the plates are incubated at 37°C for 24 h, the samples are placed into a sterile 24-well plate and gently washed with 0.85% NaCl (w/v) to remove loosely adherent bacterial cells. The samples are then placed in 1 ml of 0.85% NaCl (w/v) and vortexed vigorously for 2 min to remove bacteria adhered to the PP surface. A vortexed solution is enumerated by plate count on the MRS agar. Statistical differences of the bacterial adhesion are assessed with the Each Pair Student's Test using JMP version 12 (SAS Institute Inc., Cary, NC) and are presented as the mean ± SEM. Statistical difference is determined at a P value of 0.05 or less.

Results /Discussion

FTIR-ATR spectroscopy

The chemical changes in the surfaces of PP after the plasma process are investigated using an ATR-FTIR spectrometer for the range of 3500 cm^{-1} to 500 cm^{-1}. Fig. 1 and Fig. 2 show all spectra of before and after O_2

and N_2 plasma exposures, respectively. C-H stretching vibration bands are observed in the region between 3000 cm^{-1} and 2780 cm^{-1}: the band at 2950 cm^{-1} refers to $–CH_3$ asymmetric stretching, the band at 2916 cm^{-1} refers to $–CH_2$ asymmetric stretching, the doublet bands at 2876 cm^{-1} and 2865 cm^{-1} refer to $–CH_3$ symmetric stretching, and the band at 2837 cm^{-1} refers to $–CH_2$ symmetric stretching (Morent et al., 2008). Fig. 1 show the intensities of these C-H vibration bands increase with increasing the RF input power after O_2 plasma exposure. Increase in the intensities can be due to the formation of new functional groups on the surfaces (Liston et al., 1993, Bhat et al., 2003). In the spectra, two intense bands observed at 1452 cm^{-1} referring to an asymmetric C-H deformation and at 1370 cm^{-1} is due to a symmetric C-H bending vibration of $–CH_3$ group (Morent et al., 2008). Changes in the intensities of these bands verify the structural modification on the surfaces. The spectra show two broad bands observed at 1748 cm^{-1} and 1621 cm^{-1} corresponding to C=O stretching vibration. Moreover, a weak band observed at 1400 cm^{-1} corresponds to COO– groups (Lehocky´ et al., 2003). These bands show the presence of the oxygen-containing polar groups such as –OH, –C=O, and –C–O–O on the surfaces.

Different than O_2 plasma, N_2 plasma first leads to an increase the intensities of C-H vibration bands up to 100 W, and then a decrease is observed at 150 W, as shown in Fig. 2. A decrease in the intensities can be referred as a removal of the surface atoms due to the plasma exposure. The plasma discharge may cause more fragmentations and reactions during the process at high power value. The band observed at 1534 cm^{-1} refers to $–NO_2$ stretching vibration and this band broadens after the plasma process. The broadening is observed due to crosslinking and branched structures generated by the plasma exposure. The spectra show that the nitrogen plasma leads to form $–NH_2$, –NH, and $–NO_2$ groups on the surfaces. Moreover, both O_2 and N_2 spectra have broadband seen at 1157 cm^{-1} can refer to C-C asymmetric stretching, CH_3 asymmetric rocking, C-H wagging vibrations (Morent et al., 2008) or C-O stretching vibration (Bhat et al., 2003). They also have weak bands between 980 cm^{-1} and 650 cm^{-1}. The bending of CH_3 is observed at 893 cm^{-1}, and the alkyl peroxide is observed at 839 cm^{-1}. The band observed at 718 cm^{-1} refers to the structure of $–(CH_2)_4–$ or $–(CH_2)_4O–$ (Mistry, 2009). The bands observed at the region between 750 cm^{-1} and 700 cm^{-1} are assigned to methylene/ methyne groups (Mistry, 2009).

The oxygen plasma likely leads to the formation of the carboxylic, carbonyl, hydroxyl and peroxide groups on the PP surfaces while the nitrogen plasma leads to the formation of the amine and imine groups. The presence of these chemical groups generally causes to change and improve the properties of the PP surfaces. Increase in the number density of these groups increases the hydrophilicity of the PP surfaces and improve their adhesion. Another critical factor is the degree of the crosslinking and branched structures occurring due to fragmentation and rearrangement generated during the plasma process. The crosslinking structures can provide excellent biocompatibility by allowing a higher concentration of active molecules on the polymer surface (Gomathi et al., 2008).

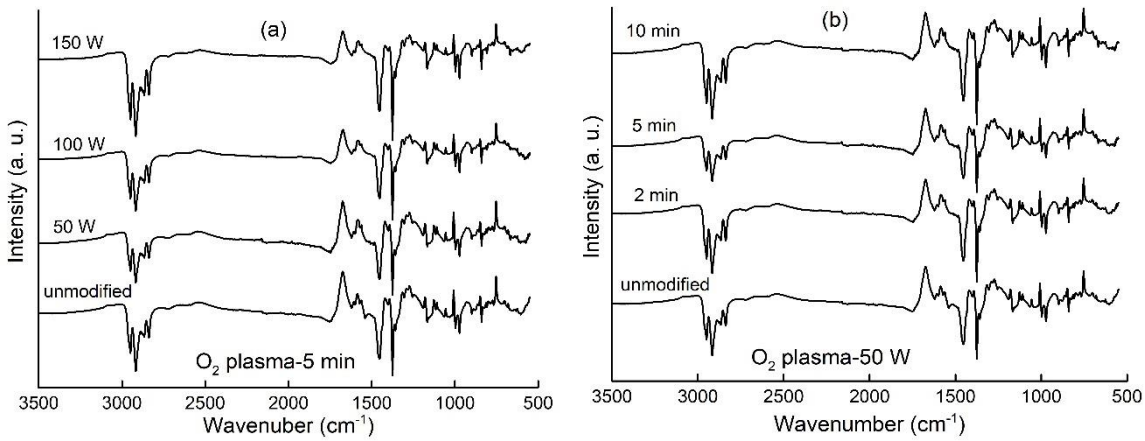

Fig. 1. The FTIR-ATR spectra of the PP surfaces before and after O_2 plasma exposure as a function of (a) the RF input power; (b) the exposure time

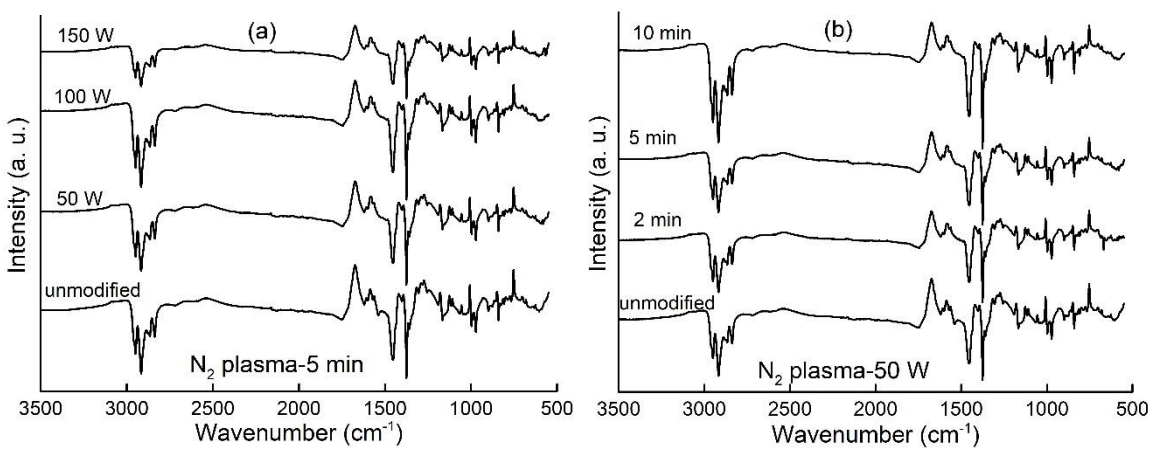

Fig. 2. The FTIR-ATR spectra of the PP surfaces before and after N_2 plasma exposure as a function of (a) the RF input power; (b) the exposure time

Bacterial adhesion

To investigate the bacterial adhesion to the PP surfaces *E. faecalis*, a non-pathogenic bacteria culture, is used. The bacteria is growth on the samples of control (without the plasma exposure) and the plasma exposed as a function of the RF input power and the exposure time. The cell population of the bacteria cultures attached to the surfaces is measured, and the results are shown in Fig. 3. The parameters having a significant difference are marked with a star as a result of the statistical analysis. The results show both O_2 and N_2 plasma exposures increase the adhesion of *E. faecalis* to the PP surfaces. Bacteria adhered to the samples exposed to the oxygen plasma is higher as compared to the nitrogen plasma exposure. This show that the presence of the oxygen-containing polar groups effectively improves the adhesion of *E. faecalis*.

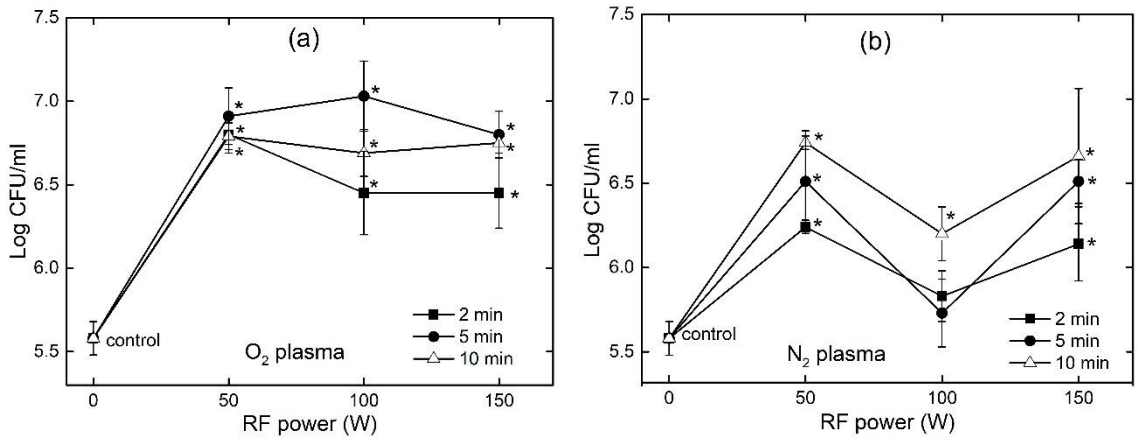

Fig. 3. The adhesion of *Enterococcus faecalis* ATCC29212 on the PP surfaces before and after the plasma exposure (a) for O_2; (b) for N_2 as a function of the RF input power and the exposure time (*p<0.05: significant differences from the control, (n:4/bar))

Fig. 3a shows the highest cell population is obtained at 50 W and 100 W of the RF input power, for 5 min of the exposure time. At 2 min, the highest value is observed at 50 W, and almost the same values are obtained at 10 min, for different power values. It can be seen that all parameters of O_2 plasma exposure have significant differences, which are consistent with the results of the FTIR-ATR spectra. For the samples exposed by N_2 plasma, the cell population of the bacteria increases effectively at 50 W and 150 W, and it increases with increasing the exposure time. Although the samples exposed at 100 W of the RF input power have an increase in the cell population of the growth as compared to the control sample, that is not significantly different at 2 min and 5 min of the exposure time. This can be due to the low number density of the nitrogen-containing groups on the surfaces to connect with the *E. faecalis* bacteria. Consequently, the adhesion of *E. faecalis* to the PP surfaces is generally improve after the oxygen and nitrogen plasma exposures.

Conclusion

The surface properties of PP polymer material are improved using O_2 and N_2 plasma exposures. The presence of the oxygen-containing and the nitrogen-containing polar functional groups are verified by the FTIR-ATR spectra. Also, it is observed that new functional groups have crosslinking structures. These crosslinking functional groups lead to improve the adhesion of PP surfaces. The results of bacterial adhesion show the cell population on the samples significantly increases after the both plasma exposures. Non-pathogenic bacteria *E. faecalis* attach the samples exposed to O_2 plasma with a higher concentration as compared to N_2 plasma.

Acknowledgements

This research is supported by the Scientific Research Project Fund of Middle East Technical University under the projects # YÖP-105-2018-2840 and # BAP-01-05-2017-006.

References

Liston, E.M., Martinu, L., Wertheimer, M.R., 1993. Plasma Surface Modification of Polymers for Improved Adhesion: A Critical Review, Journal of Adhesion Science Technology 7, p. 1091–1127.

Vesel, A., Mozetic, M., 2017. New Developments in Surface Functionalization of Polymers Using Controlled Plasma Treatments, Journal of Physics D: Applied Physics 50, p. 293001.

Barton, D., Bradley, J.W., Steele, D.A., Short, R.D., 1999. Investigating Radio Frequency Plasmas Used for the Modification of Polymer Surfaces, The Journal of Physical Chemistry B 103, p. 4423-4430.

Zille, A., Oliveira, F.R., Souto, A.P., 2015. Plasma Treatment in Textile Industry, Plasma Processes and Polymers 12, p. 98-131.

Grace, J.M., Gerenser, L.J., 2003. Plasma Treatment of Polymers, Journal of Dispersion Science and Technology 24, p. 305-341.

Pankaj, S.K., Bueno-Ferrer, C., Misra, N.N., Milosavljević, V., O'Donnell, C.P., Bourke, P. et al., 2014. Applications of Cold Plasma Technology in Food Packaging, Trends in Food Science and Technology 35, p. 5-17.

Sanchis, R., Fenollar, O., García, D., Sánchez, L., Balart, R., 2018. Improved Adhesion of LDPE Films to Polyolefin Foams for Automotive Industry Using Low-Pressure Plasma, International Journal of Adhesion and Adhesives, 28, p. 445-451.

Gomathi, N., Surechkumar, A., Neogi, S., 2008. RF Plasma-Treated Polymers for Biomedical Applications, Current Science 94, p. 1478.

Bhat, N.V., Upadhyay, D.J., 2002. Plasma-Induced Surface Modification and Adhesion Enhancement of Polypropylene Surface, Journal of Applied Polymer Science 86, p. 925-936.

Mansuroglu, D., Uzun-Kaymak, I.U., 2018. Surface Modification of Polypropylene: Surface Characterization of the Material along with the Optical Emission Results from the Argon and Nitrogen Plasmas, Surface and Coatings Technology, (submitted).

Mansuroglu, D., Mecit, G., Uzun-Kaymak, I.U., 2018. A Study of Crystallization in Plasma Modified Polypropylene, Materials Today Proceedings, (submitted).

Morent, R., De Geyter, N., Leys, C., Gengembre, L., Payen, E., 2008. Comparison Between XPS- and FTIR-Analysis of Plasma-Treated Polypropylene Film Surfaces, Surface and Interface Analysis 40, p. 597-600.

Carrino, L., Moroni, G., Polini, W., 2002. Cold Plasma Treatment of Polypropylene Surface: A Study on Wettability and Adhesion, Journal of Materials Processing Technology 121, p. 373-382.

Slepička, P., Kasálková, N.S., Stránská, E., Bačáková, L., Švorčík, V., 2013. Surface Characterization of Plasma Treated Polymers for Applications as Biocompatible Carriers, EXPRESS Polymer Letters 7, p. 535-545.

Bhanthumnavin, W., Wanichapichart, P., Taweepreeda, W., Sirijarukula, S., Paosawatyanyong, B., 2016. Surface Modification of Bacterial Cellulose Membrane by Oxygen Plasma Treatment, Surface and Coatings Technology 306, p. 272-278.

Bhat, N.V., Upadhyay, D.J., Deshmukh, R.R., Gupta, S.K., 2003. Investigation of Plasma-Induced Photochemical Reaction on a Polypropylene Surface, The Journal of Physical Chemistry B 107, p. 4550-4559.

Lehocky´, M., Drnovska´, H., Lapcikova´, B., Barros-Timmons, A.M., Trindade, T., Zembala, M. et al., 2003, Plasma Surface Modification of Polyethylene, Colloids and Surface A: Physicochemical and Engineering Aspects 222, p. 125-131.

Mistry, B.D., 2009. A Handbook of Spectroscopic Data Chemistry, Oxford Book Company.

Science and Applications of Thin Films, Conference & Exhibition (SATF 2018)
Izmir Institute of Technology, Izmir, Turkey, September 17-21, 2018

Plasma Characteristics Aiding the Enhancement of Surface Properties of Polyethylene

Dogan Mansuroglu[a,*], Devrim Ozdemir[b] and Ilker U. Uzun-Kaymak[c]

[a]*Department of Physics, Canakkale Onsekiz Mart University, Canakkale, 17100, Turkey*
[b]*Department of Physics, Middle East Technical University, Ankara, 06800, Turkey*

*Corresponding author. Tel.: +90-286-18001933; fax: +90-286-2180533.
E-mail address: mansurdogan@gmail.com

Abstract

Plasma species such as electrons, ions, and free radicals can transfer their energies by interacting with the atoms from the surface of the polymer during the plasma modification process. Although various plasma discharge methods such as microwave, dielectric barrier, or radio frequency(RF) plasma discharges can be used to enhance the surface properties of polymers, in this study a capacitively coupled RF source is preferred due to its unique characteristic to generate weakly ionized cold plasmas. The plasma discharge is generated using a 13.56 MHz source ionizing Argon gas inside a chamber kept nearly around 10^{-1} Torr. The correlation between the changes of the plasma characteristics due to the input power and the changes on the processed surface is investigated. RF input power is scanned for a wide range of power starting at 50 W to 500 W while other plasma parameters such as the gas flow rate, plasma exposure time, and the gas pressure are kept constant. The emission spectrum of the atomic and the molecular lines process are investigated using a broadband optical emission spectrometer. The change in the surface chemistry is characterized using a Fourier transform infrared-attenuated total reflection spectrometer. The results show that new functional groups are generated, and branched structures are formed on the surface. Moreover, the surface energy of the polymer is significantly improved, and this is verified by the increase in the crystallization measured using an X-Ray diffraction spectrometer before and after the plasma exposure.

Keywords: Surface modification; optical emission spectroscopy; RF plasma discharge; polyethylene.

Introduction

Polyethylene (PE) is a widely used material in many applications such as textile (Zille et al., 2015), food packaging (Pankaj et al., 2014), and biomedicine (Slepička et al., 2013) due to its high chemical resistivity, excellent versatility, and relatively low cost (De Geyter et al., 2008). However, it has low surface energy; thus its surface properties should be enhanced to provide the adequate adhesion, printability, wettability, or biocompatibility properties. Various wet- and dry-processing surface modification techniques are used to enhance the surface properties of polymers. They include chemical solvent technique, the flame process, and the plasma discharge (Liston et al., 1993, Grace and Gerenser, 2003, Lee at al., 2009). Among these techniques, the plasma discharge is the most commonly used technique because it is a fast and clean process, and depending on the gas used it can be considered environmentally clean (Liston et al., 1993, Grace and Gerenser, 2003, Morent et al., 2008, Vesel et al., 2008). Plasma discharges can be produced using various discharge techniques including radio frequency (RF), microwave (MW), dielectric barrier (DB), and corona discharges (Morent et al., 2008, Popelka et al., 2018, Gomathi and Neogi, 2009, Vesel and Mozetic, 2017).

Capacitively coupled RF source generates a self-sustained, continuous and stable discharge for a long duration compared to other plasma discharge techniques such as DBDs and plasma torches. Also, it provides a feasible reactivity with an easy control [Liston et al., 1993, Zille et al., 2015, Pankaj et al., 2014, Vesel and Mozetic, 2017). At low pressure, RF plasma discharge also etches the surface within the depth varying from 1 to 10 nm while the bulk properties of the polymer remain the same (Grace and Gerenser, 2003).

During the plasma surface modification, active plasma species such as electrons, ions, radicals, and excited atoms or molecules interact with the atoms on the upper surface layer of the polymer. As a result of these interactions, volatile products can be produced due to the plasma etching and new functional groups are produced on the surface (Liston et al., 1993, Grace and Gerenser, 2003). Formation of these new products causes changes in the surface energy while improving the surface for bonding, coating, etc. Plasma parameters such as the RF input power, exposure time, gas flow rate, pressure, gas type play an important role by significantly changing the plasma properties. Depending on the plasma parameters even polymers having chemically similar structures may produce different results (Nihlstrand et al., 1997). In this study, the purpose is to understand the effect of plasma on the surface of PE polymer material modified at various values of the RF input power, starting from 50 W to 500 W. The plasma discharge is monitored using a broadband optical emission spectrometer (OES). The chemical changes on the surfaces are examined using a Fourier transform infrared-attenuated total reflection (FTIR-ATR) spectrometer. Moreover, the crystal properties of surfaces are examined using X-ray diffraction (XRD) spectrometer.

Experiment

The experimental set up is a capacitively coupled RF plasma discharge system consisting of two parallel aluminum electrodes. 13.56 MHz RF signal is applied between the electrodes to generate the plasma discharge. First, the pressure of the vacuum chamber is reduced to a base pressure of 10^{-3} Torr, then Argon gas is introduced using an MKS multi-gas controller 647C. All experiments are carried out at the pressure of 1.2×10^{-1} Torr. The granular PE, $(C_2H_4)_n$, melting at 110 ˚C, is purchased from PETKIM. To prepare polymer samples in sizes of 1x1 cm^2 and with a thickness of 0.6 mm, a heat press is used. The prepared polymer samples are transferred using a load lock chamber attached to the vacuum vessel.

All surface modifications experiments are conducted at the same parameters except for different RF discharge power varied from 50 W to 500 W with 50 W steps. During these experiments, the plasma exposure time is 10 minutes, and the gas flow rate is fixed at 50 sccm. The plasma emission is measured during the discharge using a broadband Ocean Optics HR2000 spectrometer. The polymer results are chemically examined using a Thermo Scientific Nicolet iS10 FTIR-ATR spectrometer. A Rigaku Ultimate-IV X-ray diffractometer (Cu K_α, λ=1.54 Å) is used to measure the crystal properties of the polymer surfaces.

Results /Discussion

Optical Emission Spectrometer

OES data are measured in a wavelength range of 300 – 900 nm to investigate the emission of the Ar plasma during the plasma processing. The atomic spectral lines of Ar I observed due to the ionization of the discharge gas while the atomic lines of C I arise from the surface of the polymer. Also, molecular lines of C_2 and CH are detected in the OES data due to the interactions between the species. The wavelength spectra of these atomic and molecular lines are shown in Fig. 1 for the selected data collected at 400 W of RF input power for plasma. Strong and sharp lines observed at the red end of the visible spectrum are mainly due to Ar I atomic emission

lines (NIST atomic database). Due to the wavelength resolution of the Ocean HR2000 spectrometer, some of the observed C I lines may overlap with Ar I lines around 700 nm to 750 nm. Besides these atomic lines, the molecular lines of C_2 and CH are observed in the visible and near the ultraviolet end of the spectrum. C_2 Swan band system ($d^3\Pi_g$-$a^3\Pi_a$) is observed at bands near 473.7 nm. CH bandhead is observed at regions from 415.9 nm to 428.2 nm and from 431.0 nm to 445.0 nm (Barholm-Hansen et al., 1994).

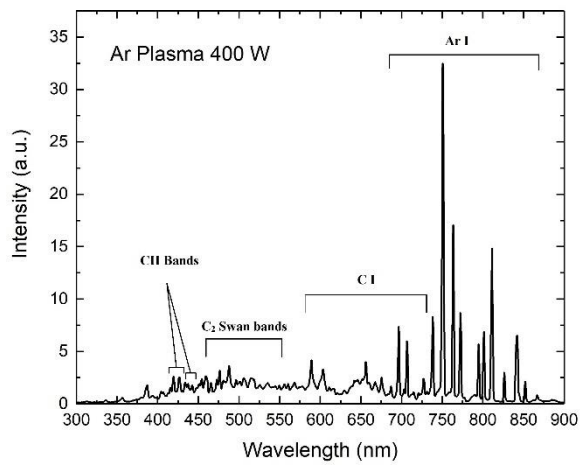

Fig. 1. The OES data for Ar plasma. (Selected for 400 W of the RF input power)

FTIR-ATR Spectrometer

The changes in the chemical structures of the polymer surface are investigated using an FTIR-ATR spectrometer operating in a wavenumber range of 3500 cm^{-1} – 600 cm^{-1}. The band intensities measured at wavenumbers are proportional to the concentration of chemical structures corresponding to these bands (Mistry, 2009). Spectra of the unmodified and the plasma modified surfaces are shown in Fig. 2. Vibrations due to the -CH_2- groups are observed at 2915 cm^{-1} and 2847 cm^{-1} referring to asymmetric and symmetric C-H stretching (De Geyter et al., 2008, Ghosh et al., 2004). Intensities of these main peaks first show a decrease in low RF power settings. This decrease in the C-H stretching bands suggests that the active plasma species dominantly interact with PE surface atoms and generate new chemical structures due to the etching. At 200 W input power, the intensities of the C-H stretching bands are measured roughly about the same as the intensities of measured using the unmodified PE. This can be interpreted as a number density equilibrium between the formation of new functional groups on the surface, and the loses due to the etching of the surface. As the RF input power increases, the intensities of these C-H stretching peaks show a small decrease until they reach a threshold near 400 W. Then, they start to increase at 450 W and at 500 W, which may possibly be due to a substantial increase in the number density of new functional groups on the surface.

In the spectra, the vibration of C-H deformation in -$(CH_2)_n$ is observed at 1462 cm^{-1} while the vibration of C-C rocking in -$(CH_2)_n$- is observed at 719 cm^{-1} (De Geyter et al., 2008). Intensities of these peaks show higher values than those of the unmodified spectra at RF input power values higher than 400 W. The peak seen at 1645 cm^{-1} corresponds to the asymmetric COO- or C=C stretching vibration (De Geyter et al., 2008, Guruvenket et al., 2004). The intensity of this peak significantly increases with increasing RF power after 150 W. Notably its maximum values are observed at 250 W and 500 W. This shows that new functional groups

are formed on the surfaces. Additionally, this peak becomes broader with increasing the RF power due to the existence of crosslinking reactions causing the formed chemical groups to have crosslinking structures (Liston et al., 1993, Grace and Gerenser, 2003, Guruvenket et al., 2004). The hydrogen bonded structures are observed at 3392 cm^{-1} and 3191 cm^{-1} corresponding to –O-H stretching vibration (Ghosh et al., 2004, Guruvenket et al., 2004). The intensities of these peaks increase with increasing input power, and broader peaks are seen due to the crosslinking reactions.

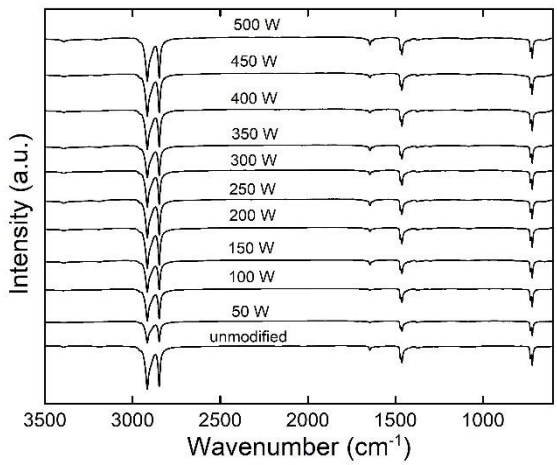

Fig. 2. FTIR-ATR spectra of unmodified and plasma modified PE samples for Argon plasma.

XRD measurements

The XRD patterns are measured between 10° and 60° with 0.02° per 1 s to investigate the structural orders of PE surfaces, as shown in Fig. 3. The pattern peaks are found at 21.6°, 24°, 29.9°, 36.3°, and 39.9°. After the plasma exposure, peaks observed at 2theta of 20.5°, 46.8° and 53.1° start to appear more clearly. Intensities of these peaks show a significant increase after the plasma surface modification. It can be considered that Argon plasma leads to improve the surface energy of PE and increase the concentration of the saturated structures on the surface. Due to the relationship between the surface energy and the structural order of the surface, it is observed that the crystal properties of PE surfaces are improved via the plasma exposure (Slepička et al., 2013, Kim et al., 2003). Additionally, the width of these peaks is inversely proportional to the crystallite size, which is observed as decreasing after the plasma exposure. This also verifies that the increase in the crystallinity. It can be suggested that the plasma exposure is effective in improving the crystallinity of PE surfaces, and maximum differences between the unmodified and modified spectra are obtained at 50 W, 150 W and 450 W. As seen in the results, there are no systematic changes with increasing RF input power.

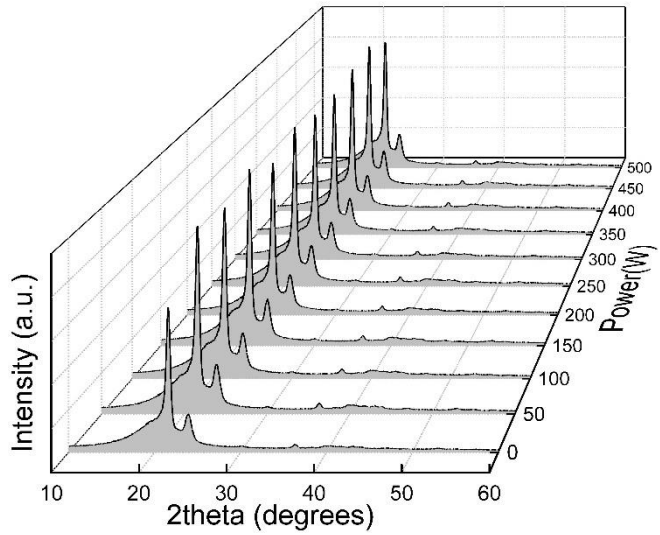

Fig. 3. XRD pattern of unmodified and plasma modified PE samples for Argon plasma.

Conclusion

A capacitively coupled RF plasma system is used to enhance the surface properties of PE polymer material. The results show that Argon plasma provides the formation of new functional groups on surfaces and the activation of the unsaturated structures existing on surfaces to increase the concentration of saturated structures. It is observed that the discharge power plays a significant role in controlling the energy required for the reactions occurring during the process. The OES spectra show the formation of the atomic and the molecular species during the plasma modification and the number density of these species generally have higher values at the high RF input power, but it is not a continuous increase due to the complex interactions. Moreover, the crystallinity of PE surfaces significantly increases with the plasma exposure. This shows that the required energy is transferring from the plasma discharge to improve the low surface energy.

Acknowledgements

This work is supported by the Scientific Research Project Fund of Middle East Technical University, under projects # YÖP-105-2018-2840 and # BAP-01-05-2017-006

References

Zille, A., Oliveira, F.R., Souto, A.P., 2015. Plasma Treatment in Textile Industry, Plasma Processes and Polymers 12, p. 98–131.

Pankaj, S.K., Bueno-Ferrer, C., Misra, N.N., Milosavljević, V., O'Donnell, C.P., Bourke, P. et al., 2014. Applications of Cold Plasma Technology in Food Packaging, Trends in Food Science and Technology 35, p. 5–17.

Slepička, P., Kasálková, N.S., Stránská, E., Bačáková, L., Švorčík, V., 2013. Surface Characterization of Plasma Treated Polymers for Applications as Biocompatible Carriers, eXPRESS Polymer Letters 7, p. 535–545.

De Geyter, N., Morent, R., Leys, C., 2008. Surface Characterization of Plasma-Modified Polyethylene by Contact Angle Experiments and ATR-FTIR Spectroscopy, Surface and Interface Analysis 40, p. 608–611.

Liston, E.M., Martinu, L., Wertheimer, M.R., 1993. Plasma Surface Modification of Polymers for Improved Adhesion: A Critical

Review, Journal of Adhesion Science Technology 7, p. 1091–1127.
Grace, J.M., Gerenser, L.J., 2003. Plasma Treatment of Polymers, Journal of Dispersion Science and Technology 24, p. 305-341.
Lee, B.K.T., Goddard, J.M., Hotchkiss, J.H., 2009. Plasma Modification of Polyolefin Surfaces and Science, Packaging Technology and Science 22, p. 139–150.
Morent, R., De Geyter, N., Verschuren, J., De Clerck, K., Kiekens, P., Leys, C., 2008. Non-thermal Plasma Treatment of Textiles, Surface and Coatings Technology 202, p. 3427–3449.
Vesel, A., Junkar, I., Cvelbar, U., Kovac, J., Mozetic, M., 2017. Surface Modification of Polyester by Oxygen- and Nitrogen-Plasma Treatment, Surface and Interface Analysis 40, p. 1444–1453.
Popelka, A., Novák, I., Al-Maadeed, M.A.S.A., Ouederni, M., Krupa, I., 2018. Effect of Corona Treatment on Adhesion Enhancement of LLDPE, Surface and Coatings Technology 335, p. 118–125.
Gomathi, N., Neogi, S., 2009. Surface Modification of Polypropylene Using Argon Plasma: Statistical Optimization of the Process Variables, Applied Surface Science 255, p. 7590–7600.
Vesel, A., Mozetic, M., 2017. New Developments in Surface Functionalization of Polymers Using Controlled Plasma Treatments, Journal of Physics D: Applied Physics 50, p. 293001.
Nihlstrand, A., Hjertberg, T., Johansson, K., 1997. Plasma Treatment of Polyolefins: Influence of Material Composition: 1. Bulk and Surface Characterization, Polymer 38, p. 3581–3589.
NIST Atomic Physics Database, https://www.nist.gov/pml/atomic-spectra-database.
Barholm-Hansen, C., Bentzon, M.D., Hansen, J.B., 1994. Optical Emission Spectroscopy During Growth of Diamond-Like Carbon From a Methane Plasma, Diamond and Related Materials 3, p. 564–568.
Mistry, B.D., 2009. A Handbook of Spectroscopic Data Chemistry, Oxford Book Company.
Ghosh, R.N., Jana, T., Ray, B.C., Adhikari, B., 2004. Grafting of Vinyl Acetate onto Low Density Polyethylene—Starch Biodegradable Films for Printing and Packaging Applications, Polymer International 53, p. 339–343.
Guruvenket, S., Rao, G.M., Komath, M., Raichur, A.M., 2004. Plasma Surface Modification of Polystyrene and Polyethylene, Applied Surface Science 236, p. 278–284.
Kim, K.S., Ryu, C.M., Park, C.S., Sur, G.S., Park, C.E., 2003. Investigation of Crystallinity Effects on the Surface of Oxygen Plasma Treated Low Density Polyethylene Using X-Ray Photoelectron Spectroscopy, Polymer 44, p. 6287–6295.

Science and Applications of Thin Films, Conference & Exhibition (SATF 2018)
Izmir Institute of Technology, Izmir, Turkey, September 17-21, 2018

Co-doped ZnO Thin Film Nanocomposites as Model Nanocatalysts

Asghar Ali[a,*] James Aluha[b], Redhouane Henda[a], Nicolas Abatzoglou[b]

[a]*School of Engineering, Laurentian University, Sudbury, ON P3E 2C6, Canada*
[b]*Department of Chemical & Biotechnological Engineering, Université de Sherbrooke, Sherbrooke, QC J1K 2R1, Canada.*

*Corresponding author. Tel.: +1-800-461-4030; fax: +1-705-675-4862.
E-mail address: aali2@laurentian.ca

Abstract

In this work, we report on the deposition of Co-doped ZnO (CZO) thin films on c-sapphire substrate using the relatively novel pulsed electron beam ablation (PEBA) method at different temperatures (450^{o}C, 600^{o}C, 800^{o}C) and under argon pressure of ~3 mTorr. Three main aspects of the films, viz., size of nanoparticles, presence of elemental cobalt and cobalt crystal phase have been assessed using complementary analytical techniques. Scanning electron microscopy (SEM) has revealed that the films consist of cobalt-rich globules dispersed over the surface, which grow out of primitive nano-particulates with an average size in the range of ~5-16 nm. Film roughness, based on atomic force microscopy (AFM) measurements, increases drastically as the deposition temperature is increased, viz., nearly 5 nm (450^{o}C), 19 nm (600^{o}C), and 18 nm (800^{o}C). X-ray diffraction (XRD) data reveal that the elevated deposition temperatures (600^{o}C-800^{o}C) result in a significant increase in hcp metallic cobalt phase and strong deformation of the hexagonal wurtzite structure of ZnO phase in the films. From crystallographic analysis, the deposition temperature has a strong bearing on ZnO and cobalt crystallite size as well. X-ray photoelectron spectroscopy (XPS) findings point to increasing metallic Co content in the films at high deposition temperature. The potential of the films as nano-catalysts has been evaluated via Fischer-Tropsch synthesis (FTS) in a 3-phase continuously-stirred tank slurry reactor (3-φ-CSTSR) using a Robinson-Mahoney stationary basket (RMSB). The preliminary results are discussed in terms of catalytic activity and selectivity. The reaction liquid product is rich in diesel and wax fractions.

Keywords: Co:ZnO/Al2O3 nanocomposites; thin film nanocatalysts; pulsed electron beam ablation; Fischer-Tropsch synthesis.

Introduction

Over the last few decades, oxide-supported metal nanoparticles have triggered increasing interest amongst researchers for their potential applications as bio- and electro-chemical sensors (White et al., 2009), for solar energy harvesting (Chan et al., 2004), in biofuel up gradation (Xu et al., 2012), and as nanocatalysts for the sustainable production of fuels and valuable chemicals (Leshkov et al., 2007; Galvis et al., 2012; Abdollahi et al., 2017). Co supported on ZnO has gained intense interest in many industrially important processes, viz., hydrogen production (Jaramillo et al., 2005), photocatalysis (Poongodi et al., 2015), steam reforming (Martono et al., 2011), and other energy-intensive processes (Pan and Bukur, 2010). Among these energy intensive processes, Fischer-Tropsch synthesis (FTS) is a potentially attractive technology for the production of clean liquid fuels from syngas. FT is a well-established catalytic process in which synthesis gas (a mixture of CO and H_2) is converted into liquid fuels. The most common practical catalysts for FTS are Fe and Co (Aluha and Abatzoglou, 2016; Dalai and Davis, 2008). The water gas shift (undesired) reaction is more

significant on iron catalyst than on Co (Tsakoumis et al., 2010). While the activities of Co and Fe based FT-catalysts are comparable and they display similar chain growth capabilities at relatively low temperature (473-523 K), the productivity at higher conversion is superior using Co based nanocatalysts (Gual et al., 2012). It has been reported that cobalt hexagonal close packed (hcp) phase exhibits higher cobalt sites yield in FT reaction so that cobalt hcp phase seems to be more active than its cobalt face-centered cubic (fcc) phase counterpart (Fischer et al., 2011). Further, cobalt based FTS catalysts are more attractive due to their low water gas shift (WGS) activity and higher productivity of long chain hydrocarbons C_{5+} (Savost'yanov et al., 2017; Jahangiri et al., 2014). Zinc oxide supported Co catalysts have many distinctive features, viz., resistance to oxidation caused by water produced during FTS (Clarkson et al., 2012), tolerance of carbon dioxide (Freide and Hardy, 2009), and, consequently, the catalyst is able to maintain its activity over a long period of time.

In general, the properties of nano-catalysts depend on phase/structure, the presence of the metal in elemental form, and particle size, so that the control of these aspects during film growth, i.e., through the optimization of process parameters, is of primary importance to achieve desirable catalytic features. Since a large portion of atoms in nanoparticles are exposed to the surface, their physico-chemical properties are strongly influenced by the nature of surface species (Gual et al., 2012). On the one hand, the structure of CZO films is significantly affected by the doping level of cobalt in ZnO. For a Co doping level of up to 10-12 wt%, the properties of CZO are practically similar to those of zinc oxide (Juang et al., 2007; Park et al., 2004). Secondary phases, viz., elemental cobalt and cobalt oxides, have been observed in CZO films for higher levels of Co doping. On the other hand, the structure/phase of CZO film is strongly dependent on deposition temperature. Higher deposition temperature is more favourable for the formation of secondary phases in CZO films. Particularly, at 500^{o}C-600^{o}C, secondary phases like Co and CoO are formed in CZO films (Ivill et al., 2008), whereas hcp metallic Co clusters appear in CZO films deposited at 700^{o}C (Kim et al., 2004). Similarly, a secondary phase of metallic Co nano-clusters near the surface has been reported for film deposited at relatively higher temperature (800^{o}C) (Su et al., 2011). The properties of FT nanocatalysts are also size dependent (Gual et al., 2012), so that it is necessary to control their size in order to achieve desired features of a model nanocatalyst. Normally FT reaction takes place on cobalt sites located on the surface of cobalt metallic nanoparticles in the range of 6-30 nm. A catalyst containing metallic cobalt particles smaller than 4-5 nm in size is expected to re-oxidize to CoO during realistic FT reaction conditions, which eventually results in the deactivation of the catalyst (Karaca et al., 2011).

The production of nanoparticulates with well controlled dimensions is a characteristic feature of PEBA, which can be advantageous in the production of nanocatalysts (Mathis and Christen, 2007). Further, many intermediate steps, viz., impregnation, drying, calcination/decomposition and activation/reduction, are involved in the preparation of FT-based catalysts by conventional wet impregnation route, whereas a single step process is possible using PEBA. PEBA is a relatively novel/unexplored technique for the preparation of high quality thin films with superior properties. Preservation of target stoichiometry in the condensing film under optimum deposition condition is another characteristic feature associated with PEBA. High power density leads to rapid heating and evaporation far from thermodynamic equilibrium, making possible solid to vapour transition practically independent from the target material phase diagram and composition (Pattini et al., 2015). Consequently, the congruent sublimation of the target materials results in stoichiometric film condensation.

Recently, we have looked into the effects of Co deposition temperature and discharge voltage on structural and morphological properties of CZO films deposited on Si (100) (Ali et al., 2017). The substrate material, being one of the significant parameters in catalyst synthesis, could affect the structural (Park et al., 2012), optical and electrical properties of the films (Taabouche et al., 2013), and potential lattice mismatch between the film and substrate may result in the development of undesired stresses in the films. The substrate material

may turn out to be a serious limitation for optimum growth of CZO films to carry out a particular catalytic application (Handuja et al., 2010).

In this work, we assess the influence of deposition temperature on morphological, chemical and structural properties of CZO films deposited on c-sapphire substrates. Discussion of the experimental data revolves around three main aspects of CZO thin films viz., presence of elemental cobalt (Co^o), cobalt crystal phase (hexagonal close-packed structure), and size of nanoparticles. The comparison between the properties of CZO films deposited on c-sapphire and Si (100) has been assessed using complementary analytical techniques. The potential of the films as model nanocatalysts has been examined in the context of FTS.

Materials and Methods

A commercial beam source (PEBS-20, Neocera Inc., USA) has been used to ablate high purity commercial grade CZO target (SINTEF, Norway) containing 20 wt% cobalt to deposit thin films of CZO on c-sapphire substrates (University Wafer, USA). PEBA system is composed of a stainless-steel chamber, which is pumped by a combination of two pumps (rotary and turbo molecular) to achieve a base pressure of 1x10-6 Torr. The beam source is composed of a hollow cathode, a trigger and a capillary tube as shown schematically in Fig. 1-a. More ample details on the beam source can be found elsewhere (Ali et al., 2017). Prior to deposition, the substrates and target were cleaned sequentially in an ultra-sonic cleaner (Cole-Parmer 8890, USA) in acetone and methanol at 50^{o}C for 30 minutes, respectively. The target has been pre-ablated before deposition by 3000 electron beam pulses at an accelerating voltage of 10 kV and a pulsed electron beam frequency of 2 Hz in order to remove any surface contamination. The films were deposited at various deposition temperatures (450^{o}C, 600^{o}C, 800^{o}C), whereas beam frequency and accelerating voltage were set to 2 Hz and 16 kV, respectively. During deposition, the substrate to target distance, capillary tube (3 mm in diameter and 18 cm in length) to target distance, beam frequency, and background Ar pressure were set to 50 mm, 2.5 mm, 2 Hz, and 3 mTorr, respectively. The target has been continuously rastered and rotated to allow for smooth ablation. The substrates have been subjected to continuous rotation to enhance film homogeneity.

A 3-phase, continuously-stirred tank slurry reactor, using the Robinson-Mahoney stationary basket (RMSB) configuration, has been used to evaluate CZO thin films for their FTS activity and selectivity. The schematic of the RMSB reactor is presented in Fig. 1-h. About 10 g of Al_2O_3 supported Co-ZnO thin film material containing was loaded into the reactor and reduced in-situ in high purity hydrogen for three hours at a flow rate and temperature of 160 cm^3/min and 673 K, respectively. The reactor was cooled down to ambient temperature under a flow of H_2. Subsequently, 150 cm^3 of squalane was introduced into the reactor. The catalyst was tested at 267^{o}C and 2 MPa under the flow (280 $cm^3.min^{-1}$) of synthesis gas composed of 60% H_2, 30% CO and 10% Ar (H_2:CO volume ratio = 2) under a stirring speed of 2000 rpm for 120 h. FT gaseous and liquid products were analyzed using two separate off-line gas chromatographs (GCs) by employing the same procedure as described in a previous study (Aluha et al., 2016).

Phase and crystallographic analyses were carried out using a bench top x-ray diffractometer (Rigaku Mini Flex 600, USA). The scan range for 2Θ has been measured from 30^o to 80^o using theta/2-theta Bragg-Brentano configuration. The system was operated at 15 mA and 40 kV. The diffractograms have been

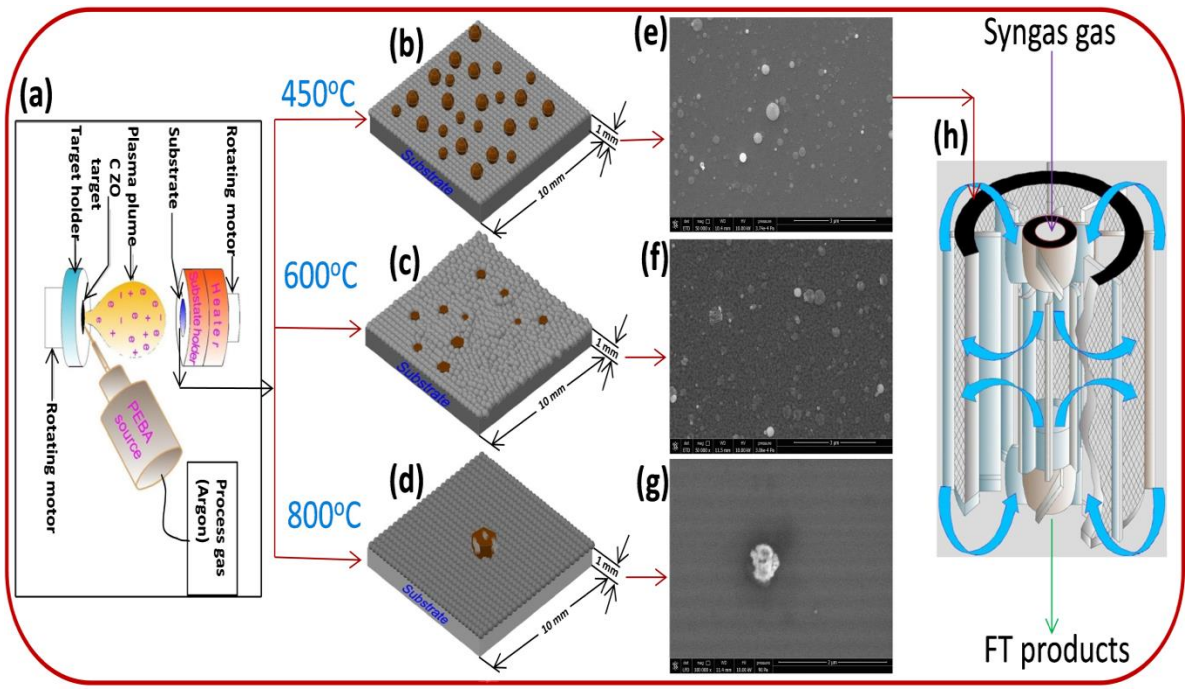

Fig. 1. Fig. 1. Morphological evolution sketch of CZO films deposited on c-sapphire. (a) Schematic pulsed electron beam ablation system. (b, c, d) Schematics of CZO films deposited at 450°C, 600°C and 800°C respectively (e, f, g) SEM images of CZO films deposited at 450°C, 600°C and 800°C respectively. (h) a Robinson-Mahoney stationary basket (RMSB) used to test the activity and selectivity of the deposited films.

generated at a step size of $2\Theta = 0.02^{o}$ and a scan speed of 1^{o}/min. The morphology of the films has been investigated by two complementary surface characterization techniques, viz., SEM (FEI Quanta FEG 250, USA) and AFM (Anasys Instruments, USA). SEM was operated under high vacuum at 10 kV, whereas AFM was operated with a scan speed of 0.2 Hz−0.5 Hz in contact mode. The elemental composition of the films was characterized by EDX. Film thickness has been measured by visible reflectance spectroscopy (M-Probe Series, Semiconsoft, USA). XPS (Thermo-Fisher Scientific, UK) K-Alpha system has been used to acquire near surface chemical composition of the films. The x-ray source consists of monochromated Al K-alpha x-rays and the measurements were made at an electron take-off of 90^{o}. The samples were analyzed using the largest x-ray spot size (400 μm ellipse) for this instrument.

Results and Discussion

The growth of Co rich globules in CZO films is shown schematically in Fig. 1(e-g). It can be clearly seen that the surface morphology of CZO films is significantly affected as the deposition temperature increases from 450°C to 800°C, and the deposited films follow two different growth modes. The growth of CZO films at 450°C seems to follow the Stranski-Krastanov (S.K.) growth model, i.e., layer plus islands. The first layer (grayish colour) largely consists of ZnO phase on top of which Co-rich globules (whitish colour) are formed and that the latter are uniformly distributed over the film matrix, as shown in Fig. 1(e). It is worth noting that the density of the Co-rich globules, whitish in the corresponding SEM images as shown in Fig. 1(e-f),

decreases as the deposition temperature increases from 450^{o}C to 800^{o}C. In S.K. model, the depositing atoms preferably bond to the substrate rather than to one another. After forming a few layers initially, as a result of a large decrease in Gibb's free energy when the depositing atoms bond to the substrate rather than bonding to one another and provided surface diffusion is fast. Due to lattice mismatch between the films and substrate, the development of strain results in the formation of 3D islands on top of the initial layer to relax the strain. The films grown at 600^{o}C appear to follow the Volmer-Weber (V-W) model, i.e., from 3D islands, which grow side by side. In V-W model, the depositing atoms are more strongly bonded to one another than to the substrate material combined with slow surface diffusion, which results in a pile-up of atoms and subsequent formation of the film out of 3D islands forming a continuous layer. The film corresponding to a deposition temperature of 800^{o}C seems to follow a different growth mode, albeit the main features of S.K. model are obvious therein. In addition, interestingly it is noted that at low deposition temperature (450^{o}C) Co-rich globules are sphere-like in shape, but at higher growth temperatures (600^{o}C and 800^{o}C), Co-rich globules are tapered (faceted). Under similar deposition conditions (450^{o}C-800^{o}C and 16 kV) for CZO films on Si (100), similar growth models have been reported in a previous study (Ali et al., 2017).

Phase analysis of CZO films has been carried out by XRD using theta/2-theta Brag-Brentano configuration. Fig. 2 shows XRD patterns of the films grown on c-sapphire at different deposition temperatures (450^{o}C, 600^{o}C, 800^{o}C). The diffraction patterns of all films show strong peaks corresponding to the c-sapphire substrate, i.e., the peak at $2\Theta \approx 41.68^{o}$ (0001). The characteristic peak of ZnO hexagonal wurtzite structure (002) can be observed at $2\Theta \approx 34.43^{o}$ for the film deposited at 450^{o}C, and the film exhibits two additional peaks corresponding to ZnO at $2\Theta \approx 36.26^{o}$ (101) and 72.6^{o} (004), as shown in Fig. 2 (bottom). For the film deposited at 600^{o}C, the diffractogram does not show any presence of ZnO peaks corresponding to planes (101) and (004), and only reveals a reflection (relatively less intense compared to the films deposited at 450oC) along the peak corresponding to plane (002), which is likely suggestive of a distortion of ZnO hexagonal wurtzite structure due to enhanced deposition temperature [26].The sharp and intense diffraction peak (002), for the films deposited at 450^{o}C and 600^{o}C, reveals that the deposited films have a preferential c-axis orientation, see Fig. 2 (bottom, middle). When the deposition temperature is further increased to 800^{o}C, the corresponding diffractogram does not reveal any signals from ZnO phase due to complete distortion of the wurtzite structure. Relatively low intensity or absence of ZnO hexagonal wurtzite structure peak (see Fig. 2- middle, top) corresponding to the plane (002) is most likely due to the low content of ZnO in the films (corroborated by XPS survey scan, see Fig. 3) or may be attributed to a significant distortion of ZnO hexagonal wurtzite structure at higher deposition temperature. Consequently, the diffractogram for the film deposited at 600^{o}C exhibits a less intense peak corresponding to (002) plane, and does not reveal any signals diffracted from ZnO hexagonal wurtzite structure for the film deposited at 800^{o}C. The phase analysis of the film deposited at 450^{o}C reveals two peaks corresponding to $2\Theta \approx 64.3^{o}$ (315), 80.2^{o} (600) attributed to hcp metallic Co. While five peaks associated with metallic Co appear at $2\Theta \approx 37.6^{o}$ (301), 52.8^{o} (313), 64.3^{o} (315), 71.5^{o} (008) and 80.2^{o} (600) for the films deposited at 600^{o}C, and three peaks appear at $2\Theta \approx 37.6^{o}$ (301), 64.3^{o} (315) and 80.2^{o} (600) corresponding to Coo (PDF card no.: 01-070-2633) for film deposited at 800^{o}C. Overall, a higher intensity of metallic Co can be observed in the film deposited at 600^{o}C and 800^{o}C, which suggests that a high deposition temperature, viz., 600^{o}C and 800^{o}C, is more favorable for the formation of hcp metallic Co in CZO films than 450^{o}C.

Phase analysis of CZO films deposited on Si (100) at 450^{o}C, as reported in a previous study (Ali et al.,

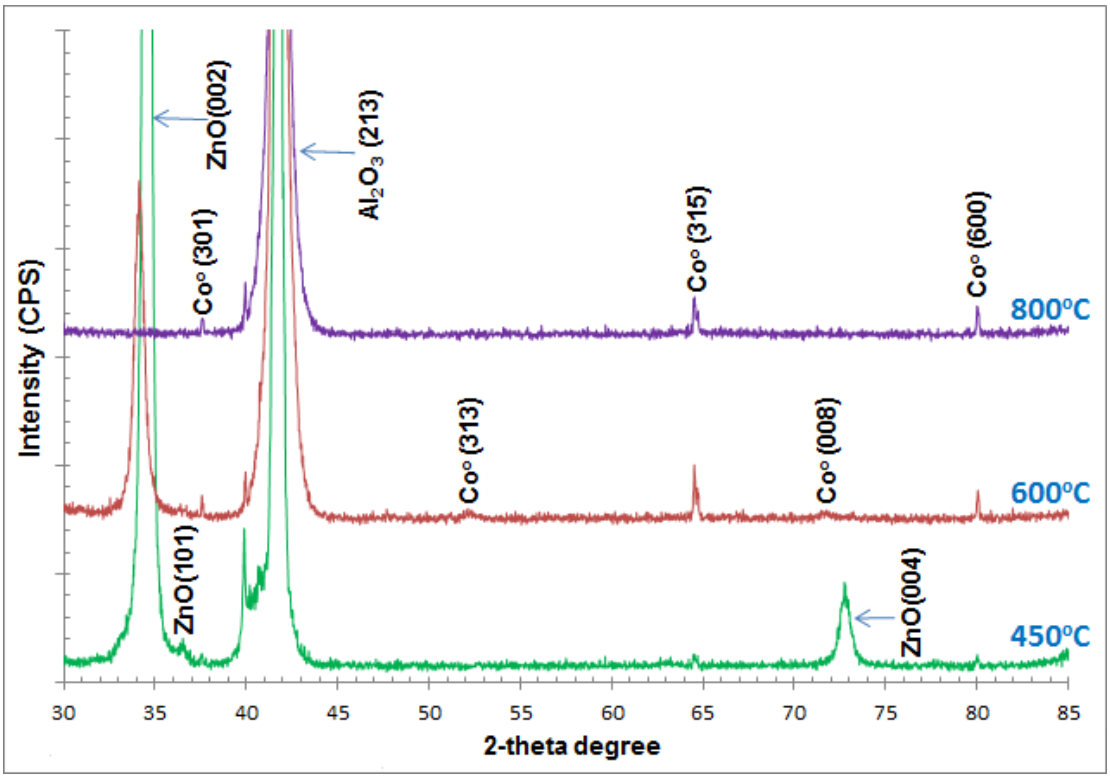

Fig. 2. XRD patterns for CZO thin films deposited on c-sapphire at different temperatures (450°C, 600°C and 800°C) and an accelerating voltage of 16 kV.

2017) reveals two peaks corresponding to hcp metallic Co at $2\Theta \approx 42.04^{o}$ (213) and 61.7^{o} (412). The film deposited at 600°C exhibits seven peaks associated with Co°, viz., $2\Theta \approx 35.7^{o}$ (203), 41.4^{o} (302), 42.5^{o} (204), 50.1^{o} (205), 51.5^{o} (304), 59.6^{o} (411), and 61.7^{o} (412), whereas the diffractogram of the film deposited at 800°C reveals three peaks of Co°, viz., 42.5^{o} (204), 50.1^{o} (205), and 61.7^{o} (412) [26]. Overall, on the one hand, a higher intensity of hcp Co content can be observed on Si (100) substrate, which suggests that under similar deposition conditions Si (100) substrate is relatively more favorable for the formation of hcp metallic Co in CZO films than c-sapphire substrate material. On the other hand, CZO film deposited on Si (100) shows dismal performance than the film on c-sapphire under similar FT reaction conditions (Ali et al., 2018).

The crystallite size of Co and ZnO can be estimated from the XRD pattern using the Debye Scherer's equation,

$$D = 0.9 \times \lambda / (B \times \cos \Theta) \quad (1)$$

where λ is the X-ray wavelength, Θ is the Brag diffraction angle, and B is the full-width at half angle maximum (FWHM) of the diffraction peak.

The crystallite size and strain have been calculated for each peak in the diffractogram corresponding to ZnO and Co phase separately, and average values are listed in Table 1. It is noticed that the maximum ZnO crystallite size (22.86 nm) is obtained for the film deposited at lower deposition temperature (450°C), while in

Table 1. Average crystallite size and strain of ZnO and Co phases at different temperatures.

Temp. (°C)	ZnO crystallite size (nm)	Stain	Co° crystallite size (nm)	Strain
450	22.86	0.0055	78.42	0.0008
600	13.65	0.009	59.63	0.0026
800	0	0	81.81	0.0009

case of metallic Co the maximum crystallite size (81.81 nm) is obtained at higher deposition temperature, i.e., 800°C. Overall, it is also noted that the crystallite size of Co is relatively higher than ZnO counterpart.

The near-surface chemical composition of the films has been investigated by XPS. Fig. 3 shows XPS survey spectra of CZO films deposited at various deposition temperatures, which shows representative peaks of Zn, Co and O for the films deposited at 450°C and 600°C, whereas the film deposited at 800°C exhibits only Co and oxygen peaks. The absence of Zn at the deposition temperature of 800°C is in accordance with XRD results. This can be explained in terms of the boiling point of Zn (907°C) nanoparticles (Viart et al., 2003). When the film is deposited at 800°C close to the boiling point of Zn, most likely Zn would have

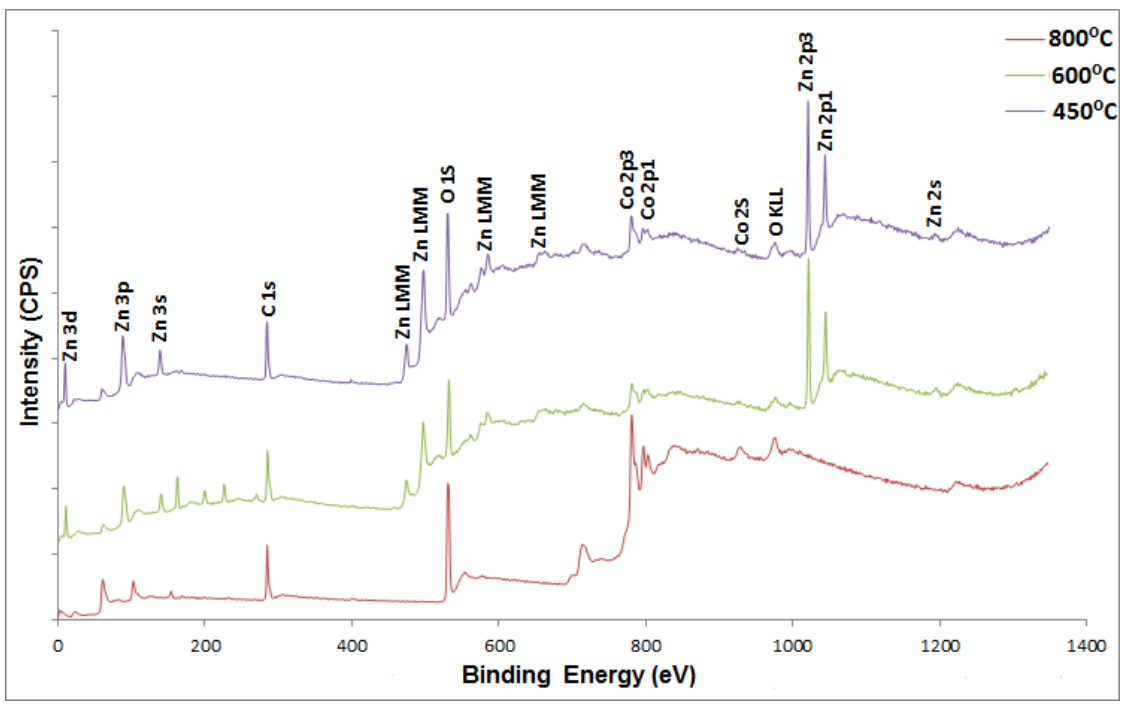

Fig. 3. XPS survey scan spectra of CZO films deposited at different deposition temperatures (shown in the inset).

re-evaporated from the film surface due to its high vapour pressure. This may lead to the elimination of Zn phase in the films and results in Co-phase rich films as can be seen from Fig.3, which is in accordance with XRD measurements.

Fig. 4 depicts spectra of Co $2p_{3/2}$ peaks (and their deconvolutions), and indicates that Co is present in oxidized (Co^{+2}, Co^{+3}) as well as in non-oxidized (Co^{o}) chemical states in CZO films. The Co $2p_{3/2}$ peak at the binding energy around 780.5 eV is assigned to Co^{+2} oxidation state (Ivill et al., 2008). The energy peak at

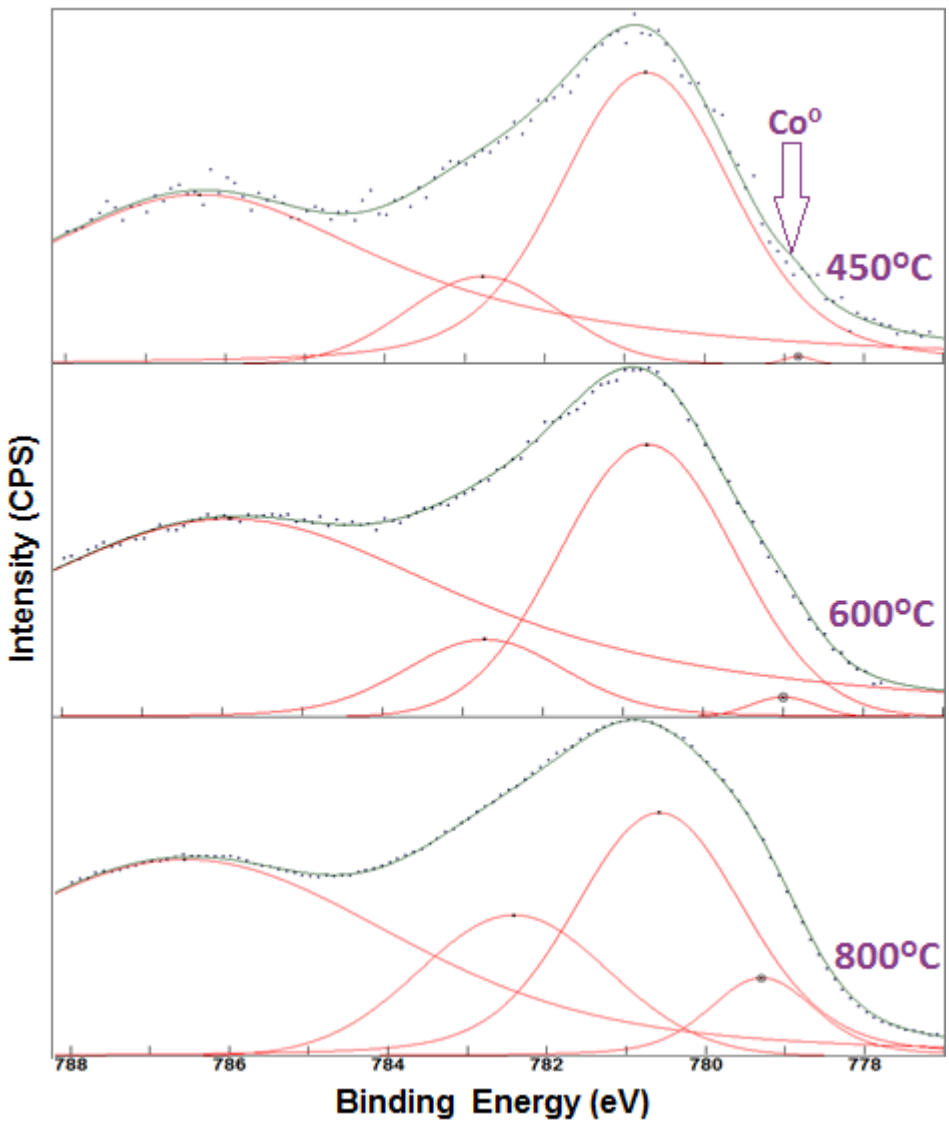

Fig. 4. XPS chemical binding spectra of Co $2p_{3/2}$ peaks (and their deconvolutions) of CZO films grown at different deposition temperatures (450°C–800°C).

around 782.8-783.3 eV is ascribed to Co^{+3} oxidation state (Zhou et al., 2008; Alves et al., 2017). The co-existence of Co^{+2} and Co^{+3} suggests the presence of CoO and Co_2O_3 phases near the surface in CZO films (Vadiyar et al., 2016). The data indicate that a substantial portion of Co atoms are present in the films as Co^{+2} oxidation state, where Co^{+2} substitutes Zn^{+2} lattice sites in ZnO. The intensity ratio of Co^{+2} and Co^{+3} signals in the films changes because of the possibility of oxidation of Co^{+2} to Co^{+3}. The exact nature of the cobalt defect in the structure is not possible to determine unequivocally with XPS measurements (Zhou et al., 2008). The small peak at the low binding energy located at 778 -779 eV is attributed non-oxidized (Co^{o}) cobalt (Tortosa et al., 2008; Peng et al., 2005). Interestingly, it is to be noted that as the deposition temperature increases, the metallic Co content in the film increases in accordance with XRD measurements. It can be concluded that high deposition temperature (800^{o}C) is more favourable for the formation of metallic Co in the deposited films near the surface. Thus, the deposition temperature plays a key role in controlling metallic Co content in CZO films, and, accordingly, film properties. Based on XRD and XPS analyses, it seems that at lower deposition temperature (450^{o}C) Co ions are largely incorporated into substitutional sites of ZnO structure, whereas for the films deposited at higher deposition temperature (600^{o}C, 800^{o}C) Co ions are located in the interstitial sites of ZnO lattice.

The compositional analysis of the films deposited at relatively high temperature (600^{o}C, 800^{o}C) has been acquired by EDX line scan as shown in Fig. 5, which clearly confirms the presence of Zn, Co and O in CZO films. Line scans provide a quantitative analysis of the elements along the dark green colour line ending with two blue circles. EDX line scan (superimposed on the corresponding SEM image) analysis confirms that the film matrix largely consists of Zn (purple line), while Co (blue line) is mainly to be found in the globules. The more whitish the color of the globule is, the higher the cobalt concentration is relatively to oxygen concentration as shown in Fig. 5(b). The oxygen content (green line) in the film is pretty high mainly due to substrate (c-sapphire) material underneath the film. The data, see Fig. 5(b), confirm that Zn content is remarkably less (1-2 wt.%) in the films deposited at 800^{o}C. This is most likely due to the re-evaporation of Zn from the film surface when the deposition is carried out at 800^{o}C (close to the boiling point of Zn) as

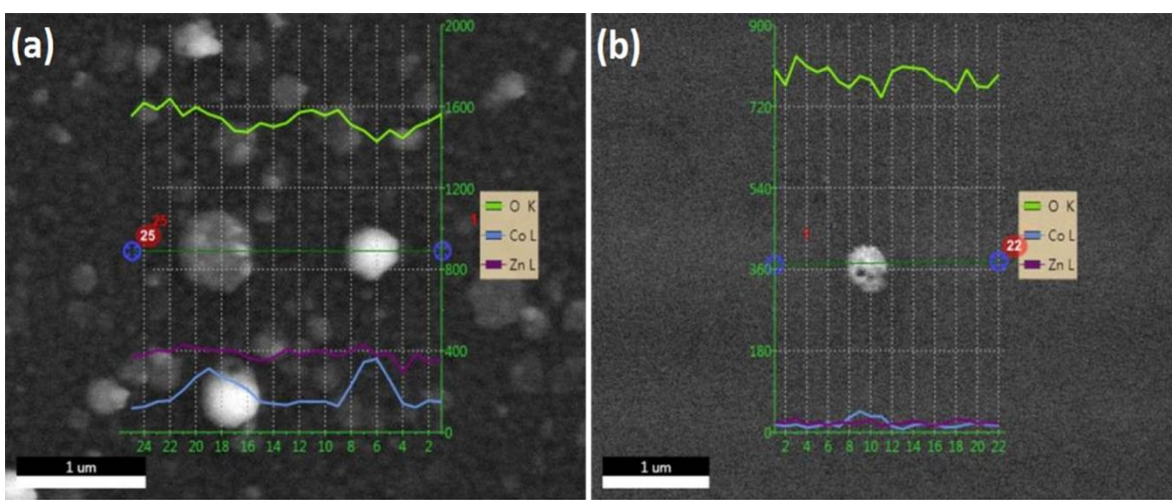

Fig. 5. Typical EDX line scans and their corresponding element profiles of the films deposited at (a) 600◦C, (b) 800◦C.

explained earlier.

Fig. 6 shows the surface morphology of CZO films grown on c-sapphire at different temperatures as per SEM analysis. Inspection of SEM images indicates that CZO films consist of nano globules, whose size is in the range of ~10-300 nm. The films consist of nano globules whose size and density seem to be strongly affected by the deposition temperature when the latter is varied from 450^{o}C to 800^{o}C. It can be seen from Fig. 6(a) that the globules are well isolated for the films deposited at 450^{o}C, while the globules grow side by side forming a continuous layer for the film deposited at 600^{o}C. The globule size decreases and density increases significantly as the temperature is increased from 450^{o}C to 600^{o}C. Cobalt nano particles start to melt at around 600^{o}C (Homma et al., 2003), and, accordingly, the higher globule density and their smaller size at high deposition temperature may be attributed to melting and spreading of Co globules over the film surface. Owing to thermodynamic (the melting process) and kinetic processes, viz., deposition flux, nucleation rate, surface diffusion and re-evaporation, Co particles disperse on the film surface resulting in smaller size and higher density. For the films deposited at 800^{o}C, see Fig. 6(c), and Fig. 5(b), it can be seen that the films consist of a very small number of Co-rich globules on the surface, and the globules exhibit holes (pores). The can be explained in terms of re-evaporation of Zn nano particles from the film surface. The data reveal that

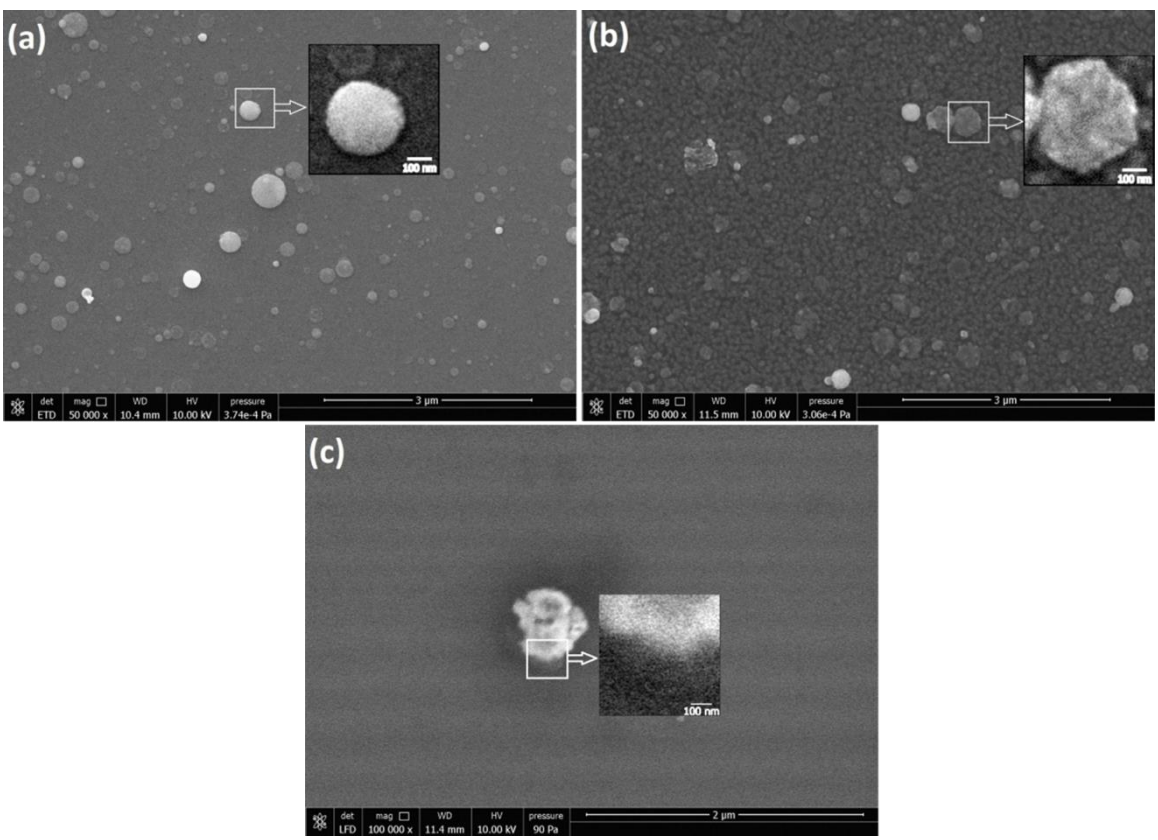

Fig. 6. SEM images of deposited films as a function of temperature at (a) 450^{o}C, (b) 600^{o}C, (c) 800^{o}C.

the films deposited at 450^{o}C on c-sapphire has a similar morphology as the film deposited on Si (100) under same process conditions as reported in an earlier study (Ali et al., 2017). Furthermore, the films deposited on Si at 600^{o}C exhibit cracks and voids, while the films on c-sapphire seem to be continuous. The films

deposited on Si at high temperature (800^{o}C) exhibit a higher number of agglomerated secondary particles relatively to the film deposited on c-sapphire at the same temperature, as depicted in Fig. 3(a-c).

A closer inspection of the films (as indicated in the zoomed-in square section of the deposited films) reveals that Co rich globules are dispersed over the film and consist of primitive nano-particles. The particle size distribution of these primitive nano-particles is depicted in Fig. 7. The data reveal that deposition temperature has substantial effect on particle size distribution. The most frequent particle size is in the range of 6 nm–10 nm for the films deposited at 450^{o}C and 600^{o}C, whereas the film deposited at 800^{o}C exhibits a significant number of particles with less than 5 nm in size. The average particle size at 450^{o}C, 600^{o}C and 800^{o}C is nearly 11.4 nm, 16.03 nm, and 5.2 nm, respectively.

From VRS measurements, the thickness of the deposited films is in the range of ~ 70-100 nm. Fig. 8 shows a typical reflectance response of CZO film deposited on c-sapphire at 450^{o}C. Film thickness is indirectly measured by means of a modified Marquardt-Levenberg built-in algorithm. The measured and calculated reflectance profiles are in good agreement, and any discrepancies are most likely due to uncertainties in the film optical properties used as input to the algorithm.

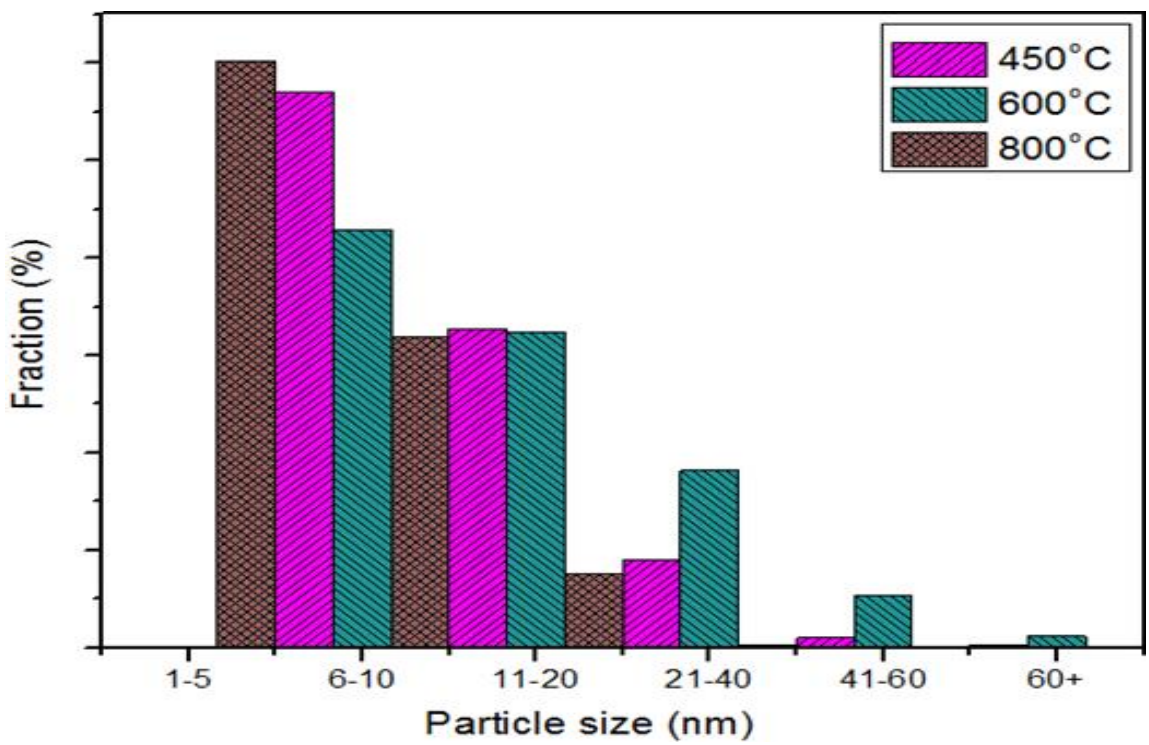

Fig. 7. Particle size distribution in films deposited c-sapphire. The deposition temperature is indicated in the inset.

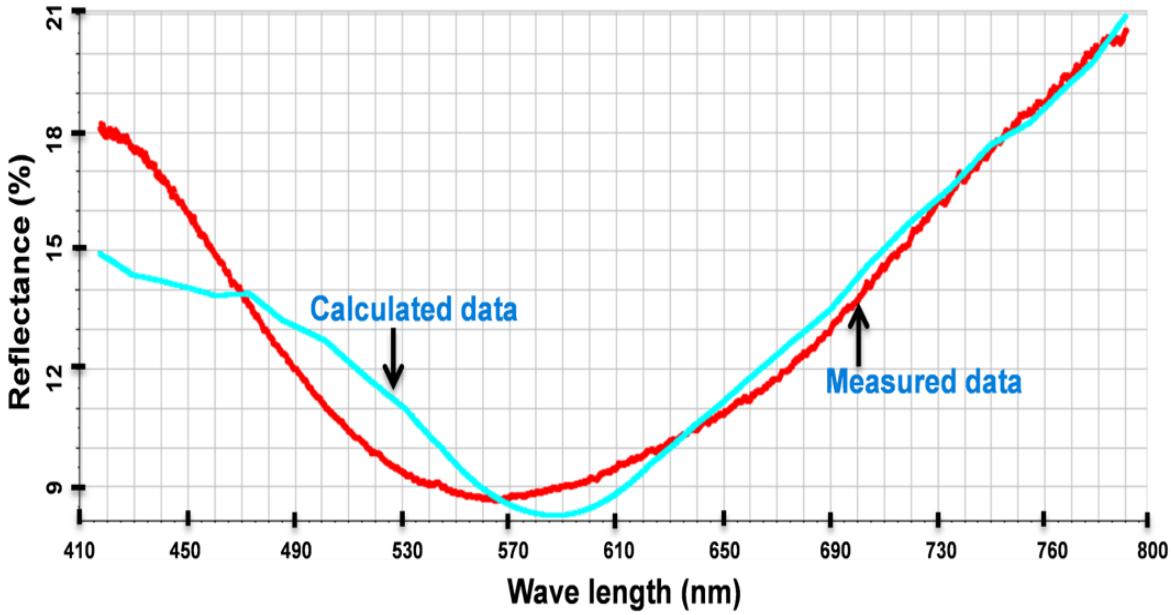

Fig. 8. Typical visible reflectance response of the film deposited at 450°C.

Film surface topography and average arithmetic roughness (Ra) are important properties for catalytic applications as they affect the physico-chemical properties of the films. Fig. 9 shows topographic images (2D, 3D) of CZO films deposited at various temperatures, whereby the findings reveal a drastic variation in film Ra (between ~4.8 nm and 18.2 nm) as the deposition temperature is increased from 450°C to 600°C. There is a marginal difference in Ra, viz., 18.2 nm to 17.6 nm, within the temperature range of 600°C-800°C. The present AFM images are consistent with SEM images reported earlier.

As per AFM data, the film deposited at 450°C consist of well isolated nano-globules, and the latter are uniformly distributed over the film matrix, which largely consists of ZnO, whereby ZnO acts as a support material and keeps the active phase highly dispersed. In the case of exothermic reactions like FTS, this may result in low energy density as ZnO is a semiconductor with a wide band gap, which helps reduce the possibility of sintering of the nano-catalyst. Based on these observations, only the films deposited at 450°C have been selected for the evaluation of FT thin film nano-catalyst activity and selectivity.

To evaluate catalyst activity, Co-ZnO/Al_2O_3 samples have been loaded into RMSBR as schematically shown in Fig. 1(h). This type of reactor has been chosen in order to avoid the stirrer coming into contact with the catalyst samples as this would have damaged the stirrer or CZO thin films. The nano-catalyst activity test procedure has been described elsewhere [31]. Carbon monoxide conversion is nearly 22% with total online time of six hours at 267°C. The catalyst shows higher productivity in the synthesis of long chain hydrocarbons ($C_{13} - C_{20}$ and C_{21+}), i.e., the liquid product is rich in diesel and wax fractions. The nano-catalyst shows a selectivity of ~4%, 31%, and 65% towards gasoline, diesel, and waxes, respectively, at a constant pressure of 2 MPa and a temperature of 267°C in continuous mode for 120 hours.

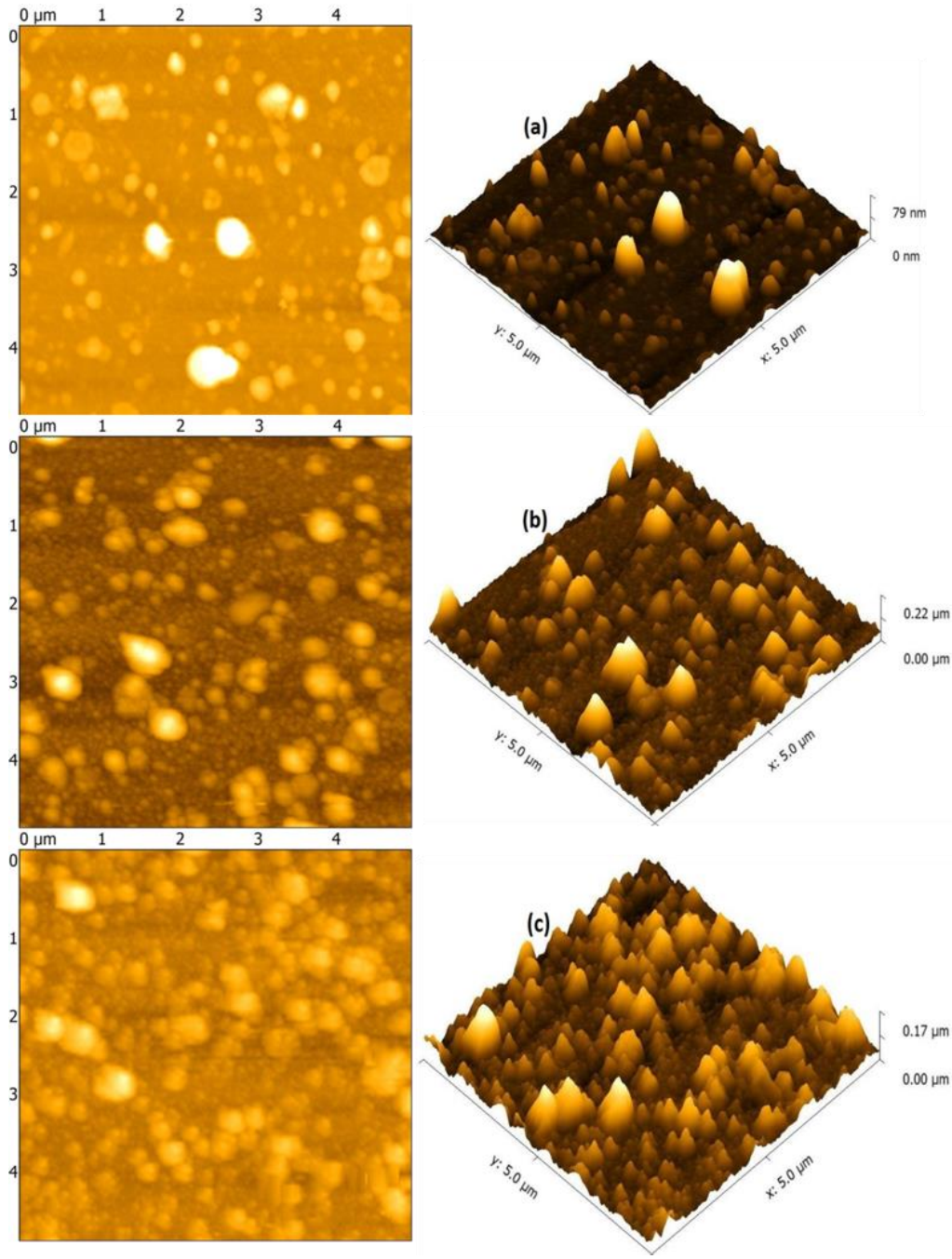

Fig. 9. AFM images (2D, 3D) of films deposited at different temperature (a) 450ºC (b).600ºC (c) 800ºC.

Conclusion

Co-ZnO thin film nano-composites supported on Al_2O_3 have been deposited in a single step from a single target containing 20 wt. % Co at different deposition temperatures (450^{o}C-800^{o}C) using PEBA technique. Experimental data reveal that the deposited films consist of rich globules, which are either dispersed on the film matrix, viz., films deposited at 450^{o}C and 800^{o}C, or grow side by side viz., films deposited at 600^{o}C, and that the mode of film growth can be described by two models. Both XRD and XPS measurements support the existence of metallic Co nanoparticle in the deposited films and that high deposition temperatures (600^{o}C, 800^{o}C) are more favourable for the formation of metallic Co in CZO films than 450^{o}C. XPS data reveal that all the deposited films exhibit cobalt in three chemical sates, viz., oxidized Co (CoO and Co_2O_3), and elemental Co (Co^o) near the film surface, and that the films deposited at 800^{o}C largely consist of a cobalt phase as corroborated by XRD measurements. Crystallographic analysis reveals that the films deposited at 450^{o}C and 600^{o}C exhibit ZnO hexagonal wurtzite structure, while at 800^{o}C ZnO hexagonal wurtzite structure is completely distorted in CZO films. The average particle size significantly decreases in the films deposited at 800^{o}C (5.2 nm) compared to the films deposited at 450^{o}C (11.4 nm) and 600^{o}C (16.03 nm). The catalyst shows higher productivity in the synthesis of long chain hydrocarbons (C_{13} – C_{20} and C_{21+}). The nano-catalyst shows a selectivity of ~4%, 31%, and 65% towards gasoline, diesel, and waxes, respectively.

Acknowledgements

A.A. is indebted to Ontario Ministry of Training, Colleges and Universities for providing an Ontario Graduate Scholarship (OGS). R.H. is thankful to the Canada Foundation for Innovation (CFI) and Natural Sciences and Engineering Research Council of Canada (NSERC) for the financial support.

References

Abdollahi, M., Atashi, H., Tabrizi, F.F., Mansouri, M., 2017. Fischer–Tropsch study over impregnated silica‐supported cobalt–iron nanocatalyst. Journal of Iranian Chemical Society 14, p. 245.

Ali, A., Aluha, J., Henda, R., Abatzoglou, N., 2018. Co-doped ZnO thin films grown by pulsed electron beam ablation as model nano-catalysts in Fischer-Tropsch synthesis. American Institute of Chemical Engineering Journal 64, p.3332.

Ali, A., Henda, R., Fagerberg, R., 2017. Effect of temperature and discharge voltage on the properties of Co-doped ZnO thin films deposited by pulsed electron beam ablation. Applied Surface Science 422, p.1082.

Aluha, J., Abatzoglou, N., 2016. Synthetic fuels from 3-φ-Fischer-Tropsch synthesis using syngas feed and novel nanometric catalysts synthesised by plasma. Biomass Bioenergy 95, p. 330.

Aluha, J., Braidy, N., Dalai, A., Abatzoglou, N., 2016. Low-Temperature Fischer-Tropsch Synthesis using Plasma-Synthesized Nanometric Co/C and Fe/C Catalysts. The Canadian Journal of Chemical Engineering 94, p.1504.

Alves, T. M. de L., Amorim, B.F., Torres, M.A.M., Bezerra, C.G., Medeiros, S. N. de., Gastelois, P.L., Outon, L.E.F., Macedo, W. A. de A., 2017. Wasp-waisted behavior in magnetic hysteresis curves of $CoFe_2O_4$ nanopowder at a low temperature: experimental evidence and theoretical approach, The Royal Society of Chemistry's Advances 7, p.22187.

Chan, K.Y., Ding, J., Ren, J., Cheng, S., Tsang, K.Y., 2004. Supported mixed metal nanoparticles as electrocatalysts in low temperature fuel cells. Journal of Materials Chemistry 14, p. 505.

Clarkson, J.S., Gamlin, T.D., Hardy, L.T., 2012. Fischer Tropsch Process. Patent No.: US 8,329,765 B2. p.1.

Dalai, A.K., Davis, B.H., 2008. Fischer-Tropsch synthesis: A review of water effects on the performances of unsupported and supported Co catalysts. Applied Catalysis A 348, p. 1.

Fischer, N., Steen, E.W., Claeys, M., 2011. Preparation of supported nano-sized cobalt oxide and fcc cobalt crystallites, Catalysis Today 171, p.174.

Freide, J.J.H.M.F., Hardy L.T., 2009. Modified catalyst and use of this catalyst for the conversion of synthesis. Patent No.: US 7, 566,678 B2. P.1.

Galvis, H.M.T., Bitter, J.H., Khare, C.B., Ruitenbeek, M., Dugulan, A.I., de Jong, K.P., Iron, S., 2012. Nanoparticles as Catalysts for Sustainable Production of Lower Olefins. Science 335, p. 835.

Gual, A., Godard, C., Castillon, S., Ferre, D.C., Claver, C., 2012. Colloidal Ru, Co and Fe nanoparticles Synthesis and application as nanocatalysts in the Fischer Tropsch process, Catalysis Today 183, p.154.

Handuja, S., Srivastava, P., Vankar, V.D., 2010. On the Growth and Microstructure of Carbon Nanotubes Grown by Thermal Chemical Vapor Deposition. Nanoscale Research Letters 5, p.1211.

Homma, Y., Kobayashi, Y., Ogino, T., 2003. Role of transition metal catalysts in single-walled carbon nanotube growth in chemical vapor deposition. The Journal Physical Chemistry B. 107, p.12161.

Ivill, M., Peartonm, S.J., Rawal, S., Leu, L., Sadik, P., Das, R., Hebard, A.F., Chisholm, M., Budai, J.D., Norton, D.P., 2008. Structure and magnetism of cobalt-doped ZnO thin films. New Journal of Physics 10, p.065002.

Jahangiri, H., Bennett, J., Mahjoubi, P., Wilson, K., Gua, S., 2014. A review of advanced catalyst development for Fischer-Tropsch synthesis of hydrocarbons from biomass derived syngas. Catalysis Science & Technology 4, p. 2210.

Jaramillo, T.F., Baeck, S.H., Shwarsctein, A.K., Choi, K.S., Stucky, G.D., McFarl, E.W., 2005. Automated electrochemical synthesis and photoelectrochemical characterization of $Zn_{1-x}Co_xO$ thin films for solar hydrogen production. ACS Combinational Science 7, p. 264.

Juang, Y., Chu, S.Y., Weng, H.C., Tyan, S.L., 2007. Phase transition of Co-doped ZnO, Solid State Communications 143, p.558.

Leshkov, Y.R., Barrett, C.J., Liu, Z.Y., Dumesic, J.A., 2007. Production of dimethylfuran for liquid fuels from biomass-derived carbohydrates, Nature 447, p. 982.

Karaca, H., Safonova, O.V., Chambrey, S., Fongarland, P., Roussel, P., Constant, A.G., Lacroix, M., Khodakov, A.Y., 2011. Structure and catalytic performance of Pt-promoted alumina supported cobalt catalysts under realistic conditions of Fischer-Tropsch synthesis. Journal of Catalysis 277, p.14.

Kim, J.H., Kim, H., Kim, D., Ihm, Y.E., Choo, W.K., 2004. The origin of room temperature ferromagnetism in cobalt-doped zinc oxide thin films fabricated by PLD. Journal of the European Ceramic Society 24, p.1847.

Martono, E., Hyman, M.P., Vohs, J.M., 2011. Reaction pathways for ethanol on model Co/ZnO (0001) catalysts. Physical Chemistry Chemical Physics 13, p. 9880.

Mathis, J.E., Christen, H.M., 2007. Factors that influence particle formation during pulsed electron deposition of YBCO precursors. Physica C: Superconductivity 459, p.47.

Pan, Z., Bukur, D.B., 2011. Fischer Tropsch synthesis on Co/ZnO catalyst-Effect of pretreatment procedure. Applied Catalysis A: General 404, p. 74.

Park, J.H., Kim, M.G., Jang, H.M., Ryu, S., 2004. Co-metal clustering as the origin of ferromagnetism in Co-doped ZnO thin films. AIP Applied Physics Letters 84, p.1338.

Park, S., Kim, S.H., Kim, T.G., 2012. Effect of Si and SiO_2 Substrates on the Geometries of As-Grown Carbon Coils. Journal of Nanomaterials 2012, p.1.

Pattini, F., Annoni, F., Bissoli, F., Bronzoni, M., Garcia, J.P., Gilioli, E., Rampino, S., 2015. Comparative study about Al-doped zinc oxide thin films deposited by pulsed electron deposition and radio frequency magnetron sputtering as transparent conductive oxide for $Cu(In,Ga)Se_2$-based solar cells. Thin Solid Films 582, p.317.

Peng, Y.Z., Liew, T., Song, W.D., An, C.W., Teo, K.L., Chong, T.C., 2005. Structural and optical properties of Co-doped ZnO thin films. Journal of Superconductivity 18, p.97.

Poongodi, G., Anandan, P., Kuma, R.M., Jayavel, R., 2015. Studies on visible light photocatalytic and antibacterial activities of nanostructured cobalt doped ZnO thin films prepared by sol-gel spin coating method. Spectrochimica Acta Part A: Molecular and Biomolecular Spectroscopy 148, p. 237.

Savost'yanov, A.P., Yakovenko, R.E., Sulima, S.I., Bakun, V.G., Narochnyi, G.B., Chernyshev, V.M., Mitchenko, S.A., 2017. The impact of Al2O3 promoter on an efficiency of C_{5+} hydrocarbons formation over Co/SiO_2 catalysts via Fischer-Tropsch synthesis. Catalysis Today 279, p.107.

Taabouche, A., Bouabellou, A., Kermiche, F., Hanini, F., Menakh, S., Bouachiba, Y., Kerdja, T., Benazzouz, C., Bouafia, M., Amara, S., 2013. Effect of substrates on the properties of ZnO thin films grown by pulsed laser deposition. Advances in Materials Physics and Chemistry 3, p.209.

Tortosa, M., Mollar, M., Manjón, F.J., Marí, B., Sánchez-Royo, J.F., 2008. Cathodic electrodeposition of ZnCoO thin films. Solid State Physics 5, p.3358.

Tsakoumis, N.E., Rønninga, M., Borg, Ø., Rytter, E., Holmen, A., 2010. Deactivation of cobalt based Fischer–Tropsch catalysts: A review. Catalysis Today 154, p.162.

Vadiyar, M.M., Kolekar, S.S., Chang,J.-Y., Kashalec, A.A., Ghulec, A.V., 2016. Reflux condensation mediated deposition of Co_3O_4 nanosheets and $ZnFe_2O_4$ nanoflakes electrodes for flexible asymmetric supercapacitor. Electrochimica Acta 222, p.1604.

Viart,N., Richard-Plouet, M., Muller, D., Pourroy, G., 2003. Synthesis and characterization of Co/ZnO nanocomposites: towards new perspectives offered by metal/piezoelectric composite materials. Thin Solid Films 437, p.1.

White, R.J., Luque, R., Budarin, V.L., Clark, J.H., D.J. Macquarrie, D.J., 2009. Supported metal nanoparticles on porous materials. Methods and applicationsChemical Society Reviews 38, p. 481.

Xu, X., Li,Y., Gong, Y., Zhang, P., Li, H., Wang, Y., 2012. Synthesis of Palladium nanoparticles supported on mesoporous N‐doped carbon and their catalytic ability for biofuel upgrade. Journal of the American Chemical Society 134, p. 16987.

Su, X., Wang, L., Chen, J., Wan, X., Zhang, X., Wang, R.P., 2011. Role of cobalt in ZnO:Co thin films. Journal of Physics D: Applied Physics 44, p. 265002.

Zhou, Z., Zhang, Y., Wang, Z., Wei, W., Tang, W., Shi, J., Xiong, R., 2008. Electronic structure studies of the spinel CoFe2O4 by X-ray photoelectron spectroscopy. Applied Surface Science 254, p.6972.

Science and Applications of Thin Films, Conference & Exhibition (SATF 2018)
Izmir Institute of Technology, Izmir, Turkey, September 17-21, 2018

Thin silver film synthesis on polymeric composite surfaces via electroless deposition technique

İpek Yoldaş[a], Berrin İkizler[b, *], Seçkin Erden[c]

[a] *Division of Material Science and Engineering, Grad Sch Nat & App Sci, Ege University, Izmir, Turkey*
[b] *Department of Chemical Engineering, Ege University, Izmir, Turkey*
[c] *Department of Mechanical Engineering, Ege University, Izmir, Turkey*

*Corresponding author. Tel.: +90-232-311-1489; fax: +90-232-388-7776.
E-mail address: berrin.ikizler@ege.edu.tr

Abstract

Highly reflective polymeric surfaces for use in solar collector systems were developed using silver films with electroless deposition method. Vinyl-ester matrix composites reinforced with glass fibers were produced and then used as polymeric substrates. As a first step, catalytically active sites on the polymer surface were generated either by acidic ($SnCl_2$/HCl) or basic (NaOH) treatments for the subsequent deposition process. Effects of treatment procedure and treatment time were investigated in detail to enhance the adhesion and surface coverage of the resultant silver coatings. Surface atomic composition and roughness profiles of the surfaces were analyzed by X-ray photoelectron spectroscopy (XPS) and atomic force microscopy (AFM), respectively. Tollens' process was then applied to deposit silver layers on the surfaces. Scanning electron microscopy (SEM) and x-ray diffraction (XRD) were employed to characterize the resultant films. XRD results proved the growth of silver film on the surface and no impurities were present in the film. Small-sized (~30 nm), and evenly distributed silver crystals with a film thickness of ~100 nm were observed over the surface in SEM images. UV/Vis spectrometer analysis confirmed the high reflectivity of the silver deposited polymeric surfaces (96-97% at 550 nm), indicating their potential applicability in solar collectors.

Keywords: Polymeric composites; Silver thin films; Electroless deposition; Reflective surfaces.

Introduction

Formation of metallic films on polymeric surfaces has attracted great attention recently, since the final product exhibits various optical, electrical, or magnetic properties (Cui et al., 2013). Polymeric substrates have many advantages such as lightweight, flexibility and shock resistance, when compared to inorganic substrates like glass (Southward and Thompson, 2001). Surface-metallized polymeric surfaces have many potential applications including bactericidal coatings, contacts in microelectronics, highly reflective thin film reflectors and concentrators (especially in space environments), lightweight optical mirrors and solar dynamic power generation (Chen et al., 2016). Silver coated polymeric surfaces have been an active area of interest for these application areas, since silver has high electrical conductivity and excellent reflectivity, besides its modest cost (Zaier et al., 2017). Among the various methods developed to deposit silver film on polymeric substrates, electroless plating technique provides a low-cost, solution-based method at atmospheric conditions, and is a promising option for large-scale production (Lili et al., 2011).

Despite plastics' broadening usage, potential for lightweight and at the same time strong materials is increasing for outdoor applications such as solar thermal system reflectors. Here comes into mind the fiber

reinforced polymers/plastics (FRPs), which also resist chemical and corrosive environments thanks to their polymer matrices, which bind together the reinforcing fibers (Masuelli et al., 2013). Polyester, epoxy, polyamide, polypropylene, polyethylene are the most known matrices with polyester being the cheapest and the earliest one in the industry. Vinyl esters, being similar chemically to unsaturated polyesters and epoxies, are somewhere between the two. They combine the crosslinking capability of polyesters with the mechanical and thermal properties of epoxies (Ku and Siores, 2004). Among the reinforcements such as carbon, aramid, boron, etc, glass is the most widespread and historical technical fiber used in polymeric composite production (Sathishkumar et al., 2014).

In light of the literature, an attempt was made in this work to find a functional application area for polymeric composites, which is the development of highly reflective polymeric surfaces for use in solar collector systems by coating silver films via electroless deposition method. Glass fabric reinforcement was preferred due its widespread usage, high strength, and low cost. For the polymer matrix, vinyl ester was used as it is between polyester and epoxy in terms of cost, and close to epoxy when it comes to strength. Besides, it is more durable under atmosphere, seawater, etc conditions (Visco et al., 2011). Therefore, glass/vinyl ester composites were produced and used as polymeric substrates in mirror production. As a first step, catalytically active sites on the polymer surface were generated either by acidic ($SnCl_2$/HCl) or basic (NaOH) treatments for the subsequent deposition process. Effects of treatment procedure and treatment time were investigated in detail to enhance the adhesion and surface coverage of the resultant silver coatings. Surface atomic composition, roughness profiles and hydrophilicity change of the surfaces before and after treatment were analyzed by X-ray photoelectron spectroscopy (XPS), atomic force microscopy and contact angle measurements, respectively. Tollens' process was then applied to deposit silver layers on the surfaces having different pretreatments. Electron microscopy (SEM), XRD and XPS methods were employed to characterize the resultant films. XRD results proved the growth of silver film on the surface and no impurities were present in the film. Small-sized (~30 nm), and evenly distributed silver crystals with a film thickness of ~100 nm were observed over the surface in SEM images. UV/Vis spectrometer analysis confirmed the high reflectivity of the silver deposited polymeric surfaces (96-97% at 550 nm), indicating their potential applicability in solar collectors.

Experimental

Production of polymeric composite substrates

Vinyl-ester matrix composites reinforced with glass fibers were used as polymeric substrates and produced using vacuum infusion technique. E-glass fabric (300 g/m^2) and vinyl ester resin was used in the synthesis. Resin amount was 1:1 weight of the fibers (10 plies of 30x30 cm fabric weighed 270 g). 2.5 ml accelerator (Cobalt octoat, %1) and 5 ml hardener (MKP-60, metil etil keton peroksit) was mixed in the resin. Open mould was vacuum sealed and release agent was applied on the mould surface. Fabric plies, peel ply, distribution medium, and vacuum bag were placed on the mould. After assembling the resin inlet and outlet connections, the resin was drawn via a tube wetting all the sections uniformly. Then the entire fabric was cured at room temperature for 2 days. Produced composite laminates were cut into 26x76 mm substrates for the experiments.

Pretreatments applied to the substrates

Pretreatments include three steps: (1) Cleaning, (2) Modification, and (3) Activation.

(I) Cleaning Step: The substrates were cleaned in dilute detergent solution and isopropyl alcohol, respectively to remove surface impurities (K1). Substrates were rinsed with distilled water thoroughly after each step. The effect of using ultrasonic bath (K2) at each step was also investigated to improve cleaning.

(II) Modification Step: Catalytically active sites on the polymer surface were generated either by sensitization treatment ($SnCl_2$) or etching treatment (NaOH) for the subsequent deposition process. Sensitization of the surfaces was conducted by immersing substrates into 0.05 M $SnCl_2$ in HCl (37%) solution for 30 min. After that, the substrates were washed with distilled water and then dried at 60°C. In the same manner, etching treatment was carried out in 3 M NaOH solution. Effects of treatment types were investigated in detail to be able to obtain smooth and continuous silver films on the surfaces.

(III) Activation Step: The substrates were soaked in $[Ag(NH_3)_2]^+$ basic solution for 30 min to activate the surface and to reach adsorption equilibrium between Ag^+ ions and the substrates. $[Ag(NH_3)_2]^+$ solution (Tollens' solution) is prepared as: NaOH solution was added to 0.1 M $AgNO_3$ solution to form brown Ag_2O precipitates. Then ammonia (NH_3, %28-30) was added dropwise to this solution until all precipitates dissolved, showing the formation of transparent $[Ag(NH_3)_2]^+$ solution.

Formation of silver films on the substrates

Tollens' process was applied to deposit silver layers on the surfaces having different pretreatments. The method is based on the adsorption of $[Ag(NH_3)_2]^+$ complex ions onto the substrate surface and then their reduction to elemental silver, Ag^0, with the addition of an reductant. Glucose ($C_6H_{12}O_6$) was chosen as the reductant of this process. The molar ratios of the components were kept constant as [Glucose]/[Ag^+]=2 and [OH^-]/[Ag^+]=4 in the coating bath. Silver metal deposition onto the surfaces was started by the addition of glucose solution into $[Ag(NH_3)_2]^+$ solution (Eq. 1). Substrates were taken out from the bath after 480 s and then washed with distilled water.

$$\left[Ag\left(NH_3\right)_2\right]^+{}_{(aq)} + 2RCOH_{(aq)} \rightarrow Ag_{(s)} + 2RCOO^-{}_{(aq)} + 4NH_4{}^+{}_{(aq)} \qquad (1)$$

Characterization

The elemental composition of the surfaces before and after pretreatments was identified on an X-ray photoelectron spectrometer (XPS, Thermo Scientific K-Alpha) using monochromatic Al Kα radiation (1486.6 eV) and Fourier transform infrared spectroscopy (Perkin Elmer ATR-FTIR) in the wavelength range of 4000-600 cm^{-1}. In addition, surface roughness profiles of the surfaces were analyzed by atomic force microscopy (AFM, Nanosurf Flex Axiom) in the tapping mode, scanning an area of 5 μm × 5 μm. The morphology of the silver films were observed by field emission scanning electron microscopy (SEM, FEI, QUANTA-FEG 250). The crystal structure of the films were determined by X-ray diffraction (XRD, Phillips X'Pert Pro), under CuKa radiation for a 2θ range from 5° to 95°. The reflectance spectras were recorded using a UV/Visible spectrophotometer (Shimadzu, UV-2600-ISR) in the wavelength range of 300-1100 nm. 550 nm, corresponding to wavelength of sunray at maximum radiation, was selected to compare the different results. Reflectance measurements are done at different regions on the same surface to observe the homogeneity of the silver coating.

Results and Discussion

FTIR analyses

Glass/vinyl ester composite FTIR spectra shown in Fig. 1 revealed peaks (1719 and 1180 cm^{-1}) of carbonyl group belonging to the ester in the structure. Ethers, alcohol-end groups, and acryloyl double bonds were observed in the spectra. The peaks present at 2921 cm^{-1} shows the presence of hydroxyl group. Aliphatic hydrocarbon skeleton and the presence of aromatic rings were all found to be typical of vinyl ester polymer. The findings confirmed the epoxy vinyl ester network based on the diglycidyl ether of bisphenol-A.

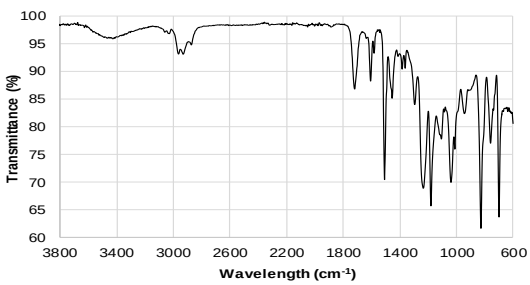

Fig. 1. FTIR spectra of the composite substrate

3.2 XPS analyses

Vinyl ester composite surfaces were found to be composed of carbon and oxygen, approximately 80% and 20%, respectively, which is in agreement with Jiao et al., 2018 and Andrew W. Signor et al., 2003. Surface atomic composition of the substrates is given in Tables 1 and 2 in means of atomic percentages.

Table 1. Wide scan XPS results

Substrate	C1s	O1s	Sn3d	Na1s	O/C
Untreated	79.24	19.41	-	-	0.245
$SnCl_2$	66.47	26.24	6.11	-	0.395
NaOH	83.11	16.83	-	0.05	0.203

For $SnCl_2$ pretreatment, decrease in the C-O and O=C amounts were observed from C1s Scan B and O1s Scan A spectra, respectively (Table 2). O1s Scan B and C values correspond to Sn-O bonds.

Table 2. High resolution XPS spectra results

Substrate	C1s Scan A	C1s Scan B	C1s Scan C	C1s Scan D	O1s Scan A	O1s Scan B	O1s Scan C	Sn3d Scan A	Sn3d Scan B
Untreated	7.17	2.8	0.22	0.16	2.35	-	-	-	-
$SnCl_2$	6.13	1.73	0.28	-	1.49	0.98	0.57	0.45	0.31
NaOH	9.43	2.59	0.10	0.25	2.31	-	-	-	-

For NaOH pretreatment, decrease in the carbonyl content and increase in the carboxylic acid content (O=C-O) was observed from C1s Scan C and C1s Scan D spectra, respectively (Table 2).

3.3 AFM analyses

Surface roughness profiles were analyzed and tabulated as can be seen in Table 3. It was found that the values did not change significantly after $SnCl_2$ pretreatment. On the other hand, NaOH pretreatment seemed to create nano cavities on the substrate surfaces. These findings correlate with SEM analyses, which can be seen in the related section below.

Table 3. Surface roughness values

Substrate	S_a [nm]	RMS [nm]
Untreated	7.57	9.74
$SnCl_2$	8.58	10.94
NaOH	10.70	13.45

3.4 SEM analyses

SEM images confirm the surface roughness values obtained by AFM analyses (Fig. 2). Almost no change in substrate surface was observed after $SnCl_2$ pretreatment while NaOH treatment created flowerlike patterns on the substrates.

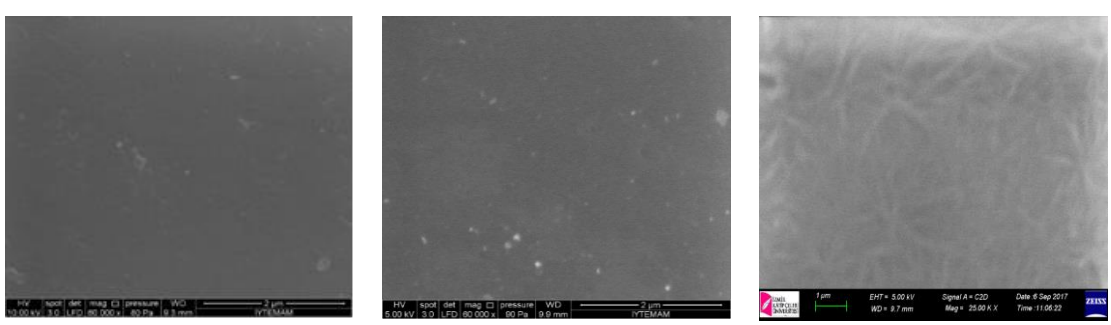

(a) (b) (c)

Fig. 2. SEM images of the substrates for the case of (a) Untreated; (b) $SnCl_2$ treated; (c) NaOH treated

3.5 Effect of the cleaning procedure on the resultant silver film

As can be seen obviously in Fig. 3, regardless of the pretreatment type, ultrasonically cleaned (K2) substrates resulted in silver thin films having higher reflectivity when compared to that of the substrates with no-ultrasonic cleaning step (K1). Therefore, ultrasonic cleaning was preferred throughout the rest of study.

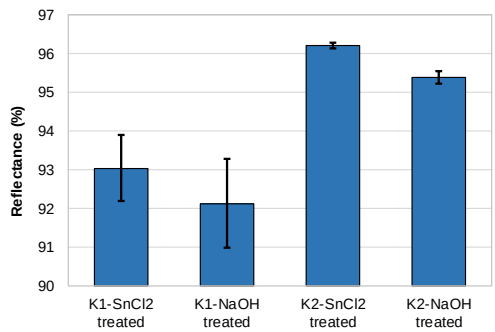

Fig. 3. Reflectance values regarding the cleaning procedure

3.6 Effect of the surface treatment procedure on the resultant silver film

Reflectivity values of silver thin films deposited on substrates having different pretreatments are shown in Fig. 4. The photographs of the silver coatings are also taken and given in Fig. 5(b-c) with the uncoated substrates (Fig. 5(a)). For $SnCl_2$ pretreated substrates, silver mirror reflectance values were measured as 96.2% and 95.5%, for front and back sides, respectively. NaOH pretreated composite substrates ended up with less reflectivity, that is 95.4% and 92.7% respectively for front and back sides. The difference between front and back sides were minimized for $SnCl_2$ case. Reflectance of the back sides of the substrates was less than their front sides. This difference must be due to the production technique. The back sides of the substrates seem to be more rough when compared to front sides. When the surfaces are treated with Sn ions, a redox reaction occurs on the surface involving the oxidation of surface Sn^{2+} to Sn^{4+} and reduction of Ag^{+} to Ag^{0}, with the addition of $Ag[NH_3]_2^{+}$ solution. This results to the formation of tiny silver seeds on the surface. Hence, small-sized and homogeneously distributed silver nanoparticles were obtained with $SnCl_2$ treatment with the deposition duration, as given in Fig. 5(d). The size of the particles is relatively larger in NaOH treated surfaces, as given in Fig. 5(e). Low reflectivity and larger error margins for NaOH pretreated mirrors confirm this finding.

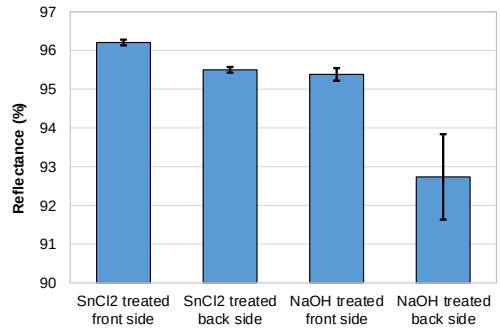

Fig. 4. Reflectivity of silver coated composite substrates

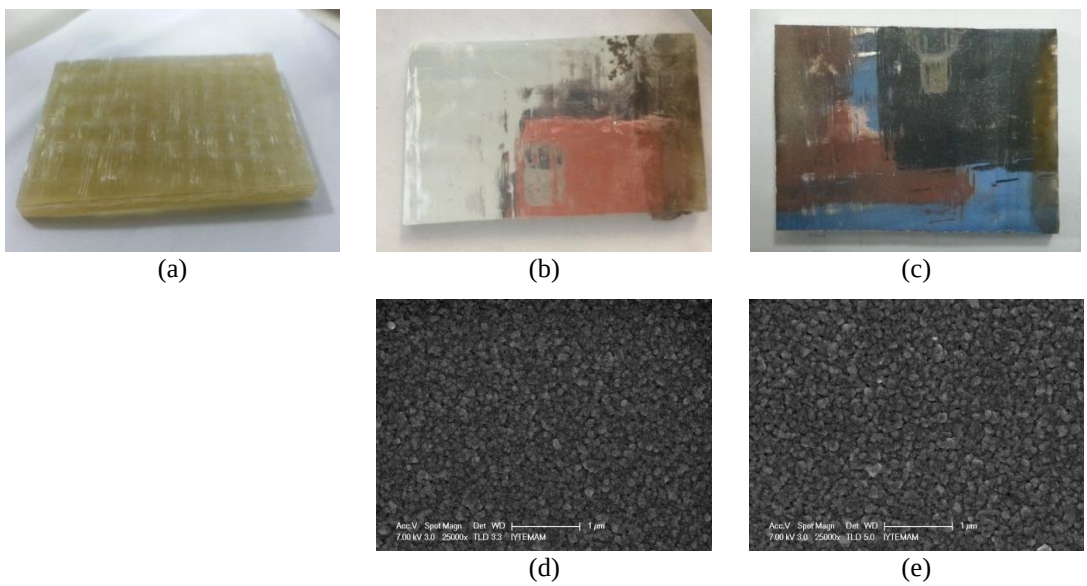

Fig. 5. Photographs and SEM images of the substrates after silver coating for the case of (a) no coating; (b,d) treated with $SnCl_2$; (c,e) treated with NaOH

Fig. 6 shows the XRD pattern of the silver film. The four peaks seen correspond to the plains of silver crystal matched with the JCPDS card no 65-2871 standard, which show the cubic structure of the metallic silver on polymeric surface. No characteristic peaks are observed for the impurities such as Ag_2O. The crystallinity of the silver particles is higher in SnC_2 treated substrates

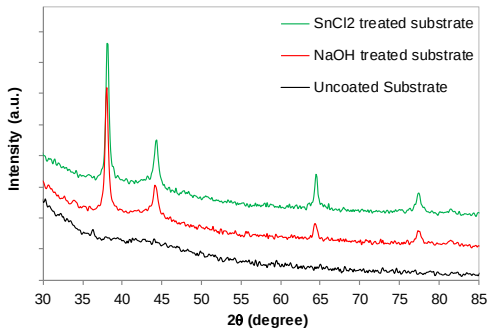

Fig. 6. XRD patterns of the composite substrate

4 Conclusion

Glass fiber reinforced vinyl ester matrix polymeric composite substrates were produced using vacuum infusion technique. Acidic ($SnCl_2$/HCl) and basic (NaOH) pretreatments were applied on the surfaces. Tollens' process was then applied to deposit silver layers on the substrates and mirrors were produced successfully. XRD results proved the growth of silver film on the surface and no impurities were present in the film. Small-sized (~30 nm), and evenly distributed silver crystals with a film thickness of ~100 nm were observed over the surface in SEM images. UV/Vis spectrometer analysis confirmed the high reflectivity of the silver deposited polymeric surfaces at 550 nm, indicating their potential applicability in solar collectors. Higher reflectivity was achieved for acidic surface pretreatment (96.2%) when compared to that of the basic pretreatment (95.4%). Besides, the difference between front and back sides were minimized for $SnCl_2$ case. Moreover, silver nanoparticle size was smaller and distribution was more even for acidic pretreatment.

Acknowledgements

This work was supported by the Scientific and Technological Research Council of Turkey (TUBITAK) through technological research project 113M936.

References

Chen, D., Y. Zhang, Y., Bessho, T., Kudo, T., Sang, J., Hirahara, H., Mori, K., Kang, Z., 2016. Ag films with enhanced adhesion fabricated by solution process for solar reflector applications, Solar Energy Materials & Solar Cells 151, p. 154.

Cui, G., Wu, D., Zhao, Y., Liu, W., Wu, Z., 2013. Formation of conductive and reflective silver nanolayers on plastic films via ion doping and solid–liquid interfacial reduction at ambient temperature, Acta Materialia 61, p. 4080.

Jiao, W., Liu, W., Yang, F., Jiang, L., Jiao, W., Wang, R., 2018. Improving the interfacial strength of carbon fiber/vinyl ester resin composite by self-migration of acrylamide: A molecular dynamics simulation, Applied Surface Science 454, p. 74.

Ku, H. S. and Siores, E., 2004. Shrinkage reduction of thermoset matrix particle reinforced composites during curing using microwaves irradiation. Transactions, Hong Kong Institution of Engineers 11 (3), p. 29.

Lili, L., Dan, Y., Le, W., Wei, W., 2012. Electroless silver plating on the PET fabrics modified with 3-mercaptopropyltriethoxysilane, J. Appl. Polym. Sci. 124, p. 1912.

Masuelli, M. A., 2013. Introduction of Fibre-Reinforced Polymers − Polymers and Composites: Concepts, Properties and Processes, IntechOpen, DOI: 10.5772/54629.

Sathishkumar, T. P., Satheeshkumar, S., Naveen, J., 2014. Glass fiber-reinforced polymer composites – a review, Journal of Reinforced Plastics and Composites 33-13, p. 1258.

Signor, A. W., VanLandingham, M. R., Chin, J. W., 2003. Effects of ultraviolet radiation exposure on vinyl ester resins: characterization of chemical, physical and mechanical damage, Polymer Degradation and Stability 79-2, p. 359.

Southward, R. E., Thompson, D. W., 2001. Reflective and conductive silvered polyimide films for spaceapplications prepared via a novel single-stageself-metallization technique, Materials and Design 22, p. 565.

Visco, A. M., Brancato, V., Campo, N., 2011. Degradation effects in polyester and vinyl ester resins induced by accelerated aging in seawater, Journal of Composite Materials 46 (17), p. 2025.

Zaier, M., Vidal, L., Hajjar-Garreau, S., Balan, L., 2017. Generating highly refective and conductive metal layers through a light-assisted synthesis and assembling of silver nanoparticles in a polymer matrix, Scientific Reports 7, DOI:10.1038/s41598-017-12617-8.

This page intentionally left blank.

Science and Applications of Thin Films, Conference & Exhibition (SATF 2018)
Izmir Institute of Technology, Izmir, Turkey, September 17-21, 2018

Investigation of mechanical and tribological properties of BCN thin films

Gökhan Gülten[a], İhsan Efeoglu[a,*], Yaşar Totik[a], Ayşenur Keles[a], Kıvılcım Ersoy[b], Göksel Durkaya[c]

[a] *Department of Mechanical Engineering, Ataturk University, Yakutiye, 25240, Erzurum, Turkey*
[b] *FNSS Defence Industry, Gölbaşı, 06830, Ankara, Turkey*
[c] *Department of Metallurgical and Materials Engineering, Atılım University, Gölbaşı, 06830, Ankara, Turkey*

*Corresponding author. Tel.: +90-442-231-4850; fax: +90-442-231-4910.
E-mail address: iefeoglu@atauni.edu.tr

Abstract

BCN thin films are one of the most attractive materials in recent years based on their high hardness values, and excellent tribological properties. Having such characteristics, BCN films are becoming crucial for industrial and scientific applications as protective coatings. BCN films are also being used as lubricating coatings for high temperature applications due to good thermal and chemical stabilities.To synthesize BCN films several different deposition techniques have been carried out successfully such as chemical vapor deposition, rf-magnetron sputtering, reactive magnetron sputtering, dc-magnetron sputtering, closed-field unbalanced magnetron sputtering (CFUMBS) and high-power impulse magnetron sputtering (HiPIMS).In this work, BCN films were deposited on 4140 steel substrates by a superimposed closed-field unbalanced and high-power impulse magnetron sputtering system using different deposition parameters. We studied the structural, mechanical and tribological properties of BCN films. To characterize the structural properties of the BCN films SEM techniques were used. Micro-hardness and scratch tester were used to determine mechanical properties of the BCN thin films. Tribological properties such as friction coefficient of the films were calculated by pin-on-disc tribometer in ambient air. The maximum hardness and friction coefficient has obtained as 17.6 GPa and 0.54, respectively. The results showed that the hardness values affected the friction coefficient negatively due to the hard abrasive particles.

Keywords: CFUMBS;HiPIMS;BCN;Friction;Critical load

Introduction

BCN is an attractive coating material that has been worked on intensively in recent years because of its superior mechanical and tribological properties. Compared to other hard coatings (diamond, DLC, CNx, B_4C and c-BN), BCN films are non-reactive with ferrous materials unlike diamond [1] and exhibit better thermal and chemical stability than DLC and CNx at high temperature [2,3]. Also, it exhibits better adhesion properties because it has lower internal stresses compared to c-BN and B_4C [4,5]. Having such characteristics, BCN films are widely used as hard, protective and lubricative coatings in industrial and scientific applications.In literature, several different deposition techniques have been carried out successfully to synthesize BCN films such as chemical vapor deposition [6], rf-magnetron sputtering [7], reactive magnetron

sputtering [8], dc-magnetron sputtering [9], closed-field unbalanced magnetron sputtering (CFUMBS) [10] and high-power impulse magnetron sputtering (HiPIMS) [11]. Among these deposition techniques, HiPIMS is the newest and most promising technology. Most importantly, HiPIMS can be used with any type of magnetron sputtering system as a power supply [12]. There is no study that examines the adhesion properties of coatings obtained with HiPIMS in literature.

In this work, BCN films were deposited on 4140 steel substrates by a superimposed closed-field unbalanced and high-power impulse magnetron sputtering system with different deposition parameters. We studied the structural, mechanical and tribological properties of BCN films. To characterize the structural properties of the BCN films SEM techniques were used. Micro-hardness and scratch tester were used to determine mechanical properties of the BCN thin films. Tribological properties such as friction coefficient of the films were calculated by pin-on-disc tribometer in ambient air.

Experimental

To deposited BCN thin films were deposited on 4140 steel (42CrMo4), Si (100) and glass substrates by a superimposed CFUMBS and HiPIMS system. The deposition parameters are presented in Table 1. Prior to coating processes, 4140 substrates were polished to roughness values of Ra $\approx$ 0.1 µm. The surface roughness (Ra) determined with a Mitutoyo profilometer. The 4140 substrates were ultrasonically cleaned using ethanol for 15 min and were dried right after mechanical polishing. After that surface of the 4140 substrates were etched in 2% nital solution. BCN thin films were grown by the CFUMBS system produced by Teer Coatings Ltd. This system is shown in Fig. 1.

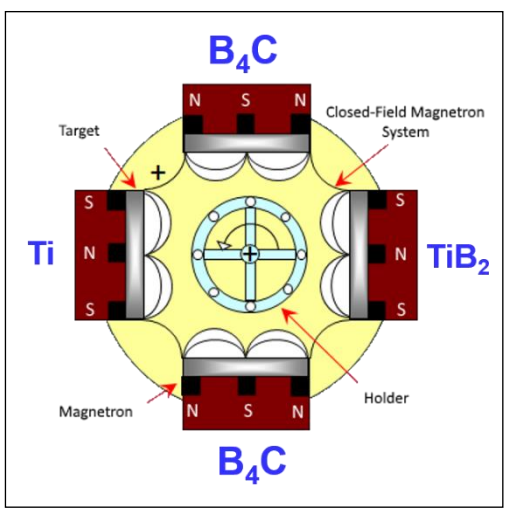

Fig. 1. CFUMBS system for BCN films

BCN films were deposited on 4140 substrate, using two B_4C one Ti and one TiB_2 targets. Ar gas was used in order to generate plasma and sputtering of the targets. The 4140, Si and glass substrates were stabled on a rotating holder. The distance between substrates and targets was fixed to 70 mm. Before deposition, the chamber pressure was set 2.0 x 10^{-5} Pa and then the surface of substrates was sputter-ion cleaned with Ar^+ at a bias voltage of -800 V under 0.26 Pa pressure for 20 min to eliminate possible contaminants and to obtain

better adhesion between the substrate and film. During the interlayers coating process, the HiPIMS voltage applied to B_4C targets is kept constant at 350 Volts. The target current applied to Ti and TiB_2 targets was varied between 0.1 A and 5 A. The amount of N_2 was set as 10 sccm to create nitride phases for TiN and TiBN interlayers. The working pressure was kept stable at 0.33 Pa through the deposition process. Firstly, Ti and TiN interlayers were deposited for 10 and 15 min respectively to increase adhesion between the substrate and film. Next, TiB_2 and TiBN interlayers were deposited for 15 min to reduce internal stress. Lastly, BCN films were deposited for 60 min. The voltage applied to B_4C targets for R1, R2 and R3 films was changed as 850 V, 750 V and 650 V respectively during the BCN film deposition process. The amount of N_2 was kept constant as 10 sccm. The architecture structure of BCN film is given in Fig 2. The deposition parameters of interlayers are presented in Table 1.

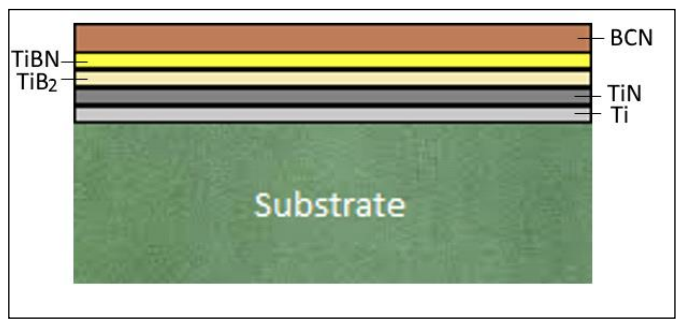

Fig. 2. The architecture structure of BCN films

Table 1. The deposition parameters of BCN films

The variable parameters	R1	R2	R3
B_4C voltage (V)	850	750	650
The constant parameters			
The amount of N_2 (sccm)		4.5	
Duty time (μs)		80	
Frequency (Hz)		500	
Duty cycle (%)		4	
The working pressure (Pa)		0.33	
The time of coated BCN films (min)		60	
Ti interlayer	Ti Target current: 5A	The working pressure: 0.33 Pa	
TiN interlayer	TiB_2 Target current :0.1A	Frequency, duty time:150 kHz, 1.5 μs	
TiB_2 interlayer	Ti Target current : 1A	Interlayer film time: 15 min	
TiBN interlayer	TiB_2 Target current :5A	The rate of Ar/N_2 (sccm/sccm): 25/10	

The structural properties of the BCN films were characterized by FEI Quanta FEG-450 SEM system. Also, the film thickness was determined by FEI Quanta FEG-450 SEM cross-section images taken from the silicon wafers. To determine the hardness values of the BCN films a Buehler Micromet 2001 microhardness tester (using a Knoop indenter under a load of 10gf load for 15s) was used. One of the most important features of the coating is the adhesion. There are several processes to determine the adhesion between substrate and film.

Many of these are based on calculating the force needed to remove the film from the substrate surface such as tensile test, indentation test, and scratch test. In this work, CSM Instruments scratch tester (using a Rockwell-C diamond indenter with a 200 μm radius hemispherical tip under a load varied from 0 to 100 N with a sliding speed of 10 mm/min at the progressive load mode) was used. The tribological properties were calculated by Teer- POD2 pin-on-disc tribometer (with a load of 2 N at 95 rpm and relative humidity of 45% at room temperature).

Results /Discussion

The elemental analysis, film thickness, hardness values and critical load values of BCN films are presented in Table 2. Microstructural analysis of the BCN films deposited on Si substrates was examined on their cross-sectional SEM micrographs. The microstructure and film thickness values of BCN films are shown in Fig.3. According to Fig. 3., microstructure of all films has dense and non-columnar structure due to coatings by HiPIMS [13,14]. The microstructure is referred to the "Zone 3" region of Thornton's Structure Zone Models (SZM) [15]. The thickness values of BCN films obtained from cross-sectional SEM micrographs for R1, R2 and R3 are 721.8 nm, 573.7 nm and 532.8 nm, respectively. With increasing the sputtering voltage, the energy of plasma ions increases, which results in an increase in the deposition rate [16]. Therefore, the highest thickness was obtained in the R1 film, which the highest voltage applied. According to the elemental analysis, R1 has the lowest nitrogen content and with the increasing nitrogen content hardness of the films decreases due to the h-BN phase [17].

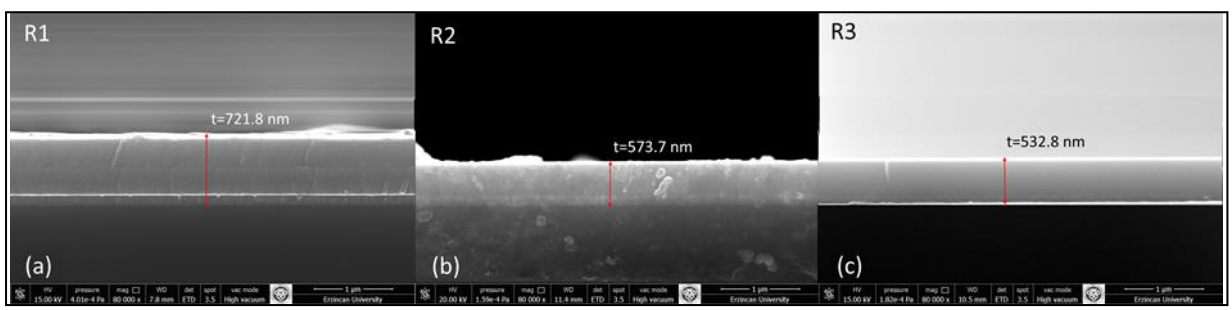

Fig. 3. The SEM images of BCN films for a) R1, b) R2, c) R3

Table 2. The elemental analysis, film thickness, hardness values and critical load values of BCN films

	N K	B K	C K	Ti K	Film Thickness(nm)	Hardness (GPa)	Critical load (N)
R1	27.37	53.73	11.61	7.29	721.8	17.6	55
R2	35.55	47.02	10,03	7.4	573.7	14.2	45
R3	38.46	45.04	9.06	7.44	532.8	8.4	35

In this work, the adhesion properties of BCN films were determined by CSM Instruments scratch tester. The maximum and minimum critical load values are achieved as 55 N and 35 N, respectively. The critical load optical images of scratch scars at 15N, 35N and critical load value are given in Fig. 4. According to results, the critical load value is increased by the increased target voltage value because as the target voltage increases the sputtering rate and the ion bombardment energy of target also increase. Thus, the films can grow more efficiently on the substrate surface [18]. For these reasons, the maximum critical load value is obtained at maximum voltage value (-850V). Furthermore, there is no failure until 15 N. After 20 N, adhesive failures are seen in all films. The volume of adhesive failure is increased by increasing load value.

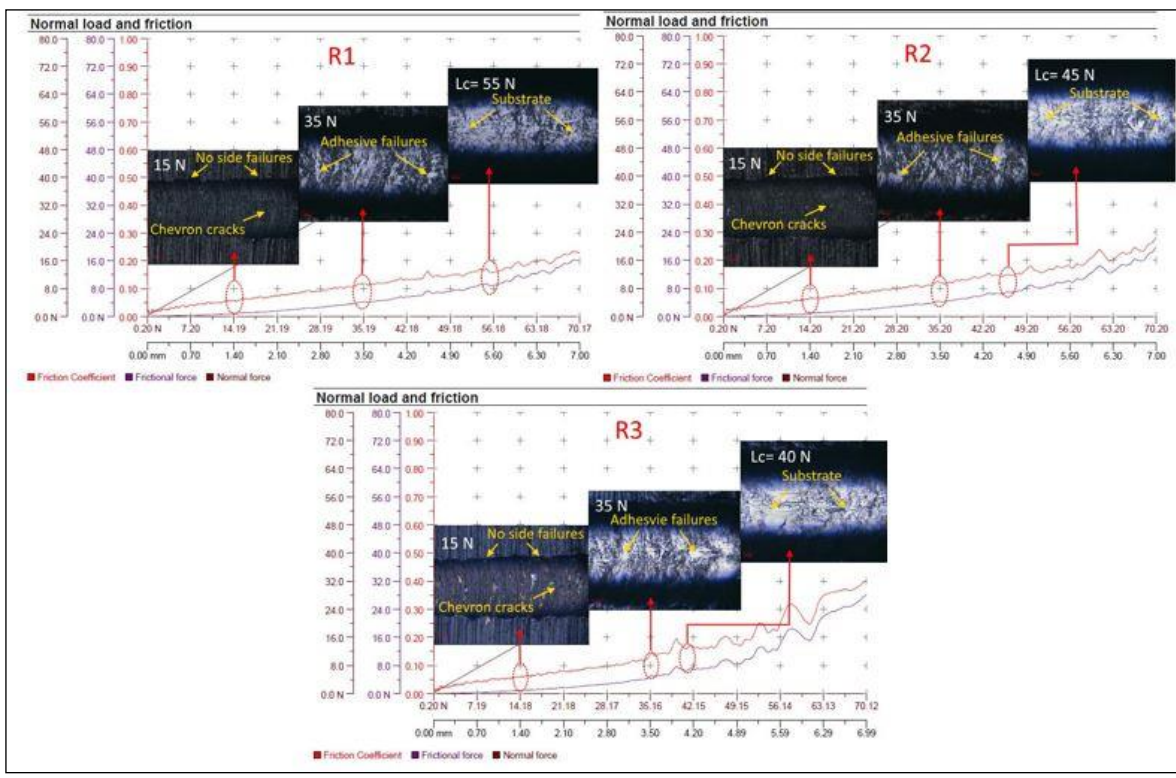

Fig. 4. The critical load values obtained from scratch test for a) R1, b) R2, c) R3

In order to determine the friction coefficient values of BCN films a pin-on-disc tribo-tester was carried out. The friction coefficient to time graphs of BCN films are given in Fig. 5. The friction coefficient values are gained as 0.54, 0.52 and 0.44 for R1, R2 and R3 films, respectively. All films have stable friction coefficient. Still, these friction coefficient values is relatively high compared to literature. This is because, increased hardness value affects the friction coefficient negatively by reason of the hard abrasive particles. Because hard abrasive particles lead to increase contact stress, resulting in increased friction coefficient [19].

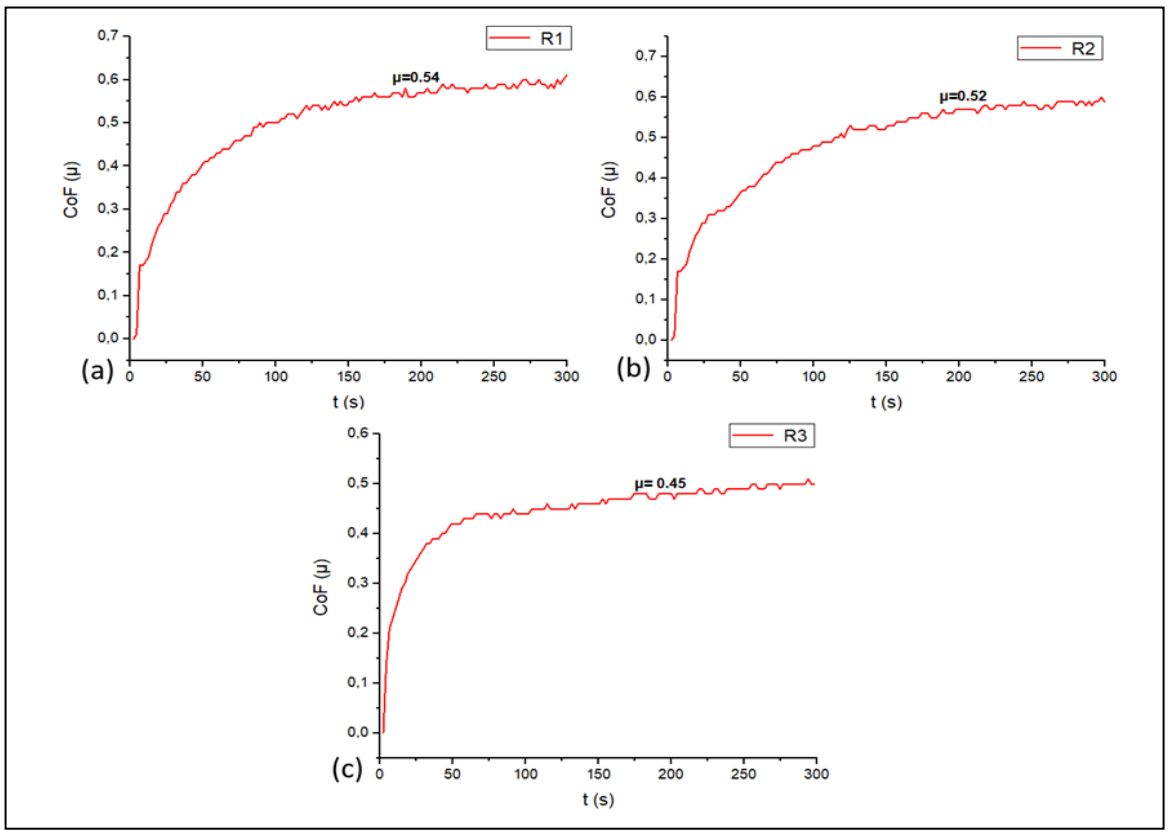

Fig. 5. The friction coefficient to time graph of BCN films for a) R1, b) R2 and, c) R3

Conclusion

In this work, BCN films were successfully deposited by a superimposed CFUMBS and HiPIMS system. Microstructure of all films has dense and non-columnar structure due to coatings by HiPIMS. The maximum hardness value was obtained as 17.6 GPa from R1 film. As a result of the scratch tests, the highest critical load value is obtained as 55 N due to the highest HiPIMS voltage value. The critical load value is increased by the increased target voltage value. Therefore, the highest critical load value was obtained in R1 film applied highest voltage to B_4C targets. All films have stable friction coefficient. The minimum friction coefficient value was obtained as 0.44 due to the hard abrasive particles.

Acknowledgements

This research is part of the TUBITAK (The Scientific and Technical Research Council of Turkey) project was supported by Grand no: MAG-215M213-215M217-215M218. The authors would like to thank to TUBITAK for funding the project.

References

Will, G., Perkins, P.G., 2001. "Is There a New Form of Boron Nitride with Extreme Hardness?", Diamond and Related Materials 10, p. 2010-2017.

Gago, R., Jimenez, I., Garcia, I., Albella, J.M., 2002. "Growth and Characterization of Boron-Carbon-Nitrogen Coatings Obtaned by Ion Beam Assisted Evaporation", Vacuum 64, p. 199-204.

Park, Y.S., Boo, J.H., Hong, B., 2012. "The Effect of Annealing Temperature on Characteristics of UBMS Sputtered CNx Films for Protective Coatings", Materials Research Bulletin 47, p. 2776-2779.

Ulrich, S., Ehrhardt, H., Schwan, J., Samlenski, R., Brenn, R., 1998. "Supplantation Effect in Magnetron Sputtered Superhard Boron Carbide Thin Films", Diamond Related Materials 7, p. 835-838.

Ulrich, S., Theel, T., Schwan, J., Ehrhardt, H., 1997. "Magnetron-sputtered Superhard Materials", Surface Coating Technology 97, p. 45-49.

Mannan, A., Masamitsu, N., Tetsuya, K., Norie, H., Yuji, B., 2009. "Characterization of BCN Films Synthesized by Radiofrequency Plasma Enhanced Chemical Vapor Deposition", Journal of Physics and Chemistry of Solids 70, p. 20-25.

Lihua, L., Yuxin, W., Kecheng F., Yingai, L., Weiqing, L., Chunhong, Z., Yongnian, Z., 2006. "Preparation of Boron Carbon Nitride Thin Films by Radio Frequency Magnetron Sputtering", Applied Surface Science 252, p. 4185-4189.

Martinez, C., Kyrsta, S., Cremer, K., Neuschütz, D., 2002. "Influence of The Composition of BCN Films Deposited by Reactive Magnetron Sputtering on Their Properties ", Anal Bional Chemistry 374, p. 709-711.

Tavsanoglu, T., Jeandin, M., Addemir, O., 2016. "Synthesis and Characterisation of Thin Films in the BCN Triangle ", Surface Engineering 32:10, p. 755-760.

Qiang, M., Fei, Z., Qianzhi, W., Zhiwei, W., Kangmin, C., Zhifeng, Z., Lawrence Kwok-Yan, L., 2016. "Influence of CrB2 Target Current on The Microstucture, Mechanical and Tribological Properties of Cr-B-C-N Coatings in water", RSC Advances 6, p. 47698

Hirte, T., Feuerfeil, R., Perez-Solorzano, V., Wagner, T.A., Scherge, M., 2015. "Influence of Composition on the Wear Properties of boron carbonitride (BCN) Coatings deposited by High Power Impulse Magnetron Sputtering", Surface and Coating Technology 284, p. 94-100

Kubart, T., Aijaz, A., 2017. "Evolution of Sputtering Target Surface Composition in Reactive High Power Impulse Magnetron Sputtering", Journal of Applied Physics 121, p. 171903

Samuelsson, M., Lundin, D., Jensen, J., Raadu, M.A., Gudmundsson, J.T., Helmersson, U., 2010. "On the Film Density Using High Power Impulse Magnetron Sputtering", Surface and Coatings Technology 205, p. 591-596

Samuelsson, M., Lundin, D., Jensen, J., Raadu, M.A., Gudmundsson, J.T., Helmersson, U., 2010. "On the Film Density Using High Power Impulse Magnetron Sputtering", Surface and Coatings Technology 205, p. 591-596

Ehiasarian, A.P., 2010, "High-Power Impulse Magnetron Sputtering and Its Applications", Pure and Applied Chemistry 82, p. 1247-1258.

Anders, A., 2010. "A Structure Zone Diagram Including Plasma-based Deposition and Ion Etching", Thin Solid Films 518, p. 4087-4090.

Mohammadtaheri, M., Qiaoqin, Y., Yuanshi, L., Corona-Gomez, J., 2018. "The Effect Of Deposition Parameters On The Structure And Mechanical Properties Of Chromium Oxide Coatings Deposited By Reactve Magnetron Sputtering", Coatings 8, p. 111.

Cicek, H., Baran, O., Demirci, E.E., Tahmasebian, M., Totik, Y., Efeoglu, I., 2014 " The Effect of Nitrogen Flow Rate on TiBN Coatings Deposited on Cold Work Tool Steel", Journal of Adhesion Science and Technology 28, p. 1140-1148.

Kai, B., Jun, L., Qixun, D., 2011, " Effect of Target Power and Bias on Adhesive Force of BCN Films", Advanced Materials Research 287-290, p. 2148-2151.

Sahariah, B.J., Vashishtha, N., Sapate, S.G., 2018, " Effect of Abrasive Particle Size on Friction and Wear Behaviour of HVOF Sprayed WC-10Co-4Cr Coating", Materials Research Express 5, p. 066424.

This page intentionally left blank.

Science and Applications of Thin Films, Conference & Exhibition (SATF 2018)
Izmir Institute of Technology, Izmir, Turkey, September 17-21, 2018

Superconducting Properties of Bi-2212 thin films produced by Pulsed Laser Deposition

B. Özçelik*

Physics Department, Faculty of Sciences and Letters, Çukurova University, Adana, Turkey

*e-mail: ozcelik@cu.edu.tr

Abstract

In this study, $Bi_2Sr_2Ca_1Cu_2O_{8+\partial}$ thin films were deposited on MgO (*100*) substrates by pulsed laser deposition (PLD). The effects of post-annealing temperature and time on the phase formation, the structural and superconducting properties of the films have been investigated by means of X-ray diffraction (XRD), scanning electron microscopy (SEM), temperature dependent resistivity (R–T), and DC magnetization measurements. The films deposited at 600^{o}C were post-annealed in an atmosphere of a gas mixture of Ar (%93) and O_2 (%7), at temperature of 860 ^{o}C for 30 minutes. All films have demonstrated a mainly single phase of Bi-2212 with a high crystallinity (FWHM ≈ 0.16^o) and *c*-axis oriented. The critical temperature, T_C, of the films was measured as 82 K and the critical current density, J_C, was calculated as 3,3x10^7 A/cm^2 for the film annealed at 860 ^{o}C.

1. Introduction

The high-*Tc* bismuth-based superconductors have three members described by the general formula of $Bi_2Sr_2Ca_{n-1}Cu_nO_x$, where n=1, 2 and 3 [1]. Here, n is related to the number of CuO_2 layers in the crystal structure, producing the Bi-2201, 2212 and 2223 phases with 20, 85, and 110 K critical temperatures, respectively [2-4]. For technological applications, a stable single phase of the superconducting material is highly desirable. Among the three phases of BSCCO superconductor, the Bi-2212 phase has a much better stability compared to other ones. Hence it makes it advantageous for applications. After the discovery of the high temperature superconductors, most of the research groups have focused on the synthesis of these materials in a specific form like a thin film in order to fabricate devices as SQUIDs and Josephson junctions. Several techniques for producing the thin films have been investigated in various laboratories to advance the qualities of thin films for devices. The parameters of the device can be controlled by the preparation techniques. Some of these techniques are involved the molecular beam epitaxy (MBE) [5,6], dc sputtering [7], rf sputtering [8], chemical vapor deposition (CVD) [9,10] and pulsed laser deposition (PLD) techniques [11-14]. Pulsed laser deposition (PLD) technique is a convenient method promising a deposition of smooth surface in nanoscale for mono or multilayer, having a good electrical property, and highly textured thin films with a complex stoichiometry by controlling on all producing parameters such as; target distance, vacuum level, conditions of the ambient gases, mechanical setups, laser parameters, substrate option, and deposition temperature.

In this research, the results on the effects of the post-annealing temperature and time on the Bi-2212 thin films deposited on MgO (100) single crystal substrates by pulsed laser deposition have been summarized.

2. Experimental

$Bi_2Sr_2Ca_1Cu_2O_y$ target has been prepared, by using a polymer matrix route described in detail elsewhere [15]. The thin films of $Bi_2Sr_2Ca_1Cu_2O_{8+\partial}$ were deposited onto MgO (100) substrates by pulsed laser deposition (PLD), using an excimer laser (248 nm) focused on the target surface at an angle of 45º. Before deposition (at base pressure $1.0x10^{-6}$ Torr), substrates were first heated up to 1000 ^oC at a rate of 30 ^oC/min, soaked during 15 min to clean remaining impurities from their surfaces, and then cooled down to 600 ºC. This helps also to relieve any stresses build up on the substrate. During the deposition, the substrates were kept at 600 ^oC while keeping O_2 gas pressure in the chamber fixed to 250 mTorr. The distance between the substrate and the target was 45 mm. The laser fluence was kept at ~2.39 J/cm^2 and with a pulse repetition rate of 5 Hz. After deposition, the substrates were cooled down to room temperature at a rate 20 ^oC/min, while maintaining the pressure of O_2 gas at 70 Torr. After deposition, the post-annealing heat treatments were performed in a quartz tube having a mixture of (Ar/O_2: 93/7) inside, and the tube was placed inside of a tubular furnace heated at temperatures at the range 860 ^oC during 30 min. Then the samples analyzed via XRD, SEM, resistivity and magnetic measurements.

3. Results and Discussion

In Fig.1, X-ray diffraction pattern of the film is given. As can be seen from the figure all main peaks were situated on (*00l*) reflections of Bi-2212 phase. Additionally, the grown film has a high crystal homogeneity resulting from formation of strongly aligned to the c-axis on MgO (*001*) surface. The lattice parameter *c* and crystal size *L* of film were calculated as 30.9 Å and 537.1 Å, respectively. This value is in good agreement with the previous publications for Bi-2212 superconductors [16].

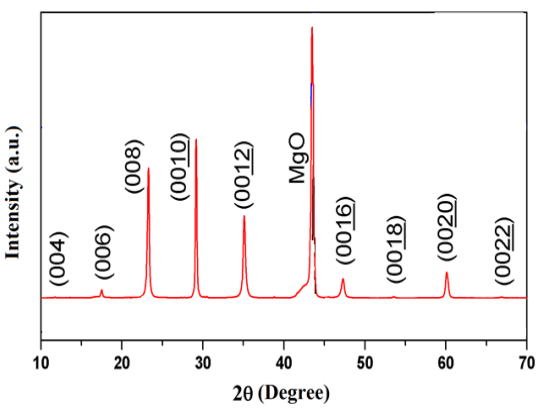

Fig.1. XRD patterns of film

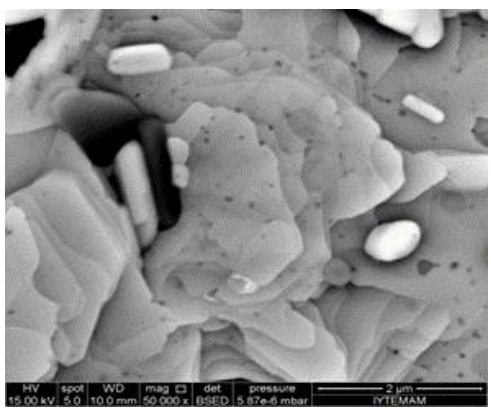

Fig.2. SEM image of the film

SEM image of the thin film annealed at 860 ^oC for 30 minute is exhibited in Fig. 2. As can be seen that a well-stacked and terrace-like typical structures of Bi-2212 grains have formed in the matrix. The appearance of surface morphology of thin film is a cogent that the *a-b* plane of large grains of the Bi-2212 films mostly oriented along *c* axis with layered growth on *a-b* plane of MgO (*100*) single crystal substrate.

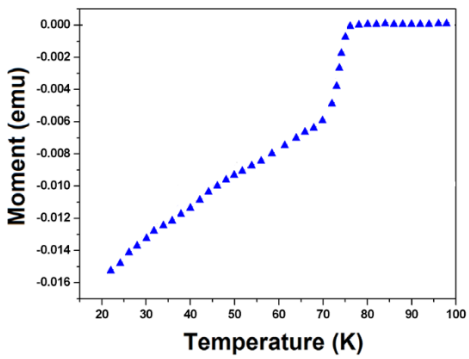

Fig. 3. M-T result of the film

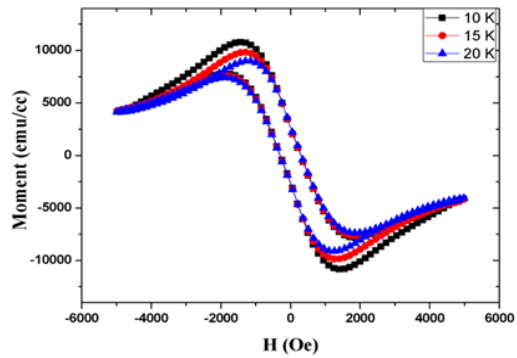

Fig. 4. Hysteresis loops of the film

The DC magnetization measurement of film is given in Fig.3. *M-T* measurement was performed on the samples under a magnetic field of 50 Oe. The field was applied parallel to the *c*-axis of the film surface. The film is exhibited a sharp diamagnetic transition around the critical temperature of 78 K.
Fig. 4 shows the temperature dependence of hysteresis curves of the film annealed at 860^{o}C for 30 minute. The M-H measurement was performed while the applied magnetic field perpendicular to the surface of the film. It is easily seen that, while the temperature decreases, the area of hysteresis loops remarkably becomes larger. It is attributed to the fact that a decrease of the temperature leads to a stronger grain structure, stemming from a better crystallization process taking place.

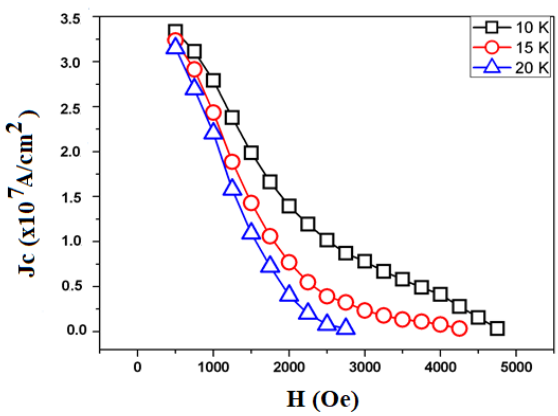

Fig. 5. Critical current densities calculated from M–H loops

The critical current density, J_C, of the film has been calculated by using the Bean model as given in [17]:

$$J_C = \frac{60a|\Delta M|}{b(3a-b)}$$

where *a* and *b* are the dimensions of the films and $\Delta M = M_+ - M_-$ is a difference of magnetization values measured in electromagnetic units per cubic. The calculated critical current density of the film as a function of the applied field, at 10, 15, and 20 K is given in Fig.5. The maximum J_C value is calculated as 3.4x10^7 A/cm^2.

4. Conclusion

In this study, the highly textured and c-axis oriented Bi-2212 thin film was deposited on MgO (*100*) single crystal substrate by using the pulsed laser deposition (PLD) technique. The film was firstly deposited on the preheated MgO substrate at 600^{o}C. Later on, post-annealing heat treatment has performed at 860^{o}C for 30 minute in argon and oxygen (Ar:93, O_2:7) atmosphere. The lattice parameter *c* and crystal size *L* of film were calculated as 30.9 Å and 537.1 Å, respectively. The critical temperature of the film was obtained as 78 K. The maximum J_C value is calculated as 3.4x10^{7} A/cm^{2}.

REFERENCES

[1] H. Maeda, Y. Tanaka, M. Fukutomi, T. Asano, Jpn. J. Appl. Phys. 27, L209 (1988).
[2] L.Gao, J. C. Huang, L. R. Meng, H. P. Hor, J.Bechtold, Y.Y. Sun, W. C. Chu, Z.Z. Sheng, M. A. Herman,: Nature 332, 623 (1988)
[3] W.C. Chu, J.Bechtold, L.Gao, H.P. Hor, J.C. Huang, L.R. Meng, Y.Y. Sun, Y.Q.Wang, Y.Y.Zue: Phys. Rev. Lett. 60,941 (1988)
[4] L.J. Tallon, G.R. Buckley, W.P.Gilbert, R.M.Presland, M.W.I. Brown, E.M. Bowder, A.L. Christian, R.Gafull: Nature 333, 153 (1988)
[5] Hiroaki Furukawa, Seiichi Tokunaga, Masao Nakao, Physica C: Superconductivity, Volumes 185–189, Part 3, 1 December 1991, Pages 2083-2084.
[6] S. Sakai, Y. Kasai, H. Tanoue, H. Matsuhata, P. Bodin, T. Oohira, Physica C: Superconductivity, Volumes 185–189, Part 3, 1 December 1991, Pages 2013-2014.
[7] Zon Mori, Toshiya Doi, Daishi Kawabata, Ken-ichi Ogata, Ken-ichiro Takahashi, Akiyoshi Matsumoto, Hitoshi Kitaguchi, Yoshinori Hakuraku, Physica C: Superconductivity, Volume 468, Issue 14, 15 July 2008, Pages 1060-1063.
[8] Masumi Inoue, Kenji Yoshida, Kazushige Ohbayashi, Yoshiaki Takai, Hisao Hayakawa, Physica C: Superconductivity, Volume 200, Issues 3–4, 1 October 1992, Pages 403-408.
[9] Anders Harsta, Jun Lu, Journal of Alloys and Compounds, Volume 251, Issues 1–2, April 1997, Pages 134-137.
[10] Per Martensson, Anders Harsta, Journal of Crystal Growth, Volume 156, Issues 1–2, 1 November 1995, Pages 67-73.
[11] P. Schmitt, L. Schultz, G. Saemann-Ischenko, Physica C: Superconductivity, Volume 168, Issues 5–6, 1 July 1990, Pages 475-478.
[12] M. Viret, J. F. Lawler, J. G. Lunney, Supercond. Sci. Technol. 6 (1993) 490-496.
[13] Akira Ishii, Takeshi Hatano, Physica C 340 (2000) 173-177.
[14] Akira Ishii, Yoshihiko Takano, Shunichi Arisawa, Takeshi Hatano, Kazumasa Togano, Physica C 372–376 (2002) 600–603.
[15] B. Ozcelik, M. Gursul, A. Sotelo, M. A. Madre J Mater Sci: Mater Electron (2015) 26:441–447.
[16] M. Nagoshi, T. Suzuki, Y. Fukuda, K. Terashima, Y. Nakanishi, M. Ogita, A. Tokiwa, Y. Syono, M. Tachiki, Phys. Rev. B 43 (1991) 10445.
[17] C.P. Bean, Phys. Rev. Lett. 8, 250 (1962)

Science and Applications of Thin Films, Conference & Exhibition (SATF 2018)
Izmir Institute of Technology, Izmir, Turkey, September 17-21, 2018

Study of Thin films of Nickel Oxide (NiO) Deposited by the Spray Pyrolysis Method

Antar Bouhank[a.*], Y. Bellal[a], H .Serrar[a], A.Khiter[a]

[a]*Research Center in Industrial Technologies (CRTI)*
P.O.Box 64Cheraga 16014 Algiers, Algeria

Abstract

In this work, thin films of nickel oxide (NiO) were deposited by a simple and inexpensive technique, which is spray pyrolysis on ordinary glass substrates heated to a fixed temperature of 500 °C, from a solution containing nickel nitrate hexahydrate as a precursor dissolved in water with deferent values of concentrations. Nickel oxide (NiO) is an interesting material because of its chemical stability [1] , it is a p-type conductivity semiconductor [2], energy bandgap value between 3.6 and 4.0 eV[3] and easy to deposit in thin layers many techniques, such as sol-gel and spray pyrolysis .The NiO thin films obtained were characterized to determine the structure with X-ray diffraction technique (XRD), the absorption domain (UV-Visible Spectroscopy), and the surface morphology (SEM).
The X-ray diffraction patterns confirm the presence of NiO phase with preferential orientation along the (111) direction. The optical gap (band gap) for nickel oxide calculated from the measurement of optical absorption is 3.6 eV, which is quite comparable to the value of the ratio.

Keywords: NiO; Thin films; Spray Pyrolysis**.**

Introduction

Advanced Oxidation Processes (AOPs) are among the most recent advances in the treatment of wastewater and industrial effluents that are a major concern today. The latter describes a novel treatment method known as heterogeneous photocatalysis which is a combination of a semiconductor catalyst with a light source.Metallic oxides are catalysts used for the degradation of pollutants existing in water by the heterogeneous photocatalysis process such as ZnO, TiO2, CuO, NiO.Nickel oxide (NiO) is a binary compound that is an important material because of its large direct optical gap of the order of 3.6-4 eV[1], it is a very resistant to oxidation and has a high chemical stability,[2] a density of 6.72 g / cm3[3].The work presented in this manuscript is focused on the study of the thin films of nickel oxide developed by the pyrolysis spray technique which presented advantages such as simplicity, inexpensive, efficient and fast with wide surfaces and good uniformity [4,5]. With their characterizations by X-ray diffraction techniques (XRD), UV-Visible Spectroscopy (SEM), with gap calculation.

5 Experimental

The preparation of thin films of NiO are made from a solution of hexa-hydrated nickel nitrate as precursor dissolved in distilled water used to prepare all concentration solutions. The water is used as a reactant to supply the oxygen atoms. The substrates in ordinary glass are well adapted for the optical characterization of our films, these latter are cleaned before use with acetone solution in the ultrasound machine for 10 minutes under 40°C, and in the ultrasound machine for 10 min and rinsed with distilled water, finally dried with a dryer. To obtain the desired molarity (0.05, 0.1, 0.15M), the precursors will be weighed by an electronic scale, where the quantities measured are mixed with a volume of distilled water. The mixture is heated to prevent breaking of the substrates, and ejected onto glass substrates placed in a pyrolysis system. Spray pyrolysis chemical deposition involves causing chemical reactions of a solution to form a solid deposit on a substrate heated between 200 °C and 500 °C.

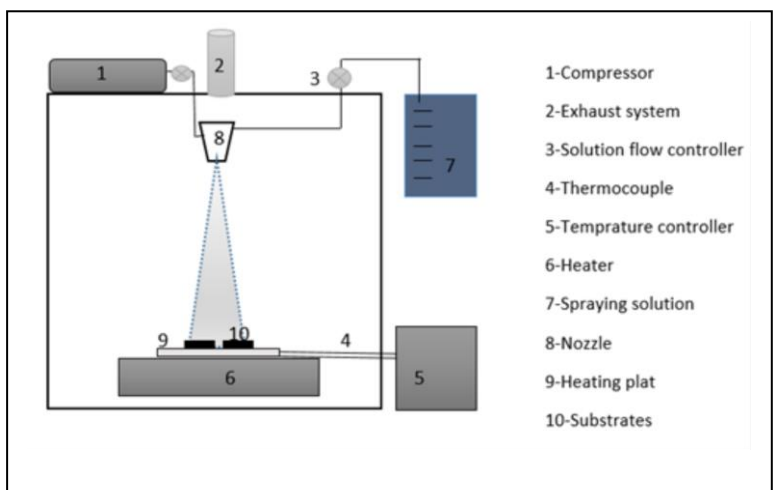

Fig. 1. Schematic the system chemical spray pyrolysis

Results /Discussion

The present chapter contains the results of our work concerning the characterization of thin films nickel oxide (NiO), which are deposited with spray method. Layers obtained were analyzed by different characterization techniques such as X-ray diffraction, scanning electron microscope, optical microscope, spectrophotometer, and so on....).

Structural Characterization

The characterizations with XDR techniques is useful for phase material identification, make it possible to have information on the crystallinity and structure of the prepared thin films.

The spectra of NiO thin films deposited at 500 ° C with a concentration of the fixed solution equal to 0.1M , shown in the figure below.

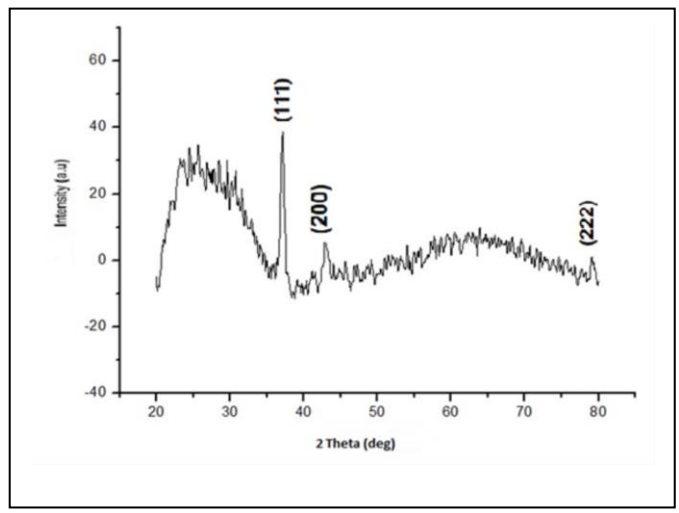

Fig.2. XRD patterns of NiO thin film

From the results of the diffractograms it can be noted that the presence of the peak (111), which confirms the cubic structure of the NiO films with the intensity of the principal peak value of 37 °.

3.2. Morphological characterization

The morphology of the prepared NiO thin films has been investigated using Scanning electron Microscope (SEM). The SEM images showed in the figure below

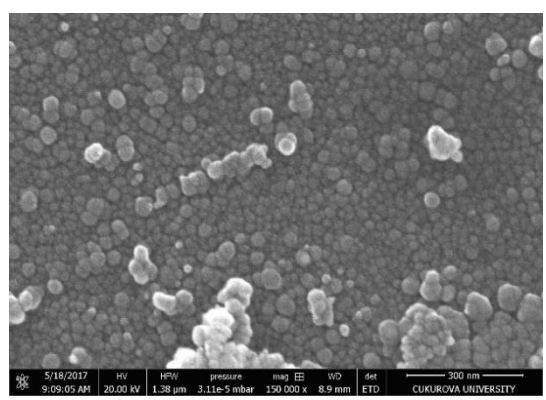

Fig. 3. SEM image of NiO thin films

The investigations obtained by this technique show that the surface of the elaborated layers is covered with material furthermore, the roughness of the surface. The particles of NiO are at the Nano-metric scale.

3.3. Absorption domain

The UV-Visible adsorption spectrum of the NiO films (0.1M) shows that the presence of a maximum adsorption band appears in the ultraviolet range at the value of 34500 cm-1.

The figure 5 shows the UV-Visible transmission spectra of the NiO layers prepared with different concentrations of the precursor dissolved in water (0.05M, 0.1M and 0.15 M).

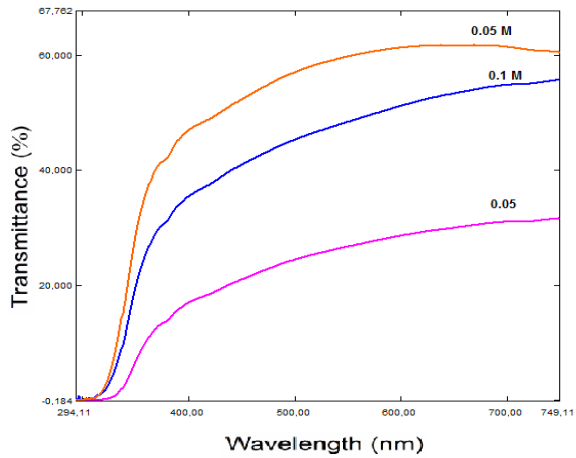

Fig. 5. UV-Visible transmission of NiO thin film with deferent value of concentration (0.05, 0.1and 0.15M)

From the figure above, we can note that the concentration has an influence on the transmission of the layers, therefore the optical gap of the Nio will affect with this variation.

3.4-Determination of the optical gap

Nickel oxide has very interesting optical properties for various applications. For this, the study of optical properties is necessary for the characterization of thin films such as transmittance, energy gap, etc.To determine the width of the optical gap of nickel oxide, we need the model proposed by Tauc where Eg is connected to the absorption coefficient α and the photon energy $h\nu$ by the following equation [6] :

$$(\alpha h\nu)^2 = A(h\nu - Eg) \quad (1)$$

Where:

h : Planck's constant $h = 6,6.10^{-34}$

The value of Eg can be obtained experimentally by extrapolating the plot of $(\alpha h\nu)^2 = f(h\nu)$ at $\alpha = 0$.

The latter is calculated in eV by [7] :

$$h\nu = \frac{hc}{\lambda} = \frac{1,24}{\lambda}(eV) \quad (2)$$

λ *and* c Are the wavelength and speed of light.

The values of the optical gap of NiO thin films deposited with deferent concentration of solution are showed in the figure below:

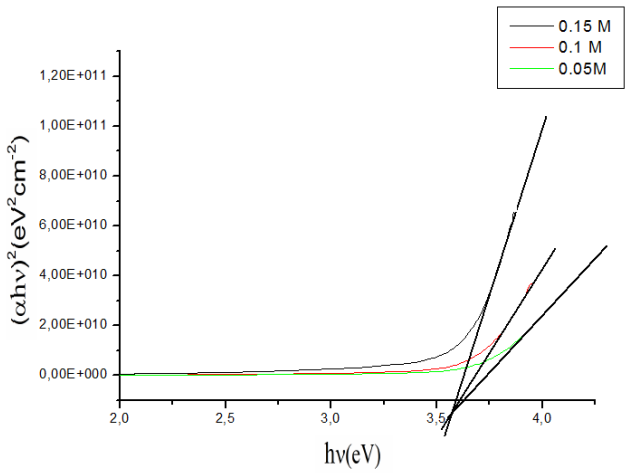

Fig. 6. Determination of the optical gap of NiO thin films (0.05 M, 0.1 M and 0.15M).

Table 1 gives the energy gap values obtained by using the concentration of diposit solutions with different concentrations.

Table.1. Values of Eg (eV) with deferent concentration

Concentration(M)	0.05	0.10	0.15
Eg (eV)	3.63	3.6	3.57

3.5-Raman spectroscopy

Raman spectroscopy (Raman analysis) is an optical spectrometry highlighting the molecular vibrations, allows us to determine the chemical structure of a sample and to identify organic molecules, polymers, biomolecules and inorganic compounds also. The figure below represents the Raman spectrum of the thin film NiO where the band positions expressed in (cm-1) which correspond to the characteristic vibration frequencies of the molecular bonds, as a function of the intensity of these bands is expressed in arbitrary units. (ua).

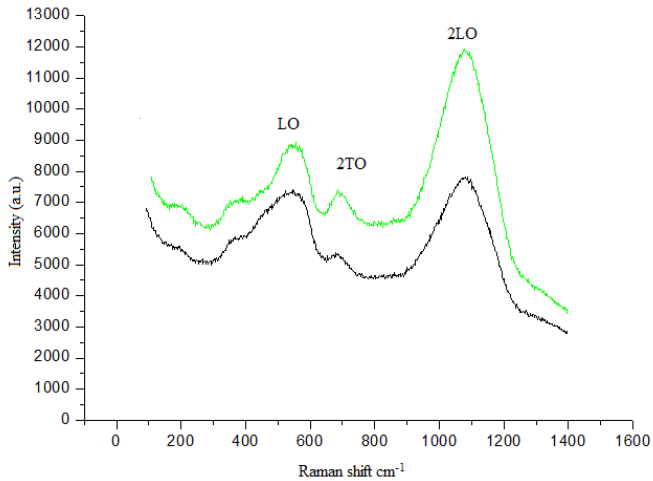

Fig. 7. Raman spectra of nickel oxide thin film (0.1M)

The Raman spectrum of the thin film NiO shows several bands a strong peak at 540 cm^{-1} corresponds to the vibrations of Ni-O [8](one-phonon TO and LO modes), at~700 cm^{-1} two-phonon 2TO modes, The last strongest band at ~1100 cm^{-1} correspond au 2LO modes.

The phonon related part of the Raman spectra indicate with (LO and 2TO modes in figure above in nanosized NiO thin film is rather similar to that in the single-crystal (u.a.).

4-Conclusion

From the results obtained, we have led to the following observations

-Spray pyrolysis of aqueous Nickel Nitrate solutions is a simple and effective method for preparing NiO thin films at moderate temperatures.

- The formation of the nickel oxide phase by X-ray diffraction analysis, the film crystallites obtained have preferential orientation in the (111) direction.

- The UV-Visible spectra of thin films developed by deferent concentration values showed that the films show optical transmission in the ultraviolet.

-The observation of the state of the surface of our thin layers by SEM shows that the latter have a uniform distribution and cover the entire surface of the substrate furthermore; there is a roughness of the surface.

- The transmittance of NiO to a good range of transmittance, which is between 30-60%.

-The use of Raman scattering spectroscopy to study the magnetic ordering in nanosized NiO thin film, prepared by the pyrolysis spray method, we observed the appearance of a characteristic band at the longitudinal vibration LO at 540 cm^{-1} corresponds to the vibration Ni-O, as well as band corresponds to 2TO and 2LO modes at (700 and 1100 cm^{-1}) .

Acknowledgement

The characterization part of this work (XRD MEB-EDX and UV-Visible) was realized at the laboratories of Cukurova University, Adana, Turkey are gratefully acknowledged

References

FANG, Guojia, LI, Dejie, et YAO, Bao-Lun. 2003. Fabrication and characterization of transparent conductive ZnO: Al thin films prepared by direct current magnetron sputtering with highly conductive ZnO (ZnAl2O4) ceramic target. Journal of Crystal Growth, , vol. 247, p. 393-400.

S. Perusin, 2004.conséquences de l'oxydation haute température sur l'injection de défauts et le comportement mécanique des matériaux métalliques, doctoral thesis, Toulouse University.

Kijatkina, o., krunks, m., mere, a., et al. 2003. CuInS2 sprayed films on different metal oxide underlayers. Thin solid films,p. 105-109.

ortiz, a., falcony, c., garcia, m., et al. 1997.Photoluminescent characteristics of lithium-doped zinc oxide films deposited by spray pyrolysis. Thin Solid Films, p. 103-107.

LIU, Zhifeng, JIN, Zhengguo, LI, Wei, et al. 2006.Assembly of ordered ZnO porous thin films by cooperative assembly method using polystyrene spheres and ultrafine ZnO particles. Materials research bulletin, p. 119-127.

J.A.A.Selvan, 1998.Ph.D.Thesis, Université de Neuchatel ISBN 3-930803-60-7.

Mironova-ulmane, n., kuzmin, a., steins, i., et al. 2007.Raman scattering in nanosized nickel oxide NiO. In : Journal of Physics: Conference Series. IOP Publishing, p. 012039.

This page intentionally left blank.

Science and Applications of Thin Films, Conference & Exhibition (SATF 2018)
Izmir Institute of Technology, Izmir, Turkey, September 17-21, 2018

$PEG_{40}St$ Squeeze out from Lipid Monolayers

Sevgi Kilic and Ekrem Ozdemir

Department of Chemical Engineering, Izmir Institute of Technology, Urla, İzmir, 35430-TURKEY

Corresponding author. Tel.: +0-90-232-750 6647; fax: +0-90-232-750 6645.
E-mail address: *sevgikilic@iyte.edu.tr.*

Abstract

Squeeze out behaviour of 1,2 Distearoyl-sn-glycero-3-phosphocholine (DSPC) and polyoxyethylene-40-stearate ($PEG_{40}St$) mixtures were investigated using Langmuir monolayer isotherms. DSPC and $PEG_{40}St$ mixtures were prepared at different molar ratios and their Langmuir isotherms were obtained. A quantification method was developed to estimate the squeeze out amount of $PEG_{40}St$ from the DSPC/$PEG_{40}St$ mixtures. It was found that almost 93% and 53% of $PEG_{40}St$ squeezed out from the 9:1 and 5:5 mixtures, respectively, at the end of the first collapse plateau and showed a decreasing trend with the $PEG_{40}St$ content. Remaining $PEG_{40}St$ squeezed out at the end of the second collapse plateau, where 20% of $PEG_{40}St$ still contained within the 5:5 composition. It was concluded that increasing $PEG_{40}St$ content would be advantageous to design more stable lipid based microbubbles.

Keywords: $PEG_{40}St$, DSPC, lipid, emulsifier, monolayer, microbubble, ultrasound, contrast agent

Introduction

Microbubbles are used as ultrasound contrast agent in medicine to improve the quality of ultrasound imaging. (Schutt, Klein et al. 2003) They are also used as efficient drug and gene delivery wheicles. (Schutt, Klein et al. 2003, Unger, Porter et al. 2004, Hernot and Klibanov 2008, Sirsi and Borden 2012) However, microbubbles are suffer from low stability during *in-vivo* applications. Thus, additional studies are needed to improve the stability of microbubbles. The miscibility of lipids with emulsifier could be one of the factors effecting the microbubble stability.

A DSPC:$PEG_{40}St$ mole ratio is commonly used as the microbubble composition. (Borden and Longo 2002, Borden, Pu et al. 2005, Feshitan, Chen et al. 2009, Kwan and Borden 2010, Mulvana, Stride et al. 2010, Chen and Borden 2011, Kwan and Borden 2012, Garg, Thomas et al. 2013) This means 90% of the mixture is lipid and any effect of emulsifier observed during their miscibility behaviours may not be thoroughly interpreted. Also, to the best of our knowledge, the miscibility behavior of DSPC:$PEG_{40}St$ at molar ratio higher than 15 mole% of $PEG_{40}St$ has not been studied in the literature.(Wang, Moser et al. 1996, Borden, Pu et al. 2004, Xing, Ke et al. 2010) Here, the miscibility of DSPC/$PEG_{40}St$ mixtures to different mole ratios from 9:1 to 5:5 were reported using Langmuir monolayer isotherms. (Kilic 2018) Brewster angle microscopy (BAM) imaging of these monolayers were also reported. (Kilic and Bolukcu 2018). A quantification method was developed to figure out the squeeze out amount of $PEG_{40}St$ from the DSPC:$PEG_{40}St$ mixtures. (Kilic 2018) It was found that almost all $PEG_{40}St$ squeezed out from the 9:1 mole ratio of DSPC: $PEG_{40}St$ mixture at the end of first plateau. The remaining $PEG_{40}St$ content increased at higher $PEG_{40}St$ mole percent of DSPC: $PEG_{40}St$ mixtures such that more than 20% of $PEG_{40}St$ remained in the 5:5 mole ratio of DSPC: $PEG_{40}St$ mixture at the end of first plateau. It was found to be advantageous using higher $PEG_{40}St$ contents in the

microbubble formulations.

Materials and Methods

Materials: 1,2 Distearoyl-sn-glycero-3-phosphocholine (DSPC, 99%) and Polyoxyethylene-40-stearate ($PEG_{40}St$) were purchased from Sigma Aldrich (St. Louis, MO). Chloroform ($CHCl_3$, 99-99.4 %) was purchased from Merck and used as a solvent to prepare spreading solutions. Ultrapure water used as subphase was produced by Millipore purification system with specific resistivity of 18 MΩ.cm. Predetermined amount of components were weighted into a clean vial and dissolved in chloroform resulting a concentration less than 1.0 mg/ml. DSPC/$PEG_{40}St$ mixtures were prepared at molar ratios of 9:1; 8:2; 7:3; 6:4 and 5:5.

Langmuir Isotherm measurements: Langmuir-Blodgett system (KSV minitrough, Finland) with two movable PTFE barriers was used. Trough was filled with ultrapure water with specific resistivity of 18 MΩ.cm produced by a Millipore purification system. Cleanness of the air-water interface was confirmed by closing and opening the barriers and ensuring that surface pressure readings do not differ by more than ±0.1 mN/m. The spreading solutions were spread on the water subphase via Hamilton micro syringe. The monolayer was allowed to evaporate the chloroform for 20 minutes. The surface pressure-area (π-A) isotherms were obtained via symmetric compression of monolayers by the two barriers. A compression speed of 5 mm/min was used in all experiments.

Results and Discussion

DSPC and $PEG_{40}St$ mixtures at different molar ratios were prepared and their miscibility behaviors were investigated using Langmuir isotherms. Figure 5a shows the surface pressure (π) versus mean area per molecule isotherms for pure DSPC, pure $PEG_{40}St$, and their binary mixtures at DSPC/$PEG_{40}St$ molar ratios of 9:1, 8:2, 7:3, 6,:4, and 5:5. The main discontinuities as the turning points were marked in Figure 5b by the arrows on the isotherms for the pure components and on the isotherm for their 8:2 mixture. As shown in the figure, pure DSPC monolayer exhibited a liquid-condensed (LC) phase at the air-water interface with a steep increase in the surface pressure. The collapse pressure for DSPC was measured to be about 59 mN/m. At the collapse pressure, the mean molecular area for DSPC was found to be about 40 $Å^2$/molecule. Unlike DSPC, $PEG_{40}St$ monolayer exhibited a non-zero surface pressure even at very low molecular densities. The surface pressure for the pure $PEG_{40}St$ increased only little as large changes occurred in its mean molecular area indicating that the emulsifier molecules did not form a continuous ordered monolayer at the air-water interface.(Tirosh, Barenholz et al. 1998) The Langmuir isotherm of $PEG_{40}St$ exhibited a collapse pressure at about 35 mN/m at which the mean molecular area for $PEG_{40}St$ is about 30 $Å^2$/molecule. Langmuir isotherms of the DSPC/$PEG_{40}St$ mixtures were located in between the isotherms for pure DSPC and pure $PEG_{40}St$. There are four discontinuities as the turning points and four plateau regions in the mixture isotherms as illustrated in Figure 5b on the isotherm for the 8:2 mixture as an example. The values for the surface pressures and the mean molecular areas for the isotherms at different $PEG_{40}St$ content are also shown in Figure 5c and Figure 5d, respectively. As shown in the figures, the surface pressures were identical for the DSPC:$PEG_{40}St$ mixtures at different mole ratios, however, the mean molecular area varied with different mole ratios of DSPC:$PEG_{40}St$ mixtures.

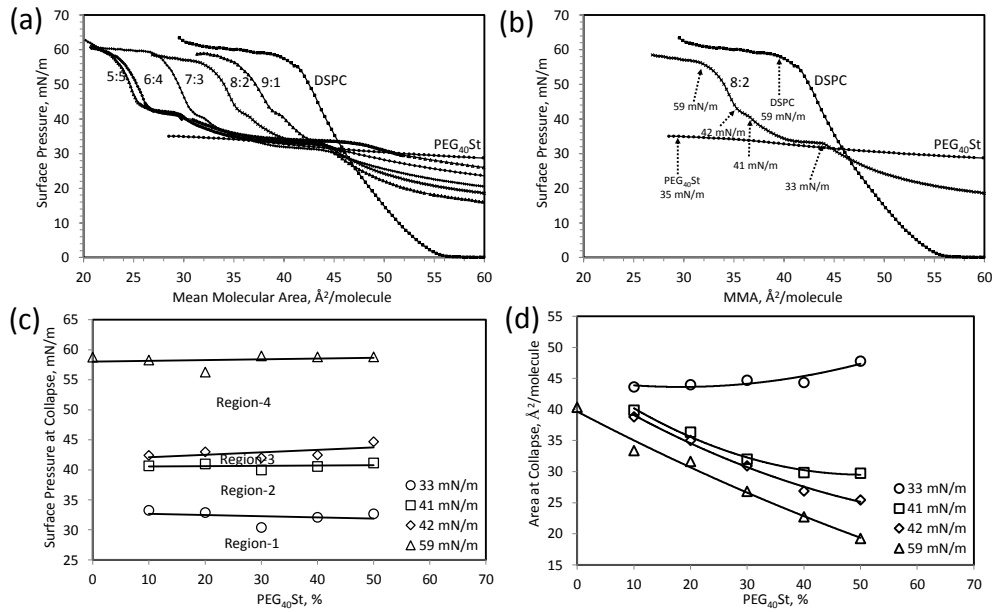

Figure 5. (a) The surface pressure–mean molecular area (π-A) isotherms of pure DSPC, pure $PEG_{40}St$, and isotherms for DSPC/$PEG_{40}St$ mixtures with different compassions at the air/water interface, (b) main turning points marked on the isotherm for the 8:2 mixture, (c) the collapse pressures for each mixture and the plateau regions on the isotherms, and (d) the mean molecular areas at the collapse pressures for the mixtures.

The average area per molecule, A_{12}, can be obtained experimentally by dividing the trough area to the number of molecules in the mixture.(Borden, Pu et al. 2004) The measured mean molecular area is the cumulative area occupied by each component in the monolayer, $A_{12}=x_1.<A_1>+x_2.<A_2>$. The mixture could be considered "ideal" if the component molecules have no irregular packing attachments, no complex formations, and form a phase separation in the monolayer.(Chou and Chu 2003, Borden, Pu et al. 2004) In such cases, the ideal average mean molecular area, A_{12}^{ideal}, can be related to the area per molecule, A_i, for each component obtained from their pure component isotherms at the specified surface pressure and mole fraction of each species, $A_{12}^{ideal}=x_1.A_1+x_2.A_2$.(Chou and Chu 2003, Borden, Pu et al. 2004)

In our approach, DSPC is a rigid molecule and can be taken as the reporting molecule for the $PEG_{40}St$ because the change in the mean molecular area for DSPC was considered to be minimum or negligable. Therefore, the squeeze out amount of $PEG_{40}St$ can be estimated from the measured surface area for the mixtures using the equation $(A_{12} = x_1A_1 + x_2A_2.\boldsymbol{y})$, where y is the percentage of $PEG_{40}St$ molecule contributed to the measured mean molecular area. The remaining of y indicated the loss percentage of $PEG_{40}St$ from the monolayer. Figure 6a shows the estimated percentage of the $PEG_{40}St$ loss from the monolayer to the subphase at different collapse pressures. As shown in the figure, almost 93% of $PEG_{40}St$ was lost at the end of the first collapse plateau for the 9:1 mixture and showed a decreasing trend for the higher $PEG_{40}St$ contents for the mixtures. Almsost 82% and 53% of $PEG_{40}St$ were lost for the 7:3 and 5:5 composions at the end of the first collapse plateau, respectively. Remaining of the $PEG_{40}St$ molecules were lost at the end of the second collapse plateau, where 20% of $PEG_{40}St$ were still present for the 5:5 mixture on the air-water interface. The $PEG_{40}St$ was entirely lost at the last collapse pressure for each mixtures studied.

The collapsed amounts of DSPC were estimated from the measured mean molecular area at the last collapse pressures. The fact that the measured surface area is lower than the estimated mean molecular area for the DSPC indicating that all the $PEG_{40}St$ and some of DSPC were lost from the 2D monolayer.(Borden, Pu et al. 2004) Then, the lost DSPC amount can be estimated from the measured mean molecular area at the last collapse pressure when the $PEG_{40}St$ molecules were omitted $(\boldsymbol{A_{12} = x_1 A_1 . z + x_2 A_2})$, where z is the percentage of DSPC contributed to the measured mean molecular area. The remaining of z indicated the percentage of DSPC loss from the monolayer. Figure 6b shows the estimated percentage of the collapsed DSPC from the monolayer with different emulsifier contents. The DSPC molecules would also be lost from the monolayer into the subphase by associating with the $PEG_{40}St$ molecules. As shown in the figure, about 5% of DSPC molecules were lost for the mixtures, which can be considered relatively negligible.

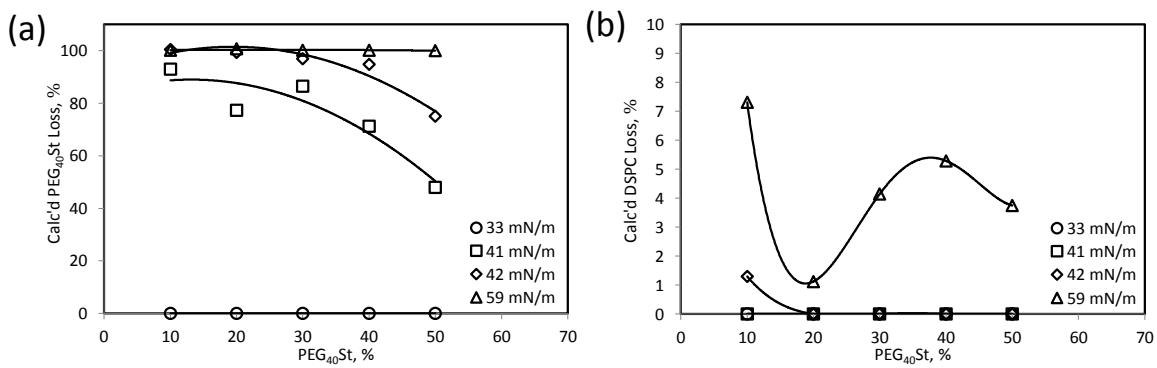

Figure 6. (a) The calculated percent amount of $PEG_{40}St$ that squeeze out from the 2D monolayer at each DSPC/$PEG_{40}St$ mixtures at each collapse points. (b) The calculated percent amount of DSPC that moved from the 2D monolayer of the mixtures at each collapse point.

Conclusion

It was shown that $PEG_{40}St$ molecules were well distributed within the DSPC molecules at lower DSPC/$PEG_{40}St$ mole ratios and mostly phase separated at higher mole ratios. It was found that $PEG_{40}St$ in 10% composition of DSPC:$PEG_{40}St$ is easily squeeze-out from the monolayer up to about 93% at the end of the first collapse plateau, at 41 mN/m, whereas almost 60% $PEG_{40}St$ squeezed out from the monolayer for the 5:5 composition of DSPC:$PEG_{40}St$, retaining almost 40% of $PEG_{40}St$ molecules in the monolayer. It was concluded that increasing $PEG_{40}St$ content would be advantageous to design more stable lipid based microbubbles as the ultrasound contrast agents.

Acknowledgements

The Scientific and Technological Research Council of Turkey (TUBITAK) is gratefully acknowledged for the financial support provided under Project No. of 113M270. The authors also thank Elif Seniz Bolukcu for help conducting part of the experiments.

References

Borden, M. A. and M. L. Longo (2002). "The dependence of lipid-coated microbubble dissolution behavior on acyl chain length." Biophysical Journal **82**(1): 35a-35a.

Borden, M. A., G. Pu, M. L. Longo, P. A. Dayton and K. W. Ferrara (2005). "Phase behavior and transport properties of the lipid-monolayer shell of a microbubble." Abstracts of Papers of the American Chemical Society **230**: U1072-U1073.

Borden, M. A., G. Pu, G. J. Runner and M. L. Longo (2004). "Surface phase behavior and microstructure of lipid/PEG-emulsifier monolayer-coated microbubbles." Colloids and Surfaces B-Biointerfaces **35**(3-4): 209-223.

Chen, C. C. and M. A. Borden (2011). "The role of poly(ethylene glycol) brush architecture in complement activation on targeted microbubble surfaces." Biomaterials **32**(27): 6579-6587.

Chou, T. H. and I. Chu (2003). "Thermodynamic characteristics of DSPC/DSPE-PEG2000 mixed monolayers on the water subphase at different temperatures." Colloids and Surfaces B: Biointerfaces **27**(4): 333-344.

Feshitan, J. A., C. C. Chen, J. J. Kwan and M. A. Borden (2009). "Microbubble size isolation by differential centrifugation." Journal of Colloid and Interface Science **329**(2): 316-324.

Garg, S., A. A. Thomas and M. A. Borden (2013). "The effect of lipid monolayer in-plane rigidity on in vivo microbubble circulation persistence." Biomaterials **34**(28): 6862-6870.

Hernot, S. and A. L. Klibanov (2008). "Microbubbles in ultrasound-triggered drug and gene delivery." Advanced drug delivery reviews **60**(10): 1153-1166.

Kilic, S. (2018). "Quantification of PEG40St squeeze out from DSPC/PEG40St monolayers at higher molar ratios." Colloids and Surfaces A: Physicochemical and Engineering Aspects **551**: 58-64.

Kilic, S. and E. S. Bolukcu (2018). "Phase behavior of DSPC/PEG40St mixtures at higher emulsifier contents." Colloids and Surfaces B: Biointerfaces **171**: 368-376.

Kwan, J. J. and M. A. Borden (2010). "Microbubble Dissolution in a Multigas Environment." Langmuir **26**(9): 6542-6548.

Kwan, J. J. and M. A. Borden (2012). "Lipid monolayer collapse and microbubble stability." Advances in Colloid and Interface Science **183**: 82-99.

Mulvana, H., E. Stride, J. V. Hajnal and R. J. Eckersley (2010). "Temperature dependent behavior of ultrasound contrast agents." Ultrasound in medicine & biology **36**(6): 925-934.

Schutt, E. G., D. H. Klein, R. M. Mattrey and J. G. Riess (2003). "Injectable microbubbles as contrast agents for diagnostic ultrasound imaging: the key role of perfluorochemicals." Angewandte Chemie International Edition **42**(28): 3218-3235.

Sirsi, S. R. and M. A. Borden (2012). "Advances in Ultrasound Mediated Gene Therapy Using Microbubble Contrast Agents." Theranostics **2**(12): 1208-1222.

Tirosh, O., Y. Barenholz, J. Katzhendler and A. Priev (1998). "Hydration of polyethylene glycol-grafted liposomes." Biophysical Journal **74**(3): 1371-1379.

Unger, E. C., T. Porter, W. Culp, R. Labell, T. Matsunaga and R. Zutshi (2004). "Therapeutic applications of lipid-coated microbubbles." Advanced Drug Delivery Reviews **56**(9): 1291-1314.

Wang, W., C. C. Moser and M. A. Wheatley (1996). "Langmuir trough study of surfactant mixtures used in the production of a new ultrasound contrast agent consisting of stabilized microbubbles." The Journal of Physical Chemistry **100**(32): 13815-13821.

Xing, Z. W., H. T. Ke, J. R. Wang, B. Zhao, X. L. Yue, Z. F. Dai and J. B. Liu (2010). "Novel ultrasound contrast agent based on microbubbles generated from surfactant mixtures of Span 60 and polyoxyethylene 40 stearate." Acta Biomaterialia **6**(9): 3542-3549.

This page intentionally left blank.

Science and Applications of Thin Films, Conference & Exhibition (SATF 2018)
Izmir Institute of Technology, Izmir, Turkey, September 17-21, 2018

Optimization of zinc oxide based metal-semiconductor junction interface properties for optoelectronic device applications

Enver Tarhan[a,*] and A. Halis Guzelaydin[a]

[a] *Department of Physics, Izmir Institute of Technology, Urla, 35430, Izmir, Turkey*
[*]Corresponding author
E-mail address: etarhan@iyte.edu.tr
Phone: +90-232-7507714, Fax: +90-232-7507707

Abstract

Zinc oxide (ZnO) is a Group II-VI compound semiconductor which drew the attention of researchers for possible applications in science and industry. It has a wide, direct band gap of 3.36 eV at room temperature and a large exciton binding energy of 60 meV. The band gap of ZnO can be tuned by forming alloys and impurity incorporation. Therefore, ZnO in the forms of quantum- and nano-structures has received considerable interest and has been recognized as a promising candidate for making efficient UV/blue light-emitting diodes, sensors, photo detectors, and laser diodes. ZnO fabrication requires interfacing of metals, semiconductors, and insulators in a coherent manner. Linear ohmic and rectifying Schottky junctions are integral to the intended operation of all electronics. In this study; we present the opto-electronic characteristics of ZnO based thin films in situ doped with Al and Ga tailored for functional optoelectronic devices fabricated via RF magnetron sputtering technique on quartz and Si substrates. UV-VIS-NIR, FTIR, and Raman, spectroscopies were used for optical characterization, 4-point probe and Hall mobility were employed for electrical studies, and SEM, AFM, and XRD were used for structural characterization. Optimum values of growth parameters, such as dopant amount, growth temperature, growth power, etc. were studied by systematically changing the growth parameters for repetitive growths. Our analysis provided a good set of growth parameters for GZO (Ga doped ZnO) and AZO (Al doped ZnO) thin films on quartz and Si with desired optical, electrical and structural properties.

Keywords: Schottky Junctions; ZnO; Functional Materials

1. Introduction

ZnO has a large abundance in the Earth's crust and it is easy to produce and process. It has a direct band gap with 3.36 eV gap energy (RT) with a A large exciton binding energy of 60 meV. Due to its natural n-type conductivity its use for TCO thin film coating material has gained a big interest (Ozgur, 2005.). It is a very important alternative to GaN, Si, and indium tin oxide (ITO) for use in solar cells LED's, OLED's, and touchscreens (Chen, 2013). It has a better thermal and chemical stability than GaN whose electrical and optical properties are similar to ZnO. Its high resistance to humidity and radiation makes it a perfect candidate for space and harsh weather applications. On the other hand, indium in ITO (also used as dopant in GaN for TCO applications) is very scarce and expensive. ZnO can easily be doped n-type with Ga, Al, H, etc. for making cheaper and better quality TCO's than those of GaN or ITO (Ozgur, 2007).

ZnO is mainly used as a transparent conducting oxide layer in light emitting diode (LED) or photo detector applications, especially as a UV detector. For that purpose it must be doped n-type. Al and Ga are two suitable dopants for obtaining well controlled n-type conductivity in ZnO. Ga doped ZnO will be called GZO and Al doped ZnO will be called AZO, in accordance with literature. Both Al and Ga have their

advantages and disadvantages over one another. Main advantage of Al doping of ZnO is that; Al is inexpensive and earth-abundant. It can easily be used in an oxide form such as Al_2O_3. AZO is mainly used for Metal-Semiconductor-Metal interfaces as in Schottky diodes which will be the main focus of the part II of this work. The part I, on the other hand, focuses on GZO for TCO applications, since Ga is more preferable due to its better crystal qualities in general. The reason for that is as follows: Firstly the atomic size of Ga is very close to that of Zn and it easily replaces Zn with a minimum local stress. Ionic bonding radius of Ga is 0.062 nm, while its covalent bonding radius is 0.126 nm. For Zn, the ionic bonding radius is 0.074 nm while the covalent bonding radius is 0.131 nm. Hence, both ionic and covalent bond lengths are almost identical for Zn and Ga which explains why Ga replaces Zn easily in ZnO with almost no distortion of the lattice. Thus, this reduces the density of defects compared to those doped with Al for which the ionic and covalent bonding radii are: 0.054 and 0.121 nm respectively. Hence, it is expected that Ga will produce lesser local stress in ZnO when it replaces Zn substitutionaly compared to Al. This reduced defect densities lead to increased mobilities due to decreased rate of carrier scattering from such defects. Such an n-type doped ZnO (GZO or AZO) is commonly used as the TCO window for optical detectors. Growth of AZO thin films, on the other hand are carried out with a better control of growth parameters due to availability of good quality Al_2O_3 target materials. Hence for a Schottky device applications AZO is more preferable. The main motivation for growing a Schottky diode AZO device in this study is to utilize its rectifying behavior for signal modulation for electronic or optical device applications as discussed in part II. (Ozgur, 2005)

2. Experimental Methods

4. 2.1 Ga doped ZnO growth and characterization for TCO applications

We have grown thin films of GZO and AZO samples on glass, quartz, and Si substrates with varying thicknesses using the ATC Orion 5 UHV Magnetron sputtering system (AJA International Inc.). Fig. 1(a) and (b) illustrates the working principle of a magnetron sputtering system and its growth chamber, respectively. High purity Al_2O_3 and Ga_2O_3 (99.999% or better) targets are placed in the growth chamber. The system can hold five different targets with 3 RF and 2 DC sputtering guns. For insulating targets such as the ones we used RF (radio frequency, or alternating) power is more suitable to avoid charge accumulation on the sample while DC (direct current) power is more suitable for the growth of conducting samples. The growth is carried out under the Ar gas flux (at about 20 sccm) at a few millitorr pressure. The substrate is rotated (about 15 rpm) for a uniform sample thickness. The distance between the target and the substrate is kept about 10 cm. For a controllable growth the shutter of each target was opened and closed when needed. The system is entirely computer controlled during the growth. Glass, or quartz slide substrates were first cleaned in an ultrasonic bath containing a mixture of alcohol and acetone. Then, the slides were placed onto the sample holder in the growth chamber and plumbed down to very a high vacuums (about 10^{-7} millibar). The growth is carried out under the Ar gas flux. The growth power was kept constant at 100 W while changing growth durations for various thicknesses. For doped ZnO films, the shutters of targets containing Al or Ga were opened and closed in a controlled manner to control the doping concentration. The growth parameters were computer controlled. For GZO samples high level doping ($n \sim 10^{19}$ cm^{-3}) is needed and we kept the shutter open durations much longer than those for AZO samples which require low doping concentrations ($n \sim 10^{16}$ cm^{-3}) due to Schottky effect. Usually 200 nm thickness is achieved for 100 W growth power with 100 min duration.

AZO, GZO, and undoped films on quartz and glass substrates were than characterized using several techniques. Crystal structure was determined using an X-ray diffractometry (XRD) system (Philips X'Pert Pro). Raman measurements were carried out for structural analyses using a confocal Raman system (S&I monovista, Germany) employing an Ar+ ion laser operating at 488 and 514 nm's, an Olympus BX51 upright microscope, and a 750 mm focal length Acton monochromator (Princeton instruments). Raman system was also used for photoluminescence (PL) measurements. A Shimadzu UV-Visible spectrometer was employed for the transmission measurements. For a thickness *t* of the sample film, absorption coefficient was found from the transmission (T) data using the formula:

$$\alpha = -\ln(T)/t \quad (1)$$

The band gap of the ZnO film was then obtained using the well known equation;

$$\alpha = (T - R)(h\nu - E_g)^{1/2}/h\nu \quad (2)$$

where T is transmission, R; reflection; hν; the photon energy, and E_g; the band gap energy of ZnO. We ignored R in calculations since it is much less than one. SEM images are obtained from a SEM FEI QUANTA FEG 250 system. A DEKTAK profilometer is employed for film thickness measurements. Electrical measurements are carried out using a home-made system based on 4 probe technique to measure the resistance R of a film with a thickness t. Resistivity is calculated from

$$\rho = 4.53/R \quad (3)$$

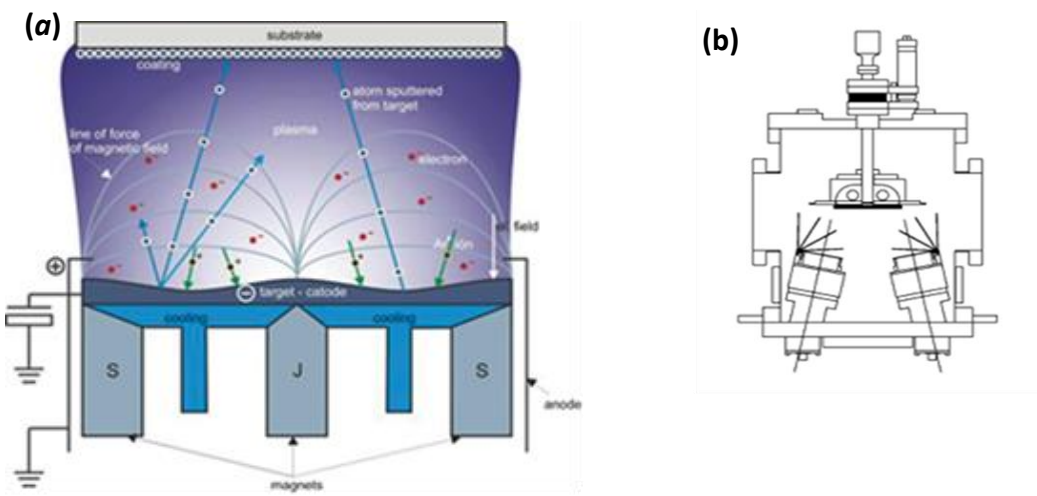

Figure 1 (a) ; illustration of the working mechanism of the magnetron sputtering system, (b); the schematic representation of the growth chamber of the AJA sputtering system used in the current work. (Ref. http://www.umms.sav.sk/6493-en/physical-vapor-deposition)

2.1.a Burstein-Moss shift

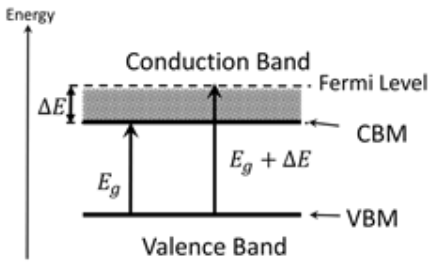

Figure 2. Schematic illustration of Burstein-Moss shift For a n-type doped semiconductor. CBM: conduction band minimum, VBM: valence band maximum.

Figure 2 illustrates the working principle of the Burstein-Moss shift. N-type doping of ZnO populates the lower energy levels of the conduction band. When heavily doped, this effectively increases the Fermi level over the conduction band minimum (CBM). When light is incident, only those photons having higher energies than the difference between the Fermi level and valence band maximum (VBM) can be absorbed. This results in a "blue shift" in the optical band gap. While high energy transparency cut-off frequency blue-shifts to UV region, conductivity increases with high doping concentration. The shift in the absorption edge of the doped semiconductor can be calculated from:

$$\Delta E = \frac{\hbar^2}{2m^*_{eh}}(3\pi^2 n)^{2/3} \quad (4)$$

where ΔE is the energy shift, m^*_{eh} is the reduced electron-hole effective mass, and n is the free electron concentration.

2.2. Al doped ZnO growth and characterization for photo detector device applications

In the second part we have grown aluminium doped n-type ZnO films on quartz substrates. RF power was chosen to be 100 watts which ensures 100 nm growth in 50 minutes. Three different growth temperatures were used: 50, 100, and 200 ^{o}C. Metallic electrodes were deposited on the films after growth to apply external bias and to collect photocurrent. Current-voltage (I-V) characterizations were carried out using a 4-probe Hall technique. In order to characterize the optoelectronic properties of the fabricated ZnO based devices, we used a rapid and flexible measurement platform to assess the fabricated devices. A four pin point configuration electronic measurement platform with a 0,3 T permanent neodymium magnet was used to perform electrical characterization of the thin film devices (Figure 3 (a)). We extracted current-voltage (I-V) behavior, sheet resistance, mobility, and carrier concentration information of the devices via voltage sweep and Hall Effect experiments. The probe station was used to carry out these measurements on a standard 10 mm x 10 mm sample with four-contact Van der Pauw geometry having constant contact area and spacing on the sample. Structural SEM, EDX, XRD, and AFM analysis were made to determine fabricated thin films' surface morphology, chemical composition, crystalline structure, surface topography, and thickness properties at two different RF power levels, respectively. Surface features of AZO thin films such as morphology, roughness, pinholes, cracks and particulation was examined via SEM. Crystallinity, degree of crystallization and crystallite size of the thin films were evaluated by XRD. The instrument had a characteristic Cu Kα X-ray radiation source with a wavelength of λ= 1.5444 Å. Topographic features of film surfaces were mapped and thicknesses of the thin films were measured via AFM.

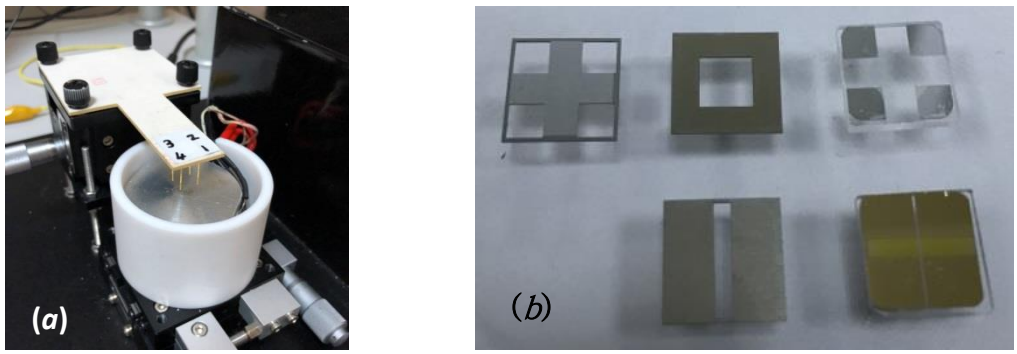

Figure 3 (a). The 4-point probe setup used for Hall measurements in the Van der Pauw geometry to determine current-voltage (I-V) characteristics, (b) shadow masks and electrode coated substrates designed for Hall measurements.

3. Results and discussions

5. 3.1. Ga doped ZnO

An SEM image of an undoped ZnO thin film grown on glass is given in Figure 4 (a) while its theta-2 theta XRD spectrum is given in figure 4 (b). We see a very flat surface in the SEM image except for a few 'bumps' indicating a very good surface quality. The XRD peak observed at 2theta = 36^o comes from the (0002) planes of the wurtzite ZnO, while the weaker peak at 2theta = 72^o is due to the (0004) planes of the same structure. We can claim that our films are highly oriented along (0002) direction with minimum structural defects as expected from a good quality wurtzite ZnO crystal. In Figure 5 (a) we see the transmission spectrum of a Ga doped an undoped ZnO film while the Raman spectrum of the doped ZnO film is given in Fig. 5 (b). The transmission spectrum of the undoped ZnO film shows a very high transparency (over 90%) in the band gap energy region of ZnO as expected from a good quality film, while that of the Ga doped film exhibits a clear 'blue shift' in the absorption edge due to high level n-type doping with Ga with a high transmission in general but a clear reduction in the infrared region, indicating the free carrier absorption resulting from heavy doping. The observed shift in the band edge is $\Delta E = 0.048\, eV$ which results in a free carrier concentration of n = $2.5\text{x}10^{20}$ cm^{-3} with an electron effective mass m* = $0.28m_0$, m_0 being the free electron mass. One can also measure the film thickness from the channelled spectrum due to the interference effect from the parallel surfaces of a transparent film. The thickness of the interference films can be calculated from;

$$t = \lambda^2/2n\Delta\lambda \qquad (5)$$

where $\Delta\lambda$ is t is the difference between the wavelengths of two neighboring maxima in transmission and n, the refractive index of ZnO at the wavelength λ. For $\lambda \approx 500\, nm$, $n \approx 2.0$, and $\Delta\lambda \approx 340\, nm$ we deduce the film thickness as $t \cong 180\, nm$ which is very close to the value $t_m = 185\, nm$ measured by the profilometer. The Raman spectrum of the Ga doped ZnO film gives the E_2^{low} and E_2^{high} vibrational modes of Ga impurities at 102 and 440 cm-1, respectively, which are very closed to the values given in the literature by a Arguello et al. The A_1(TO), E_1(TO), A_1(TO), and E_1(TO) phonon modes of ZnO are also observed. The results are summarized in Table I. It is clear that observed peak positions are in good agreement with literature indicating a good sample quality. Figure 5 (a) and (b) shows the PL spectra of Ga doped and undoped ZnO samples,

respectively. The red luminescence observed in the broad band range, in the PL spectrum of undoped ZnO, is due to impurities such as Li (Shirmer *et al.*, 1970). The broad peak extending from ~1.9 to ~2.8 eV in the PL spectrum of Ga doped ZnO, is known as the green band; the origin of its luminescence is still not well understood and has been attributed to a variety of different impurities and defects. The band near 2.5 eV is usually attributed to the O vacancies. But it can also be due to impurities such as Cu (Dahan *et al.*, 1998). The yellow band near 2.2 eV might be due to Li impurities (Shirmer *et al.*, 1970). Ga defects modify the PL spectrum. Electrical measurements show 170 ohm/cm surface resistivity.

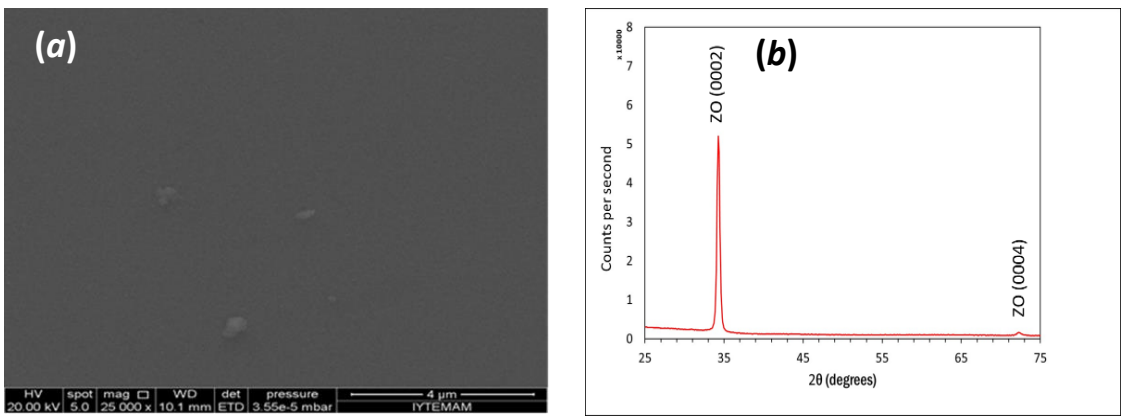

Figure 4. (a) SEM image of an undoped ZnO film grown on glass, (b) XRD theta-2theta spectrum of the film.

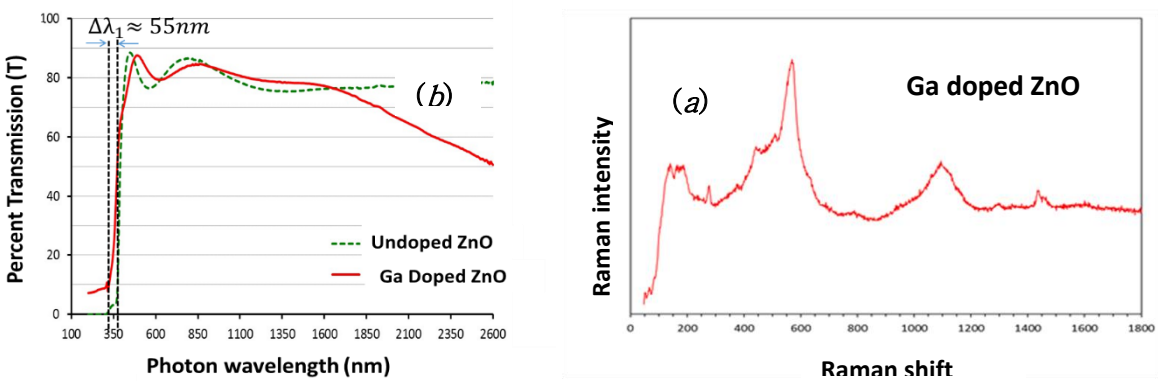

Figure 5 (a). Transmission spectrum of a Ga doped (continuous curve) and an undoped (dashed curve) ZnO film and (b) Raman spectrum of Ga doped ZnO film.

Table I. Observed and literature (Arguello *et al.*) values of some vibrational modes of Ga in ZnO and a few phonon odes of ZnO lattice.

Mode	Literature (cm^{-1})	This work (cm^{-1})
E_2^{low}	101	102
E_2^{high}	444	440
$A_1(TO)$	380	375
$E_1(TO)$	413	440
$A_1(LO)$	579	570
$E_1(LO)$	591	600

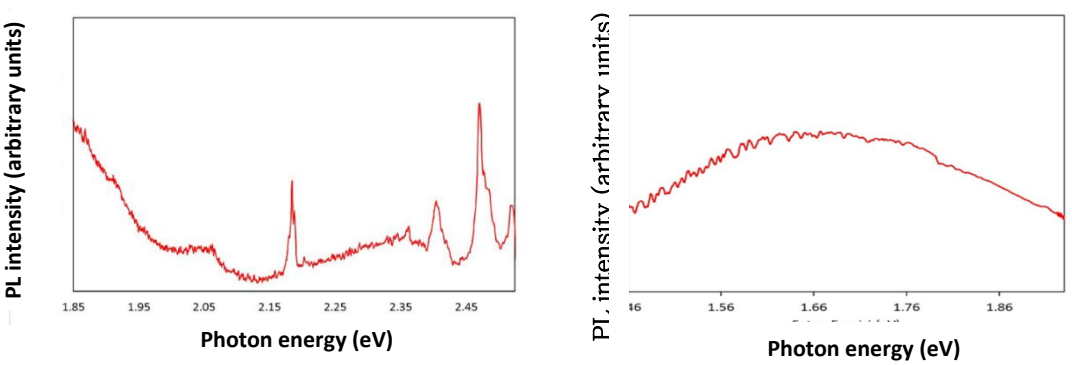

Figure 6. Photoluminescence spectrum of Ga doped (a) and undoped (b) ZnO films.

3.2 Al doped ZnO

Structural, morphological and optoelectronic characterizations of Al doped ZnO films on quartz substrates show similar results to those for Ga doped ZnO. Our Al doped ZnO thin film produced at 50 W showed smooth and intact surfaces even at relatively high magnifications. There were very few disruptions on the film surface, albeit existing ones possibly resulting from substrate defects. At higher magnifications, the film exhibited a very fine grain structure which is a sign of high homogeneity and superordinate degree of crystallinity. This can be correlated with the low sputtering power which induces mild erosion of the target, thus yielding refined sputtered species (Doyan *et al.*). This allows the fine sputtered particles to arrive at substrate surface with lower kinetic energies just enough to precipitate on it. Consequently, crystallites that grow at nucleation sites form a regular film surface. Figure 7 (a) and (b) shows SEM images of the film surface at different magnifications to indicate morphological features on the surface. The sample named AZO 2 was grown at room temperature with 50% shutter intervals for Al, while AZO 4 was grown at 200 °C with 50% shutter interval, and AZO 5 was grown at 200 °C with 20% shutter interval of Al target. The well known (0002) orientation of wurtzite ZnO structure was generally observed, implying that the surface free energy of

(0002) plane is the lowest while forming ZnO thin films via magnetron sputtering technique (Muchuweni *et al.*2017). This results in the favored formation of (0002) oriented texture in ZnO thin films which have a c-axis preferred crystal orientation on the (0002) plane, along the c-axis orthogonal to the substrate surface (Solookinejad *et al.*, 2016).

To demonstrate the topographic features of ZnO thin films, 20 μm x 20 μm areal scans in tapping mode AFM were performed on the film surfaces. The topographic features revealed by AFM showed details of the surface morphology previously generated via SEM inspections. In accordance with SEM results, AFM inspection of the ZnO thin film deposited at 50 W power exhibited fine grains on the film surface along with homogenous and continuous surface features. The thickness measurements for varying growth powers are summarized in Table I while Table II gives the results of electrical measurements obtained from the four-probe Hall measurements. The most convenient way to determine the contact characteristics of a metal-semiconductor junction is to perform an I-V experiment (Chen *et al.*, 2009). In a pre-determined potential range, change in the junction current versus a bias current is plotted. By this experiment, we can determine whether the junction behaves linear (ohmic), conducting in both forward and reverse bias or exponential (rectifying), conducting only in forward bias as in a diode. A probe station setup for 4-point van der Pauw measurements was used to determine the sheet resistance, carrier concentration and Hall mobility of intrinsic and Al-doped ZnO thin film samples (Gautam *et al.*, 2010). In order to determine the 'metal-semiconductor junction' electronic properties, I-V measurements were conducted. Those measurements revealed ohmic contacts for all samples with both gold and aluminum electrodes. Which indicates the defects plays a major role in the junction characteristics leading to ohmic conduction channels instead of Schottky type conduction. Hence, improvements are needed in the sample quality by changing growth conditions.

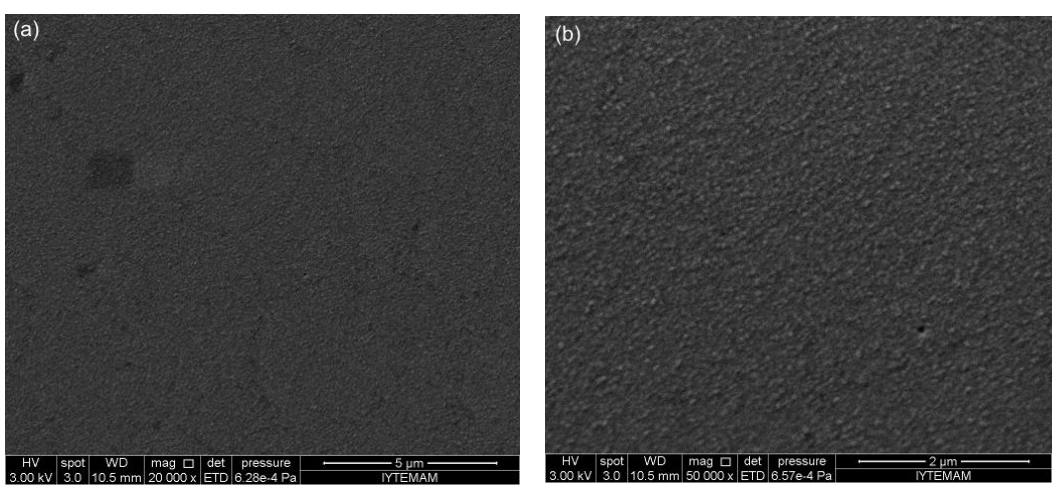

Figure 7. SEM images of Al doped ZnO thin film surface deposited at 50 W. (a) 20.000 x magnification. (b) 50.000 x magnification.

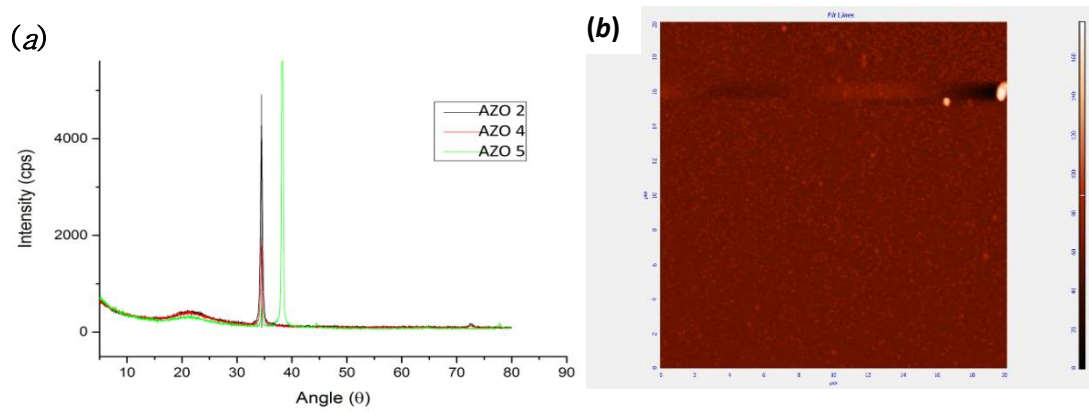

Figure 8 (a) XRD spectra of the Al-doped ZnO thin film samples AZO 2, AZO 4, and AZO 5 samples (see the text); (b) AFM image of the surface of Al doped ZnO thin film deposited at 50W.

Table II. Thickness values for various growth durations and temperatures.

Sample Number	RF Power (W)	Time (min)	Temperature (^{o}C)	Thickness (nm)
1	100	50	200	~100
2	100	50	100	~100
3	100	50	50	~100

Table III. Results from the electrical measurements

Sample Number	Temperature (min)	Sheet Resistance (Ω/□)	Carrier Concentration (cm^{-3})	Mobility $Cm^2/V.s$
1	200	$5x10^6$	$6x10^{16}$	1,50
2	100	$7x10^7$	$8x10^{15}$	0,45
3	50	NA	NA	NA

4. Conclusions

Both GZO and AZO samples we produced exhibit good crystaline quality as confirmed from their XRD, AFM, and SEM anaysis. GZO samples show a high transmission and the UV visible spectrum absorption edge is blue shifted due to Ga doping widening the transparent 'window'. Raman and PL spectra displays some phonon and electronic transitions commonly observed in most GZO structures. There exist native and impurity defects giving rise to common red, green and yellow luminescence bands. Electrical measurements show 170 ohm/cm surface resistivity which should be improved down to smaller values for better sample quality. AZO samples we produced give ohmic conduction instead of expected rectifying behavior from a Schottky device and improvements in the sample preparation technique is needed.

Acknowledgements

This research was funded by the research grand number 2017G_IYTE4.

References

Ü. Özgür, Ya. I. Alivov, C. Liu, A. Teke, M. A. Reshchikov, S. Doğan, V. Avrutin,S.-J. Cho, and H. Morkoç, Journal of Apllied Phsics, 98, 041301 (2005)

Umit Ozgur, Member IEEE, Daniel Hofstetter, and Hadis Morkoc, Proceedings of the IEEE | Vol. 98, No. 7, July 2010.

N. Izyumskaya, V. Avrutin, Ü. Özgür, Y. I. Alivov, and H. Morkoç, Preparation and properties of ZnO and devices, phys. stat. sol. (b) 244, No. 5, 1439–1450 (2007)

Schirmer, O.F. and Zwingel, D. (1970) Solid State Communications, 8, 1559.

C. A. Arguello, D. L. Rousseau, and S. P. S. Porto 1969, "First-Order Raman Effect in Wurtzite-Type Crystals" Phys. Rev. **181**, 1351

Dahan, P. et al. (1998), Journal of Physics: Condensed Matter, 10, 2007.

Schirmer, O.F. and Zwingel, D. (1970) Solid State Communications, 8, 1559.

E. Muchuweni, T. S. Sathiaraj, H. Nyakotyo. 2017. "Synthesis and characterization of zinc oxide thin films for optoelectronic applications", Heliyon, 3, Art. Nr. e00285.

A. Doyan, Susilawati, S. A. Fitri, S. Azhan. 2017. "Crystal structure characterization of thin layer zinc oxide", 2017, IOP Conf. Ser.: Mater. Sci. En., 196, 012004.

U. Gautam, M. Imura, C. S. Rout. 2010. "Unipolar assembly of zinc oxide rods manifesting polarity-driven collective luminescence ", PNAS, 107, pp. 13588–13592.

G. Solookinejad, A. S. H. Rozatian, M. H. Habibi. 2016. "Zinc Oxide Thin Films Characterization, AFM, XRD and X-ray Reflectivity", Experimental Techniques, 40, 4, pp. 1297–1306.

R. Serhane, S. Abdelli-Messaci, S. Lafane. 2014. "Pulsed laser deposition of piezoelectric ZnO thin films for bulk acoustic wave devices", Applied Surface Science, 288, pp. 572–578.

Y. Chen, P. I. Reyes, Z. Duan. 2009. "Multifunctional ZnO-Based Thin-Film Bulk Acoustic Resonator for Biosensors", Journal of Electronic Materials, 38, 8, pp. 1605–1611.

Science and Applications of Thin Films, Conference & Exhibition (SATF 2018)
Izmir Institute of Technology, Izmir, Turkey, September 17-21, 2018

Synthesis of $MnCo_2O_4$ nanowires on flexible carbon fiber cloth for high-performance supercapacitors

Yasar Ozkan Yesilbag[a,d,*] , Fatma Nur Tuzluca[a,d] and Mehmet Ertugrul[b,c,d]

[a]*Department of Physics, Erzincan Binali Yıldırım University, Erzincan 24100, Turkey*
[b]*Department of Electrical and Electronics Engineering, Ataturk University, Erzurum 25240, Turkey*
[c]*Department of Nanoscience and Nanoengineering, Ataturk University, Erzurum 25240, Turkey*
[d]*Nanoscience and Nanoengineering Application and Research Center, Ataturk University, Erzurum 25240, Turkey*

* Corresponding author. Tel.: +90 446 224 30 32; fax: +90 446 224 30 16
E-mail address: *oyesilbag@erzincan.edu.tr*

Abstract

$MnCo_2O_4$ nanowires (NWs) array is directly synthesized on carbon cloth using hydrothermal method. The structure, morphology and electrochemical performance of $MnCo_2O_4$ NWs arrays are systematically characterized by X-Ray Diffraction Spectroscopy (XRD), Field Emission Scanning Electron Microscopy (FESEM), Energy Dispersion X-Ray Spectroscopy (EDS), Cyclic Voltammetry (CV) and Galvanostatic Charge/Discharge (GCD). This electrode structure demonstrates good electrochemical performance with a maximum areal capacitance of 0.77 F cm^{-2} at 0.25 mA cm^{-2}. Areal capacitance value after a 4000 charge-discharge cycle, indicating excellent cycle stability 87.3%.

Keywords: $MnCo_2O_4$ nanowires; supercapacitor; carbon fiber cloth; hydrothermal method.

Introduction

Supercapacitors are a new generation of eco-friendly energy storage devices that do not require maintenance and repair, and also have the ability to charge-discharge hundreds of thousands of times, low internal resistance, high power density, extremely long operating life, safe running performance at low/high temperatures (Burke, 2000; Yu et al. 2015; Fic et al. 2018). In addition to prolonging the life of batteries when used with them, these devices optimize the system size and cost, increase the power efficiency in all electric and hybrid electric vehicles and also address a wide range of applications from renewable energy sources, automotive sector (Rolison ve Nazar 2011; Huang et al. 2013a). Supercapacitors store energy by means of ion adsorption at the electrode/electrolyte interface (Electric Double Layer Capacitor–EDLC) or by means of rapid and reversible redox reactions (pseudocapacitor) in the vicinity and the surface of the electrode materials. Pseudocapacitors usually offer much higher specific capacitance than supercapacitor made of carbonaceous materials based on double-layer charge storage (Huang et al. 2013b). Transition metal oxides and hydroxides are the most popular materials for the electrode of supercapacitors because of their high theoretical capacitance, low cost, and low toxicity (Zhang et al. 2015). However, transition metal oxides with low electrical conductivity reduce electrochemical performance after long charge/discharge processes. For this reason, transition metal oxides in the AB_2 spinel structure (two different transition metals A and B; Co, Mn, Ni, and Zn) with two different metal cation ions as the electrode material are preferred (Li et al. 2014; Yunyun et al. 2015; Waghmode and Torane 2017). On the other hand, metal substrate introduces comparable extra weight due to their large mass density, decreasing the actual specific capacitance to a great deal when

considering the substrate weight (Tang et al. 2015). Carbon fiber cloth (CFC), a network of micro-sized carbon fibers, has large surface area, high porosity, flexibility, good electric conductivity, low-weight structure and excellent chemical stability in a wide variety of liquid electrolytes (Huang et al. 2013a; Tang et al. 2015; Xiong et al. 2015). In this work, manganese cobaltite ($MnCo_2O_4$) nanowires were grown homogenously on carbon fiber cloth (CFC) to obtain a binder-free CFC@$MnCo_2O_4$ positive electrode through a simple hydrothermal method followed by calcination.

Materials and Methods

The carbon cloth was cleaned in ultrasonic cleaner for acetone, ethanol and de-ionized water 15 minutes respectively. In a typical synthetic process, 1 mmol of $Mn(NO_3)_2.4H_2O$, 2 mmol of $Co(NO_3)_2.6H_2O$ were dissolved 35 mL de-ionized water under magnetic stirring for 30 min. Then, 2 mmol of NH_4F and 5 mmol urea (CH_4N_2O) were added into the solution successively. The solution with carbon cloth was transferred into a teflon-lined stainless steel autoclave and heated at 100°C for 12 h. After reaction, the precursor electrode was taken out, cleaned with ethanol and deionized water and dried in air. The precursor electrode was then annealed in air at 300 °C and kept for 3 h to obtain $MnCo_2O_4$ nanowires (Figure 1).

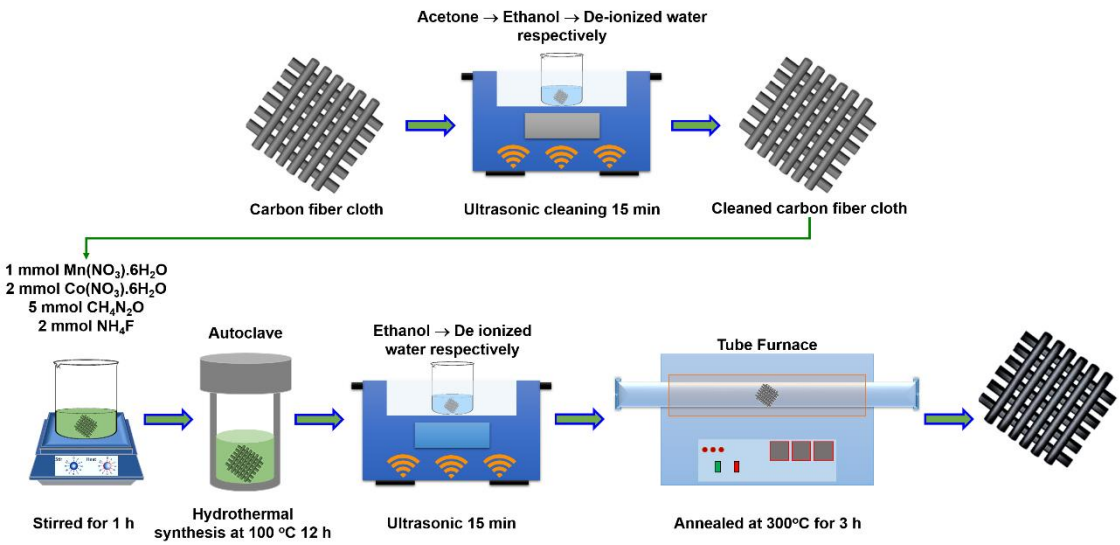

Fig. 1. Schematic illustration synthesis of $MnCo_2O_4$ NWs on CFC substrate.

The crystal structures and morphologies of the $MnCo_2O_4$ NWs were determined by using X-Ray Diffraction (PANalytical Empyrean, Cu-Ka, λ=1.54060 Å), Field Emission Scanning Electron Microscopy (FEI Quanta 450 FEG) and Energy Dispersion X-Ray Spectroscopy (EDAX, AMETEK Materials Analysis Division). The electrochemical performance were determined by Cyclic Voltammetry and Galvanostatic Charge Discharge analyses using a Gamry Reference 1010E potentiostat instrument.

The electrochemical measurements were performed using 1 M KOH aqueous electrolyte solution. Platinum foil (2 × 1 cm^2 in area) and the Ag/AgCl were used as the counter and reference electrodes, respectively. The

$MnCo_2O_4$ electrode (2×1 cm^2) were immersed in electrolyte and were used directly as a working electrode. The electrochemical measurements were performed in a three-electrode electrochemical cell at room temperature. The areal capacitance (C) was calculated by equation (1):

$$C = \frac{Ixt}{AxV} \tag{1}$$

where I is the constant discharge current, t is the discharge time, V is the potential window and A is the electrode area.

Results and Discussion

The crystal structures and morphologies of the $MnCo_2O_4$ nanowires were determined by using X-Ray Diffraction (PANalytical Empyrean, Cu-Kα, λ=1.54060 Å). The XRD diffraction patterns of the sample taken over a 15° to 80° (2θ) range are given in Figure 2. As seen in figure 2, there are 8 peaks – in addition to the 1 peak originating from the carbon cloth substrate – corresponding to the values of (111), (220), (311), (222), (400), (422), (511) and (440) that are the crystal planes of the $MnCo_2O_4$ nanowires according to JCPDS Card No: 23-1237.

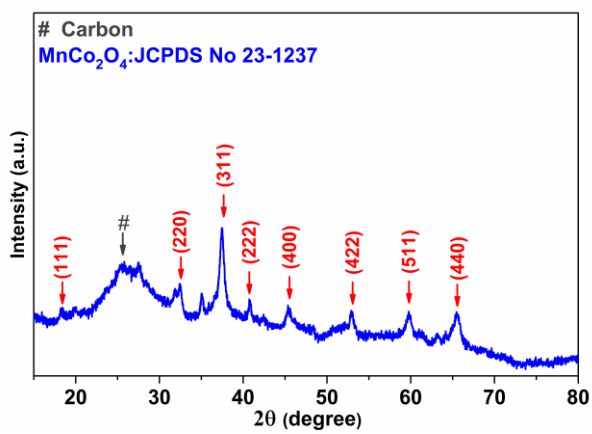

Fig. 2. XRD patterns of $MnCo_2O_4$ NWs.

Figure 3 and Figure 4 shows the FESEM images and EDS analyzes of the morphology of $MnCo_2O_4$ NWs arrays respectively. As seen in figure 3, high density of $MnCo_2O_4$ nanowires were formed and grown uniformly on the carbon cloth after calcination. The purity and composition of the $MnCo_2O_4$ NWs were further confirmed by EDS analysis shown in figure 4. EDS spectrum revealing the existence of C, O, Mn and Co elements in the electrode material and the atomic contents are 33.4%, 42.2%, 2.67% and 21.69%, respectively.

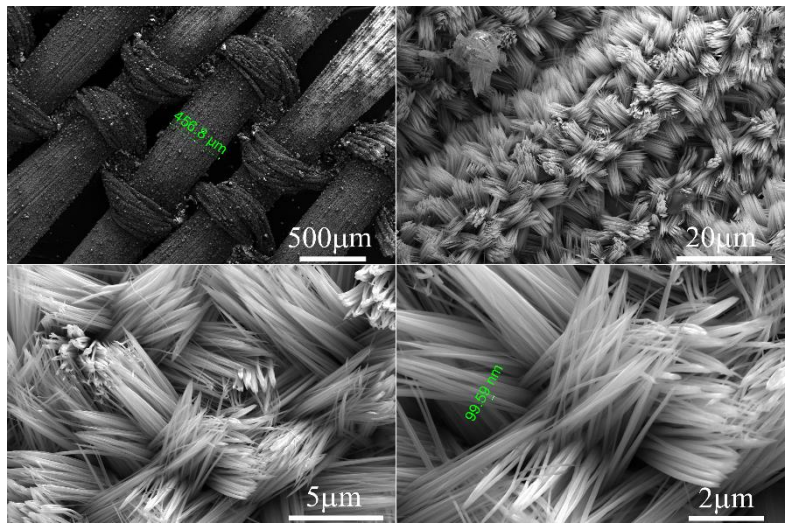

Fig. 3. Low and high magnification FESEM images of $MnCo_2O_4$ NWs.

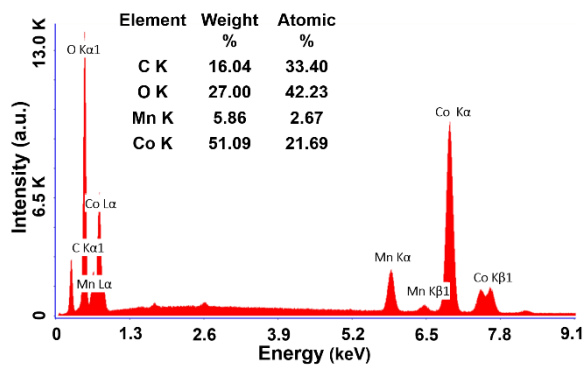

Fig. 4. EDS analyzes of $MnCo_2O_4$ NWs.

Electrochemical properties of $MnCo_2O_4$ electrode in 1 M KOH aqueous electrolyte are shown in Figure 5-7. CV measurements of the CFC@$MnCo_2O_4$ electrode were taken in the 0 to 0.5 V potential range with different scan rate (Figure 5a-b). In the CV curve taken at 5 mV s^{-1}, the contribution from the substrate material (carbon cloth) is negligible Figure 5a. The increase of scan rate allows access ions only on the external surface and, in this case, decreasing the charge storage values. The charge storage process for $MnCo_2O_4$ in a KOH aqueous electrolyte solution is expressed by the reactions in equation (2) and (3):

$$MnCo_2O_4 + OH^- + H_2O \rightarrow 2CoOOH + MnOOH + e^- \quad (2)$$

$$MnOOH + OH^- \rightarrow MnO_2 + H_2O + e^- \quad (3)$$

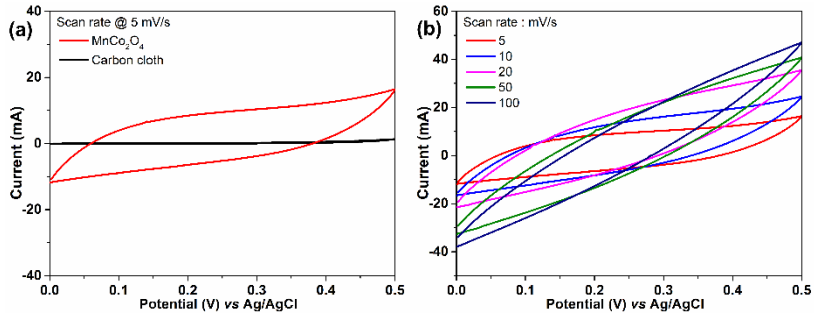

Fig. 5. CV measurements of (a) the bare CFC and CFC@$MnCo_2O_4$ electrode @ 5mV s^{-1}, (b) CFC@$MnCo_2O_4$ electrode @ 5-100 mV s^{-1}.

In order to evaluate the areal capacitance, GCD measurements were performed. The GCD curves of the $MnCo_2O_4$ electrode in the voltage range of 0 to 0.4 V at various current densities of 0.25 to 5 mA cm^{-2} are illustrated in Figure 6a. The areal specific capacitance of the CFC@$MnCo_2O_4$ electrodes are calculated to be 0.77, 0.67, 0.55, 0.43 and 0.25 F cm^{-2} at current densities of 0.25, 0.5, 1, 2 and 5 mA cm^{-2}, respectively, according to equation (1) (Figure 6b). The areal capacitance gradually decreased at higher current density due to the incremental voltage drop and insufficient active material involved in redox reaction at a higher current density. At the end of 4000 charge discharge cycles, the change in capacitance value was found as 87.3% and indicating excellent cycle stability (Figure 7a). Figure 7b shows the Nyquist plots of the EIS spectra for the $MnCo_2O_4$ electrodes and the inset shows equivalent circuit and values. At the high frequency, the intersection of the curve at the real part (Z') indicates the resistance of the electrochemical system which is about 1 Ω. In the low frequency area, the slope of the curve shows the constant phase element (CPE), which represents the electrolyte diffusion to the electrode surface. Experimental data and the expected equivalent circuit are consistent with each other. Equivalent series resistance (**R_s**) and charge transfer resistance (**R_{ct}**) values obtained from this circuit were found to be 0.7 and 7.6 Ω respectively.

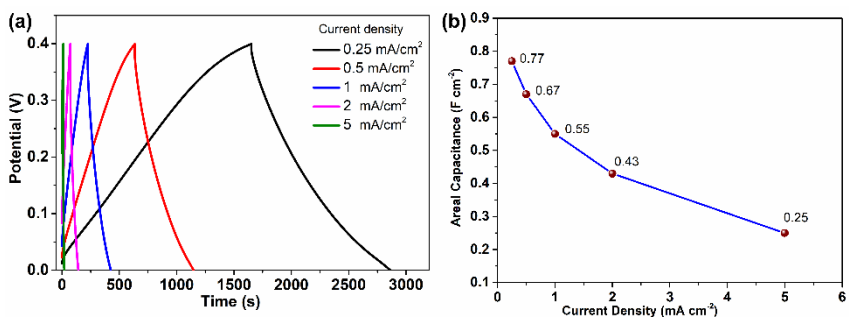

Fig. 6. (a) GCD curves and (b) the areal capacitances vs different current densities of $ZnCo_2O_4$ NWs.

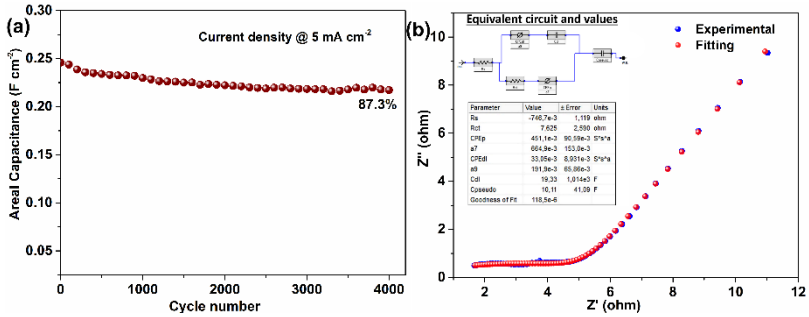

Fig. 7. (a) Long term cycling stability, (b) EIS measurement and inset the equivalent circuit and values.

Conclusion

In conclusion, $MnCo_2O_4$ NWs were synthesized on carbon cloth by hydrothermal method. According to GCD measurements at 0.25 mA cm^{-2} current density, areal capacitance were obtained 0.77 F cm^{-2} for $MnCo_2O_4$ NWs. Voltammetric and galvanostatic results indicate that the porous structure and large surface area of the carbon fiber cloth and also presence of the $MnCo_2O_4$ nanowires play are mainly responsible for obtaining optimum capacitance values and long cycle life. This electrode design can be extended to grow other mesoporous metal oxides on the substrate to fabricate high-performance supercapacitor electrode. Chemically precipitated $MnCo_2O_4$ nanowires on carbon fiber cloth were employed as the electro-active materials for the supercapacitor. This study also gives different point of view into the design of metal oxide heterostructure electrodes used in a various range of applications.

Acknowledgements

This research is partially supported by Erzincan Binali Yıldırım University Scientific Research Project Unit (Project number: FBA-2017-468).

References

Burke, A. (2000). Ultracapacitors: why, how, and where is the technology. Journal of power sources, 91(1), 37-50.

Fic, K., Platek, A., Piwek, J., & Frackowiak, E. (2018). Sustainable materials for electrochemical capacitors. Materials Today.

Huang, L., Chen, D., Ding, Y., Feng, S., Wang, Z. L., & Liu, M. (2013b). Nickel–cobalt hydroxide nanosheets coated on $NiCo_2O_4$ nanowires grown on carbon fiber paper for high-performance pseudocapacitors. Nano letters, 13(7), 3135-3139.

Huang, L., Chen, D., Ding, Y., Wang, Z. L., Zeng, Z., & Liu, M. (2013a). Hybrid composite $Ni(OH)_2$@$NiCo_2O_4$ grown on carbon fiber paper for high-performance supercapacitors. ACS applied materials & interfaces, 5(21), 11159-11162.

Li, L., Zhang, Y. Q., Liu, X. Y., Shi, S. J., Zhao, X. Y., Zhang, H., ... & Tu, J. P. (2014). One-dimension $MnCo_2O_4$ nanowire arrays for electrochemical energy storage. Electrochimica Acta, 116, 467-474.

Rolison, D. R., & Nazar, L. F. (2011). Electrochemical energy storage to power the 21st century. Mrs Bulletin, 36(7), 486-493.

Tang, Q., Chen, M., Wang, L., & Wang, G. (2015). A novel asymmetric supercapacitors based on binder-free carbon fiber paper@nickel cobaltite nanowires and graphene foam electrodes. Journal of Power Sources, 273, 654-662.

Waghmode, R. B., & Torane, A. P. (2017). Role of deposition time on synthesis of high-performance NiCo2O4 supercapacitors. Journal of Materials Science: Materials in Electronics, 28(13), 9575-9583.

Xiong, W., Hu, X., Wu, X., Zeng, Y., Wang, B., He, G., & Zhu, Z. (2015). A flexible fiber-shaped supercapacitor utilizing hierarchical $NiCo_2O_4$@polypyrrole core–shell nanowires on hemp-derived carbon. Journal of Materials Chemistry A, 3(33), 17209-17216.

Yu, Z., Tetard, L., Zhai, L., & Thomas, J. (2015). Supercapacitor electrode materials: nanostructures from 0 to 3 dimensions. Energy & Environmental Science, 8(3), 702-730.

Yunyun, F., Xu, L., Wankun, Z., Yuxuan, Z., Yunhan, Y., Honglin, Q., ... & Fan, W. (2015). Spinel $CoMn_2O_4$ nanosheet arrays grown on nickel foam for high-performance supercapacitor electrode. Applied Surface Science, 357, 2013-2021.

Zhang, Y., Li, L., Su, H., Huang, W., & Dong, X. (2015). Binary metal oxide: advanced energy storage materials in supercapacitors. Journal of Materials Chemistry A, 3(1), 43-59.

This page intentionally left blank.

Efficiency Analysis of CZTS Based Solar Cells

A Cantas[1,2 *], G Aygun[1]

1 Department of Physics, Izmir Institute of Technology, Urla 35430, Izmir, Turkey
2 Department of Electric and Energy, Pamukkale University, Kınıklı 20160, Denizli, Turkey

*Corresponding author E-mail address: abagdas@pau.edu.tr
Phone: +90-258-2123788-1201

Abstract

Cu_2ZnSnS_4 (CZTS) thin films were grown on Mo-coated soda lime glass (SLG) substrate by sulfurization of DC magnetron-sputtered Zn, Sn and Cu metallic precursors. The sulfurization occurred under a sulfur atmosphere at 550 °C for 30 and 60 min. To obtain efficient solar cells, understanding the surface composition of the CZTS absorber layer is necessary. With this aim, X-ray photoelectron spectroscopy was used to investigate the surface quantification of CZTS absorber layers. XRD technique was used to detect crystal structure of grown CZTS films. For device characterization, CZTS-based solar cells were prepared using a SLG/Mo/CZTS/CdS/ZnO/AZO solar cell configuration. Device analysis showed that electrical characteristics of solar cells strongly depend on the surface composition of absorber layer.

[keywords] Cu_2ZnSnS_4 (CZTS), thin film solar cells, magnetron sputtering, XPS.

1. Introduction

The quaternary compound of Cu_2ZnSnS_4 (CZTS) is a newly explored p-type semiconductor photovoltaic material which attracts so much attention in photovoltaic industry due to its low cost, earth abundant properties as well as consisting of non-toxic elements contrary to other chalcogenide based solar cells such as $CuIn(Ga)(S,Se)_2$ (CIGS) and CdTe. Although, CZTS studies have been newly started, recently 12.6% efficiency has been achieved which demanding further improvement [1]. The CZTS thin films show p-type conductivity, high absorption coefficient (10^4 cm^{-1}) and a band gap of 1.45-1.5 eV that is ideal to achieve the highest solar-cell conversion efficiency [2]. The high efficient Cu_2ZnSnS_4 (CZTS) based thin film solar cells needs the synthesis of phase pure CZTS absorbers [3]. Due to the difficulties of preparation pure phase CZTS films (i.e., a film lack of secondary phases), the structural and compositional properties of CZTS films must be systematically studied. In this work, Mo coated soda lime glasses (SLG) were used as a substrates. CZTS absorber layers were grown on Mo coated SLG substrates using two stages which are the magnetron sputtering of metallic precursors, followed by a heat treatment under sulfur vapor atmosphere. To obtain CZTS absorber films, all precursors were sulfurized using sulfur powder at 550 °C for 30 and 60 min under Ar gas atmosphere. The surface quantification of CZTS films were investigated from X-Ray photoelectron spectroscopy (XPS) quantitive analysis. CZTS based solar cells were fabricated using

SLG/Mo/CZTS/CdS/ZnO/AZO structure. This study revealed a correlation between the surface composition of absorber layer and efficiency of CZTS based solar cells.

2. Experimental

2.1 Absorber layer preparation

In this work the precursor of CZTS thin films were deposited sequentially stacked. Mo-coated SLGs were used as substrates. The Mo-coated SLG substrates were cleaned by ultrasonication in acetone, ethanol, and distilled water for 5 min each, and then exposed to N_2 plasma for 15 min at a 100 W RF bias. CZTS absorber layers with thickness between 1.2 and 1.4 μm were grown by a two-step process. In the first step, 630 nm thick CZT metallic precursors were sputtered on Mo coated SLG substrates from bottom to top SLG/Mo/Cu(120 nm)/Sn/Zn/Cu(55 nm) by a multi-target DC magnetron-sputtering system on Mo-coated SLG substrates. As shown in Figure 1, multi-target DC magnetron-sputtering system consists of three two-inch targets and a rotating sample holder. During a growth, for each target of Cu (99.999%), Sn (99.999%), and Zn (99.99%), 41 W, 40 W, and 20 W DC powers were used, respectively. The magnetron sputtering chamber was evacuated down to about 10^{-6} Torr pressures by a turbo molecular pump. After reaching the required pressure levels, a constant flow rate of 30 sccm Ar gas was send to the chamber using a mass flow controller. During the deposition process, operating pressure was 1.5×10^{-2} Torr. For the metallic precursors, SLG/Mo/Cu (120 nm)/Sn/Zn/Cu (55 nm) stacking order was selected in order to decrease the Sn loss and to prevent ZnS phase formation at the surface of the absorber layer during the sulfurization. The thickness of CZT metallic precursor was measured by A Veeco DEKTAK 150 profilometer.

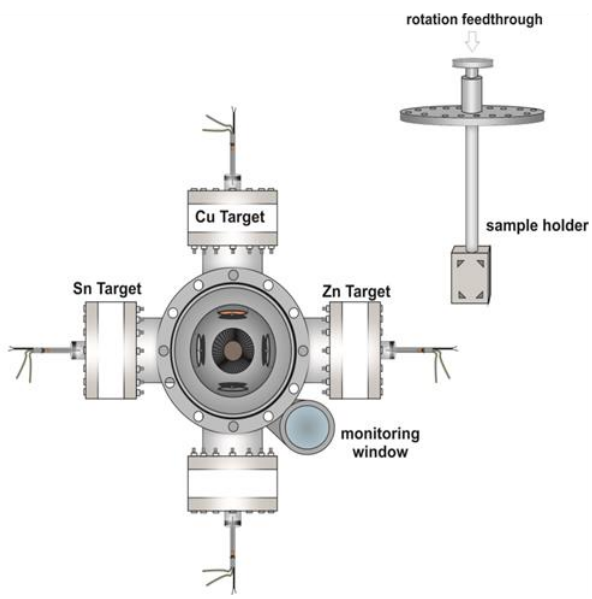

Figure 1. Top view of magnetron sputtering system [2]

CZT precursors were annealed under S vapour and Ar atmosphere to obtain CZTS p-type absorber layer. During the sulfurization procedure, 600 mg sulfur powder and 100 sccm Ar gas was used. The sulfurization was performed at 550 °C for 30 and 60 min inside a quartz glass tube in a furnace (Figure 2). After the sulfurization, the crystal structures of the CZTS films were determined using X-Ray Diffraction (XRD) in the Bragg-Brentano focusing geometry on a Phillips X'Pert Pro X-Ray diffractometry, with Cu Kα radiation (λ=1.5406 Å). XRD measurements were taken from 2θ=20–80° with step size of 0.016° for all samples. SPECS Phoibos 150 3D-DLD model X-ray photoelectron spectroscopy (XPS) was used to identify the core level of constituent elements. For the XPS measurements of the CZTS films, monochromatic Mg *Kα* radiation source (*hv* = 1254 eV) with a power of 200 W and take off angle of 45°was used. During the measurement, the analyzer pass energy, the step size, dwell time and the spot size were set to 30 eV, 0.05 eV, 2 s and 2 mm, respectively,

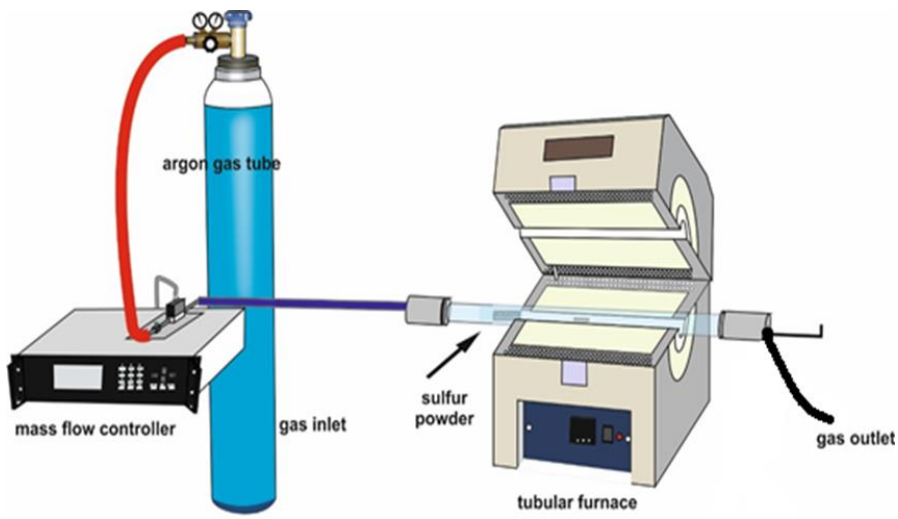

Figure 2. Sulfurization system [4]

2.2. Buffer Layer Preperation

In this work, n-type CdS was used as a buffer layer. CdS buffer layer was deposited using chemical bath deposition (CBD) technique. The bath solution was prepared using 1.2 ml of 0.5 M cadmium acetate ($Cd(CH_3CO_2)_2$), 6 ml of 2M ammonium acetate ($NH_4CH_3CO_2$), 7 ml of 0.5 M thiourea $SC(NH_2)_2$, and 12 ml of 14.4 M (25% of NH_3 solution) ammonium hydroxide (NH_4OH) and 270 ml of de-ionized water. The CdS buffer layer was deposited on CZTS absorber layer at 85 C for 60 min.

2.3. Solar cell device fabrication

In this research, substrate structure was used for fabrication of solar cells. As window layers, i-ZnO and Al doped ZnO (AZO) were deposited on SLG/Mo/CZTS/CdS layer stacks. The window layers ZnO and

AZO were deposited using single targets by RF and DC magnetron sputtering, respectively. The thickness of ZnO and AZO layers were 40 nm and 300 nm, respectively. The electrical performance of SLG/Mo/CZTS/CdS/ZnO/AZO solar cells was investigated using the current–voltage (*I–V*) measurement system. *I–V* characteristics were measured at room temperature by A Keithley 2182A Source Meter and Labview program. The calibration of our system was done using a Newport 91192 model 300 W solar simulator under ambient conditions (1 kW m^{-2}, AM 1.5G illumination, room temperature).

3. Results

3.1. X-Ray Diffraction Analysis of CZTS

Figure 3 shows the XRD analysis of CZTS films. XRD pattern confirms the existence of kesterite phase CZTS. Diffraction peaks detected at 37.0, 29.67, 37.96, 44.99, 58.97, 69.23 and 76.44°can be indexed to (202), (103), (211), (105), (224), (008) and (332) crystallographic directions, respectively.

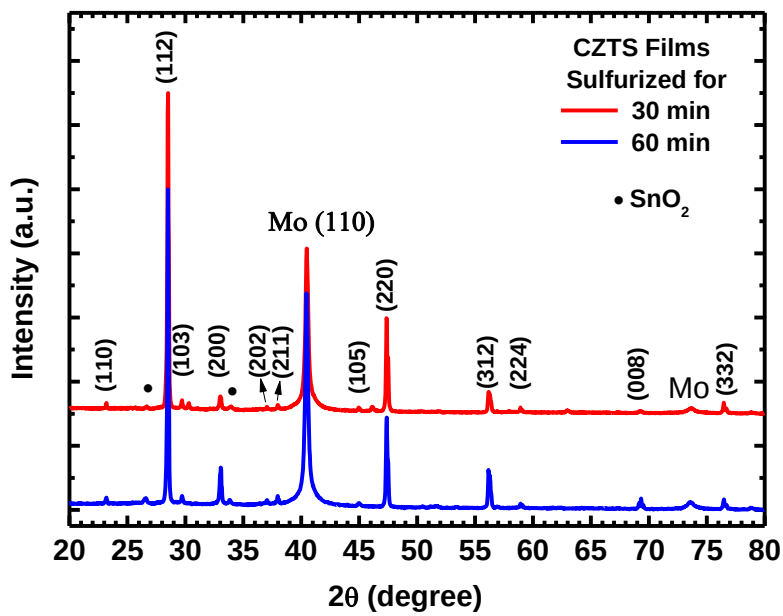

Figure 3. XRD analysis of CZTS films.

XRD analysis showed that both CZTS films have good crystallinity with preferential orientation of kesterite CZTS along (112) direction. Both CZTS films have extra peaks detected at 26.61° and 33.89°, which are attributed to presence of tin dioxide (SnO_2) phase at (110) and (101) crystallographic directions (JCPDS 041-1445), respectively. For the CZTS films, the segregation of SnO_2 at the grain boundaries is reported [5]. According to XRD analysis, sulfurization time The XRD analyzes of the samples that were sulfurized at different times were almost the same.

3.2. X-Ray Photoelectron Spectroscopy Analysis of CZTS

The XPS spectra of CZTS films were analyzed so as to identify the surface composition distribution and chemical bonding states of the constituent elements. The high resolution spectra of C*1s*, S*2p* Cu*2p*, Sn*3d* and Zn*2p* valence regions were measured in detail and calibrated with respect to C*1s* peak at 284.6 eV [2]. In order to identify the atomic multivalency of each element in CZTS, high resolution spectra were de-convoluted. In addition, to calculation the atomic concentration of constituent elements, the area of peaks and sensitivity factors of each elements provided by the CASAXPS software were used. Before the de-convolution, the Shirley type background was subtracted to the high resolution spectra of each elements and Gaussian-Lorentzian product GL(p) function was used by considering the theoretical assumptions. The Zn, Cu, S *2p* and Sn *3d* peaks occur as doublets of 2*p3/2*, 2*p1/2* and 3d*5/2*, 3d*3/2*.

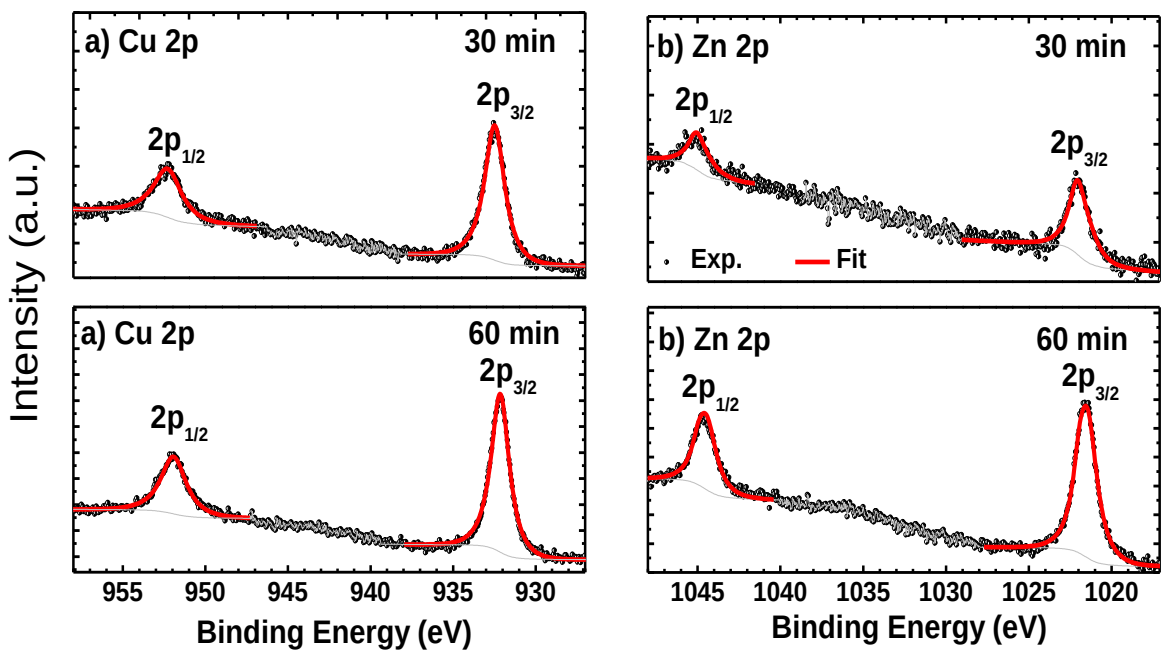

Figure 3. XPS peak fitting results of CZTS films a) Cu, b) Zn *2p* valence regions.

Figure 3. (a) and (b) demonstrates the peak fitting results of Cu and Zn *2p* valence regions, respectively of CZTS films. In Figure 3 (a), the Cu *2p* core levels are seen as Cu *2p1/2* and *2p3/2* coupled doublets with peak splitting of 19.8 eV which is indicative of monovalent copper, Cu (I), and it is consistent with the reported literature values [6]. During the peak fitting of Cu *2p* regions, GL(90) line shape was used and the results were listed in Table 1. *2p3/2* peak positions are detected at 932.5 and 932.2 eV for the CZTS films sulfurized for 30 and 60 min, respectively. Cu *2p3/2* peak detected between 932.0 [7] and 932.5 eV [8] position assign the +1 oxidation state of Cu. The intensity of Cu 2p peaks of CZTS film sulfurized for 60 min were higher than that of the CZTS film sulfurized for 30 min. This result indicated that the amount of Cu element increased at the film surface with sulfurization time. This might be the result of constituent elemental loss during the sulfurization. Figure 3 (b) demonstrates Zn *2p* spectra of both CZTS films. This region was fitted using GL(90) line shape and consist of 2*p1/2* and 2*p3/2* with a doublet separation of 23.0 eV which can

be attributed to bivalent zinc Zn (II) [9]. Figure 3 (b) shows peak fitting of Zn *2p* valence regions of both CZTS films. The *2p3/2* peaks were appeared at 1021.9 and 1021.6 eV for the films sulfurized for 30 and 60 min, respectively. These peaks could be attributed to the existence of Zn^{2+}. The peak position of Zn *2p3/2* attributes to Zn in CZTS or Zn in ZnO. However, the formation of ZnO phase was not detected by XRD analysis. From Table 1, it is clearly seen that the Cu and Zn $2p_{3/2}$ peak positions shifted to lower binding energy side with increasing the sulfurization time of CZTS. The reason of this shifting is not clear.

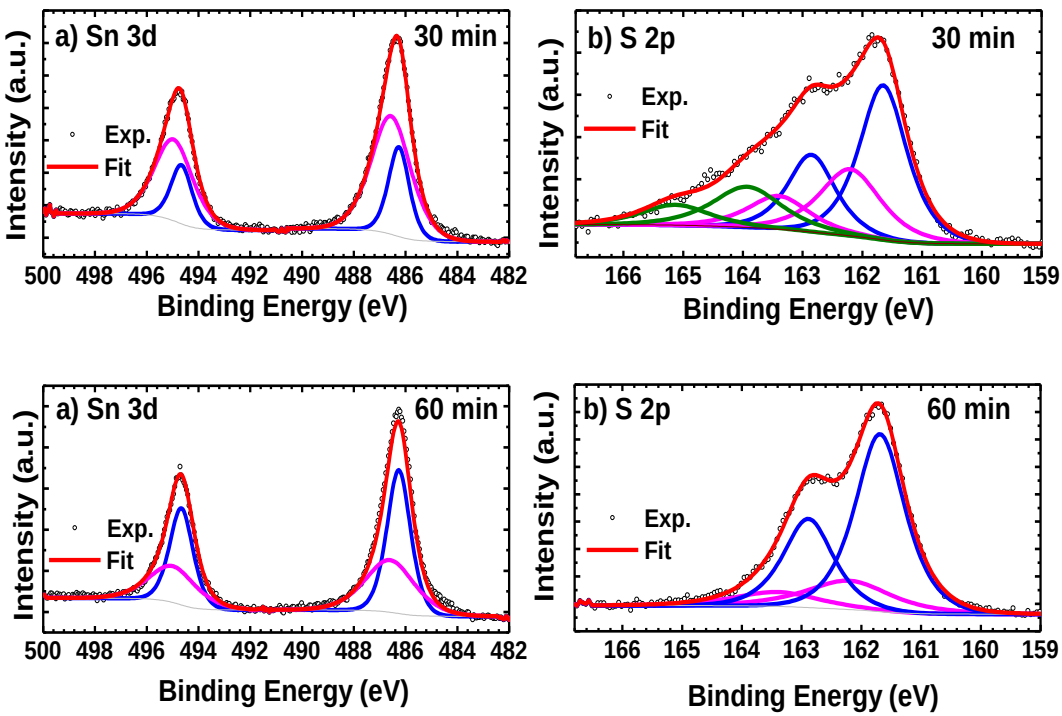

Figure 4. XPS peak fitting results of CZTS films a) Sn 3d, b) S *2p* valence regions.

The peak fitting analysis of Sn *3d* core level (Figure 4 (a)) was done according to GL(55) line shape and the spectra were observed as 3*d3/2* and 3*d5/2* doublets with peak separation of 8.4 eV. Deconvolution of both CZTS films showed more than one valence states. As a result of de-convolution, one of Sn *3d5/2* peak was observed at 486.6 for both CZTS films. These peak positions match with Sn *3d5/2* peak of SnO [10] phases. The other Sn *3d5/2* peaks were observed at 486.3 for both CZTS films. In the literature, Sn *3d5/2* peak is given at 485.3 [9], 486.2 [11] and 486.4 (Hurtado et al., 2014) eV which confirms the Sn(IV) electronic state as expected for CZTS formation. The Sn 3d peaks of CZTS film sulfurized for 60 min were broader than that of CZTS film sulfurized for 30 min. This result indicates that the amount of Sn element decreases with sulfurization time which is a result of Sn loss. The S *2p* spectra (Figure 4 (b)) observed from 160 to 164 eV assigns to the S in metal sulfides [12]. GL(75) line shape was used to fit this valence region. The peak fitting result of all S *2p* spectra show more than one *2p3/2* and *2p1/2* doublets each of which is constrained to have a binding energy difference of 1.2 eV. The S *2p* region of CZTS film sulfurized for 30 min is wider than the other film. This represents the existence of additional S peaks. Therefore, the peak

fitting results of this film contained three couples of S *2p* peaks. The detected peak at 161.6 and 161.7 eV attributed to monosulfide S^{-2} [12] as expected for CZTS structure. An additional peak was observed for both film at 162.2 Ev, respectively. The position of these peaks were assigned to disulfide (S_2^{-2}) [2]. At the higher binding energy side, for the film sulfurized for 30 min, the peak at 163.9 eV was detected which corresponding to S-S bonds [13]. Table 1 summarized the peak fitting results of both CZTS film. Both Zn and Cu 2p valence peaks for the CZTS film sulfurized for 30 min were detected at lower binding energy side than that of the CZTS film sulfurized for 60 min. This might be result of the presence of different structure at the film surface. The existence of third S 2p valance state for the film sulfurized for 30 min represents the higher amount of sulfur at the surface than the other CZTS film. After the deconvolution process, the surface quantification of CZTS films were calculated using equation 1 given below.

$$C_x = \frac{(I_x/S_x)}{\sum I_i/S_i} * 100 \quad \text{(Eq. 1)}$$

In Eq. 1, C_x, I_x and S_x are the atomic %, area and the atomic sensitivity factor of element x which constitutes the sample. The I_i and the S_i are the area and the atomic sensitivity factor of i-th element inside the sample. The atomic sensitivity of each element is obtained from CASAXPS software. Table 2 gives the quantification results.

Table 1. Peak fitting results of main XPS core levels of CZTS films.

Sample Sulfurization Time (min)	**Zn $2p_{3/2}$ (eV)**	**Cu $2p_{3/2}$ (eV)**	**1st Sn $3d_{5/2}$ (eV)**	**2nd Sn $3d_{5/2}$ (eV)**	**1st S $2p_{3/2}$ (eV)**	**2nd S $2p_{3/2}$ (eV)**	**3rd S $2p_{3/2}$ (eV)**
30	1021.9	932.5	486.3	486.6	161.7	162.2	163.9
60	1021.6	932.2	486.3	486.6	161.7	162.2	-

Table 2. The surface quantification of CZTS films.

Sample Sulfurization Time (min)	**Atomic %**				**Cu/(Zn+Sn)**	**Zn/Sn**	**S/Metal**
	Cu	**Zn**	**Sn**	**S**			
30	17.8	8.3	19.4	54.5	0.6	0.4	1.2
60	19.0	19.3	18.3	43.4	0.5	1.1	0.8

In Table 2, it is seen that CZTS film sulfurized for 60 min is sulfur deficient at the surface. However, the situation is opposite for the CZTS film sulfurized for 30 min. Sulfur vacancy (V_S) is important parameter for the CZTS conductivity. Vs is a donor type defect and it is dominantly observed due to its low formation energy. The S-poor CZTS film results high concentration of V_S which might change the conduction type of CZTS from p-type to n-type as well as decrease the holes concentration [14]. Therefore, high content S is important to diminish V_S and obtain p-type conductivity of CZTS. Based on these facts, short sulfurization duration is better in terms of conductivity of CZTS.

3.3. CdS Buffer Layer Characterization

CdS buffer layers were deposited using chemical bath deposition technique (CBD). The thickness of CdS layers were measured using spectroscopic ellipsometer (SE). According to SE results, CdS film deposited for 60 min has approximately 120 nm thickness. In the visible wavelength range (400-700 nm), the optical transmission measurement of CdS showed transmission in the range of 70 %. According to transmission measurement, the bandgap of film was calculated as 2.46 eV [15].

3.4. Device Characterization

In this work using both CZTS films, SLG/Mo/CZTS/CdS/ZnO/AZO solar cells were fabricated in this structure. Figure 5 (a) and (b) demonstrate J-V curve of solar cells fabricated using CZTS films sulfurized for 30 and 60 min, respectively. As seen Fig. 5s, the J-V curve under dark and light showed the same results.

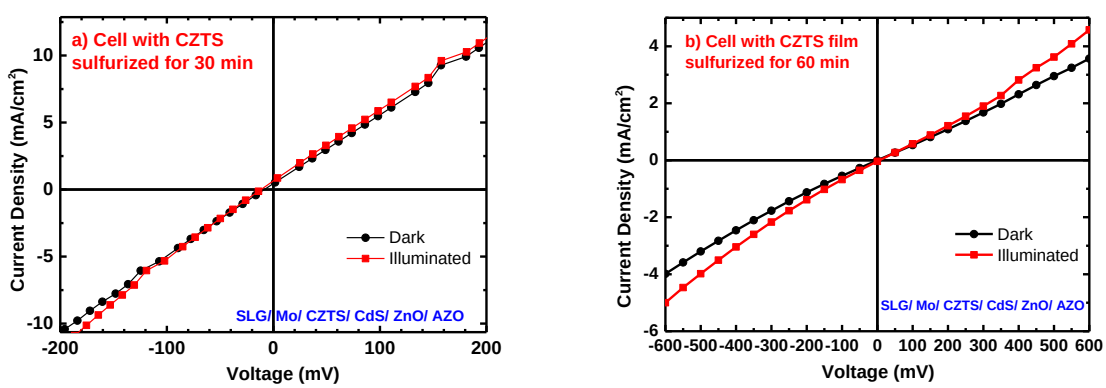

Figure 5. J-V characteristics of solar cells with CZTS films sulfurized for a) 30 and b) 60 min.

There may be many reasons why efficiency cannot be obtained from constructed solar cells. The bandgap of SnO_2 is 3.6 eV. Since SnO_2 has higher E_g than CZTS, the positive CBO might be formed. For the CZTS(e) solar cells, it has been reported that the SnO_2 phase occurs at the grain boundaries and the CBO with CZTS(e) absorber layer was calculated between 0.6 and 0.8 eV [16]. Due to the positive CBO value, the barrier is formed and neither electrons nor holes trapping is detected. The other reason might be related with

amount of sulfur. From the XPS surface quantification, it was detected that CZTS film sulfurized for 60 min was sulfur deficient. When S concentration is lower than 50%, it means that the CZTS formation reaction is not completed well. Sulfur vacancies might decrease the p-type conductivity of CZTS film. Another reason which did not searched in this work might be poor quality interface between CdS buffer and CZTS absorber layer. The quality of buffer/absorber interface is highly important in terms of charge carrier transition at the junction. Therefore, XPS depth profile is necessary to shed on light to this poor J-V characteristics.

4. Conclusions

In this study, two-stage process were used to grown CZTS absorber layers on Mo-coated SLG substrates. Firstly, metallic precursor was formed from sequentially deposition of Cu–Zn–Sn metallic layers by a DC magnetron-sputtering technique and secondly, precursors were annealed under an Ar + S_2(g) atmosphere for 30 and 60 min. XRD analysis of CZTS films revealed that the sulfurization time did not showed remarkable difference in the crystal structure of films. From the diffraction peaks, the presence of kesterite CZTS was detected for both films. However, the formation of undesired SnO_2 phase was also detected by XRD. By XPS quantification analysis, we have also demonstrated that surface composition of CZTS films highly depends on sulfurization time. Sulfur deficiency which might decrease p-type conductivity of absorber film was detected for the CZTS film sulfurized for 60 min. SLG/Mo/CZTS/CdS/ZnO/AZO solar cells were fabricated using both CZTS films. Both solar cells showed poor J-V characteristic. This might be a result of formation of impurity (SnO_2) in the CZTS absorber. Since CdS/CZTS interface has highly significant role in charge carrier transport in the junction region, XPS depth profile analysis should be performed to explain poor J-V characteristics.

Acknowledgements

This research is financially supported by TUBITAK with the project number of 114F341 and by the Pamukkale University with BAP project number of 2018HZDP041.

References

[1] Wang, W., Winkler, M. T., Gunawan, O., Gokmen, T., Todorov, T. K., Zhu, Y., & Mitzi, D. B. (2014). Device characteristics of CZTSSe thin-film solar cells with 12.6% efficiency. *Advanced Energy Materials*, *4*(7), 1301465.

[2] Yazici, S., Olgar, M. A., Akca, F. G., Cantas, A., Kurt, M., Aygun, G., Tarhan, E., Yanmaz, E., Ozyuzer, L. (2015). Growth of Cu_2ZnSnS_4 absorber layer on flexible metallic substrates for thin film solar cell applications. *Thin Solid Films*, *589*, 563-573.

[3] Buldu, D. G., Cantas, A., Turkoglu, F., Akca, F. G., Meric, E., Ozdemir, M., ... & Aygun, G. (2018). Influence of sulfurization temperature on Cu2ZnSnS4 absorber layer on flexible titanium substrates for thin film solar cells. *Physica Scripta*, *93*(2), 024002.

[4] Cantas, A., Turkoglu, F., Meric, E., Akca, G., Ozdemir, M., Tarhan, E., ... & Aygun, G. (2018).

Importance of CdS Buffer Layer Thickness on Cu2ZnSnS4 Based Solar Cell Efficiency. *Journal of Physics D: Applied Physics*.

[5] Hazama, H., Tajima, S., Masuoka, Y., Asahi, R. (2016). Transport properties of the Cu_2ZnSnS_4 bulk systems: Effects of nonstoichiometry and defect formation. *Journal of Alloys and Compounds, 657*, 179-183.
[6] Mali, S. S., Patil, B. M., Betty, C. A., Bhosale, P. N., Oh, Y. W., Jadkar, S. R., . . . Patil, P. S. (2012). Novel synthesis of kesterite Cu_2ZnSnS_4 nanoflakes by successive ionic layer adsorption and reaction technique: characterization and application. *Electrochimica Acta, 66*, 216-221.
[7] Moholkar, A., Shinde, S., Babar, A., Sim, K.-U., Lee, H. K., Rajpure, K., . . . Kim, J. (2011). Synthesis and characterization of Cu_2ZnSnS_4 thin films grown by PLD: solar cells. *Journal of Alloys and Compounds, 509*(27), 7439-7446.
[8] Hurtado, M., Cruz, S., Becerra, R., Calderón, C., Bartolo-Pérez, P., & Gordillo, G. (2014, June). *XPS analysis and structural characterization of CZTS thin films prepared using solution and vacuum based deposition techniques.* Paper presented at the Photovoltaic Specialist Conference (PVSC), 2014 IEEE 40th (pp. 0368-0370) IEEE.
[9] Deepu, D. R., Rajeshmon, V. G., Kartha, C. S., Vijayakumar, K. P., Murli, C., Bhattacharyya, D., & Gadkari, S. (2014, April). *XPS depth profile study of sprayed CZTS thin films.* Paper presented at the AIP Conference Proceedings, (pp. 1666-1668). AIP.
[10] Kwoka, M., & Krzywiecki, M. (2017). Impact of air exposure and annealing on the chemical and electronic properties of the surface of SnO_2 nanolayers deposited by rheotaxial growth and vacuum oxidation. *Beilstein Journal of Nanotechnology, 8*, 514.
[11] Shin, S. W., Pawar, S., Park, C. Y., Yun, J. H., Moon, J.-H., Kim, J. H., & Lee, J. Y. (2011). Studies on Cu_2ZnSnS_4 (CZTS) absorber layer using different stacking orders in precursor thin films. *Solar Energy Materials and Solar Cells, 95*(12), 3202-3206.
[12] Das, S., Frye, C., Muzykov, P. G., & Mandal, K. C. (2012). Deposition and characterization of low-cost spray pyrolyzed Cu_2ZnSnS_4 (CZTS) thin-films for large-area high-efficiency heterojunction solar cells. *ECS Transactions, 45*(7), 153-161.
[13] Krylova, V., & Andrulevičius, M. (2009). Optical, XPS and XRD studies of semiconducting copper sulfide layers on a polyamide film. *International Journal of Photoenergy, 2009*, 304308.
[14] Yeh, M.-Y., Lei, P.-H., Lin, S.-H., & Yang, C.-D. (2016). Copper-Zinc-Tin-Sulfur Thin Film Using Spin-Coating Technology. *Materials, 9*(7), 526.
[15] Cantaş Bağdaş, A. (2017). X-ray photoelectron spectroscopy analysis of magnetron sputtered Cu2ZnSnS4 based thin film solar cells with CdS buffer layer.
[16] Sardashti, K., Haight, R., Gokmen, T., Wang, W., Chang, L. Y., Mitzi, D. B., & Kummel, A. C. (2015). Impact of Nanoscale Elemental Distribution in High-Performance Kesterite Solar Cells. *Advanced Energy Materials, 5*(10), 1402180.